DISS. ETH NO. 29379

Effects of Earthquakes on the Mechanics of Active Landslides

Submitted to obtain the title of

DOCTOR OF SCIENCES

(Dr. sc. ETH Zurich)

Presented by

MARC SÉBASTIAN KOHLER

MSc Civil Eng., ETH Zurich

born on 06.10.1991

Accepted on the recommendation of

Prof. Dr. A. M. Puzrin
Prof. Dr. J. Gaume
Prof. Dr. I. Einav

2023

To my grandfather

Abstract

Landslides are a global threat in mountainous regions, causing thousands of fatalities every year. Less attention is paid to active, slow-moving landslides because they do not usually manifest themselves in catastrophic events, but can cause severe damage to buildings and infrastructures. They are characterised by a mobile state that is highly sensitive to environmental influences. As a result, they are often thought to be particularly susceptible to seismic acceleration, which is even supported by conventional simplified models. Unfortunately, corresponding field observations are very rare, but they tend to show only small co-seismic landslide displacements. The potential consequences of a landslide collapse, for instance on the flank of a water reservoir, underlines the importance of reliable mechanical models and a better understanding of the behaviour.

This thesis presents a framework based on the material point method for the large-deformation seismic response analysis and in particular for the simulation of active landslides. This approach is applied to the slow-moving La Sorbella landslide in Italy, where co-seismic displacements were recorded during three moderate earthquakes. The results not only validates the landslide model, but also shows that geometry and rate effects in the shear zone are responsible for such small displacements. Furthermore, the subsequent simulation for strong motions shows that a catastrophic collapse can only be provoked by softening mechanisms.

A phenomenon often observed in active landslides is an increased post-seismic activity for days to several months. It has been suggested that excess pore water pressure is generated outside of the shear zone during seismic shaking and later migrates into this zone by seepage, causing an acceleration of the landslide. A numerical model, using the hydro-mechanically coupled finite element method, confirms the plausibility of this hypothesis. A detailed parametric study reveals the underlying mechanisms and identifies the most controlling factors as ground motion intensity, rate-dependency, pre-seismic velocity and consolidation time.

While rate effects in clay-dominated soils has been well investigated, less is known about silts and sands with various clay content. Shear zones from alpine landslides are often characterised by this type of material, making their understanding crucial for a reliable risk assessment. Therefore, an improved ring shear apparatus is presented and applied to investigate rate, pore water pressure and temperature effects in the shear zone from two alpine landslides. For both a moderate rate-hardening for slow to rapid shearing was observed. Together with extensive field investigations, this leads to a comprehensive case study of the slow-moving Marsc landslide at the Luzzone reservoir in Switzerland. The whole process of formulating an appropriate geotechnical landslide model and assessing its behaviour under earthquake loading is presented. This provides a general approach that can be applied to other active landslides.

Kurzfassung

Rutschungen sind eine weltweite Bedrohung in Gebirgsregionen und fordern jedes Jahr tausende Todesopfer. Weniger Beachtung erfahren aktive, sich langsam bewegenden Rutschungen, sogenannte Kriechhänge, da diese in der Regel keine katastrophalen Ergebnisse verursachen. Diese können jedoch grosse Schäden an Gebäuden und Infrastruktur verursachen. Kriechhänge sind charakterisiert durch einen mobilen Zustand, welcher anfällig auf Umwelteinflüsse ist, weswegen davon ausgegangen wird, dass diese besonders leicht durch Erdbeben beschleunigt werden können. Diese Vermutung wird durch konventionelle, vereinfachte Modelle gestützt. Leider sind entsprechende Feldmessungen äusserst selten, zeigen aber bei den wenigen bekannten Fällen meist nur kleine koseismische Verschiebungen der Rutschung. Die potentiellen Konsequenzen im Falle eines Kollapses, zum Beispiel bei einer Rutschung am Ufer eines Stausees, betonen die Bedeutung zuverlässiger mechanischer Modelle und eines besseren Verständnisses deren Verhaltens.

Basierend auf der «Material Point Method» wird in dieser Arbeit wird ein Model präsentiert, welches die seismische Analyse bei grossen Deformationen ermöglicht und insbesondere für die Simulation von aktiven Rutschungen geeignet ist. Diese Methode wird auf den La Sorbella Kriechhang in Italien angewendet, bei welchen koseismische Verschiebungen während drei Erdbeben gemessen wurden. Dadurch wird nicht nur das Model validiert, sondern es wird auch gezeigt, dass die Geometrie und die Rateneffekte in der Scherzone ursächlich für diese kleinen Verschiebungen sind. Ausserdem zeigt die anschliessende Simulation für starke Erdbeben, dass ein katastrophaler Kollaps nur durch entfestigenden Mechanismen verursacht werden kann.

Ein häufig beobachtetes Phänomen bei aktiven Rutschungen, ist eine erhöhte Aktivität in den Tagen bis Monate nach einem Erdbeben. Es wird vermutete, dass Porenwasserüberdrücke während dem Erdbeben ausserhalb der Scherzone erzeugt werden. Diese wandern später in die Scherzone und verursachen daher eine Beschleunigung der Rutschung. Ein numerisches Modell, basierend auf der hydromechanischen gekoppelten Finite Elemente Methode, bestätigt die Plausibilität dieser Hypothese. Eine ausführliche Parameterstudie enthüllt die zugrundeliegenden Mechanismen und identifiziert die Erdbebenintensität, die Ratenabhängigkeit in der Scherzone, die präseismische Geschwindigkeit und die Konsolidationszeit als die wichtigsten Einflussfaktoren.

Während Rateneffekte in stark tonhaltigen Böden umfangreich untersucht wurde, sind Silte und Sande mit unterschiedlichem Tongehalt weniger erforscht. Scherzonen alpiner Rutschungen sind oft genau durch solches Material charakterisiert, weshalb deren Verständnis für eine zuverlässige Risikobeurteilung besonders wichtig ist. Daher wird zur Untersuchung von Raten-, Porewasserdruck- und Temperatureffekte in den Scherzonen zweier alpiner Rutschungen eine verbesserte Ringscherapparatur präsentiert und angewendet. In beiden Fällen konnte dabei eine moderate Ratenverfestigung bei langsamem und schnellem Abscheren beobachtet werden. Zusammen mit

umfangreichen Felduntersuchungen führt dies zu einer umfassenden Fallstudie des Kriechhangs Marsc beim Luzzone Stausee in der Schweiz. Der gesamte Prozess der Formulierung eines geeigneten geotechnischen Models der Rutschung und der Beurteilung des Verhaltens unter Erdbebenbelastung wird vorgestellt. Dies stellt ein allgemeines Vorgehen dar, welches auch auf andere aktive Rutschungen angewendet werden kann.

Acknowledgments

Table of Contents

1 Introduction

1.1. Motivation

Landslides are a widespread natural hazard in mountainous regions and pose a threat to people and infrastructure. A special class are active slow-moving landslides, which are characterized by continuous very slow movements controlled by environmental influences (Lacroix et al., 2020). The growing demand for space in monotonous areas leads to increased interaction between manmade structures and existing landslides. Of particular concern are active landslides along lakes and reservoirs, where a sudden rapid acceleration, so-called collapse, of the slide can cause a tsunami leading to catastrophic consequences. The Vajont landslide of 1963, remains one of the most devastating examples of such an event. As a result of this disaster, around 2000 people lost their lives and tremendous damage was caused (Hendron & Patton, 1987). In recent years, similar events of landslide-generated tsunamis (Gylfadóttir et al., 2017; Harbitz et al., 2014; Roberts et al., 2013) have highlighted the importance of better understanding the behaviour of landslides and its consequences.

Slow-moving landslides are usually not directly associated with catastrophic events and are more likely to cause slowly growing damage to infrastructure (Cevasco et al., 2018; Mansour et al., 2011; Puzrin et al., 2012). By nature these landslides exist in a state of dynamic equilibrium and are thus highly sensitive to changes in environmental conditions such as rainfall and earthquakes (Alvarado et al., 2019; Bontemps et al., 2020). This makes them potentially susceptible to a transition from slow motion to a rapid acceleration and can therefore pose a dormant hazard. The main triggers of this transition are precipitation and earthquakes, and while the former has been studied extensively, there are still many questions about seismic triggering. It is well known that landslides can be influenced and triggered by earthquakes (Jibson et al., 1994; Keefer, 2002), the response of slow-moving landslides to seismic shaking is poorly reported and not well understood. The mechanics of a landslide during and after an earthquake is given by a complex interaction of different processes in the landslide mass, the underlying stable material and especially in the interface between these two, the so-called shear zone. This makes predicting the seismic behaviour of slow-moving landslides a major challenge. Conventional modelling techniques neglect many of this processes and are very sensitive to the choice of input parameters. They can lead to inconsistent results and predict large co-seismic displacements even for light-to-moderate ground motions. In reality, however, negligibly small displacements have often been observed for such earthquakes (Bontemps et al., 2020; Lacroix et al., 2014; Ruggeri et al., 2020). It is therefore crucial to develop advanced modelling techniques to gain a better understanding of the underlying processes and to enable more reliable risk assessment.

1.2. Active landslides

1.2.1. Terminology

A landslide is a mass movement that evolves over time through the stages of pre-failure, failure and post-failure (Skempton & Hutchinson, 1969; Terzaghi, 1950). While in pre-failure the mass movement is initiated and start to slowly accelerate, failure usually refers to the single most significant movement episode of a landslide and often corresponds to the formation of a fully developed sliding surface (or shear zone) as a displacement or strain discontinuity (Hungr et al., 2014). The following post-failure stage span the period just after failure until it essentially stops (Leroueil & Locat, 1998). The behaviour during this stage depends on the mechanical, physical and geometrical properties of the landslide. This includes different types of failure mechanisms (Figure 1.1) that can occur simultaneously or in sequence and can last from seconds to several years or even decades (Cruden & Varnes, 1996; Hungr et al., 2014; Varnes, 1978). Many landslides even exhibit a series of movement or reactivation episodes separated by periods of quiescence. In addition to the type of failure mechanism, landslides are often classified by their velocity, which ranges from extremely slow (a few millimetres per year) to extremely rapid (metres per second) (Cruden & Varnes, 1996).
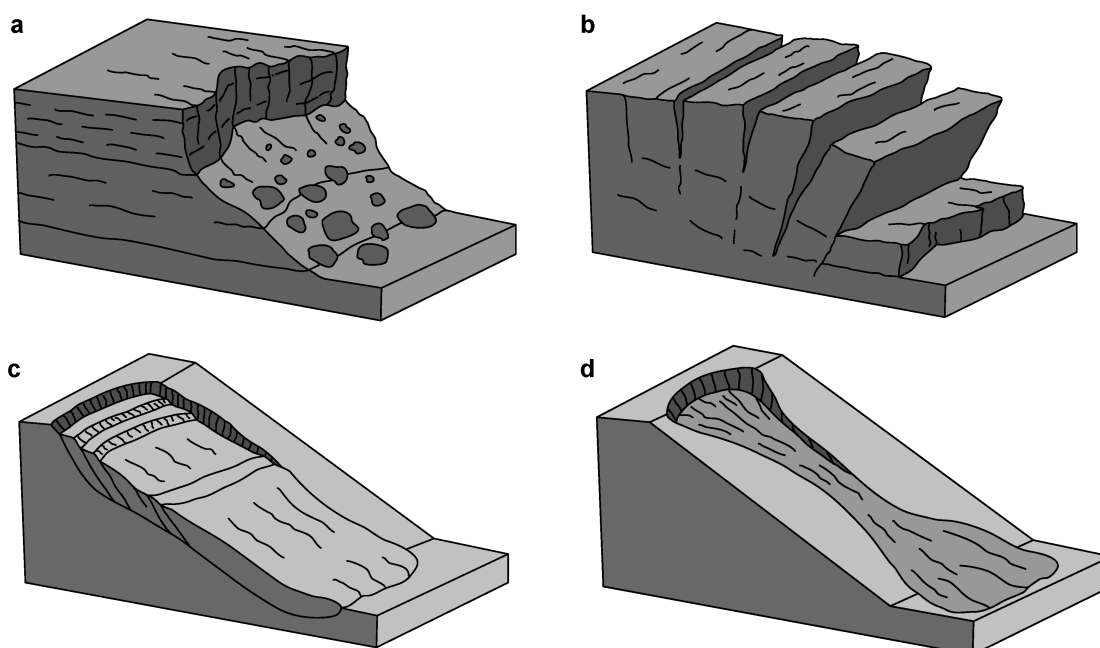
Figure 1.1: Schematic illustration of most common types of failure mechanisms: (a) fall, (b) topple, (c) slide, (d) flow (after Varnes, 1978).

In this thesis, the term active landslide refers to landslides in the failure and post-failure state regardless of type or velocity. It includes also those with alternating phases of reactivation. However, the main focus is on so-called slow-moving landslides, sometimes referred to as creeping landslides (e.g. Oberender & Puzrin, 2016; Puzrin & Schmid, 2011). These are defined according to Lacroix et al. (2020) as masses of coherent soil and rock that are primarily sliding along a discrete shear zone at rates ranging from a few mm/year to 100 m/year (Figure 1.2). Depending on the material and the degree of fracturing, this shear zone measures from a few millimetres to around a metre. Such landslides can change from slow-moving to fast-moving and from sliding to a debris flow or a rock fall (Carlà et al., 2019; Handwerger et al., 2019; Hendron & Patton, 1987; Intrieri et al., 2018).
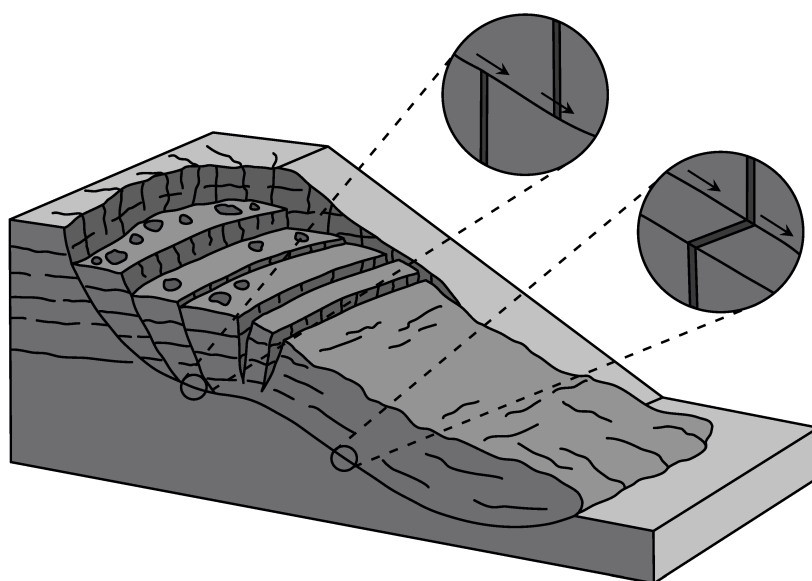
Figure 1.2: Schematic illustration of a slow-moving landslide (after Varnes, 1978).

1.2.2. Response to earthquakes

Landslides triggered by earthquakes are a widely observed and well-documented phenomenon (Bommer & Rodríguez, 2002; Jibson et al., 1994; Keefer, 2002; Rodríguez et al., 1999). In particular, with the help of airborne and satellite imagery, it is possible to make a comprehensive inventory of landslides in the aftermath of major earthquakes. This allowed the detection of more than 20'000 triggered landslides for the 1999 M_w 7.6 Chi-Chi earthquake in Taiwan (Dadson et al., 2004), more than 60'000 for the 2008 M_w 7.9 Wenchuan earthquake in China (Dai et al., 2011) and more than 25'000 for the 2015 M_w 7.8 Gorkha earthquake in Nepal (Roback et al., 2018). There are also numerous single case reports of such events, one of the largest being the Tsaoling landslides in Taiwan triggered by the Chi-Chi earthquake (Chigira et al., 2003). This rockslide of about 120 Mm^3 caused 29 fatalities and dammed the Ching-Shui River, creating a lake with a volume of about 45 M^3 (Chen et al., 2004).

Most of these earthquake-induced landslides are first-time failures of slopes, which were stable under purely gravitational loading. Among these catastrophic failures, it is difficult to distinguish the pre-existing landslide, especially from airborne and satellite imagery. Therefore, much less is known about the behaviour of active landslides during earthquakes and only a few cases can be found in the literature. Most of these landslides show only small displacements during the earthquake (so-called co-seismic displacements), ranging from less than a millimetre for La Sorbella landslide in Italy (Ruggeri et al., 2020) and a few centimetres for the Maca landslide in Peru (Bontemps et al., 2020; Lacroix et al., 2014) to a metre for several landslides in Nepal (Lacroix et al., 2022). It seems that active landslides are not triggered as quickly as one would expect based on their pre-seismic dynamic state.

A phenomenon often observed in active landslides is increased post-seismic activity (Lacroix et al., 2022). For example, the Maca landslide in Peru showed co-seismic displacements of only 1-2 cm, followed by cumulative displacements three times larger during the following month (Bontemps et al., 2020; Lacroix et al., 2014). Rather different time scales of this post-seismic activity have been observed in recent years, ranging from weeks to years. At annual scales, both landslide acceleration (Song et al., 2022) and increased landslide rates (Marc et al., 2015) have been reported and are thought to be controlled by the combined effect of earthquakes and precipitation. This is usually explained by damage to the landslide material by earthquake shaking in the form of micro- and macro-fractures that increase permeability and create preferential pathways for water infiltration (Bontemps et al., 2020). The closure of these fractures can take months or several years, making the landslide more susceptible to precipitation-induced movement. On the time scale of weeks to months, increased landslide activity has been observed even in the absence of rainfall, suggesting a different underlying mechanism (Bontemps et al., 2020; Cheaib et al., 2022; Lacroix et al., 2022). It was suggested by Lacroix et al. (2022) that excess pore water pressure is generated outside of the shear zone during seismic shaking and later migrates into this zone by seepage, causing an acceleration of the landslide.

1.2.3. Models for the seismic analysis

Numerous techniques, ranging from the pseudo-static limiting equilibrium approach to permanent-displacement analysis and stress-deformation analysis have been developed in the past to assess the stability slopes during earthquakes (Jibson, 2011). The permanent-displacement analysis was first introduced by Newmark (1965) in his Rankine lecture and is better known as Newmark's sliding block analysis. The landslide or any potential sliding mass is simplified as a rigid block on an inclined plane (Figure 1.3a). Based on the so-called critical acceleration, which is the acceleration required to overcome basal resistance and initiate sliding, the evolution of displacement can be calculated for any earthquake record. The critical acceleration can be derived from the slope inclination and the static factor of safety or the friction at the interface. Due to the oversimplification of the sliding mass as rigid, where all internal deformation is neglected, more sophisticated approaches have been proposed (Kramer & Smith, 1997; Lin & Whitman, 1986; Makdisi & Seed, 1978; Rathje & Bray, 1999). In the so-called fully coupled analysis (Rathje & Bray, 1999), the dynamic response of the sliding mass and its permanent displacement on the inclined slope are modelled simultaneously (Figure 1.3b). These methods use simple reflective boundary conditions and thus the drawback that waves are trapped within the sliding mass. In most cases, this lead to an overestimation of the amplification. The assumption of a rigid subsoil underneath the sliding plane can only be justified for soft landslides that slide directly on the underlying bedrock.
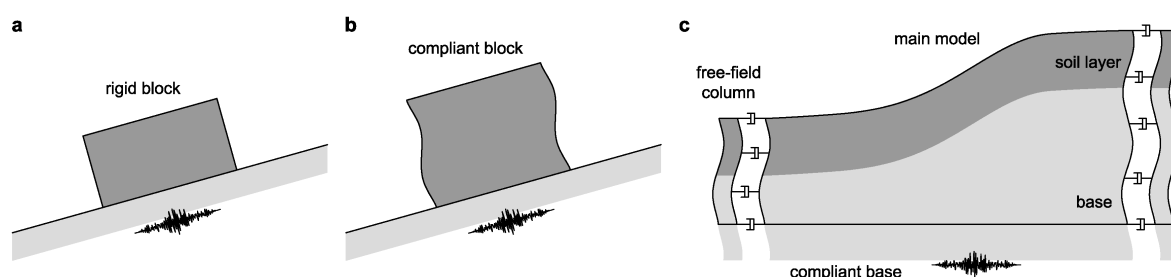
Figure 1.3: Slope and landslide simulation techniques. (a) Newmark's rigid sliding block analysis, (b) compliant sliding block analysis, (c) stress-deformation analysis with seismic boundary conditions.

It is important to note that all these Newmark-type methods were originally developed for the analysis of statically stable landslides. They only work if the factor of safety is greater than one. For active landslides, however, this poses a fundamental problem, as they have by nature a safety factor of one in their mobile state and must be considered as a dynamic system rather than a static one. In fact, the conventional Newmark's sliding block analysis predicts infinite landslide displacement for a factor of safety approaching one and thus its selection is problematic. Active landslides are primarily controlled by the rate-dependent strength of the shear zone (Wang et al., 2010), and therefore more sophisticated material models are required to simulate their movement. This has been addressed in several studies to model the seasonal behaviour of landslides in response to hydrological changes (Li et al., 2023;

Oberender & Puzrin, 2016; van Asch et al., 2007). However, these models neglect the actual geometry of the landslide and are only of limited use for seismic analysis, as rigorous modelling of wave propagation inside and outside the landslide is not possible.

In recent years, the stress-deformation analysis has become the state-of-the-art technique for deterministic seismic slope stability analysis (Kramer, 1996). This allows the application of non-linear, elastoplastic constitutive models, the consideration of complex geometries and a rigorous modelling of the propagation of seismic waves. This requires solving the dynamic equation of motion, for which the finite element method (FEM) is most commonly used. To adequately simulate the propagation of seismic waves, appropriate boundary conditions must be applied to avoid reflection and trapping of waves within the model domain. Therefore, the concept of a compliant base (Lysmer & Kuhlemeyer, 1969) and free-field columns (Wolf, 1989; Zienkiewicz et al., 1989) are recommended (Figure 1.3c). When dealing with landslides, special techniques need to be applied, which include a proper large deformation formulation and do not suffer from mesh distortion. A comprehensive review of different numerical approaches has been provided by Soga et al. (2016). However, suitable seismic boundary conditions for these techniques are generally either not available or difficult to implement. This has recently been addressed by Stoecklin (2019) using a multi-stage approach where seismic triggering of submarine landslides is modelled by conventional Lagrangian FEM, where such boundary conditions are available. Subsequently, a coupled Eulerian Lagrangian (CEL) post-failure analysis is performed. This approach assumes that the earthquake is only the triggering mechanism and that no large deformations occur during the seismic shaking. For active landslides, this assumption cannot be made due to their mobile state and especially within the shear zone, considerable deformations can take place. Furthermore, the material is tracked and evolves through the Eulerian mesh based on its volume fraction, which leads to a smearing of the state variables and is thus less suitable for the distinct contrast given by shear zones in slow-moving landslides. The Material Point Method (MPM), originally proposed by Sulsky et al. (1994), is another large deformation technique that has become increasingly popular for simulating landslides (e.g. Andersen & Andersen, 2010; Soga et al., 2016). It seems therefore obvious to apply this method to active landslides. However, no implementation of seismic boundary conditions existed at the onset of this work and had to be developed to use this method for seismic simulations.

1.3.   Main objectives of the thesis

The main goal of the thesis is to improve the understanding of the mechanism involved in active landslides and their response to earthquakes. This includes (*i*) the development of appropriate analysis techniques, (*ii*) the investigation of the shear behaviour of shear zones, and (*iii*) field observations and measurements for calibration and validation of the models. Towards this goal, the main objectives are formulated as follows:

- Development of a mechanical and numerical model to simulate the co- and post-seismic motion of active landslides.

- Theoretical investigation into the co- and post-seismic motion of active landslides and identification of the most influencing factors and potential scenarios using the developed models.

- Development of a new dynamic ring shear apparatus to investigate the behaviour of landslide shear zones.

- Experimental investigation into the rate effects and mechanics of landslides shear zones using the developed ring shear apparatus.

- Application of the results for a field study with extensive data from field monitoring of a selected active landslide.

1.4. Structure of the thesis

The thorough research of landslides comprises three main components: *mechanical modelling*, *experimental testing* and *field investigation*. This thesis is built upon all three components with the aim of gaining a better understanding of the behaviour of active landslides during earthquakes (Figure 1.4). While parts I (chapters 2-4) and II (chapters 5) cover the first two aspects, Part III (chapter 6) focuses on the field investigation, but incorporates also the knowledge described in the previous chapters to demonstrate an exemplary comprehensive analysis of an active landslide under seismic loading. Each of the chapters 2-6 represent independent publications on the subject of this thesis. In chapter 7 the main findings are summarized and ideas for future research are discussed.
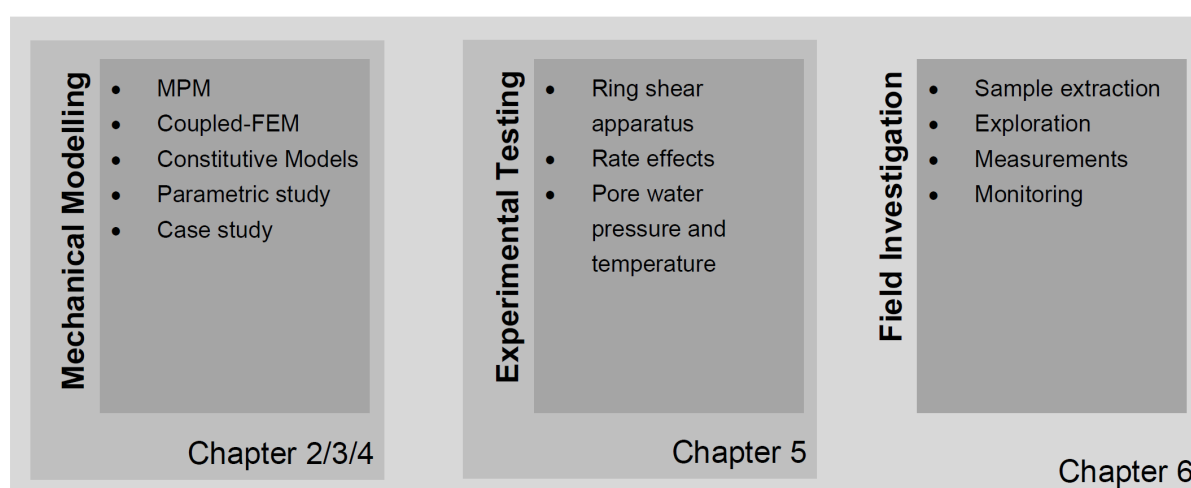
Figure 1.4: Components of landslide research and structure of the thesis

1.4.1. Part I – Mechanical modelling

In this part the mechanical and numerical models for the analysis of active landslides are derived and applied for parametric and case studies. First, the MPM framework for large-deformation seismic response analysis is presented (Chapter 2). A high-performance MPM code has been implemented in C++ for shared-memory systems using OpenMP (Dagum & Menon, 1998). This provides the required flexibility to implement the seismic boundary conditions and any constitutive model. After outlining the basic methodology and the main equations of MPM, the seismic boundary conditions and their implementation are presented. The application to an example slope illustrates the proposed procedure and is benchmarked against the results obtained using an independent simulation technique, based on a multi-step FE analysis.

While the presented framework can be used for all types of seismic-related simulations, it is applied in Chapter 3 as a rigorous modelling approach for active landslides under seismic loading. Therefore, a large-deformation constitutive model for shear zones is introduced and a benchmark model is compared with the conventional Newmark's sliding block analysis and FE approach. The application of this methodology to the La Sorbella landslide in Italy will provides better understanding of the relative contribution of geometric effects, groundwater level and rate dependence of soil strength to the co-seismic displacements.

Chapter 4 examines the phenomena of post-seismic landslide activity. A hydro-mechanically coupled FE model for infinite landslide conditions is presented together with appropriate constitutive models. This allows the mechanism of excess pore water pressure generated outside the shear zone during seismic shaking and its subsequent diffusion into the shear zone to be investigated. The simulations provide insight into the relationships between their co- and post-seismic behaviour and its main controlling parameters.

1.4.2. Part II – Experimental testing

Since the behaviour of the shear zone is one of the main controlling factors of an active landslide, a major effort is being made to develop an improved ring shear apparatus. The aim is to investigate the thermo-hydro-mechanical processes of shearing at velocity changing from low to high. In Chapter 5, this new ring shear apparatus, developed at the ETH Zurich, is presented in all its details. An extensive testing program on samples from two alpine landslides in Switzerland provides insights into rate, pore water pressure and temperature effects in shear zones. Known phenomena concerning rate effects in soils can be confirmed and extended to silty and sandy soils with non-negligible clay content. The measurement of pore water pressure and temperature during very rapid shearing provides physical evidence for the widely debated hypothesis of the generation of excess pore water pressure due to frictional heating.

1.4.3. Part III – Field investigation and Case study

In chapter 6, a case study of the Marsc landslides at the flank of the Luzzone water reservoir in the Swiss Alps is presented. In course of a field campaign in 2020 by ETH Zurich, new core drillings were carried out to extract samples from various depths in particular including the shear zone. The landslide has been instrumented with state-of-the-art measuring systems to monitor the landslide displacement and the ground water level, as well as to record earthquake signals. This provides a profound understanding of the landslide geometry and its seasonally varying kinematics. Combing these observations with the results from ring shear tests on shear zone material, allows formulating a well-founded geotechnical landslide model. Finally, the behaviour of the landslide during different potential earthquakes is investigated using the presented MPM framework. This allows for the examination of possible scenarios and the assessment of the risk of catastrophic failure.

References

Alvarado, M., Pinyol, N. M. & Alonso, E. E. (2019). Landslide motion assessment including rate effects and thermal interactions: Revisiting the canelles landslide. *Canadian Geotechnical Journal*, *56*(9), 1338–1350. https://doi.org/10.1139/cgj-2018-0779

Andersen, S. & Andersen, L. (2010). Modelling of landslides with the material-point method. *Computational Geosciences*, *14*(1), 137–147. https://doi.org/10.1007/s10596-009-9137-y

Bommer, J. J. & Rodríguez, C. E. (2002). Earthquake-induced landslides in Central America. *Engineering Geology*, *63*(3–4), 189–220. https://doi.org/10.1016/S0013-7952(01)00081-3

Bontemps, N., Lacroix, P., Larose, E., Jara, J. & Taipe, E. (2020). Rain and small earthquakes maintain a slow-moving landslide in a persistent critical state. *Nature Communications*, *11*(1), 1–10. https://doi.org/10.1038/s41467-020-14445-3

Carlà, T., Intrieri, E., Raspini, F., Bardi, F., Farina, P., Ferretti, A., … Casagli, N. (2019). Perspectives on the prediction of catastrophic slope failures from satellite InSAR. *Scientific Reports*, *9*(1), 1–9. https://doi.org/10.1038/s41598-019-50792-y

Cevasco, A., Termini, F., Valentino, R., Meisina, C., Bonì, R., Bordoni, M., … De Vita, P. (2018). Residual mechanisms and kinematics of the relict Lemeglio coastal landslide (Liguria, northwestern Italy). *Geomorphology*, *320*, 64–81. https://doi.org/10.1016/J.GEOMORPH.2018.08.010

Cheaib, A., Lacroix, P., Zerathe, S., Jongmans, D., Ajorlou, N., Doin, M. P., … Abdallah, C. (2022). Landslides induced by the 2017 Mw7.3 Sarpol Zahab earthquake (Iran). *Landslides*, *19*(3), 603–619. https://doi.org/10.1007/S10346-021-01832-0

Chen, T. C., Lin, M. L. & Hung, J. J. (2004). Pseudostatic analysis of Tsao-Ling rockslide caused by Chi-Chi earthquake. *Engineering Geology*, *71*(1–2), 31–47. https://doi.org/10.1016/S0013-7952(03)00124-8

Chigira, M., Wang, W. N., Furuya, T. & Kamai, T. (2003). Geological causes and geomorphological precursors of the Tsaoling landslide triggered by the 1999 Chi-Chi earthquake, Taiwan. *Engineering Geology*, *68*(3–4), 259–273. https://doi.org/10.1016/S0013-7952(02)00232-6

Cruden, D. M. & Varnes, D. J. (1996). Landslide types and processes. *Special Report - National Research Council, Transportation Research Board*, *247*.

Dadson, S. J., Hovius, N., Chen, H., Dade, W. B., Lin, J. C., Hsu, M. L., … Stark, C. P. (2004). Earthquake-triggered increase in sediment delivery from an active mountain belt. *Geology*, *32*(8), 733–736. https://doi.org/10.1130/G20639.1

Dagum, L. & Menon, R. (1998). OpenMP: an industry standard API for shared-memory programming. *IEEE Computational Science and Engineering*, *5*(1), 46–55. https://doi.org/10.1109/99.660313

Dai, F. C., Xu, C., Yao, X., Xu, L., Tu, X. B. & Gong, Q. M. (2011). Spatial distribution of landslides triggered by the 2008 Ms 8.0 Wenchuan earthquake, China. *Journal of Asian Earth Sciences*, *40*(4), 883–895. https://doi.org/10.1016/J.JSEAES.2010.04.010

Gylfadóttir, S. S., Kim, J., Helgason, J. K., Brynjólfsson, S., Höskuldsson, Á., Jóhannesson, T., … Løvholt, F. (2017). The 2014 Lake Askja rockslide-induced tsunami: Optimization of numerical tsunami model using observed data. *Journal of Geophysical Research: Oceans*, *122*(5), 4110–4122. https://doi.org/10.1002/2016JC012496

Handwerger, A. L., Fielding, E. J., Huang, M. H., Bennett, G. L., Liang, C. & Schulz, W. H. (2019). Widespread Initiation, Reactivation, and Acceleration of Landslides in the Northern California Coast Ranges due to Extreme Rainfall. *Journal of Geophysical Research: Earth Surface*, *124*(7), 1782–1797. https://doi.org/10.1029/2019JF005035

Harbitz, C. B., Glimsdal, S., Løvholt, F., Kveldsvik, V., Pedersen, G. K. & Jensen, A. (2014). Rockslide tsunamis in complex fjords: From an unstable rock slope at Åkerneset to tsunami risk in western Norway. *Coastal Engineering*, *88*, 101–122. https://doi.org/10.1016/J.COASTALENG.2014.02.003

Hendron, A. J. & Patton, F. D. (1987). The vaiont slide — A geotechnical analysis based on new geologic observations of the failure surface. *Engineering Geology*, *24*(1–4), 475–491. https://doi.org/10.1016/0013-7952(87)90080-9

Hungr, O., Leroueil, S. & Picarelli, L. (2014). The Varnes classification of landslide types, an update. *Landslides*, *11*(2), 167–194. https://doi.org/10.1007/S10346-013-0436-Y

Intrieri, E., Raspini, F., Fumagalli, A., Lu, P., Del Conte, S., Farina, P., … Casagli, N. (2018). The Maoxian landslide as seen from space: detecting precursors of failure with Sentinel-1 data. *Landslides*, *15*(1), 123–133. https://doi.org/10.1007/S10346-017-0915-7

Jibson, R. W. (2011). Methods for assessing the stability of slopes during earthquakes-A retrospective. *Engineering Geology*, *122*(1–2), 43–50. https://doi.org/10.1016/j.enggeo.2010.09.017

Jibson, R. W., Prentice, C. S., Borissoff, B. A., Rogozhin, E. A. & Langer, C. J. (1994). Some observations of landslides triggered by the 29 April 1991 Racha earthquake, Republic of Georgia. *Bulletin Seismological Society of America*, *84*(4), 963–973.

Keefer, D. K. (2002). Investigating landslides caused by earthquakes - A historical review. *Surveys in Geophysics*, *23*(6), 473–510. https://doi.org/10.1023/A:1021274710840

Kramer, S. L. (1996). *Geotechnical Earthquake Engineering*. *Engineering* (Vol. 6). https://doi.org/10.1007/978-3-540-35783-4

Kramer, S. L. & Smith, M. W. (1997). Modified Newmark Model for Seismic Displacements of Compliant Slopes. *Journal of Geotechnical & Geoenvironmental Engineering*, *123*(July), 635–644. https://doi.org/10.1061/(ASCE)1090-0241(1997)123:7(635)

Lacroix, P., Gavillon, T., Bouchant, C., Lavé, J., Mugnier, J. L., Dhungel, S. & Vernier, F. (2022). SAR and optical images correlation illuminates post-seismic landslide motion after the Mw 7.8 Gorkha earthquake (Nepal). *Scientific Reports*, *12*(1), 1–13. https://doi.org/10.1038/s41598-022-10016-2

Lacroix, P., Handwerger, A. L. & Bièvre, G. (2020). Life and death of slow-moving landslides. *Nature Reviews Earth and Environment*, *1*(8), 404–419. https://doi.org/10.1038/S43017-020-0072-8

Lacroix, P., Perfettini, H., Taipe, E. & Guillier, B. (2014). Coseismic and postseismic motion of a landslide: observations, modelling, and analogy with tectonic faults. *Geophysical Research Letters*, *41*, 6676–6680. https://doi.org/10.1002/2014GL061170

Leroueil, S. & Locat, J. (1998). Slope movements — Geotechnical characterization, risk assessment and mitigation. In *Geotechnical Hazards* (pp. 95–106). CRC Press. https://doi.org/10.1201/9781003078173-6

Li, X., Handwerger, A. L. & Buscarnera, G. (2023). Viscoplastic modelling of rainfall-driven slow-moving landslides;application to California Coast Rangers. *Landslides*, 1–13. https://doi.org/10.1007/S10346-023-02039-1

Lin, J. S. & Whitman, R. V. (1986). Earthquake Induced Displacements of Sliding Blocks. *Journal of Geotechnical Engineering*, *112*(1), 44–59. https://doi.org/10.1061/(ASCE)0733-9410(1986)112:1(44)

Lysmer, J. & Kuhlemeyer, R. L. (1969). Finite Difference Model for Infinite Media. *Journal of Engineering Mechanics*, *95*, 859–877.

Makdisi, F. I. & Seed, H. B. (1978). Simplified Procedure for Estimating Dam and Embankment Earthquake-Induced Deformations. *Journal of the Geotechnical Engineering Division*, *104*(7),

849–867. https://doi.org/10.1061/AJGEB6.0000668

Mansour, M. F., Morgenstern, N. R. & Martin, C. D. (2011). Expected damage from displacement of slow-moving slides. *Landslides*, *8*(1), 117–131. https://doi.org/10.1007/S10346-010-0227-7

Marc, O., Hovius, N., Meunier, P., Uchida, T. & Hayashi, S. (2015). Transient changes of landslide rates after earthquakes. *Geology*, *43*(10), 883–886. https://doi.org/10.1130/G36961.1

Newmark, N. M. (1965). Effects of Earthquakes on Dams and Embankments. *Géotechnique*, *15*(2), 139–160. https://doi.org/10.1680/geot.1965.15.2.139

Oberender, P. W. & Puzrin, A. M. (2016). Observation-guided constitutive modelling for creeping landslides. *Géotechnique*, *66*(3), 232–247. https://doi.org/10.1680/jgeot.15.LM.003

Puzrin, A. M. & Schmid, A. (2011). Progressive failure of a constrained creeping landslide. *Proceedings of the Royal Society A: Mathematical, Physical and Engineering Sciences*, *467*(2133), 2444–2461. https://doi.org/10.1098/rspa.2011.0063

Puzrin, A. M., Schmit, A. & Schwager, M. V. (2012). Case studies of constrained creeping landslides in Switzerland. *Proceedings of 11th International Symposium on Landslides and Engineered Slopes ISL*, *2*, 1795–1800.

Rathje, E. M. & Bray, J. D. (1999). An examination of simplified earthquake-induced displacement procedures for earth structures. *Canadian Geotechnical Journal*, *37*(3), 731–732. https://doi.org/10.1139/cgj-37-3-731

Roback, K., Clark, M. K., West, A. J., Zekkos, D., Li, G., Gallen, S. F., … Godt, J. W. (2018). The size, distribution, and mobility of landslides caused by the 2015 Mw7.8 Gorkha earthquake, Nepal. *Geomorphology*, *301*, 121–138. https://doi.org/10.1016/J.GEOMORPH.2017.01.030

Roberts, N. J., McKillop, R. J., Lawrence, M. S., Psutka, J. F., Clague, J. J., Brideau, M. A. & Ward, B. C. (2013). Impacts of the 2007 landslide-generated Tsunami in Chehalis Lake, Canada. *Landslide Science and Practice: Risk Assessment, Management and Mitigation*, *6*, 133–140. https://doi.org/10.1007/978-3-642-31319-6_19

Rodríguez, C. E., Bommer, J. J. & Chandler, R. J. (1999). Earthquake-induced landslides: 1980-1997. *Soil Dynamics and Earthquake Engineering*, *18*(5), 325–346. https://doi.org/10.1016/S0267-7261(99)00012-3

Ruggeri, P., Fruzzetti, V. M. E., Ferretti, A. & Scarpelli, G. (2020). Seismic and Rainfall Induced Displacements of an Existing Landslide: Findings from the Continuous Monitoring. *Geosciences 2020, Vol. 10, Page 90*, *10*(3), 90. https://doi.org/10.3390/GEOSCIENCES10030090

Skempton, A. W. & Hutchinson, J. N. (1969). Stability of natural slopes and embankment foundations. In *International conference of soil mechanics and foundation engineering* (pp. 291–340). Mexico.

Soga, K., Alonso, E., Yerro, A., Kumar, K. & Bandara, S. (2016). Trends in large-deformation analysis of landslide mass movements with particular emphasis on the material point method. *Géotechnique*, *66*(3), 248–273. https://doi.org/10.1680/jgeot.15.LM.005

Song, C., Yu, C., Li, Z., Utili, S., Frattini, P., Crosta, G. & Peng, J. (2022). Triggering and recovery of earthquake accelerated landslides in Central Italy revealed by satellite radar observations. *Nature Communications*, *13*(1), 1–12. https://doi.org/10.1038/s41467-022-35035-5

Stoecklin, A. (2019). *Sedimentation, Seismic Triggering and Post-failure Evolution of Submarine Landslides*. *Doctoral Thesis*. ETH Zürich. https://doi.org/https://doi.org/10.3929/ethz-b-000380139

Sulsky, D., Chen, Z. & Schreyer, H. L. (1994). A particle method for history-dependent materials. *Computer Methods in Applied Mechanics and Engineering*, *118*(1–2), 179–196. https://doi.org/10.1016/0045-7825(94)90112-0

Terzaghi, K. (1950). Mechanism of Landslides. *Application of Geology to Engineering Practice*, 83–123. https://doi.org/10.1130/BERKEY.1950.83

van Asch, T. W. J., Van Beek, L. P. H. & Bogaard, T. A. (2007). Problems in predicting the mobility of slow-moving landslides. *Engineering Geology*, *91*(1), 46–55. https://doi.org/10.1016/J.ENGGEO.2006.12.012

Varnes, D. (1978). Slope Movement Types and Processes. *Special Report*, *176*, 11–33.

Wang, G., Suemine, A. & Schulz, W. H. (2010). Shear-rate-dependent strength control on the dynamics of rainfall-triggered landslides, Tokushima Prefecture, Japan. *Earth Surface Processes and Landforms*, *35*(4), 407–416. https://doi.org/10.1002/esp.1937

Wolf, J. P. (1989). Soil-structure-interaction analysis in time domain. *Nuclear Engineering and Design*, *111*(3), 381–393. https://doi.org/10.1016/0029-5493(89)90249-5

Zienkiewicz, O. C., Bicanic, N. & Shen, F. Q. (1989). Earthquake Input Definition and the Trasmitting Boundary Conditions. In *Advances in Computational Nonlinear Mechanics* (pp. 109–138). Vienna: Springer Vienna. https://doi.org/10.1007/978-3-7091-2828-2_3

2   A MPM framework for large-deformation seismic response analysis

Abstract

Landslides are often triggered by earthquakes and can cause immense damage due to large mass movements. To model such large-deformation events, the material point method (MPM) has become increasingly popular in recent years. A limitation of existing MPM implementations is the lack of appropriate boundary conditions to perform seismic response analysis of slopes. In this article, an extension to the basic MPM framework is proposed for simulating the seismic triggering and subsequent collapse of slopes within a single analysis step. Original implementations of a compliant base boundary and free-field boundary conditions in the MPM framework are presented, enabling the application of input ground motions while accounting for the absorption of outgoing waves and the free-ground movement at the lateral boundaries. An example slope is analysed to illustrate the proposed procedure and to benchmark it against the results obtained using an independent simulation technique, based on a three-step finite element (FE) analysis. The comparison generally shows a good agreement of the results obtained from the two independent procedures and highlights advantages of the presented "all-in-one" MPM approach, in particular for long duration strong motions.

2.1.   Introduction

Earthquake shaking can trigger the failure of slopes, which are stable under purely gravitational loading. The damage of such seismically triggered landslides can be large and, for many earthquake events, exceed the damage from all other seismic hazards combined (Kramer, 1996). Numerous seismically triggered landslides highlight the severity of such catastrophic events (Havenith et al., 2016; Keefer, 2002; Rodríguez et al., 1999). Seismic slope stability analysis is therefore a key component for earthquake hazard assessments. A number of techniques and methods have been developed for this purpose (see Section 1.1). A comprehensive risk assessment, however, includes not only an analysis of the slope stability during seismic shaking, but also of the further evolution of a potential slope collapse. The simulation of the movement of unstable soil masses often imposes a large deformation problem and hence requires different analysis techniques (see Section 1.2). Due to limitations in existing numerical approaches, these two stages are typically analysed separately, using different methodologies. In reality, however, the evolution of seismically triggered landslides is a continuous process, which cannot be strictly separated into separate steps. In this article, this issue is addressed and a methodology is presented, for the simulation of seismically triggered landslides as a continuous process using a single analysis step.

2.1.1.   Modelling the seismic response of slopes

Assessing slope stability under seismic loading requires an adequate modelling of the effect of the seismic action on the soil structure. Numerous techniques of varying sophistication have been developed in the past for such applications, ranging from pseudo-static limiting equilibrium approaches for stability analyses, to Newmark's sliding block analysis (Newmark, 1965) for computing permanent displacements, to stress-deformation analyses for assessing the dynamic response of slopes (e.g. Hashash & Groholski, 2010). The later has become the state of the art technique for deterministic seismic slope stability analysis. They can be divided into two main categories – frequency domain and time domain analyses (Hashash & Groholski, 2010). For seismic slope stability analyses, where the shear stress reaches or even exceeds the shear resistance of the soil, the latter is often the preferred method (Kramer, 1996) as it enables the use of non-linear, elasto-plastic constitutive models. This requires solving the dynamic equation of motion, for which the finite element method (FEM) and the material point method (MPM) are commonly used.

To simulate the propagation of seismic waves adequately, appropriate boundary conditions have to be applied to avoid the reflection and trapping of waves within the model domain. Special boundary conditions have been developed within the FEM in the past, for both the lateral boundaries and the base boundary of the model.

Lateral boundaries: At the lateral model boundaries, outgoing waves should be able to leave the model without reflection. At the same time, the free-field movement of the soil should not be restricted. One possible way to satisfy these requirements is by applying the free-field boundary method (Wolf, 1989; Zienkiewicz et al., 1989). Free-field columns are included on both sides of the main model (see Figure 2.1). The movement of the columns corresponds to the far-field response of the horizontally layered ground and is unaffected by the main model but not the other way around. To absorb outgoing waves, the main model is connected to the free-field columns with dashpot elements (Nielsen, 2006).
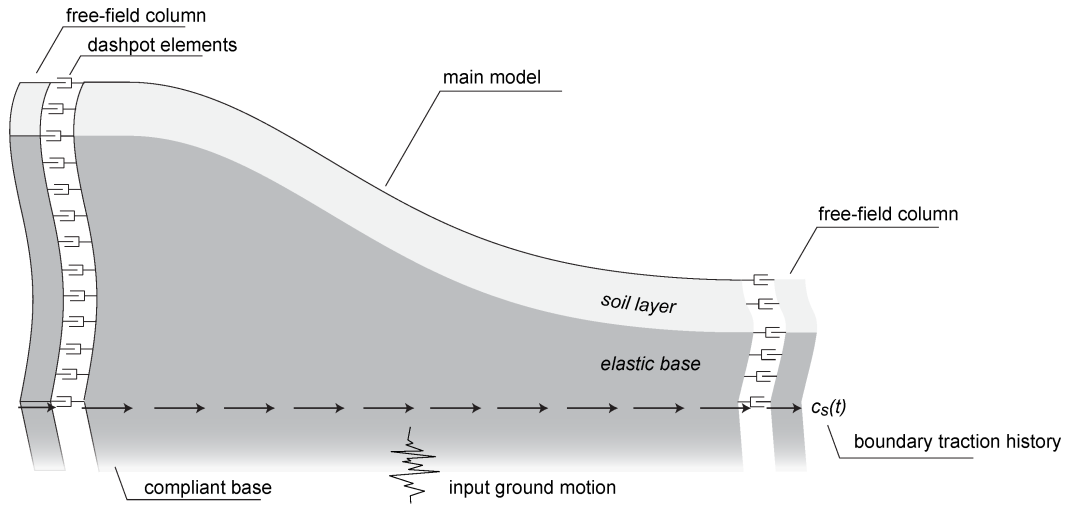
Figure 2.1: Illustration of the computational model for seismic response analysis of slopes.

Base boundary: Typically, the input ground motion is applied at the base of the model domain to model the incoming waves (Figure 2.1). The simplest way to do this is to prescribe the input acceleration or velocity directly. This, however, is equivalent to a rigid base, where downwards propagating waves are reflected. In many cases, this is not justified. This limitation can be overcome by applying a *compliant base boundary condition* (Zienkiewicz et al., 1989). It allows for the direct application of the input ground motion without prescribing the movement and causing a reflection of outgoing waves. First, viscous elements are connected to the base of the model, which are absorbing outgoing waves (Lysmer & Kuhlemeyer, 1969). Second, instead of applying the acceleration time history, the input motion is transformed into a boundary traction. This traction time history is then applied at the base of the model and computed as

$$t_s(t) = 2v_{su}(t)\rho c_s = 2v_{su}(t)\sqrt{\rho G} \tag{2.1}$$

where ρ is the bulk density, G is the shear modulus of the base material and v_{su} is the particle velocity of the upward propagating wave, i.e. half the 'outcrop' motion (Mejia & Dawson, 2006). The factor of two is required as half of the applied stress is absorbed by the viscous elements.

2.1.2. Solving large deformation problems in geotechnical engineering

With the methodology described above the seismic response of slopes can be adequately simulated. If the applied ground motion is sufficiently strong, it can initiate a collapse of the slope. In this case, the velocity of the unstable soil mass increases rapidly and the deformations in the model can become very large. Traditional geotechnical continuum analysis techniques are not well suited to analyse such large deformation problems. In recent years, however, a number of advanced techniques have been developed. A comprehensive review of different numerical approaches was provided by Soga et al. (2016). Two of the most frequently used approaches are the coupled Eulerian Lagrangian (CEL) FEM and the MPM.

Material Point Method (MPM): The MPM is a hybrid method, where the material is represented as Lagrangian particles. The equations of motion are solved on an Eulerian grid. The Eulerian solution procedure allows for the material to undergo large deformations, while the Lagrangian material representation presents a convenient way of tracking material properties and constitutive state variables. MPM is a generalization of the particle in cell (PIC) and the fluid implicit particle (FLIP) method for solid mechanics, first proposed by (Sulsky et al., 1994). Nowadays, numerous variations of the original algorithm have been introduced, tailored for a range of different applications (Bardenhagen & Kober, 2004; Jiang et al., 2015; Steffen et al., 2008). In recent years the MPM has been successfully applied to model landslides (Andersen & Andersen, 2010; Soga et al., 2016) and significant advances have been made, such as the development of hydro-mechanically coupled approaches (Abe et al., 2014; Bandara & Soga, 2015; Zabala & Alonso, 2011). Also seismic slope failure (Bhandari et al., 2016; Ering & Sivakumar Babu, 2020) and landslides triggered by earthquakes (Alsardi & Yerro, 2021; He et al., 2019) have been modelled with MPM. In these studies, the ground motion was prescribed as a velocity boundary condition and the lateral boundaries were modelled as either rigid or free moving, leading to a reflection of outgoing waves back into the model domain. Whereas this correctly represents the boundary conditions of the simulated shaking table experiments, it is a source of inaccuracy when modelling the seismic response of real slopes.

Coupled Eulerian Lagrangian (CEL) Method: With the CEL finite element (FE) analysis technique a traditional Lagrangian phase, in which elements deform with the material, is followed by a Eulerian phase, during which elements with significant deformation are remeshed and material flow between neighbouring elements is computed (Dassault Sysèmes Simulia, 2012). The material is tracked as it moves through the Eulerian mesh by computing its volume fraction, which represents the proportion of an element filled with a specific material. This allows for multiple materials to move within the model domain. The methodology has been successfully applied in recent years to simulate the progressing collapse of both subaerial and subaqueous slopes (Dey et al., 2015, 2016; Stoecklin et al., 2020). Similar to the MPM, existing CEL codes do not include appropriate seismic boundary conditions, and hence cannot be applied directly for seismic response analyses.

2.1.3. Goal and objectives

As outlined above, different techniques have been developed in recent years to simulate and analyse different processes related to earthquake-induced landsliding. However, to simulate seismically triggered slope failures as one continuous process, a unifying methodology is required. In recent attempts to develop such a framework (e.g., Stoecklin and Puzrin, 2020) the co-seismic and post-seismic slope collapse analysis were performed in separate analysis steps. The effects of this simplification, however, could not be assessed.

In this article, an attempt is made to develop a unified approach for performing co- and post-seismic landslide analysis, based on the MPM method. The main challenge lies in the implementation of appropriate seismic boundary conditions within the MPM framework. The resulting procedure is applied to simulate the seismic triggering and subsequent collapsing of an example slope and the results are compared to the Stoecklin and Puzrin (2020) type analysis. It is shown that for individual stages, the two independent approaches provide very similar results, thus validating the developed methodology. Furthermore, the proposed MPM framework enables the application of ground motion loading throughout the post-failure stage, and for the first time an assessment of the effects of seismic shaking on the co-seismic landslide evolution.

2.2. General MPM framework

Rather than using existing codes, an in-house MPM framework has been implemented in C++. This provides the required flexibility to implement the seismic boundary conditions and the necessary adaptions for performing seismic response analyses. The general implementation closely follows Stomakhin et al. (2013) and Jiang et al. (2015), using explicit time integration. Subsequently, the basic methodology and main equations are outlined, to provide the necessary background information. This serves as a summary of the essential equations rather than a stepwise derivation starting from the weak form of the balance equations. For simplicity, the subsequent equations are presented for the plane strain case where the deformations are restricted to two dimensions. The formulation, however, can be readily extended to the three-dimensional case.

2.2.1. General procedure

The concept of MPM is to use particles (so-called material points) to discretize the material and track mass, momentum, deformation and constitutive state variables. In order to solve Newton's law of motion, an Eulerian background grid is introduced which allows for the computation of the derivatives needed for the stress-based force evaluation. Initially, each material point is assigned a position $x_p = (x_p, y_p)$, volume V_p and mass m_p. All the other quantities (i.e. velocity v_p, deformation gradient F_p and

Cauchy stress tensor $\boldsymbol{\sigma}_p$) are set to zero. Following the initialization, the motion of the material points is computed, based on the basic 4-step MPM algorithm (see Figure 2.2).
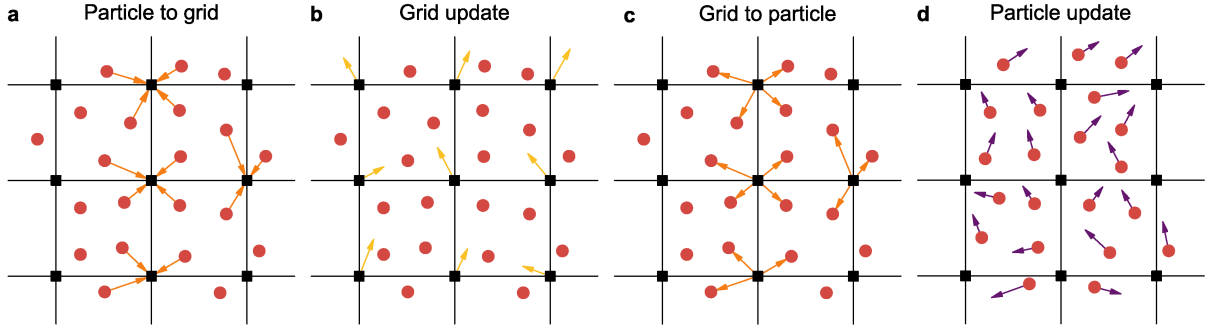
Figure 2.2: General 4-step algorithm of the MPM: (a) transfer of mass, linear momentum and forces from the material points to the grid, (b) solving the equation of motion on the grid, (c) transfer the updated grid velocities back to the material points and (d) evolve the material points and updated the deformation and stress state (after Soga et al., 2016).

2.2.2. Interpolation functions

Interpolation functions are defined over the nodes of the background Eulerian grid. The interpolation function at grid node i is denoted with $N_i(\boldsymbol{x})$ and is evaluated at the material point position $\boldsymbol{x}_p = (x_p, y_p)$. Often the more compact notation $N_i(\boldsymbol{x}_p) = w_{ip}$ is used, referring to the weight of material point p associated with the grid node i. As proposed by Steffen et al. (2008), a dyadic product of one-dimensional interpolation functions was used

$$N_i(\boldsymbol{x}_p) = N\left(\frac{1}{h}(x_p - x_i)\right) N\left(\frac{1}{h}(y_p - y_i)\right) \tag{2.2}$$

where h is the grid spacing and $\boldsymbol{x}_i = (x_i, y_i)$ is the grid node position. To avoid the common problem of so-called grid-crossing errors, quadratic or cubic B-splines should be used. The application of B-splines offers a straightforward extension of standard MPM and greatly improves the accuracy of the solution (Steffen et al., 2008; Tielen et al., 2017). Moreover, it allows for an efficient parallel computing implementation. Due to the longer span of the B-splines, special considerations have to be taken regarding boundary conditions. However, in the presented framework only rectangular truncated models are considered and therefore the concept of mirror particles (Schulz & Sutmann, 2019) can be easily applied. Despite being computationally more expensive, cubic B-splines are applied in this work, as they are numerically more stable. Especially in cases where strain localization is expected to occur, this is of particular importance. The cubic basis function is defined as

$$N(x) = \begin{cases} \frac{1}{2}|x|^3 - x^2 + \frac{2}{3} & 0 \le |x| < 1 \\ \frac{1}{6}(2 - |x|)^3 & 1 \le |x| < 2 \\ 0 & 2 \le |x| \end{cases} \tag{2.3}$$

In addition, for computing the internal force vector and the velocity gradient, the gradient of the interpolation functions evaluated at the material point position $\nabla N_i(\boldsymbol{x}_p) = \nabla w_{ip}$ is needed

$$\nabla N_i(\boldsymbol{x}_p) = \begin{pmatrix} \frac{1}{h}N'\left(\frac{1}{h}(x_p - x_i)\right)N\left(\frac{1}{h}(y_p - y_i)\right) \\ N\left(\frac{1}{h}(x_p - x_i)\right)\frac{1}{h}N'\left(\frac{1}{h}(y_p - y_i)\right) \end{pmatrix} \tag{2.4}$$

where $N'(x)$ is the derivative of the basis function $N(x)$. In contrast to the finite element method, the interpolations functions and its gradients have to be recalculated in each time step, as the material points are moving relative to the grid. Therefore, in the following derivations the index n referring to time step n is added to both the weight (w_{ip}^n) and the gradient (∇w_{ip}^n).

2.2.3. Particle to grid

In a first step, mass and linear momentum are transferred from the material points to the grid nodes using the weight w_{ip}^n at time step n

$$m_i^n = \sum_p m_p w_{ip}^n \tag{2.5}$$

$$(m\boldsymbol{v})_i^n = \sum_p m_p \boldsymbol{v}_p^n w_{ip}^n \tag{2.6}$$

where m_p is the mass and $\boldsymbol{v}_p^n$ is the velocity vector of material point p. In case the affine particle in cell method (APIC) is used, the transfer of linear moment involves an additional term to preserve affine velocity fields and therefore conserve the angular momentum (Jiang et al., 2015)

$$(m\boldsymbol{v})_i^n = \sum_p m_p w_{ip}^n (\boldsymbol{v}_p^n + \boldsymbol{B}_p^n (\boldsymbol{D}_p^n)^{-1}(\boldsymbol{x}_i - \boldsymbol{x}_p^n)) \tag{2.7}$$

where $\boldsymbol{B}_p^n$ is a matrix stored at each material point and is defined in section 2.5. $\boldsymbol{D}_p^n = \frac{1}{3}h^2 \boldsymbol{I}$ for cubic interpolation functions. In geotechnical problems, large rotations are normally associated with plastic yielding and failure. These phenomena introduce considerable dissipation and therefore the loss of angular momentum is of minor importance. To be fully consistent, the APIC transfer should be adopted. Furthermore, the internal force vector at the grid nodes can be computed as

$$\boldsymbol{f}_{int,i}^n = -\sum_p V_p^n \boldsymbol{\sigma}_p^n \nabla w_{ip}^n \tag{2.8}$$

where V_p^n is the volume and $\boldsymbol{\sigma}_p^n$ the Cauchy stress tensor at material point p. External forces (body forces and tractions) can be introduced at the material points by an external force vector $\boldsymbol{f}_p$. The external force vector is transferred from the material point to the grid as

$$f_{ext,i}^n = \sum_p f_p w_{ip}^n = \sum_p (b_p + t_p) w_{ip}^n \tag{2.9}$$

where it must be distinguished between body forces b_p and traction forces t_p. Body forces can easily be defined as a function of the volume or mass of the material point. For the definition of the tractions, on the other hand, the corresponding surface area is needed for distributed forces, which has to be recomputed in each time step in case it changes. It should be noted that in general cases also the direction of the surface traction can change in each time increment. Tractions can also be prescribed at the grid and are considered separately in the following section as they do not have to be transferred.

2.2.4. Grid velocity update

Following the transfer described above from each material point inside the domain, calculations on the grid are performed. The resulting force at the grid nodes is computed as

$$f_i^n = f_{int,i}^n + f_{ext,i}^n + f_{bc,i}^n \tag{2.10}$$

where $f_{bc,i}^n$ denotes possible traction boundary conditions prescribed directly on the grid. For quasi-static analyses (e.g. computation of the initial stress field) so-called local damping can be used (Cundall, 2002). Therefore, an additional damping force $f_{d,i}^n$ proportional to the resulting grid force (or out-of-balance force) f_i^n and in the opposite direction of the velocity is introduced as

$$f_{d,i}^n = -\mathrm{sign}(v_i^n)\beta|f_i^n| \tag{2.11}$$

where each component is evaluated separately and β is a dimensionless damping factor. For the seismic response analysis, where a compliant base and far-field boundary conditions are used, the application of damping is crucial for the computation of the initial stress conditions under static conditions. This ensures that velocities remain under a certain numerical threshold value, preventing the model from drifting away during the seismic analysis after replacing the kinematic boundary conditions with tractions. In case of an implicit solver, the equilibrium equation could be solved instead of the equation of motion and no numerical damping would be required.

Applying explicit time integration, the linear momentum can be updated according to

$$(m v)_i^{n+1} = (m v)_i^n + \Delta t(f_i^n + f_{d,i}^n) \tag{2.12}$$

At this point, kinematic boundary conditions on the grid can be applied. The corresponding nodal values of a kinematic boundary cannot simply be overwritten by its desired value, because the B-spline basis functions range outside of the domain and hence do not maintain unity inside the domain (Steffen et al., 2008). To overcome this problem, the method of mirrored particles has been applied in this work (Schulz & Sutmann, 2019). Material points are reflected across the boundary in different ways depending on the type of boundary condition (slip or no-slip). These additional material points are not included in the

calculation and serve purely for the formulation of the boundary conditions. Further details can be found in (Ding et al., 2020).

Finally, the grid velocities can be computed as

$$v_i^{n+1} = \frac{(mv)_i^{n+1}}{m_i^n} \tag{2.13}$$

2.2.5. Grid to particle and particle update

After updating the grid velocities, they are transferred back to the material points. For a PIC or APIC transfer scheme the material point velocity is given by

$$v_{\text{PIC},p}^{n+1} = v_{\text{APIC},p}^{n+1} = \sum_i v_i^{n+1} w_{ip}^n \tag{2.14}$$

whereas for a FLIP scheme only the velocity increment is transferred

$$v_{\text{FLIP},p}^{n+1} = v_p^n + \sum_i (v_i^{n+1} - v_i^n) w_{ip}^n \tag{2.15}$$

In case APIC is used, the **B**-matrix has to be updated to

$$B_p^{n+1} = \sum_i w_{ip}^n v_i^{n+1} (x_i - x_p^n)^T \tag{2.16}$$

Not only velocities but also the velocity gradient L_p^{n+1} and deformation gradient F_p^{n+1} have to be updated

$$L_p^{n+1} = \sum_i v_i^{n+1} (\nabla w_{ip}^n)^T \tag{2.17}$$

$$F_p^{n+1} = \left(I + \Delta t L_p^{n+1}\right) F_p^n = \Delta F_p^{n+1} F_p^n \tag{2.18}$$

where ΔF_p^{n+1} is called the incremental deformation gradient. The updated deformation gradient also serves to update the volume of each material point

$$V_p^{n+1} = det(F_p^{n+1}) V_p^0 \tag{2.19}$$

The material point position is updated as

$$x_p^{n+1} = x_p^n + \Delta t \sum_i v_i^{n+1} w_{ip}^n \tag{2.20}$$

which can be simplified for a PIC or APIC scheme as

$$x_p^{n+1} = x_p^n + \Delta t v_p^{n+1} \tag{2.21}$$

2.2.6. Material update

Finally, the stress tensor and potential internal variables are updated. Constitutive laws are implemented analogous to the finite element method, where a relation has to be defined between the deformation gradient F_p^n (or the velocity gradient L_p^n in case of viscosity) and the Cauchy stress tensor σ_p^n. Depending on the constitutive model, this might include some additional internal variables such as plastic strain and other state variables. However, it must be emphasized that MPM is a large strain solution method and hence the choice of stress- and strain measures should be assessed carefully in terms of objectivity. For geotechnical engineering applications of the MPM, small strain constitutive models are often extended by using the Jaumann rate of Cauchy stress

$$\overset{\triangledown}{\boldsymbol{\sigma}} = \dot{\boldsymbol{\sigma}} - \boldsymbol{W}\boldsymbol{\sigma} + \boldsymbol{\sigma}\boldsymbol{W} \tag{2.22}$$

where $\dot{\boldsymbol{\sigma}}$ is the rate of Cauchy stress and the spin tensor $\boldsymbol{W} = \text{skew}[\boldsymbol{L}]$ is the skew symmetric part of the velocity gradient. Applying an explicit numerical integration, the stress update can be written in incremental form as

$$\boldsymbol{\sigma}^{n+1} = \boldsymbol{\sigma}^n + \Delta t \dot{\boldsymbol{\sigma}} = \boldsymbol{\sigma}^n + \Delta t(\overset{\triangledown}{\boldsymbol{\sigma}} + \boldsymbol{W}^{n+1}\boldsymbol{\sigma}^n - \boldsymbol{\sigma}^n \boldsymbol{W}^{n+1}) \tag{2.23}$$

The stress updated includes a rotational component due to rigid body motion and a change in stress due to straining. The latter is described by the constitutive law in form of a relationship between the Jaumann rate of Cauchy stress and the rate of deformation tensor $\boldsymbol{D} = \text{sym}[\boldsymbol{L}]$

$$\overset{\triangledown}{\boldsymbol{\sigma}} = \overset{\triangledown}{\boldsymbol{\sigma}}(\boldsymbol{D}) \tag{2.24}$$

Often, the stress update is implemented in a slightly different way. The current stress is rotated according to

$$\boldsymbol{\sigma}_{rot}^n = \boldsymbol{\sigma}^n + \Delta t(\boldsymbol{W}^{n+1}\boldsymbol{\sigma}^n - \boldsymbol{\sigma}^n \boldsymbol{W}^{n+1}) \tag{2.25}$$

and subsequently updated using well-established stress integration algorithms (e.g. elastoplastic return mapping)

$$\boldsymbol{\sigma}_{rot}^n \xrightarrow{\Delta\varepsilon = \Delta t \boldsymbol{D}} \boldsymbol{\sigma}^{n+1} \tag{2.26}$$

It must be pointed out that equation (2.22) lacks incremental objectivity (Hughes & Winget, 1980) and is only justified if displacement increments are sufficiently small, which is true for the explicit time integration in the MPM algorithm. In this work the incremental objective stress integration after Hughes & Winget (1980) was used. Not only will this guarantee incremental objectivity but also allow for a better comparison with results of the FE analyses, as the same algorithm is implemented in FE code ABAQUS (Simulia, 2012). Equation (2.22) is therefore replaced by

$$\sigma_{rot}^{n} = \boldsymbol{R}\sigma^{n}\boldsymbol{R}^{T} \tag{2.27}$$

where the rotation tensor is given by

$$\boldsymbol{R} = \left(\boldsymbol{I} - \frac{1}{2}\Delta t \boldsymbol{W}^{n+1} \right)^{-1} \left(\boldsymbol{I} + \frac{1}{2}\Delta t \boldsymbol{W}^{n+1} \right) \tag{2.28}$$

The application of small strain plasticity models in a finite strain framework comes with certain drawbacks. It has been shown, that this can lead to different inconsistencies, such as spurious stress oscillations or improper energy dissipation (Bažant et al., 2012). However, it should be emphasized that these inconsistencies remain negligible for most applications in geotechnical engineering where elastic strains remain rather small (Simo & Pister, 1984). The aim of this work is to present a basic methodology to perform seismic response analyses with the MPM, rather than discussing the appropriate choice of constitutive law and its implementation. Hence, this topic is not discussed any further here. For the elastoplastic seismic slope analysis performed in this study, a von Mises constitutive model with isotropic softening was used. The model was implemented using an implicit elastoplastic return mapping algorithm, which is consistent with the implementation in the FE code ABAQUS (Dassault Systèmes Simulia, 2012). Further information regarding the implementation can be found in Simo & Hughes (1998).

2.3.   Extension of the MPM framework for seismic analysis

In this section, the extensions of the general MPM framework to perform the seismic response analysis are outlined and the implementation of seismic boundary conditions are described.

2.3.1. General modelling procedure

The analysis is commenced in a static step to compute the initial static stress field, followed by a dynamic analysis step. Although the term static is used here, the equation of motion is solved in this step (eq. 2.12) rather than any equilibrium equation. Static conditions are ensured by smoothly ramping up gravity forces over a sufficiently large time period and using local damping according to equation (2.11). For the static analysis kinematic boundary conditions are applied. At the bottom boundary a no-slip condition is used whereas at the lateral boundaries the material points are allowed to move freely in the vertical direction using a slip condition (see Figure 2.3). Both the static and the dynamic analysis steps are performed on same model. Only the boundary conditions are changed in between steps. The material points can be carried forward with all the stored information of their constitutive state variables. To ensure a correct treatment of the boundary conditions, it is crucial to align the external model boundaries with the background grid. For the dynamic analysis, two free-field columns are included in the model to simulate the far-field movement (see Figure 2.3b). The base is assumed to behave elastically, which is a prerequisite for the ground motion to be prescribed as stress-time history according to equation (2.1).

Hence, the model truncation boundary has to be chosen sufficiently far below the surface where plastic deformations remain negligible. For the soil above the base, any suitable constitutive model can be used to represent the soil behaviour.
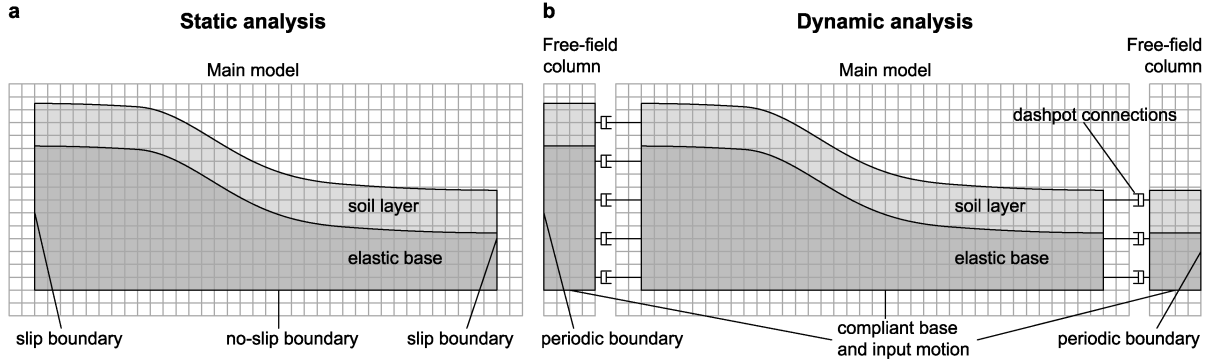
Figure 2.3: Illustration of the MPM-modelling procedure in two main steps: (a) Simulation of the static stress-field within the slope followed by (b) the seismic analysis.

2.3.2. Base boundary

As pointed out in section 2.2.4, the MPM requires a different treatment of kinematic boundaries compared to FE analyses. In this work, the method of mirrored particles was applied (Schulz & Sutmann, 2019). As shown in Figure 2.4a, the grid is extended with additional nodes and particles are mirrored across the boundary to mimic no-slip boundary conditions. However, the mirrored particles are not explicitly included in the model and only the boundary nodes need a special treatment.

For the seismic model the concept of wave-absorbing viscous elements (Lysmer & Kuhlemeyer, 1969) was adapted to the MPM framework. Therefore, the kinematic boundary condition used for the static analysis is replaced by a traction boundary condition and absorbing elements are connected to the model boundary. In previous studies, the latter were directly connected to the boundary grid nodes (Al-Kafaji, 2013; Shen & Zhen, 2005). Due to the use of B-spline rather than bilinear shape functions in this study, the same procedure cannot be applied, as the unity condition is not fulfilled at the grid nodes. Only rectangular boundaries are used, which are aligned with the material points. For this layout, a novel approach is proposed here. Dashpots are directly applied to the bottom row of material points in the form of a traction force t_p (see Figure 2.4b). Similarly, the input motion is applied to the same row of material points as a traction force time history. Hence, the traction for a bottom material point can be expressed as the sum of three components: (*i*) a viscous surface traction representing the dashpot element, (*ii*) a reaction force derived from the static analysis and (*iii*) a traction time history representing the applied input ground motion

$$t_p = \begin{pmatrix} t_{px} \\ t_{py} \end{pmatrix} = \delta_p \begin{pmatrix} \tau_{p,s} + 2v_{su}\sqrt{\rho G} - \eta_s v_{px} \\ \sigma_{p,s} + 2v_{pu}\sqrt{\rho M} - \eta_p v_{py} \end{pmatrix} \tag{2.29}$$

26

where $\delta_p = h/\sqrt{n_{\mathrm{MP}}}$ is the surface area related to the material point (see Figure 2.4), which can be easily determined for a regular distribution of material points along the bottom boundary (h: grid-spacing ; n_{MP}: number of material points inside a grid cell). The material point velocities in the x- and y-directions are v_{px} and v_{py} respectively, whereas the corresponding viscosities of the dashpots $\eta_s = \rho c_s$ and $\eta_p = \rho c_p$ are given by the shear- and pressure-wave speed of the base material, $c_s = \sqrt{G/\rho}$ and $c_p = \sqrt{M/\rho}$ (M is the elastic P-wave modulus). The input ground motion is represented by the particle velocity of the upwards propagating shear and pressure wave (v_{su} and v_{pu}). Finally, in order to ensure the static equilibrium of the model by the static shear stress $\tau_{p,s}$ and normal stress $\sigma_{p,s}$ of the corresponding material point are applied as an initial condition and kept constant through the analysis. For the sake of simplicity, the index of the time step n is omitted.
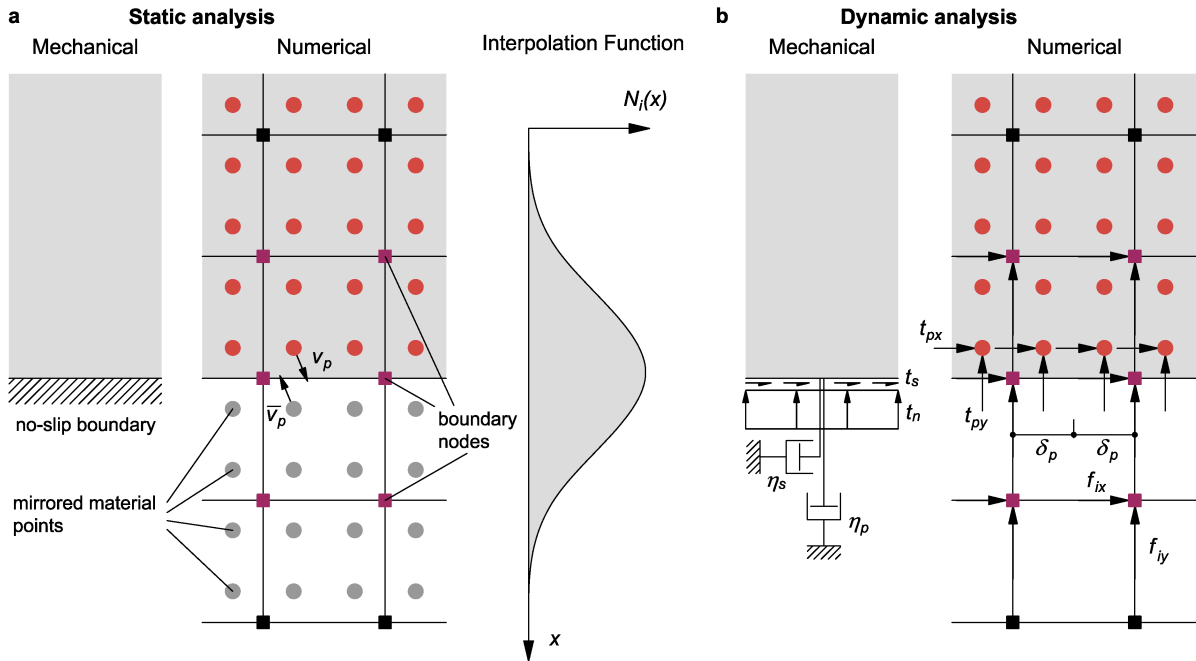
Figure 2.4: Illustration of the base boundary conditions for the (a) static and (b) dynamic analysis.($\overline{v}_p$: Velocity vector of the mirrored material point; f_{ix}, f_{iy}: Out-of-balance force as traction on the grid; t_{px}, t_{py}: Traction on the material point due to the dashpot elements and the input motion; δ_p: surface area related to material point p).

It should be pointed out that switching from a kinematic boundary condition (using mirrored particles) to a traction boundary, where forces are applied to material points, does not usually represent a perfect transfer as this traction is mapped to several grid nodes in the particle to grid phase. This could lead to a slight lack of balance static equilibrium at the lower boundary, causing a slow drift of the model. Nevertheless, the influence of these redistributions is usually negligible and the problem of drifting can be solved by replacing the dashpots by Kelvin-Voigt elements (Al-Kafaji, 2013). In this work, however, a more strict approach is proposed, where the static reaction forces are directly applied to the nodes as the equation of motion is solved on the grid. After the stress initialization in the static analysis, the

particle to grid transfer is performed in order to get internal and external nodal forces but this time without the mirrored material points. Hence, at the boundary nodes equilibrium of force is not strictly fulfilled anymore. The resulting out-of-balance forces are then applied as a traction boundary $f_i = (f_{ix}, f_{iy})$ on the grid for the dynamic analysis with the opposite sign (see Figure 2.4b).

2.3.3. Lateral boundaries

Similar to the base boundary, the lateral boundaries are also modelled by the mirrored particle approach for the static analysis. In contrast to the base, a slip boundary is used to allow for vertical deformations. Therefore, only the horizontal components of the nodal forces at the boundary nodes (see Figure 2.5) need a special treatment (Schulz & Sutmann, 2019). For the free-field columns (Wolf, 1989; Zienkiewicz et al., 1989) separate models are created because a different grid is needed. Their movement is not influnced by the main model and hence can either be precomputed or computed in parallel to the main calculation. The free-field columns represent infinitely flat ground, which can be model by using so-called periodic boundary conditions. This is achieved by giving the node at the right boundary the same number as the corresponding node on the left boundary and hence both nodes refer to the same memory. The column is modelled with a width of four grid cells, which is exactly the span of the cubic shape function. In theory, a width of only one cell would be sufficient but this would lead to a rather cumbersome implementation. Following Nielsen (2006), the free-field columns are connected to the main model using dashpot elements (see Figure 2.5). The connection is imposed directly on the boundary material points in the form of a traction force similarly to the bottom boundary. However, the viscous component is defined as a function of the relative motion between the corresponding material points of the free-field (index fp) and the main model (index p). The traction follows as

$$t_p = \begin{pmatrix} t_{px} \\ t_{py} \end{pmatrix} = \delta_p \begin{pmatrix} \sigma_{p,s} + \sigma_{fp,d} + \eta_p(v_{fpx} - v_{px}) \\ \tau_{fp,d} + \eta_s(v_{fpy} - v_{py}) \end{pmatrix} \tag{2.30}$$

where δ_p is the surface area related to the material point, v_{fpx} and v_{fpy} are the velocity components of the material point in the free-field column and v_{px} and v_{py} the corresponding material point velocity in the main model (remark: the time/step index n is omitted for simplicity). The viscosities of the dashpots $\eta_s = \rho c_s$ and $\eta_p = \rho c_p$ are given by the shear- and pressure-wave speed of the material, which might be depth-dependent. Similar to the base boundary, static equilibrium is ensured by the static normal stress component $\sigma_{p,s}$. Moreover, the dynamic traction due to the seismic excitation of the free-field column has to be applied on the main model (Nielsen, 2006) and is retrieved from the dynamic stress tensor of the corresponding free-field material point

$$\boldsymbol{\sigma}_{fp,d} = \boldsymbol{\sigma}_{fp} - \boldsymbol{\sigma}_{fp,s} \tag{2.31}$$

where $\boldsymbol{\sigma}_{fp}$ is the actual stress tensor and $\boldsymbol{\sigma}_{fp,s}$ is the stress tensor at the end of the static analysis of the free-field column. The components of the dynamic surface tractions $\sigma_{fp,d}$ and $\tau_{fp,d}$ follow by multiplying the dynamic stress tensor with the outer normal vector of the lateral surface.

Analogously to the bottom boundary, the static support is implemented in a more stringent approach by a traction force f_{ix}, which is directly applied to the boundary nodes (see Figure 2.5). It should be emphasized, that this approach is limited to models where the horizontal deflections of the lateral material points are small compared to the grid size. Otherwise, material points might fall out of the influence zone of the boundary nodes defined by the shape function span and static support is not ensured anymore. In this case, static tractions should be applied on the boundary material points instead.
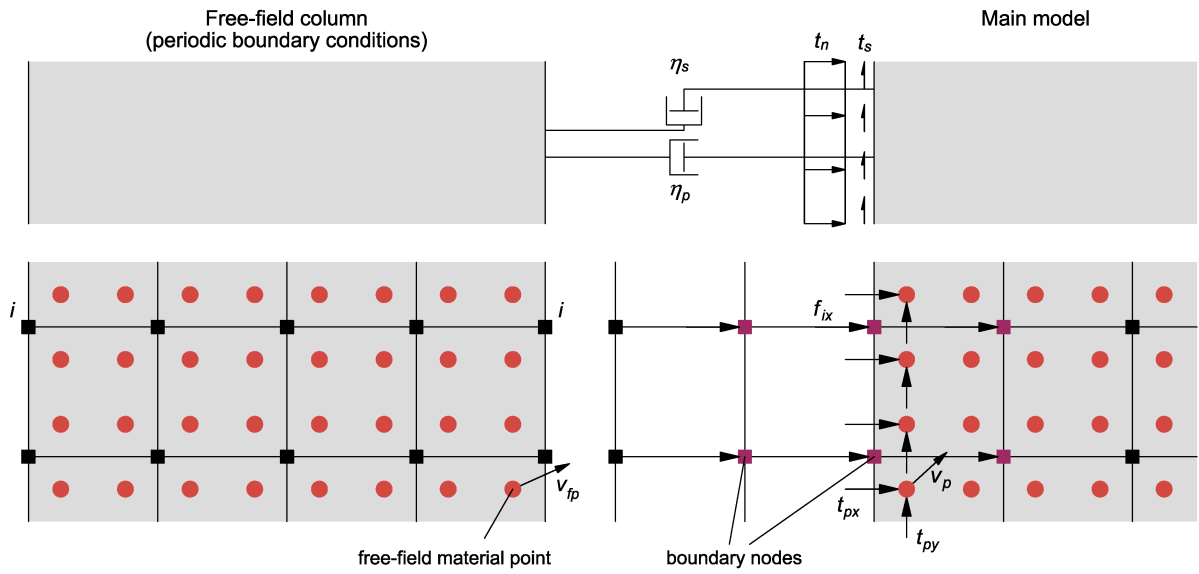
Figure 2.5: Illustration of the lateral boundary condition including the free-field column (left). (v_{fp}: Velocity vector of corresponding material point in the free-field; f_{ix}: Out-of-balance force as traction on the grid; t_{px}, f_{py}: Traction on the material point due to the dashpot elements and the dynamic surface traction).

In contrast to the bottom boundary, the computation of the surface area related to the material point δ_p in equation (2.30) is not straightforward and has to be performed for each boundary material point separately. Since the deformation gradient is stored for each material point δ_p can be computed as

$$\delta_p = \lambda\delta_p^0 = \sqrt{\boldsymbol{s} \bullet \boldsymbol{Cs}}\,\delta_p^0 \qquad (2.32)$$

where λ is the stretch of a normalized line element in the initial configuration and δ_p^0 is the initial surface related to the material point before any deformation occurred (which is before the static analysis). The stretch is given by the normalized line element $\boldsymbol{s} = (0\ \ 1\ \ 0)^{\mathrm{T}}$ and the Right-Green deformation tensor $\boldsymbol{C} = \boldsymbol{F}^{\mathrm{T}}\boldsymbol{F}$. In case large deformations at the boundary material points are expected during the seismic analysis, δ_p could be updated in each time increment. However, for most applications this is rather

unlikely. Although in the current work this would not be necessary, the stretch is updated in each time increment for consistency.

Material points and grid nodes at the corners (i.e. where the lateral and the base boundaries intersect) do not need to be treated specially. The contributions of both boundaries can simply be superimposed. Special consideration is only required for the mirrored particle approach in case of a parallel computing implementation where possible race conditions must be carefully checked and avoided.

2.4.   FE / Eulerian Methodology

To benchmark the results obtained using the MPM procedure described above, the slope failure process is simulated with an alternative methodology in a sequence of three steps: (*i*) A static analysis step to compute the pre-failure static stress field within the slope, (*ii*) a dynamic analysis step to simulate earthquake events followed by (*iii*) a post-failure analysis step to compute the motion of the collapsing slope. Each analysis step is based on a different approach, because the seismic boundaries are not available within the applied CEL framework. They are connected by prescribing the results from the preceding step as initial conditions for the subsequent step (see Figure 2.6). The framework was developed within the ABAQUS computing environment (Dessault Systèmes Simulia, 2012). It has been successfully applied in previous studies to analyse the behaviour earthquake-induced subaqueous landslides (Stoecklin & Puzrin, 2020; Stoecklin et al., 2020). In this section, the three main analysis steps are described briefly.
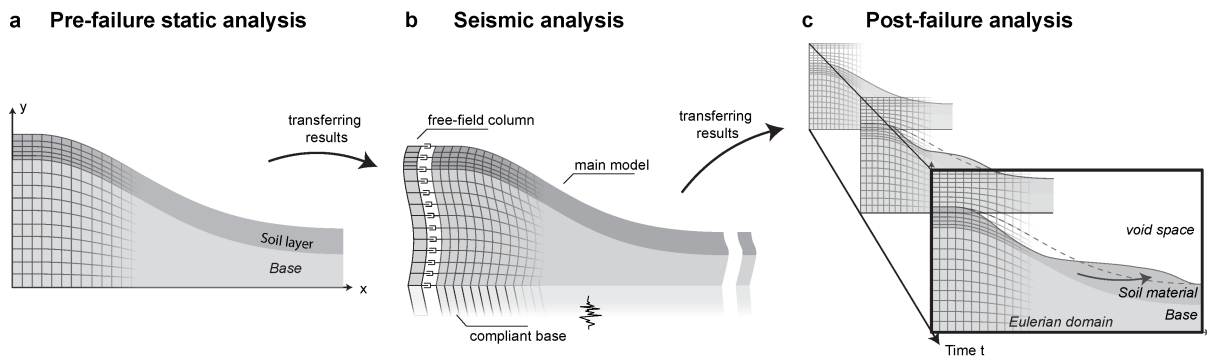
Figure 2.6: Illustration of the analysis procedure in three main steps: (a) Computation of the pre-failure stress-field within the slope followed by (b) a simulation of the earthquake event and (c) the post-failure evolution of the collapsing slope.

2.4.1. Static analysis

In this first step, the pre-failure stress field within the slope is computed under static conditions, using a total stress-based, implicit, plane-strain Lagrangian FE analysis (Figure 2.6a). The same kinematic boundary conditions are applied as in the MPM simulation: No-slip condition at the bottom boundary, where the displacements in the x- and y-directions are fixed, and slip conditions at the lateral boundaries,

where the displacements are only fixed in the y-direction. The resulting stress values are then transferred for each integration point to the subsequent seismic analysis step.

2.4.2. Seismic analysis

In this second analysis step, the impact of a seismic event is simulated by subjecting the slope to an earthquake ground motion (Figure 2.6b). A dynamic, implicit, total stress-based, plane-strain FE Lagrangian analysis procedure was employed. At the lateral boundaries, the free-field boundary method was applied to avoid reflection of stress-waves without restricting the free field movement (see Section 2.1.1). The free-field columns were a large out-of-plane thickness to ensure that they move nearly independently from the main model, which was connected to the lateral free-field columns with dashpot elements. At the base of the model, viscous elements were connected to the model to achieve the effect of a compliant boundary condition. To ensure stress-equilibrium under static conditions, the boundary tractions obtained from the static analysis are prescribed as initial stress-conditions at the lower and lateral model boundaries. The ground motion was applied as a traction-time history at the nodes where the viscous elements are connected to the main model (Mejia & Dawson, 2006). The modelling procedure was described in more detail by (Stoecklin & Puzrin, 2018).

If the analysed slope becomes unstable as a result of the applied ground motion and the degradation of the shear resistance, the displacements in the unstable soil mass accumulate at an increasing rate. Hence, the solution loses accuracy due to excessive mesh distortion and the analysis has to be terminated. To simulate the motion of the collapsing slope past this point, the results are transferred to the post-failure analysis.

2.4.3. Post-failure analysis

In this final step, the motion of the collapsing slope is simulated until it reaches a static equilibrium once again. The velocity-, strength- and stress-fields are mapped to the post-failure model, serving as starting conditions (Figure 2.6b). The analysis is based on the CEL FE approach, allowing for the materials in the model to undergo extreme straining without suffering from excessive mesh distortion (see Section 2.1.2). A void space was included above the soil layer, facilitating the free movement of the material within the specified Eulerian domain. The procedure was described in more detail by (Stoecklin et al., 2020).

While the method enables the computation of the large displacements within the collapsing soil mass, the absorbing boundary conditions cannot be implemented easily. To avoid trapping seismic stress waves in the model, the input ground motion was not applied anymore during this final step. At this stage, however, the movement of the unstable soil mass is self-driven and in many cases only marginally affected by the ground motion. In some cases, however, this simplification can lead to an underestimation of the predicted displacements (see Section 2.5.4).

2.5. Analysis of an example case and comparison between different procedures

To compare the results obtained with the MPM and the CEL methodologies, an example case is analysed in this section. The comparison of the results serves as a benchmark for the developed MPM extension and illustrates how the procedure can be applied. Following a description of the example case, the MPM vs. CEL comparison is presented, providing validation for both approaches.

2.5.1. Description of the example case

The example case comprises a 10m thick soil layer on top of an elastic base (Figure 2.7a). The slope curvature was chosen to follow a Gaussian shape (Adams & Schlager, 2000), with a maximum inclination of about 22 degrees (Figure 2.7b). The applied soil parameters are listed in Table 2.1. The slope was subjected to two input ground motions: (*i*) a motion recorded from the Loma Prieta event in 1989 (RSN 769, H2 direction) and (*ii*) a motion recorded from the Imperial Valley event in 1979 (RSN 165, H2 direction). The time histories were retrieved from the Pacific Earthquake Engineering Research (PEER) strong motion database (Ancheta et al., 2014). The recordings were chosen arbitrarily for the purpose of demonstration of the procedure.
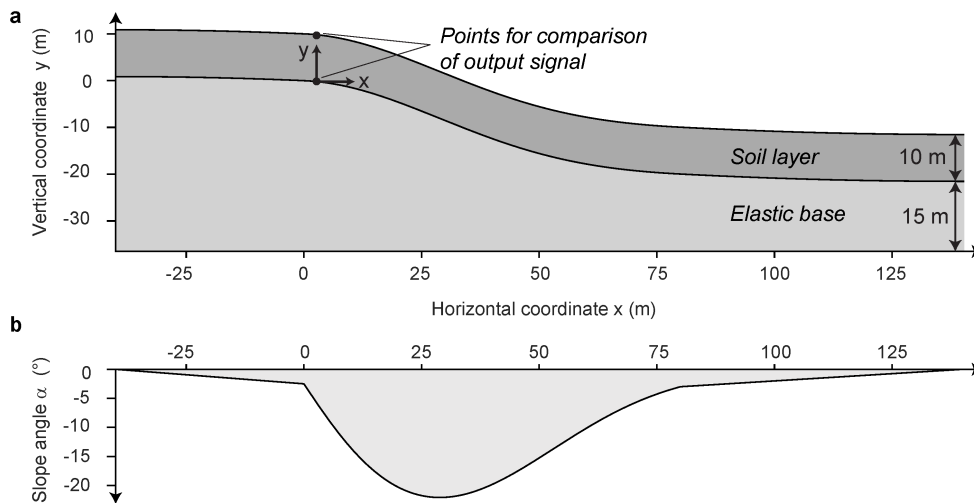
Figure 2.7: Illustration of (a) the slope geometry and (b) the curvature of the example case.

For the MPM model a square grid with element size $h = 0.25m$ and a regular distribution of 3x3 material points has been chosen to reasonably represent the slope curvature and to accurately model higher frequencies in the seismic analysis (see Figure 2.8a). For more complex slope geometries, a finer grid may be chosen or the concept of isoparametric elements could be introduced (Tjung et al., 2020). A structural mesh with quadrilateral 4-node finite elements (Q4) that follows the slope curvature is used for the CEL model (see Figure 2.8b). The mesh size h_{el} is chosen identical to the MPM.
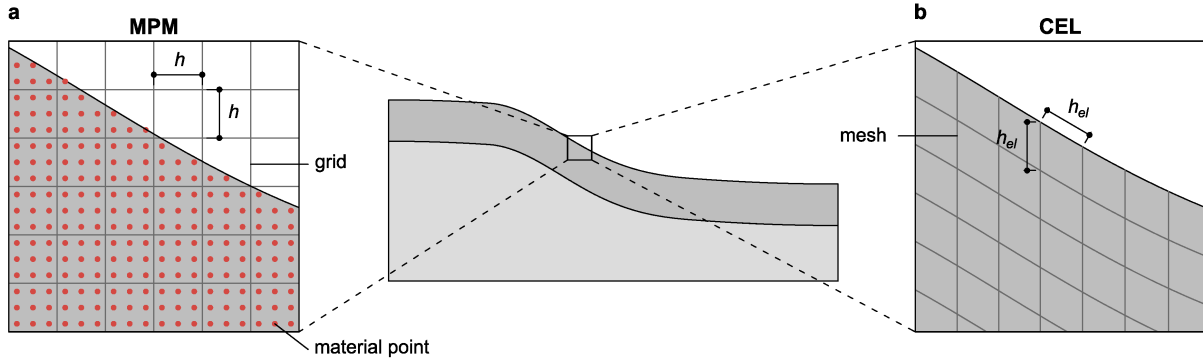
Figure 2.8: Illustration of (a) the computational grid and the initial material point arrangement for MPM and (b) the computational mesh for CEL. (h: grid size for MPM; h_{el}: element size for CEL).

Undrained soil behaviour was assumed, represented by a von Mises constitutive model with isotropic softening in combination with an isotropic, linear elastic model. The stress-strain response is linear and elastic up to the peak shear strength, followed by linear softening until the value of the remoulded shear strength is reached and the strength remains constant (Figure 2.9).

It should be mentioned, that the presented example case is a theoretical example and does not represent a particular slope. The slope shape and curvature as well as the used soil parameters were chosen to represent typical values (see Table 2.1).
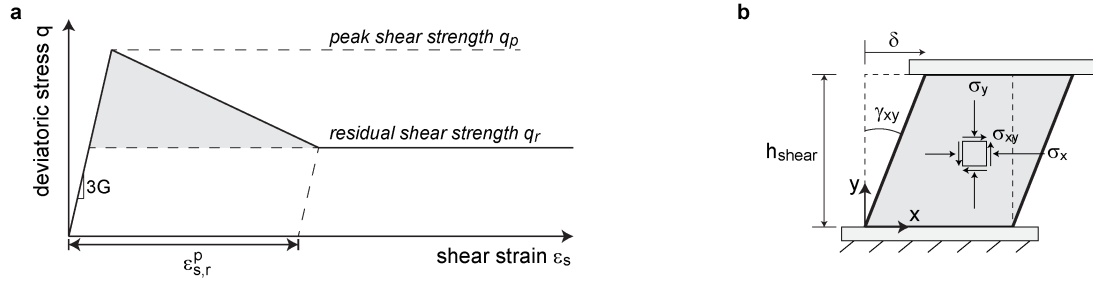
Figure 2.9: Illustration of (**a**) the assumed constitutive behaviour and (**b**) the adopted simplified scaling method.

The residual shear strength is defined by the peak shear strength q_p and the sensitivity of the material S.

$$q_r = \frac{q_p}{S} \tag{2.33}$$

As the specified strain-softening constitutive behaviour can lead to mesh-dependent results, a smeared crack approach was employed as a regularization technique (Rots et al., 1985). This approach is often employed for MPM-simulations featuring strain-softening materials (e.g. Soga et al., 2016; Yerro, 2015) and provides the advantage that the numerical shear band thickness does not have to match the in-situ zone of intensive shearing. Therefore, a much coarser mesh can be used. It should, however, be assured that the mesh is fine enough to allow the shear bands to develop and propagate. A shear displacement in simple shear loading was used rather than a shear strain to define the post-peak softening curve.

Assuming simple shear conditions, the plastic shear strain at which the material is fully softened was scaled as a function of the shear band thickness

$$\varepsilon_{s,r}^{p} = \frac{\delta_r}{\sqrt{3}h_{\text{shear}}}$$ (2.34)

where δ_r is the displacement at which the material is fully softened and h_{shear} the shear band thickness in the computational model (Figure 2.9b). A typical value of $\delta_r = 0.2m$ was chosen for the calibration (Skempton 1985). For the FE-analysis it was assumed that the shear band develops within a single element. Hence, the element size is equal to the shear band thickness ($h_{\text{shear}} = h_{el}$). Due to the longer span of the B-Spline in the MPM analysis, the scaling parameter h_{shear} was calibrated prior to running the analysis, based on a numerical simple shear element test. The calibration showed, that this leads to a shear band thickness of about twice the grid cell size ($h_{\text{shear}} \cong 2h$), which corresponds to exactly half the span of the cubic B-spline. However, this topic is not discussed in detail here and will be the subject of future investigations.

Table 2.1: Parameters for example case analysis.

Type	Parameter	Symbol	Value
Geometry	Element and grid size	h_{el} and h	0.25 m
	Number of MP's per grid cell	n_{MP}	3x3
Elastic base	Young's modulus	E_{Base}	250 MPa
	Poisson's ratio	v_{Base}	0.25
	Density	ρ_{Base}	2200 kg/m^3
Soil layer	Young's modulus	E_{Layer}	40 MPa
	Poisson's ratio (initial conditions)	v_{Layer}	0.35
	Poisson's ratio (dynamic analysis)	v_{Layer}	0.495
	Density	ρ_{Layer}	1800 kg/m^3
	Peak von Mises shear strength	q_p	70 kPa
	Sensitivity	S	1.8
	Residual shear displacement	δ_r	0.2 m

2.5.2. Results of the seismic response analysis

In a first step, the implementation of the seismic boundary conditions was benchmarked. For this purpose, the resulting motion within the slope was compared for the MPM and the FE methodologies. The comparison shows whether (*i*) the input ground motion is prescribed correctly, (*ii*) the wave propagation is simulated correctly and (*iii*) whether outgoing waves are absorbed at the model

boundaries. In order to exclude effects of strain localization and scaling, both the soil layer and the base were assigned a purely isotropic, linear elastic behaviour.

A comparison of the computed motion is shown in Figure 2.10 for two arbitrarily chosen points within the model domain – a point at the ground surface and a point at the boundary between the soil layer and the base (see Figure 2.7a). The comparison shows that the solution obtained with the MPM and the FEM analysis approach are nearly identical. The same holds for any other point within the model and other output quantities, such as acceleration or deformations. The results therefore validate the implementation of the seismic boundary conditions in the MPM framework.
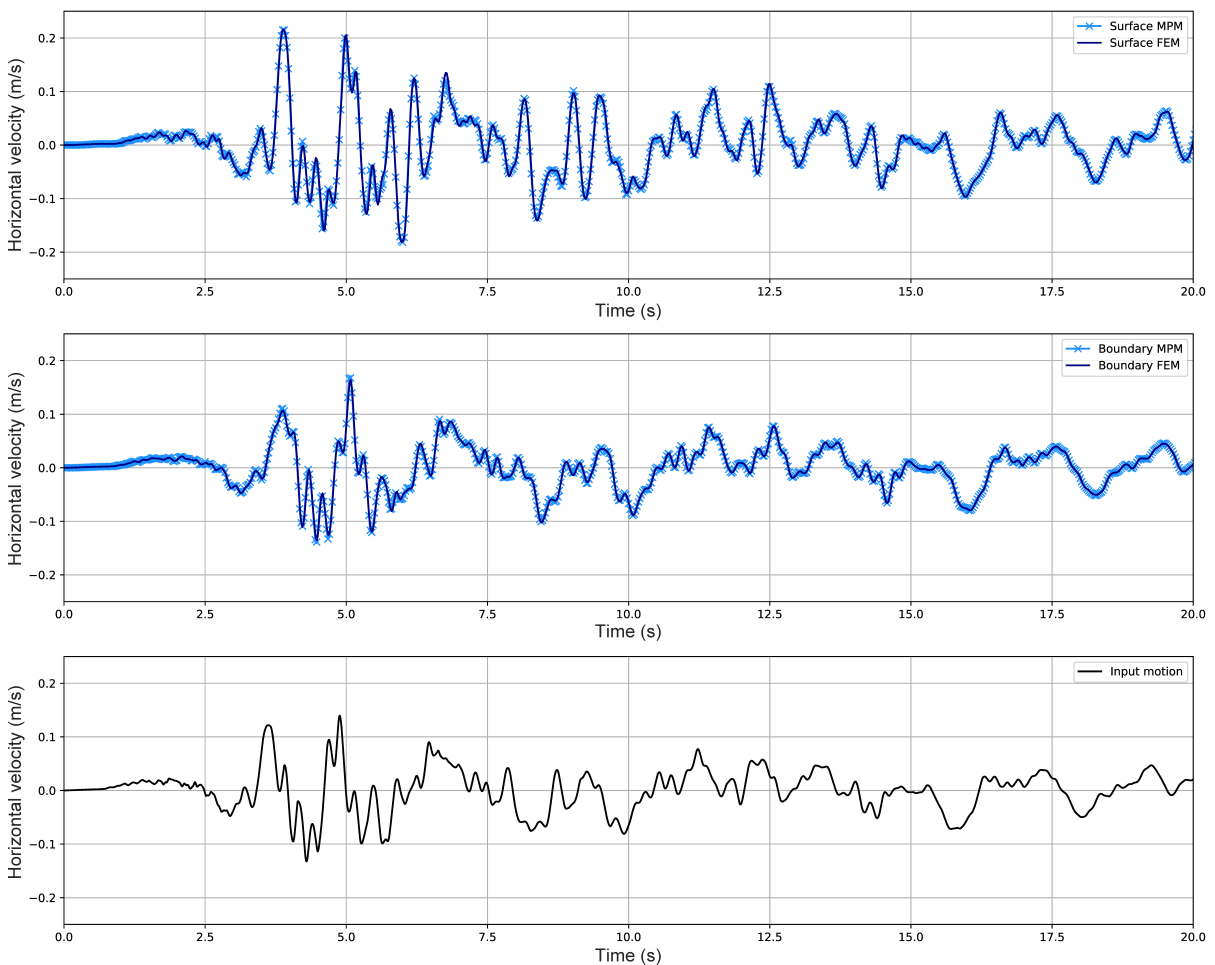
Figure 2.10: Comparison of the resulting horizontal velocity for a point at the ground surface (top) and boundary between the soil layer and the base (middle) using the MPM and the FEM analysis procedure. The Loma Prieta (RSN 769) recording was applied as an input ground motion (bottom).

2.5.3. Results of the slope failure analysis

Having validated the implementation of the seismic boundary conditions, the process of failure initiation and propagation by seismic ground motion was analysed next. This comparison provides an indication whether (*i*) the degradation of the shear resistance by cyclic loading (*ii*) the initiation of a failure mechanism and (*iii*) its propagation along localized shear bands is captured adequately in the simulations. The soil material was assigned a strain-softening constitutive behaviour (see Section 2.5.1), whereas the base was assumed to behave elastically.

The resulting displacements and distribution of plastic strain within the soil layer are shown in Figure 2.11. It can be observed that the slope failure is initiated nearly at the same time in both simulations. Following failure initiation, a very similar failure mechanism develops in both simulations. As the slope collapse evolves further, some differences emerge between the two solutions in terms of the development of secondary shear bands. A more distinct difference can be identified at the newly formed toe. In MPM the shear band localizes less and a steeper toe is formed, whereas in the CEL simulation the toe collapses and results in a milder gradient. These differences are most likely a result of the often reported sticky behaviour of MPM (Huang et al., 2011; Soga et al., 2016) as material points remain numerically in contact when they have a node in common. The long span of cubic B-splines might lead to an even more pronounced phenomenon. However, this does not affect the main results of this analysis. Modelling strain localization problems using MPM in general has room for improvement and is the subject of ongoing research studies.

Nonetheless, the geometry of the final deposit is remarkably similar. The comparison thus improves the confidence in the obtained solution and validates the two independent methodologies against each other. For consistency, the ground motion was applied only until the failure became self-driven for both simulations. This simplification can be avoided with the MPM methodology, which is discussed in the next section.
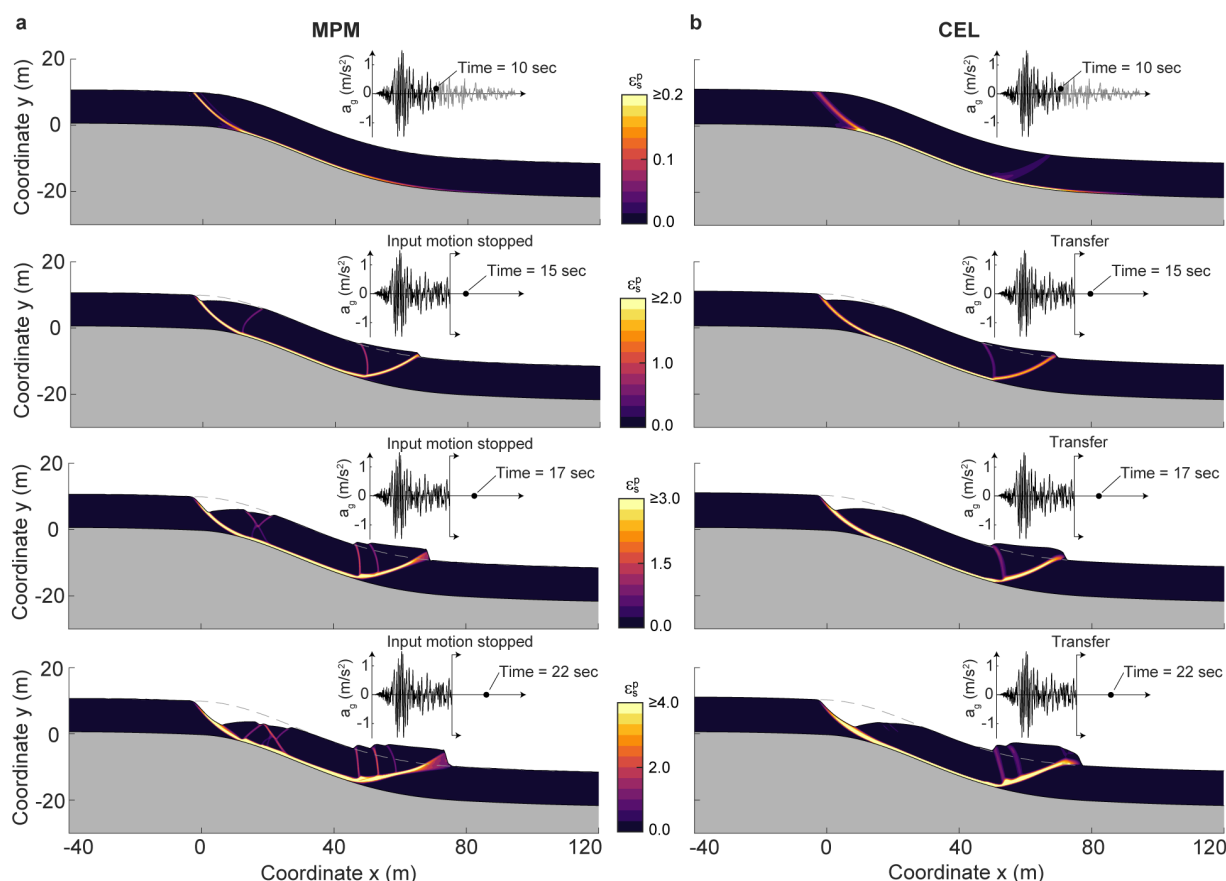
Figure 2.11: Comparison of the evolution of plastic strain within the example slope at different time points during the analysis for both the MPM (a) and the CEL simulation (b). The slope was subjected to the Loma Prieta (1989) ground motion until the failure became self-driven.

2.5.4. Advantages of the MPM procedure

As shown in the previous sections, the developed MPM framework provides very similar results to the FE analysis procedure. As the MPM analysis is computationally more expensive, the FE analysis procedure remains, in the authors' opinion, the preferred method for seismic response analysis of problems where deformations remain limited. However, for applications where earthquake loading leads to the initiation of instabilities and large deformations within the ground, the MPM approach offers a significant advantage. It offers an "all-in-one" approach, allowing for the simulation of seismic ground excitation and the evolution of large deformations within the ground at the same time. For some applications it can therefore provide more accurate results.

To demonstrate this effect, the results of two simulations were compared – one where the ground motion was applied throughout the entire duration of the analysis and one where the ground motion was applied until the slope failure becomes self-driven. When applying the relatively short Loma Prieta (1989) ground motion the results are nearly indistinguishable, showing that the ground motion does not influence the movement of the slide significantly upon failure initiation. However, as shown in Figure

2.12, applying the Imperial Valley (1979) ground motion, which has a much longer strong motion, leads to significantly different results. It can be observed that early on, a similar failure mechanism is triggered. However, with a continuing ground excitation, the failure mechanism propagates further down- and uphill into stable parts of the slope, resulting in a considerably larger landslide. Therefore, applying the unified MPM procedure can provide more reliable risk assessment results for certain cases.
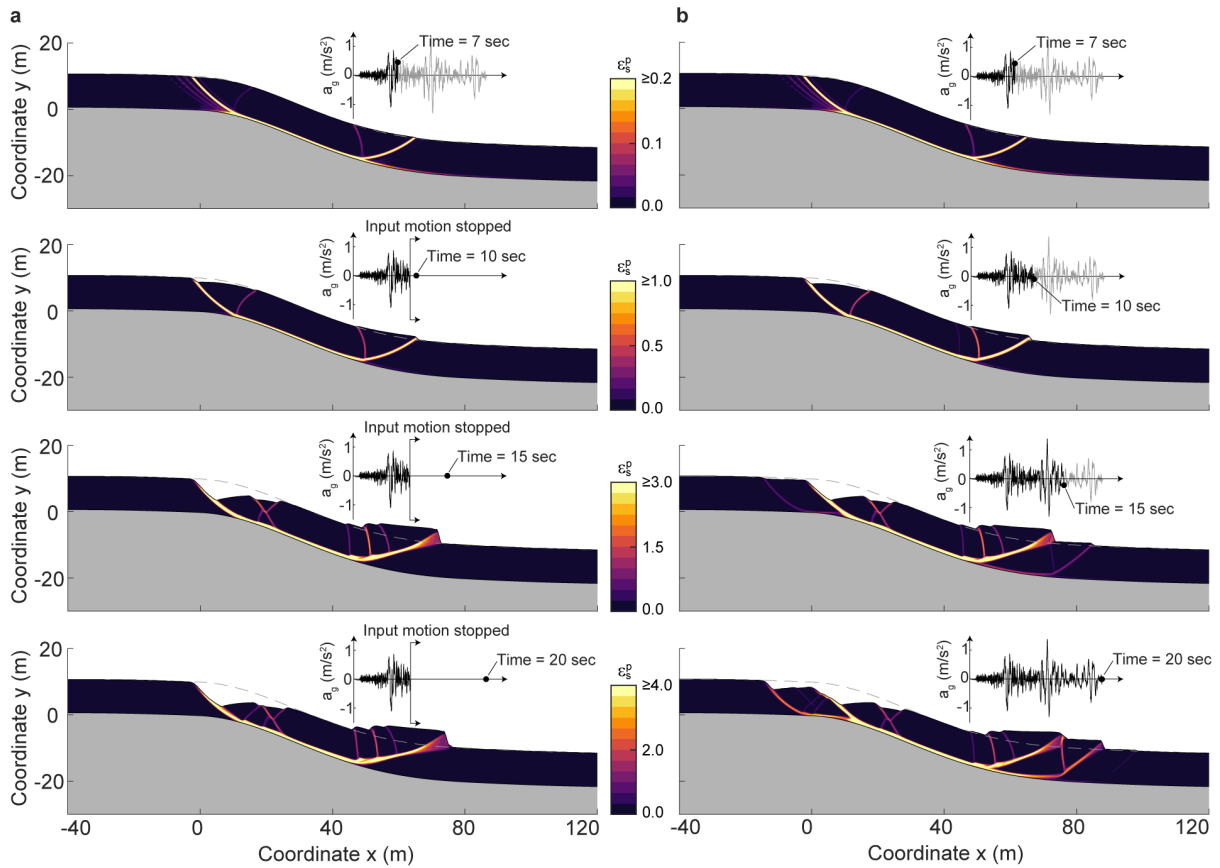
Figure 2.12: Comparison of the evolution of plastic strains for a model where the motion is applied (a) until the slope becomes self-driven and (b) throughout the entire analysis. The Imperial Valley (RSN 165) recording was applied as an input ground motion.

2.5.5. Limitations

The presented approach has a number of limitations, which should be refined in future studies. For the validation of the procedure, both geometry and the employed constitutive models were kept as simple as possible and are therefore not necessarily appropriate to represent real-life slopes. Nevertheless, the methodology can readily be applied to include more complex geometries and more advanced constitutive models.

Furthermore, other effects, which have been shown to influence the failure behaviour of slopes, such as the effect of heat and excess pore-water pressure generation (e.g., Abe et al., 2014; Bandara & Soga,

2015; Zabala & Alonso, 2011) were out of the scope of this study. The presented framework could be applied in combination with such techniques in future investigation to investigate for these effects.

Another potential shortcoming is that the ground motion was applied as a stress history distributed uniformly along the entire base of the model, implying that the earthquake signal arrives simultaneously at each point of the base. A way to overcome this shortcoming in future investigations would be to apply a non-uniform input signal from a larger seismological model (Bielak, 2003).

It should be mentioned that using the compliant base boundary and free-field columns lead to an unsupported model during the seismic analysis, regardless of the numerical method. This can cause a drifting of the model. This problem might be more pronounced in MPM and must be carefully considered when evaluating permanent displacements. It is crucial to apply local damping for the stress initialization to keep the initial material point velocities small. In combination with prescribing the static support directly on grid nodes during the seismic analysis, this often helps to reduce the model drift to an acceptable level. For the presented example analysis, the associated stress redistributions at the boundaries and the effect of the model drift are negligible. In cases where the simulation is continued after the seismic event for a longer time span, kinematic boundary conditions could be reapplied or the dashpots exchanged with Kelvin-Voigt elements.

2.6. Conclusions

Dynamic response analysis in the time domain is considered the state of the art technique for assessing the stability of slopes under seismic loading. For a comprehensive risk assessment, however, not only the stability of a slope during earthquake loading is of interest, but also the subsequent mass movement. Traditional approaches to seismic response analysis, such as the standard finite element method, solve the equation of motion using Lagrangian framework and fail to provide accurate solutions in case large deformations occur, due to excessive mesh distortion.

The material point method, on the other hand, has become a successful tool to model such large deformation problems. However, so far it has not been widely applied for seismic response analyses, partly due to the unavailability of appropriate boundary conditions. In this article, this gap is addressed and a procedure is presented to model the entire process from initiation to post-failure evolution of seismically triggered landslides within a single analysis step.

For this purpose, an extension to the basic MPM framework is presented. Special considerations for the computation of initial stress conditions and the switch to dynamic boundary conditions are outlined and a formulation and implementation of suitable dynamic boundary conditions is presented. For the latter, boundary conditions that are established for dynamic FE analyses were adapted and implemented in the MPM framework, namely the compliant base boundary and the free-field boundary method.

A comparison between the computed seismic response of an example slope using the MPM- and a traditional FEM procedure shows, that the obtained results are nearly indistinguishable. Furthermore, the results of the co- and post-seismic analysis obtained from the two procedures compare remarkably well in terms of the time of triggering, the resulting failure mechanism and the post-failure geomorphology for the analysed case. An important advantage of the proposed unified MPM approach is that the seismic shaking can be applied continuously throughout the analysis, even after the slope collapsed and large deformations have occurred. For the first time we were able to quantify this phenomenon for a case of a long duration strong ground motion and to demonstrate that it can have a significant effect on the landslide evolution.

Acknowledgments

Notations

Small Latin letters

a_g	horizontal ground acceleration	p	material point
c_p	pressure wave velocity	q	deviatoric stress
c_s	shear wave velocity	q_p	peak von Mises shear strength
$\boldsymbol{f}_{d,i}$	local damping force vector at grid node i	q_r	residual shear strength
$\boldsymbol{f}_{ext,i}$	external force vector of grid node i	$\boldsymbol{s}$	normalized line element
$\boldsymbol{f}_{int,i}$	internal force vector of grid node i	t	time
$\boldsymbol{f}_{bc,i}$	traction boundary prescribed on grid node i	$\boldsymbol{t}_p$	traction force vector of material point p
$\boldsymbol{f}_i$	resulting force at grid node i	t_s	traction time history
h	grid spacing (MPM)	$\boldsymbol{v}_{fp}$	velocity vector of corresponding material point in free field
h_{el}	mesh size (FE)	$\boldsymbol{v}_p$	velocity vector of material point p
h_{shear}	shear band thickness in computational model	$\overline{\boldsymbol{v}}_p$	velocity vector of mirrored material point
i	grid node	v_{pu}	particle velocity of upward propagating pressure wave
m_i	mass of node i	v_{su}	particle velocity of upward propagating shear wave
m_p	mass of material point p	w_{ip}	weight of material point p associated with rid node i
n	time step	$\boldsymbol{x}_i$	position vector of grid node i
n_{MP}	number of material points inside a grid cell	$\boldsymbol{x}_p$	position vector of material point p

Capital Latin letters

APIC	affine particle in cell	M	P-wave modulus
$\boldsymbol{D}$	rate of deformation tensor	$N(x)$	basis function
$\boldsymbol{D}_p^n$	auxiliary matrix for APIC transfer	$N'(x)$	derivative of basis function
E_{base}	Young's modulus (elastic base)	$N_i(\boldsymbol{x})$	interpolation function at grid node i
E_{layer}	Young's modulus (soil layer)	PIC	particle in cell
$\boldsymbol{F}_p$	deformation gradient of material point p	$\boldsymbol{R}$	rotation tensor
FLIP	fluid implicit particle	S	sensitivity of material
G	shear modulus	V_p	volume of material point p
$\boldsymbol{I}$	identity tensor	$\boldsymbol{W}$	spin tensor
$\boldsymbol{L}_p$	velocity gradient of material point p		

Small Greek letters

α	slope angle	ρ	bulk density
β	dimensionless damping factor	ρ_{Base}	density (elastic base)
γ_{xy}	engineering shear strain	ρ_{Layer}	density (soil layer)
δ	shear displacement	$\boldsymbol{\sigma}_{fp}$	stress tensor of corresponding free-field material point
δ_p	surface related to material point p	$\sigma_{fp,d}$	dynamic normal stress of corresponding free-field material point
δ_r	residual shear displacement	$\boldsymbol{\sigma}_{fp,d}$	dynamic stress tensor of corresponding free-field material point
ε_s	shear strain	$\boldsymbol{\sigma}_{fp,s}$	static stress tensor of corresponding free-field material point
$\varepsilon_{s,r}^{p}$	plastic shear strain at residual state	$\boldsymbol{\sigma}_p$	Cauchy stress tensor of material point p
η_p	viscosity of pressure dashpot	$\sigma_{p,s}$	static normal stress of material point p
η_s	viscosity of shear dashpot	$\overset{\nabla}{\boldsymbol{\sigma}}$	Jaumann rate of Cauchy stress
λ	stretch of normalized line element in initial configuration	$\dot{\boldsymbol{\sigma}}$	rate of Cauchy stress
ν_{Base}	Poisson's ratio (elastic base)	$\tau_{fp,d}$	dynamic shear stress of corresponding free-field material point
ν_{Layer}	Poisson's ratio (soil layer)	$\tau_{p,s}$	static shear stress of material point p

References

Abe, K., Soga, K. & Bandara, S. (2014). Material Point Method for Coupled Hydromechanical Problems. *Journal of Geotechnical and Geoenvironmental Engineering*, *140*(3), 04013033. https://doi.org/10.1061/(ASCE)GT.1943-5606.0001011

Adams, E. W. & Schlager, W. (2000). Basic Types of Submarine Slope Curvature. *Journal of Sedimentary Research*, *70*(4), 814–828. https://doi.org/10.1306/2DC4093A-0E47-11D7-8643000102C1865D

Al-Kafaji, I. K. J. (2013). *Formulation of a Dynamic Material Point Method (MPM) for Geomechanical Problems*. University of Stuttgart.

Alsardi, A., & Yerro, A. (2021). Runout Modeling of Earthquake-Triggered Landslides with the Material Point Method, 21–31. https://doi.org/10.1061/9780784483428.003

Ancheta, T. D., Darragh, R. B., Stewart, J. P., Seyhan, E., Silva, W. J., Chiou, B. S. J., … Donahue, J. L. (2014). NGA-West2 database. *Earthquake Spectra*, *30*(3), 989–1005. https://doi.org/10.1193/070913EQS197M

Andersen, S. & Andersen, L. (2010). Modelling of landslides with the material-point method. *Computational Geosciences*, *14*(1), 137–147. https://doi.org/10.1007/s10596-009-9137-y

Bandara, S. & Soga, K. (2015). Coupling of soil deformation and pore fluid flow using material point method. *Computers and Geotechnics*, *63*, 199–214. https://doi.org/10.1016/J.COMPGEO.2014.09.009

Bardenhagen, S. G. & Kober, E. M. (2004). The generalized interpolation material point method. *CMES - Computer Modeling in Engineering and Sciences*, *5*(6), 477–495. https://doi.org/10.3970/cmes.2004.005.477

Bažant, Z. P., Gattu, M. & Vorel, J. (2012). Work conjugacy error in commercial finite-element codes: its magnitude and how to compensate for it. *Proceedings of the Royal Society A: Mathematical, Physical and Engineering Sciences*, *468*(2146), 3047–3058. https://doi.org/10.1098/rspa.2012.0167

Bhandari, T., Hamad, F., Moormann, C., Sharma, K. G., & Westrich, B. (2016). Numerical modelling of seismic slope failure using MPM. Computers and Geotechnics, 75, 126–134. https://doi.org/10.1016/j.compgeo.2016.01.017

Bielak, J. (2003). Domain Reduction Method for Three-Dimensional Earthquake Modeling in Localized Regions, Part I: Theory. *Bulletin of the Seismological Society of America*, *93*(2), 817–824. https://doi.org/10.1785/0120010251

Cundall, P. A. (2002). A Discontinuous Future for Numerical Modeling in Soil and Rock (pp. 3–4). American Society of Civil Engineers (ASCE). https://doi.org/10.1061/40647(259)1

Dassaulr Systèmes Simulia, (2012). Abaqus 6.12 documentation. *Providence, Rhode Island, US*, 6.

Dey, R., Hawlader, B., Phillips, R. & Soga, K. (2015). Large deformation finite-element modelling of progressive failure leading to spread in sensitive clay slopes. *Géotechnique*, *65*(8), 657–668. https://doi.org/10.1680/geot.14.P.193

Dey, R., Hawlader, B., Phillips, R. & Soga, K. (2016). Modeling of large-deformation behaviour of marine sensitive clays and its application to submarine slope stability analysis. *Canadian Geotechnical Journal*, *53*(7), 1138–1155. https://doi.org/10.1139/cgj-2015-0176

Ding, O., Shinar, T. & Schroeder, C. (2020). Affine particle in cell method for MAC grids and fluid simulation. *Journal of Computational Physics*, *408*, 109311. https://doi.org/10.1016/j.jcp.2020.109311

Ering, P., & Sivakumar Babu, G. L. (2020). Effect of spatial variability of earthquake ground motions on the reliability of road system. Soil Dynamics and Earthquake Engineering, 136, 106207. https://doi.org/10.1016/J.SOILDYN.2020.106207

Hashash, Y. M. a & Groholski, D. R. (2010). Recent advances in non-linear site response analysis. *Fifth Interantional Conference on Recent Advances in Geotechnical Earthquake Engineering and Soil Dynamics and Symposium in Honor of Professor I.M. Idriss*, *29*(6), 1–22. https://doi.org/10.1016/j.soildyn.2008.12.004

Havenith, H.-B., Torgoev, A., Braun, A., Schlögel, R. & Micu, M. (2016). A new classification of earthquake-induced landslide event sizes based on seismotectonic, topographic, climatic and geologic factors. https://doi.org/10.1186/s40677-016-0041-1

He, M., Ribeiro e Sousa, L., Müller, A., Vargas, E., Sousa, R. L., Oliveira, C. S., & Gong, W. (2019). Numerical and safety considerations about the Daguangbao landslide induced by the 2008 Wenchuan earthquake. Journal of Rock Mechanics and Geotechnical Engineering, 11(5), 1019–1035. https://doi.org/10.1016/J.JRMGE.2019.05.004

Huang, P., Zhang, X., Ma, S., & Huang, X. (2011). Contact algorithms for the material point method in impact and penetration simulation. International Journal for Numerical Methods in Engineering, 85(4), 498–517. https://doi.org/10.1002/NME.2981

Hughes, T. J. R. & Winget, J. (1980). Finite rotation effects in numerical integration of rate constitutive equations arising in large-deformation analysis. *International Journal for Numerical Methods in Engineering*, *15*(12), 1862–1867. https://doi.org/10.1002/nme.1620151210

Jiang, C., Selle, A., Teran, J. & Stomakhin, A. (2015). The Affine Particle-In-Cell Method. *ACM Transactions on Graphics*, *34*(4).

Keefer, D. K. (2002). Investigating landslides caused by earthquakes - A historical review. *Surveys in Geophysics*, *23*(6), 473–510. https://doi.org/10.1023/A:1021274710840

Kramer, S. L. (1996). *Geotechnical Earthquake Engineering*. *Engineering* (Vol. 6). https://doi.org/10.1007/978-3-540-35783-4

Lysmer, J. & Kuhlemeyer, R. L. (1969). Finite Difference Model for Infinite Media. *Journal of Engineering Mechanics*, *95*, 859–877.

Mejia, L. H. & Dawson, E. M. (2006). Earthquake deconvolution for FLAC. *Proceedings of the 4th International FLAC Symposium on Numerical Modeling in Geomechanics*, (1969), 1–9.

Newmark, N. M. (1965). Effects of Earthquakes on Dams and Embankments. *Géotechnique*, *15*(2), 139–160. https://doi.org/10.1680/geot.1965.15.2.139

Nielsen, A. H. (2006). Absorbing Boundary Conditions for Seismic Analysis in ABAQUS. *2006 ABAQUS Users' Conference*.

Rodríguez, C. E., Bommer, J. J. & Chandler, R. J. (1999). Earthquake-induced landslides: 1980-1997. *Soil Dynamics and Earthquake Engineering*, *18*(5), 325–346. https://doi.org/10.1016/S0267-7261(99)00012-3

Rots, J. G., Nauta, P., Kusters, G. M. A. & Blaauwendraad, J. (1985). Smeared Crack Approach and Fracture Localization in Concrete. *Heron*, *30*(1).

Schulz, S. & Sutmann, G. (2019). A consistent boundary method for the material point method - using image particles to reduce boundary artefacts. *International Conference on Particle-Based Methods*, 522–533.

Shen, L. & Zhen, C. (2005). A silent boundary scheme with the material point method for dynamic analyses. *CMES - Computer Modeling in Engineering and Sciences*, *7*(3), 305–320. https://doi.org/10.3970/cmes.2005.007.305

Simo, J. C. & Hughes, T. J. R. (1998). *Computational Inelasticity*. *Computational Inelasticity*. Springer-Verlag. https://doi.org/10.1007/b98904

Simo, J. C. & Pister, K. S. (1984). Remarks on rate constitutive equations for finite deformation problems: computational implications. *Computer Methods in Applied Mechanics and Engineering*, *46*(2), 201–215. https://doi.org/10.1016/0045-7825(84)90062-8

Skempton, A. W. (1985). Residual strength of clays in landslides, folded strata and the laboratory. Géotechnique, 35(1), 3–18. https://doi.org/10.1680/geot.1985.35.1.3

Soga, K., Alonso, E., Yerro, A., Kumar, K. & Bandara, S. (2016). Trends in large-deformation analysis of landslide mass movements with particular emphasis on the material point method. *Géotechnique*, *66*(3), 248–273. https://doi.org/10.1680/jgeot.15.LM.005

Steffen, M., Kirby, R. M. & Berzins, M. (2008). Analysis and reduction of quadrature errors in the material point method (MPM). *International Journal for Numerical Methods in Engineering*, *76*(6), 922–948. https://doi.org/10.1002/nme.2360

Stoecklin, A. & Puzrin, A. M. (2018). 2D Seismic Analysis of Overpressured Submerged Slopes. In *Proceedings of 26th European Young Geotechnical Engineers Conference* (pp. 1–10). Graz.

Stoecklin, A. & Puzrin, A. M. (2020). A combined analysis procedure for submarine landslide evolution. In *Proceedings of the 4th International Symposium on Frontiers in Offshore Geotechnics, ISFOG 2020*. Austin, TX.

Stoecklin, A., Trapper, P. & Puzrin, A. M. (2020). Controlling factors for post-failure evolution of subaqueous landslides. *Géotechnique*, 1–14. https://doi.org/10.1680/jgeot.19.P.230

Stomakhin, A., Schroeder, C., Chai, L., Teran, J. & Selle, A. (2013). A material point method for snow simulation. *ACM Transactions on Graphics*, *32*(4), 1. https://doi.org/10.1145/2461912.2461948

Sulsky, D., Chen, Z. & Schreyer, H. L. (1994). A particle method for history-dependent materials. *Computer Methods in Applied Mechanics and Engineering*, *118*(1–2), 179–196. https://doi.org/10.1016/0045-7825(94)90112-0

Tielen, R., Wobbes, E., Möller, M., & Beuth, L. (2017). A High Order Material Point Method. *Procedia Engineering*, *175*, 265–272). https://doi.org/10.1016/j.proeng.2017.01.022

Tjung, E. Y. S., Kularathna, S., Kumar, K., & Soga, K. (2020). Modeling Irregular Boundaries Using Isoparametric Elements in Material Point Method. Geo-Congress 2020, 39–48. https://doi.org/10.1061/9780784482803.005

Wolf, J. P. (1989). Soil-structure-interaction analysis in time domain. *Nuclear Engineering and Design*, *111*(3), 381–393. https://doi.org/10.1016/0029-5493(89)90249-5

Yerro, A. (2015). MPM modelling of landslides in brittle and unsaturated soils. Universitat Politècnica de Catalunya (UPC).

Zabala, F. & Alonso, E. E. (2011). Progressive failure of Aznalcóllar dam using the material point method. *Géotechnique*, *61*(9), 795–808. https://doi.org/10.1680/geot.9.P.134

Zienkiewicz, O. C., Bicanic, N. & Shen, F. Q. (1989). Earthquake Input Definition and the Trasmitting Boundary Conditions. In *Advances in Computational Nonlinear Mechanics* (pp. 109–138). Vienna: Springer Vienna. https://doi.org/10.1007/978-3-7091-2828-2_3

3   Mechanism of co-seismic deformation of the slow-moving La Sorbella landslide in Italy revealed by MPM analysis

Abstract

Predicting the seismic behaviour of slow-moving landslides presents a significant challenge. Their yearly displacements of a few millimetres to several metres indicate that even before any earthquake they are balancing at the verge of instability. It is therefore not surprising that conventional analysis predicts large co-seismic displacements even for light-to-moderate ground motions. In reality, however, negligibly small displacements have often been observed for such earthquakes, while strong ground motions can still lead to catastrophic failure. This discrepancy challenges both our understanding of the underlying mechanisms and the reliability of conventional analysis, resulting in significant uncertainties for risk assessment. Progress in this field has been further hindered by incompleteness of the available monitoring data and a lack of reliable numerical models capable of dealing simultaneously with small and large deformations under seismic loading. In this article, recently published monitoring data on La Sorbella landslide in Italy and the latest developments in seismic material point method (MPM) analysis are used to gain insights into the mechanisms controlling the co-seismic behaviour of slow-moving landslides. This forms the basis for a subsequent investigation of the potential landslide behaviour during strong motions, using various material models. The study demonstrates that the co-seismic behaviour of La Sorbella slide is strongly influenced by the interplay between geometrical and viscous effects, as well as potential softening in the shear zone and the surrounding soil mass. The proposed approach paves a way towards quantification of these effects in risk assessment for slow-moving landslides.

3.1. Introduction

3.1.1. Slow-moving landslides

Landslides are one of the major threats in mountainous regions globally and cause thousands of fatalities every year (Froude & Petley, 2018). Some of the landslides are characterized by very slow movements, and these are often referred to as creeping landslides (Bontemps et al., 2020; Oberender & Puzrin, 2016; Puzrin & Schmid, 2011, 2012; Schulz & Wang, 2014). Although it is well known that landslides are influenced and triggered by earthquakes (Dai et al., 2011; Jibson et al., 1994; Keefer, 2002; Rodríguez et al., 1999), the seismic behaviour of creeping landslides is sparsely reported and not well understood. One reason for this is that only a handful of such cases can be found in the literature, and most of them are not monitored and documented in detail (Lacroix et al., 2015, 2020, 2014). Another reason is that modelling of such landslides requires a combination of small- and large-deformation approaches, as well as kinematic and seismic techniques, which is not always possible within a single computational framework. Recently published monitoring data on La Sorbella landslide in Italy (Ferretti et al., 2019; Ruggeri et al., 2020), as well as the latest developments in seismic material point method (MPM) analysis (Kohler et al., 2021) therefore provide an important opportunity to gain some insights into the mechanisms of co-seismic behaviour of slow-moving landslides.

3.1.2. Modelling the seismic response of slopes and landslides

Numerous techniques have been developed in the past for assessing the stability of slopes (Jibson, 2011), ranging from the pseudo-static limiting equilibrium approach to Newmark's sliding block analysis (Newmark, 1965), and to stress-deformation analyses (Hashash & Groholski, 2010; Kramer, 1996). Whereas the former allows the stability of the slope to be estimated during the seismic event, Newmark's sliding block analysis provides a method to assess the co-seismic displacements of a rigid block. However, for real case geometries and non-linear soil behaviour, this simplified approach cannot be relied on to evaluate earthquake-induced slope deformations. For rigorous stress-deformation analysis, the finite element method (FEM) is the most frequently used technique and has been successfully applied for seismic analyses (Stoecklin et al., 2021; C. Wang et al., 2019; Zheng et al., 2005). However, for mesh-based methods (e.g. FEM), special consideration has to be used when dealing with large deformations, owing to the problem of mesh distortion. To overcome this difficulty, several alternative numerical methods have been proposed, in particular the coupled Eulerian Lagrangian finite element method (CEL) and the material point method (MPM). A comprehensive review of different numerical approaches was provided by Soga et al. (2016). With the CEL a traditional Lagrangian phase, in which elements deform with the material, is followed by an Eulerian phase, during which elements with significant deformation are remeshed and material flow between neighbouring elements is computed (Dassault Système Simulia, 2019). The material is tracked and evolves through the Eulerian mesh based

on its volume fraction, which entails a smearing of the state variables and therefore is less suitable for the distinct contrast given by shear zones in slow-moving landslides. The main disadvantage is that existing CEL implementations do not include appropriate seismic boundary conditions and hence cannot be applied for seismic response analyses. Traditional Lagrangian FEM does include appropriate boundary conditions (Nielsen, 2014) and could theoretically be used to model moderate displacements where large strains are concentrated in the shear zone. This requires that the shear zone is introduced using a contact formulation (Wriggers, 1995). However, this methodology comes with convergence and accuracy issues, which are exacerbated by the nonlinear geometry of a real shear zone. MPM, on the other hand, represents a suitable framework for the seismic response of slopes, because it combines the advantages of standard Lagrangian and large-strain Eulerian approaches, but until recently it has lacked a rigorous implementation of the seismic boundary conditions. This implementation was recently performed by Kohler et al. (2021), making the MPM framework applicable for investigation of co-seismic displacements of slowly moving landslides.

3.1.3. Material point method (MPM)

The MPM is a hybrid approach in which the material is represented as Lagrangian particles, while the equations of motion are solved on an Eulerian grid. The Eulerian solution procedure allows for the material to undergo large deformations, while the Lagrangian material representation provides a convenient way of tracking material properties and constitutive state variables (e.g. stresses and strains). MPM is a generalization of the Particle In Cell (PIC) and the Fluid Implicit Particle (FLIP) methods for solid mechanics and was first proposed by Sulsky et al. (1994). Nowadays, numerous variations of the original algorithm have been introduced, tailored for a range of different applications (Bardenhagen & Kober, 2004; Jiang et al., 2015; Steffen et al., 2008). In recent years, the MPM has been successfully applied to model seismic slope failure (Bhandari et al., 2016; Ering & Sivakumar Babu, 2020; Kohler et al., 2021) and landslides triggered by earthquakes (Alsardi & Yerro, 2021; He et al., 2019). Alvarado et al. (2019) used a hydro- and thermo-mechanically coupled MPM to model the non-seismic behaviour of active landslides.

3.1.4. Goal and structure of this paper

As will be shown in the following section, a surprising feature of the co-seismic behaviour of La Sorbella landslide is that its displacements recorded in 2016 during three significant earthquakes were extremely small (<1 mm). This is for an intrinsically unstable slope, which can move around 0.5 mm/day in the absence of earthquakes. There exist other cases where relatively small co-seismic displacements of active landslides have been reported (Al-Homoud & Tahtamoni, 2000; Bontemps et al., 2020; Lacroix et al., 2014). As will be shown in this paper, the conventional Newmark's sliding block analysis would predict, for a slow-moving landslide whose safety factor approaches unity, a displacement magnitude

tending to infinity. To resolve this contradiction and to give some insight into the controlling factors, an effort has been made to develop a more rigorous modelling approach dealing with active landslides under seismic loading.

In the first part of this paper, La Sorbella landslide is introduced, and the necessary geological and geotechnical properties are discussed. Special focus is placed on its behaviour during three recent earthquakes. This is followed by a section in which a modelling technique for assessing the co-seismic behaviour of active landslides based on the MPM is presented. These landslides often feature distinct zones of intensive shearing which will be addressed by introducing the large-deformation constitutive model for shear zones. This approach offers the advantage of the same model being used both for lighter earthquakes resulting in small deformations and for stronger motions causing a non-linear soil response that leads to a catastrophic failure. For a mechanical and numerical validation of this technique, a benchmark model for infinite slope conditions is presented and compared to the conventional Newmark's sliding block analysis and a finite element approach. Applying this methodology to La Sorbella landslide for recorded moderate earthquakes will allow an understanding of the relative contribution of geometric effects, groundwater level and rate dependency of soil strength to the reduction in co-seismic displacements. Finally, the potential of the presented methodology will be shown by subjecting the model to stronger motions and investigating the influence of the shear zone behaviour.

3.2.   La Sorbella landslide

3.2.1.   Geological description

La Sorbella is an active deep-seated landslide in central Italy located near Valfabbrica (Figure 3.1a), which was already shown as active in the map by Guzzetti & Cardinali (1989). Monitoring of the landslide began in 2001, whereas intensive data acquisition through inclinometers started in 2014. All the necessary information and data concerning La Sorbella landslide have been adopted from Ferretti et al. (2019) and Ruggeri et al. (2020), where the monitoring campaign and measurement results are presented in detail. The landslide spans a slope of an average inclination of 8°. It has a length of 550 m and a maximal width at the toe of 600 m (Figure 3.1b). According to Ferretti et al. (2019), soil samples from the landslide mass consist of 70–90% silt and clay and are classified as CL (clay of low plasticity) and ML (silt of low plasticity). Unfortunately, the available data from laboratory tests are rather limited. According to Ferretti et al. (2019), cohesion in the sliding layer is negligible, the peak friction angle ranges from 28° to 32° and the residual friction angle lies between 14° and 18° (Table 3.1). No tests were performed on the material from the shear zone, but the residual friction angle is assumed to be smaller than 14°, otherwise the slope would remain stable. This assumption can be justified by the fact that the material in the shear zone is likely to be weaker than in the sliding layer and has undergone very

large deformations. A possible range of the residual strength in the shear zone will be back-calculated in Section 3.4.3 using a strength reduction analysis. The underlying bedrock in this region can be assigned to the Marnoso-Arenacea formation, which is characterized by alternating arenaceous and pelitic layers (Guerrera et al., 2012). Geophysical properties are not directly available for La Sorbella landslide and are assumed based on cross- and downhole seismic tests from a similar landslide in the Marnoso-Arenacea formation (Assefa et al., 2017). These assumptions are confirmed by the geophysical profile available for the seismic station IV-ATCC (Russo et al., 2022) which is located 6 km from the landslide and reaches the Marnoso-Arenacea formation.

Based on inclinometer measurements, whose locations are shown in Figure 3.1a, the currently active landslide can be clearly identified from a distinct shear zone of less than 1 m thickness, where almost all the deformation takes place (Ruggeri et al., 2020). The shear zone runs mostly at a depth between 20 m and 36 m along the transition from the bedrock to the overlying landslide mass. A scarp at the top of the landslide and no significant deformations at the inclinometer AI8 at the toe indicate that the shear zone runs through the landslide mass to the surface at the lower and upper ends (Ruggeri et al., 2020). Moreover, the inclinometer measurements (Figure 3.1c) suggest that the landslide moves largely as a rigid body with little internal deformation and at a very slow rate of 1.0–1.5 cm/year (Ruggeri et al., 2020). According to Ferretti et al. (2019), the groundwater level oscillates seasonally between 2 m and 6 m below the surface, but the actual piezometer data are not available. In the study by Ruggeri et al. (2020), it is clearly shown that the landslide displacements are closely linked to rainfall events.

Table 3.1: Geotechnical and geophysical parameters of La Sorbella landslide.

Type	Parameter	Symbol	Value
Bedrock: Marnoso-Arenacea formation	Pressure wave velocity	$v_{p,\text{base}}$	2.0–4.0 km/s
	Shear wave velocity	$v_{s,\text{base}}$	0.8–1.5 km/s
	Density	ρ_{base}	2500 kg/m^3
Landslide mass (CL and ML)	Pressure wave velocity	$v_{p,\text{slide}}$	500–1000 m/s
	Shear wave velocity	$v_{s,\text{slide}}$	300–500 m/s
	Density	ρ_{slide}	2000 kg/m^3
	Friction angle slide	φ_{slide}	28°-32°
	Residual friction angle	$\varphi_{r,\text{slide}}$	14°–18°
	Cohesion	c_{slide}	0 kPa
	Residual friction angle shear zone	$\varphi_{r,\text{shear}}$	<14°
	Shear zone thickness	δ_s	<1.0 m
	Depth of groundwater level	d_w	2–6 m
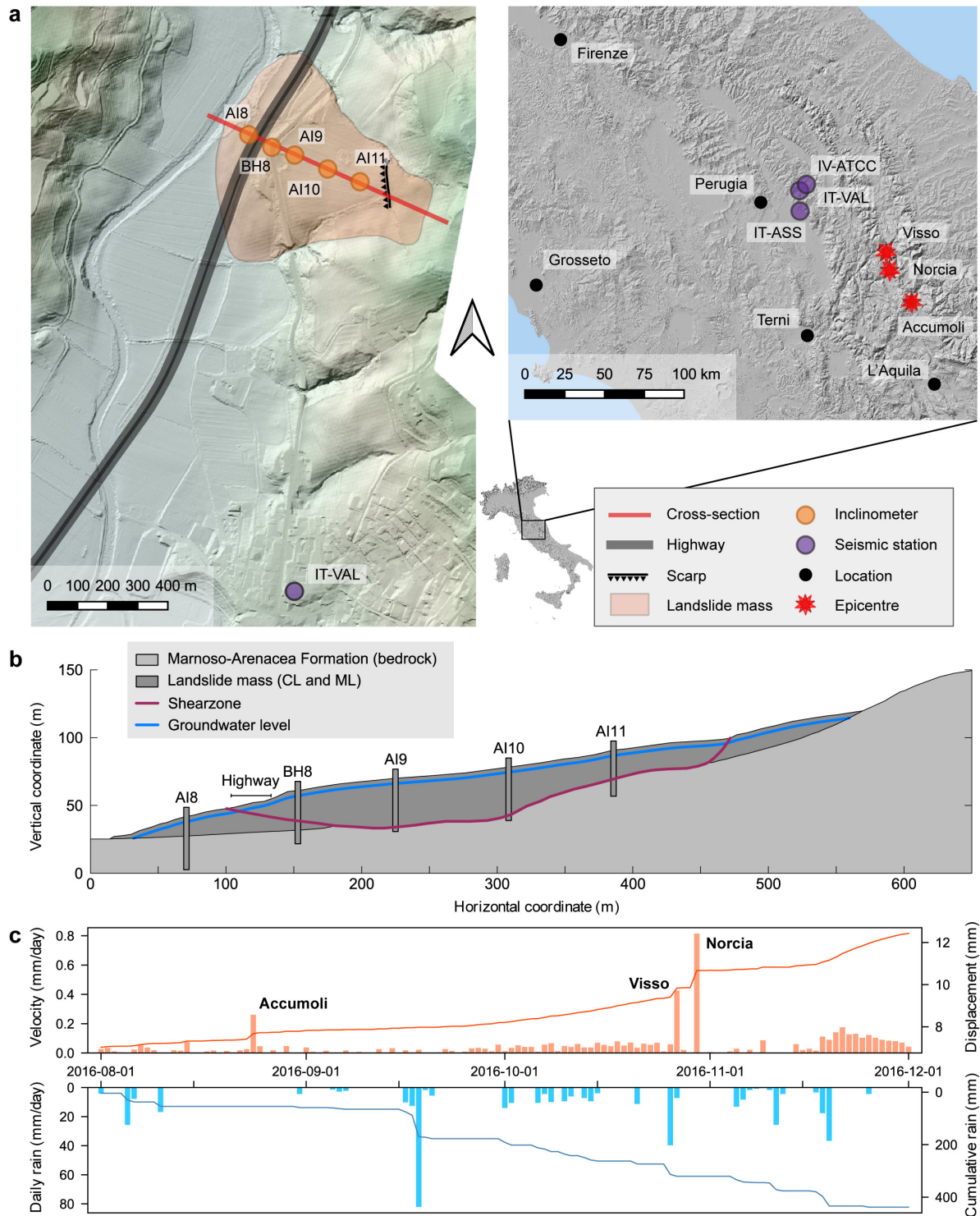
Figure 3.1: (a) Overview of La Sorbella landslide in Italy and the location of seismic stations and earthquake epicentres Accumoli, Visso and Norcia (Ministero dell'Ambiente e della Tutela del Territorio e del Mare, 2013). (b) Cross section of La Sorbella landslide (after Ferretti et al., 2019). (c) Landslide displacements recorded in borehole AI11, and the precipitation data from the Casanuova dam (after Ferretti et al., 2019).

3.2.2. Seismic behaviour

In 2016, a long series of earthquakes occurred along an Apennine fault system located around 50 km southeast from La Sorbella landslide (Figure 3.1a). In this sequence, three events were characterized with a magnitude $M_w \geq 5.5$ (Table 3.2) and were recorded by the Valfabbrica seismic station IT-VAL (Russo et al., 2022) which is located less than 1 km from the landslide. Only limited information is available about the site characteristics of the station. The seismograph is installed in the basement of a building, and the site is classified based on the surface geology as ground type B (deposit of very dense soil at least several tens of metres in thickness and a gradual increase of mechanical properties with depth, $v_{s,30} = 360 - 800$ m/s) according to Eurocode 8 (Comité Européen de Normalisation, 2004). In the station report (Russo et al., 2022), the average shear wave velocity in the top 30 m is estimated as $v_{s,30} = 550$ m/s. The H/V spectral analysis shows only an indistinct peak at a frequency of 4.8 Hz for ambient vibrations according to SESAME (European Commission, 2004), and the seismic H/V analysis for 49 earthquake motions did not reveal any peak or eigenfrequency (Russo et al., 2022).

The displacements recorded by an automatic in-place inclinometer system located in borehole AI11 and the precipitation data from the Casanuova dam weather station (Servizio Idrografico Regione Umbria, 2016), located 2 km from the landslide, are presented for the days around the earthquake series in Figure 3.1c, which has been adapted from Ferretti et al. (2019). The co-seismic displacement corresponding to the recorded earthquakes can be clearly distinguished, as well as the fact that the landslide has been in an active state of slow movement during this period. Detailed analysis by Ruggeri et al. (2020) of the data from several years of measurements demonstrated that, except for these three earthquake events, a maximal displacement rate of 0.4 mm/day is reached only during periods of heavy precipitation over several days. Another interesting fact pointed out by Ruggeri et al. (2020) is that no change in sliding regime after the seismic events could be identified. In contrast, Lacroix et al. (2014) and Bontemps et al. (2020) reported that in the case of the Maca landslide in Peru, the co-seismic displacements are followed by three times greater post-seismic slip over the following five-week period. The lack of post-seismic acceleration in the La Sorbella case can be explained by the presence of a distinct and well developed shear zone, where the clayey soil reached the residual state with shearing taking place at constant volume, without changes in pore water pressure (Skempton, 1985).

Table 3.2: Recorded earthquakes and displacements from La Sorbella landslide.

Earthquake	**Accumoli**	**Visso**	**Norcia**
Earthquake characteristics (Russo et al., 2022)			
Date	24-08-2016	26-10-2016	30-10-2016
Magnitude M_w	6.0	5.9	6.5
Depth (km)	8.1	7.5	9.2
Signal at Valfabbrica station IT-VAL (Russo et al., 2022)			
Epicentral distance R_{epi} (km)	71.5	50.7	54.6
Arias intensity (m/s)	0.02	0.02	0.06
Peak ground acceleration (in slide direction) PGA_h (m/s^2)	0.55	0.44	0.66
Peak ground acceleration (vertical) PGA_v (m/s^2)	0.14	0.26	0.31
Records from La Sorbella landslide (Ruggeri et al., 2020)			
Recorded co-seismic displacement (mm)	0.3	0.4	0.8

3.3. Modelling the seismic response of landslides using MPM

3.3.1. MPM framework

The basis for modelling the seismic response of landslides is the MPM framework proposed by Kohler et al. (2021), where the implementation of appropriate boundary conditions for the seismic model is presented. The MPM code closely follows the concepts proposed in Jiang (2015) and Stomakhin et al. (2013) and can be described in a four-step algorithm, shown in Figure 3.2.

The seismic response of slopes is modelled in two main steps (Kohler et al., 2021). First, the static stress field within the slope is computed using kinematic boundary conditions. In a second step, the actual seismic simulation is performed by applying the concept of a compliant base (Lysmer & Kuhlemeyer, 1969) and free-field columns (Wolf, 1989; Zienkiewicz et al., 1989). In order to model the existing landslide, the shear zone is pre-defined by assigning the corresponding material points to a different constitutive model (see Figure 3.2b). The thickness of the shear zone δ_s has to be chosen based on the span of the interpolation functions to allow the material points to move accordingly. For cubic B-splines, a thickness of at least double the grid size is recommended. Except for very small landslides, it is not reasonable to match the numerical shear band thickness to the in-situ zone of intensive shearing, as a very small grid size would be needed. The computational cost would be rather high, owing to the small stable time increment and the large number of material points in the case of a regular grid. However, the numerical thickness has to be taken into account for the constitutive model, and an appropriate scaling approach has to be applied. Therefore, the smeared crack approach introduced by Rots et al. (1985) is often applied in MPM (Kohler et al., 2021; Soga et al., 2016; Yerro, 2015).
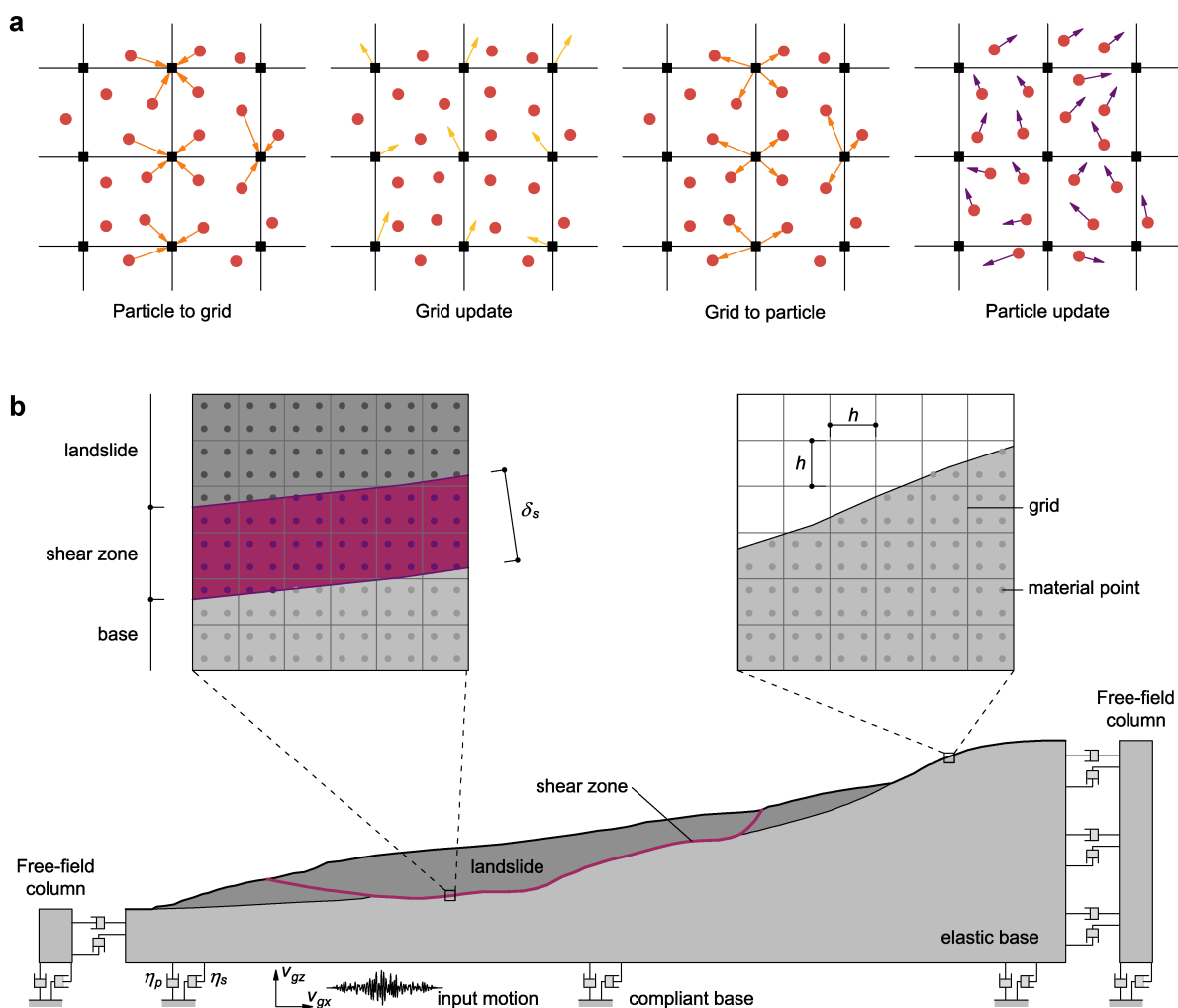
Figure 3.2: (a) General four-step algorithm of the MPM: transfer of mass, linear momentum and forces from the material points to the grid; solving the equation of motion on the grid; transfer of the updated grid velocities back to the material points; evolving the material points and update of the deformation and stress state (after Soga et al., 2016). (b) Illustration of the presented MPM model for the co-seismic simulation of active landslides based on the geometry of La Sorbella landslide (Ferretti et al., 2019).

3.3.2. Constitutive model for the shear zone

For modelling a creeping landslide, an appropriate constitutive model for the shear zone needs to be implemented. Considering that MPM is a large-strain solution method, the choice of stress- and strain measures should be carefully assessed in terms of objectivity. The seismic behaviour of active landslides must be simulated regardless of the magnitude of displacements since they might vary significantly depending on the initial conditions, material parameters and input motion. It has been shown that the straightforward extension of small-strain models to finite strains based on rate form equations leads to various inconsistencies, such as spurious stress oscillations or improper energy dissipation (Bažant et al., 2012; Perić et al., 1992; Simo & Pister, 1984).

Therefore, it is advantageous to use the multiplicative decomposition of the deformation gradient $\boldsymbol{F}$ into an elastic and plastic contribution, as introduced by Lee (1969)

$$\boldsymbol{F} = \boldsymbol{F}^e\,\boldsymbol{F}^p \tag{3.1}$$

where $\boldsymbol{F}^e$ and $\boldsymbol{F}^p$ are the elastic and plastic deformation gradients. A convenient expression for describing the elastic deformation is provided by the Eulerian logarithmic strain or Hencky strain (Hencky, 1928)

$$\boldsymbol{\varepsilon} = \frac{1}{2}\ln\boldsymbol{B}^e = \frac{1}{2}\ln\left(\boldsymbol{F}^e(\boldsymbol{F}^e)^T\right) \tag{3.2}$$

where $\boldsymbol{B}^e$ denotes the elastic left Cauchy–Green strain tensor. The elastic constitutive relation is given by the energy density as

$$\Psi(\boldsymbol{\varepsilon}) = \mu\mathrm{tr}\left(\boldsymbol{\varepsilon}^2\right) + \frac{\lambda}{2}\mathrm{tr}(\boldsymbol{\varepsilon})^2 \tag{3.3}$$

with the Lamé constants μ and λ. The Kirchhoff stress can be defined analogously to the small-strain approach as

$$\boldsymbol{\tau} = \frac{\partial\Psi(\boldsymbol{\varepsilon})}{\partial\boldsymbol{\varepsilon}} = 2\mu\boldsymbol{\varepsilon} + \lambda\mathrm{tr}(\boldsymbol{\varepsilon})\boldsymbol{I} \tag{3.4}$$

where $\boldsymbol{I}$ represents the identity tensor. For the framework presented here, a viscoplastic material based on the consistency model (W. M. Wang et al., 1997) is applied, where, in contrast to over-stress models, a rate-dependent yield surface is introduced. Based on the constitutive model proposed by Wedage et al. (1998), a Drucker–Prager yield surface matched to a Mohr–Coulomb surface in plane strain for flow at constant volume is assumed

$$f(\boldsymbol{\tau}, \alpha, \dot{\alpha}) = \sqrt{J_2(\boldsymbol{s})} + \frac{J_1(\boldsymbol{\tau})}{3}\sin(\varphi(\alpha, \dot{\alpha})) \tag{3.5}$$

where $J_2(\boldsymbol{s})$ denotes the second invariant of the deviatoric stress tensor $\boldsymbol{s} = \boldsymbol{\tau} - 1\!/3\,\mathrm{tr}(\boldsymbol{\tau})\boldsymbol{I}$ and $J_1(\boldsymbol{\tau}) = \mathrm{tr}(\boldsymbol{\tau})$ the first invariant of the stress tensor. The friction angle φ is introduced as a function of the equivalent plastic strain α and its rate $\dot{\alpha}$, which will be derived below. This function can be chosen to model the frictional behaviour of the shear zone (e.g. based on ring shear test results) and is normally defined through some function $h(\alpha, \dot{\alpha})$ as

$$\tan\varphi = h(\alpha, \dot{\alpha}) \tag{3.6}$$

In order to define the rate of the equivalent plastic strain, the so called spatially rotated rate of plastic deformation is introduced (De Souza Neto et al., 2008)

$$\overline{\boldsymbol{D}^p} = \boldsymbol{R}^e\,\boldsymbol{D}^p(\boldsymbol{R}^e)^T = \boldsymbol{R}^e\mathrm{sym}[\boldsymbol{L}^p](\boldsymbol{R}^e)^T \tag{3.7}$$

where $\boldsymbol{D}^p$ is the rate of plastic deformation, $\boldsymbol{L}^p = \dot{\boldsymbol{F}}^p(\boldsymbol{F}^p)^{-1}$ the plastic velocity gradient and $\boldsymbol{R}^e$ the elastic rotation tensor given by the polar decomposition of the elastic deformation gradient. For the proposed model, the rate of the equivalent plastic strain is defined as

$$\dot{\alpha} = \sqrt{\frac{2}{3}\overline{\boldsymbol{D}^p}:\overline{\boldsymbol{D}^p}} \tag{3.8}$$

A non-associated flow rule is introduced by the Lie derivative of the elastic left Cauchy–Green strain tensor (Simo & Miehe, 1992)

$$\frac{1}{2}\mathcal{L}_v\boldsymbol{B}^e = -\dot{\gamma}\frac{\partial g(\boldsymbol{\tau})}{\partial\boldsymbol{\tau}}\boldsymbol{B}^e \tag{3.9}$$

with $\dot{\gamma}$ denoting the plastic multiplier. Assuming flow at constant volume, the plastic potential is introduced

$$g(\boldsymbol{\tau}) = \sqrt{J_2(\boldsymbol{s})} \tag{3.10}$$

By assuming plastic isotropy, it can be shown that the spatially rotated rate of plastic deformation can be written as (De Souza Neto et al., 2008)

$$\overline{\boldsymbol{D}^p} = \dot{\gamma}\frac{\partial g(\boldsymbol{\tau})}{\partial\boldsymbol{\tau}} = \dot{\gamma}\frac{1}{2\sqrt{J_2(\boldsymbol{s})}}\boldsymbol{s} \tag{3.11}$$

This type of evolution law emphasizes the analogous extension of the small-strain constitutive law. Inserting equation (3.11) into the definition of the rate of equivalent plastic strain (equation 3.8), the following evolution law follows:

$$\dot{\alpha} = \frac{\dot{\gamma}}{\sqrt{3}} \tag{3.12}$$

In contrast to the over-stress viscoplastic models, the Kuhn–Trucker conditions remain valid and hence the consistency condition completes the definition of the model (W. M. Wang et al., 1997)

$$\dot{f}(\boldsymbol{\tau},\alpha,\dot{\alpha}) = \frac{\partial f}{\partial\boldsymbol{\tau}}:\dot{\boldsymbol{\tau}} + \frac{\partial f}{\partial\alpha}\dot{\alpha} + \frac{\partial f}{\partial\dot{\alpha}}\ddot{\alpha} = 0 \tag{3.13}$$

The model presented here is implemented as a fully implicit exponential return mapping algorithm (Simo & Meschke, 1993). Implementation details can be found in Appendix 3.1.

3.3.3. Benchmark analysis

In a first step, the presented procedure for evaluating co-seismic landslide displacements is applied to the infinite slope conditions shown in Figure 3.3a for a rate-independent material behaviour. The same problem is solved using FEM within the ABAQUS computing environment (Dassault Système Simulia, 2019), providing a benchmark for the MPM simulation. Furthermore, both methods are compared to the Newmark's sliding rigid block analysis to show the influence of compliance within the sliding mass. Infinite slope conditions are incorporated by using periodic boundary conditions. Wave-absorbing infinite elements (Lysmer & Kuhlemeyer, 1969) are added to the bottom of the MPM and FEM model. The only difference between the two procedures lies in the modelling technique of the shear zone. Whereas MPM can deal with the large deformations encountered in the shear zone, special techniques (e.g. remeshing or Eulerian-FEM) would be required for FEM. Therefore, the shear zone is modelled using a contact interface in FEM with the corresponding friction coefficient $\mu = \tan\varphi$. The applied parameters for the benchmark analysis are listed in Table 3.3. The benchmark slope was subjected to the input motion recorded from the Irpinia event in 1980 (RSN 292, H2 direction). The time history was retrieved from the PEER strong motion database (Ancheta et al., 2014).

The evolution of displacements shows that the presented approach of continuous modelling of the shear zone leads to nearly the same results as the corresponding simulation using an interface in FEM (Figure 3.3b). The slight difference in the displacements is mainly attributed to differences in the numerical scheme (e.g. different shape functions and additional transfer in MPM). Therefore, the FEM and MPM approaches can be seen as identical for this special case of infinite slope conditions, as both account for compliance of the landslide. In contrast, the Newmark's sliding block analysis neglects any wave propagation, but nevertheless it results in rather similar displacements for the selected parameters. To highlight the influence of compliance, results for MPM are also presented for a softer and stiffer landslide which is reflected in different shear wave velocities v_s (Figure 3.3b). It can be seen that for a lower shear wave velocity the displacements get slightly larger but still remain similar to the other cases. A more detailed discussion on the influence of compliance can be found elsewhere (Kramer & Smith, 1997; Rathje & Bray, 1999). However, the coupled approach proposed by Rathje & Bray (2000) should only be applied with reservation as, owing to the use of a rigid base, seismic waves are trapped in the model, which for most cases results in excessively strong amplifications and an overprediction of displacements.
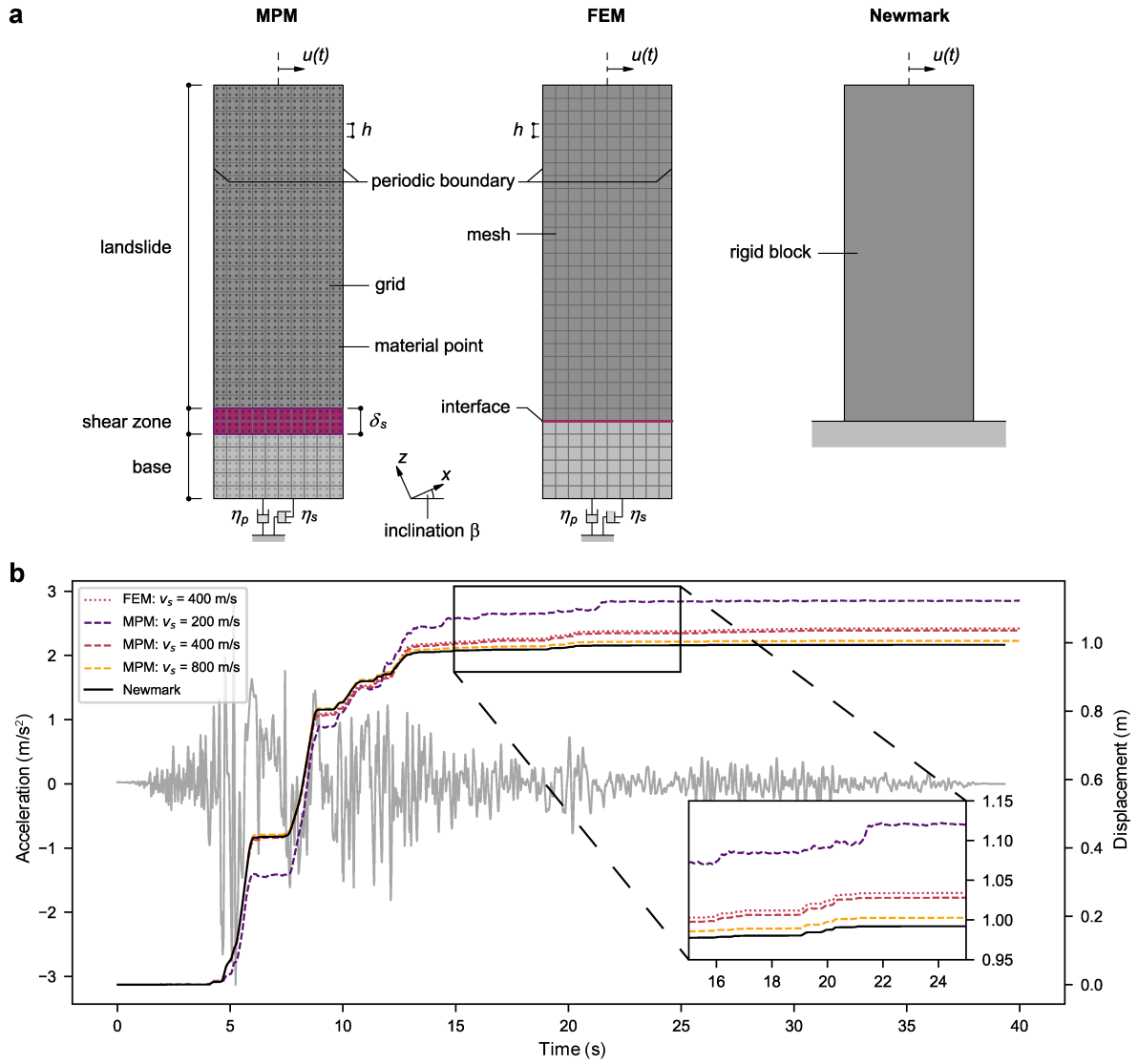
Figure 3.3: (a) Illustration of the numerical models for the benchmark analysis: material point method (MPM), finite element method (FEM), Newmark's sliding block analysis (Newmark). (b) Input motion and resulting evolution of displacements for the benchmark analysis.

Table 3.3: Parameters for benchmark analysis.

Type	Parameter	Symbol	Value
Geometry	Element and grid size	h_{el} and h	0.5 m
	Number of MP's per grid cell	n_{MP}	2x2
	Inclination	β	8°
	Landslide height	h_{slide}	25 m
	Shear zone thickness	δ_s	1.0 m
Elastic base	Pressure wave velocity	$v_{p,base}$	2000 m/s
	Shear wave velocity	$v_{s,base}$	1000 m/s
	Density	ρ_{base}	2500 kg/m³
Landslide and shear zone	Pressure wave velocity	$v_{p,slide}$	400-1600 m/s
	Shear wave velocity	$v_{s,slide}$	200–800 m/s
	Density	ρ_{slide}	2000 kg/m³
	Friction angle in the shear zone	φ	9.6°

3.4. Co-seismic behaviour of La Sorbella landslide

3.4.1. Model description

The geometry of the MPM model is based on the cross section presented in Figure 3.1b, where the shear zone is pre-defined according to the inclinometer measurements with a numerical thickness of $\delta_s =$ 1.0 m. The groundwater table is introduced at various depths parallel to the surface, and the corresponding water pressure distribution is pre-calculated by solving numerically the problem of saturated flow through porous media. The bedrock is modelled as a linear-elastic base, where the parameters are chosen at the lower end of the range presented in Section 3.2 as this range covers the bedrock properties up to several hundreds of metres in depth. For the landslide mass, an elasto-plastic model with a Mohr–Coulomb failure criterion is applied using the values for the friction and wave velocities as an average of the presented ranges (Table 3.4). As shown in the benchmark analysis (Section 3.3.3), the resulting displacements do not significantly depend on the wave velocities for this range. The use of an average value for the friction angle inside the landslide mass is justified because the range is rather narrow and most of the shearing is concentrated in the shear zone anyway. For the shear zone, the constitutive model from Section 3.3.2 is applied using different sets of parameters described in the following sections. Owing to the assumed residual state of shearing at constant volume in the shear zone, the effective pressure of the corresponding material points is kept constant during the seismic analysis and is given by the pre-seismic state.

In the following analyses, the landslide displacements are calculated as the relative movement between a material point from the sliding layer and the base close to the shear zone. The ground motion is applied as both the vertical and horizontal components, where the latter is calculated by rotating the horizontal signals in the direction of sliding.

Table 3.4: Parameters for La Sorbella analysis.

Type	Parameter	Symbol	Value
Geometry	Element and grid size	h_{el} and h	0.5 m
	Number of MP's per grid cell	n_{MP}	2x2
Elastic base	Pressure wave velocity	$v_{p,base}$	2000 m/s
	Shear wave velocity	$v_{s,base}$	1'000 m/s
	Density	ρ_{base}	2500 kg/m³
Landslide and shear zone	Pressure wave velocity	$v_{p,slide}$	800 m/s
	Shear wave velocity	$v_{s,slide}$	400 m/s
	Density	ρ_{slide}	2000 kg/m³
	Friction angle of slide	φ_{slide}	30.0°
	Cohesion of slide	c_{slide}	0.0 kPa
	Residual friction angle of slide (Section 3.5.3)	$\varphi_{r,slide}$	16.0°
	Shear zone thickness	δ_s	1.0 m
	Depth of groundwater level (if not specified)	d_w	4 m
	Critical friction angle ($d_w = 4$ m)	φ_{crit}	10.8°
Viscosity of shear zone (Sections 3.4.3 and 3.5.1)	Reference friction angle	φ_0	9.5°
	Reference velocity	v_0	0.001 mm/day
	Viscosity parameter	A	0.04

3.4.2. Effects of geometry

In the first step, the landslide is investigated without considering any rate-dependent behaviour of the shear zone, in order to show the importance of geometrical effects. A strength reduction analysis was performed for an assumed depth of the groundwater of $d_w = 4$ m to determine the critical friction angle φ_{crit} of the shear zone such that equilibrium could just be met. The following seismic analysis is done for different friction angles described by the static safety factor $SF = \tan \varphi / \tan \varphi_{crit}$ using the recorded Norcia input motion.

For an active landslide, the most interesting case is represented for a static safety factor $SF \cong 1.0$ where a Newmark's sliding block analysis would suggest that the final co-seismic displacements would tend to infinity. However, the MPM analysis shows, for the Norcia event, a maximal displacement of only 58 mm at the landslide's toe and around 36 mm in the main part (Figure 3.4a). This illustrates the effect of geometry, where the slide does not move as a single block but is characterized by three zones with different behaviour: (*i*) an unstable upper part, where the friction angle of the shear zone is smaller than its inclination, which represents the driving force of the slide; (*ii*) a stable middle part, which prevents the upper part from a catastrophic failure and decelerates it back to full rest; (*iii*) the toe of the slide, which is not restrained by any soil mass in front of it and therefore is displaced more than the upper part. The latter is particularly amplified by the release of elastic strain energy stored in this compression zone. Considering the modelled displacements as small to medium, the term geometrical hardening is deliberately avoided.

The comparison to the measurements in borehole A11 shows that the numerical simulation significantly overestimates the landslide displacements. To gain a better understanding of the influence of the strength of the shear zone, the same analysis is performed for different static safety factors (Figure 3.4b and c). This clearly shows that a higher static safety factor leads to smaller landslide displacements, with the corresponding Newmark's sliding block analyses (for an average inclination of 8° degrees) showing the fastest decrease. However, even for Newmark's analysis, in order to reproduce the measured displacements a safety factor larger than 1.2 would be necessary. Noting that the landslide was slowly moving in the days before the event, such a high safety factor seems unreasonable.
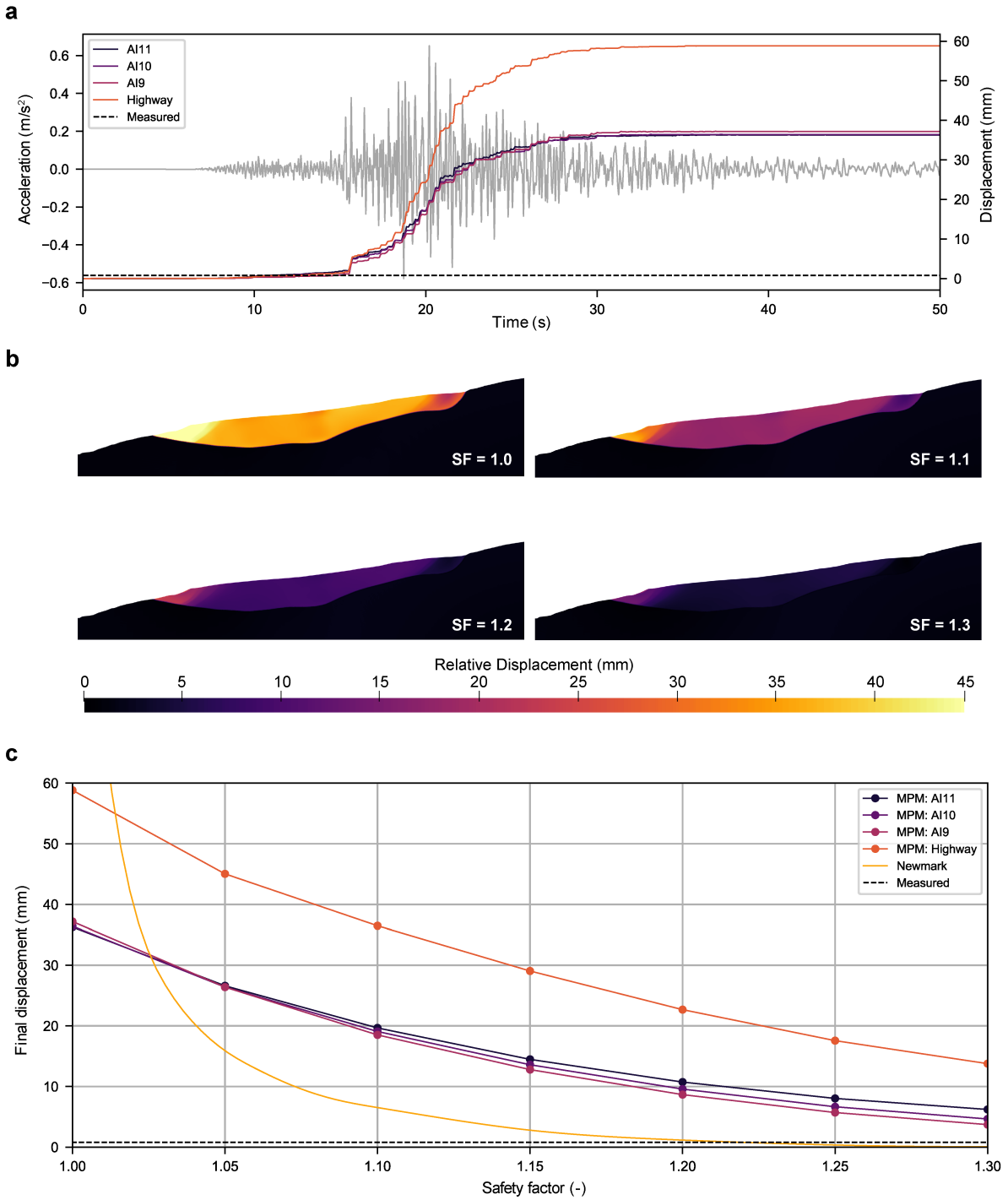
Figure 3.4: Results for the rate-independent analysis. (a) Ground motion and evolution of landslide displacement for the Norcia event. (b) Illustration of the co-seismic displacements from the MPM analysis for different safety factors. (c) Comparison of the co-seismic displacements at different locations, for various safety factors, to the measured displacement in borehole AI11 and a corresponding Newmark's sliding block analysis.

3.4.3. Effects of rate dependency

The overestimation of landslide displacement for rate-independent shear zone behaviour indicates that it is unreasonable to neglect viscous effects. Moreover, the reported large fluctuation of the groundwater level (Ruggeri et al., 2020) and the creeping velocities emphasize that viscosity should be taken into account. Therefore the critical friction angle φ_{crit} of the shear zone was also determined for the minimal (2 m) and maximal (6 m) groundwater level. Based on the continuous monitoring and the direct connection between the landslide movements and the hydrological conditions, a corresponding measured value of velocity was defined for each depth of the groundwater level (Figure 3.5). In dry periods, almost no movements were observed, and hence it was assumed that the landslide is exactly in static equilibrium (zero velocity) for a groundwater depth of 6 m with a reference friction angle φ_0. To ensure a quasi-static steady state (safety factor $SF = 1$) for the different water levels, a logarithmic law describing the rate-dependent shear behaviour (equation 3.6) is introduced as

$$\tan \varphi = \tan \varphi_0 \left(1 + A \bullet \ln \left(\frac{\dot{\alpha} + \dot{\alpha}_0}{\dot{\alpha}_0} \right) \right) \tag{3.14}$$

where φ_0, A and $\dot{\alpha}_0$ are material parameters. This kind of relation is often chosen for clayey shear zones in active landslides (Alonso et al., 2016; Puzrin & Schmid, 2011; Wedage et al., 1998), but the reference rate $\dot{\alpha}_0$ is also added in the numerator to avoid the singularity in the logarithm. The application of a logarithmic law ensures that the resistance is not overestimated for higher velocities during a seismic event. The landslide velocity v can be linked to the rate of the equivalent plastic strain $\dot{\alpha}$ for a given shear zone thickness δ_s, assuming simple shear conditions, as

$$\dot{\alpha} = \frac{v}{\sqrt{3}\delta_s} \tag{3.15}$$

The same relation can also be applied to link the reference landslide velocity v_0 to the reference strain rate $\dot{\alpha}_0$. This link between velocity and strain rate (and the same holds for displacement and strain) is critical for defining the thickness of the numerical shear zone, which does not match the real conditions. This procedure is based on the smeared crack approach proposed by Rots et al. (1985) and ensures that the results do not depend on the shear zone thickness. The influence of the viscosity parameter A on the friction angle is illustrated in Figure 3.5 for a wide range of velocities, from the annual creeping rate to the behaviour during strong motions. The value of $A = 0.04$ leads to a good fit and will be applied for the following simulations. As has been shown using ring shear testing, a relatively large increase of 4% in resistance per log cycle indicates the presence of a sizeable content of clay minerals in the shear zone material (Duong et al., 2018; Scaringi et al., 2018; Tika et al., 1996). For accurate calibration, experimental testing of material from the shear zone for the full range of velocities is necessary. Nonetheless, this serves as a reasonable first assumption for the following calculations and will be investigated in a subsequent sensitivity analysis.
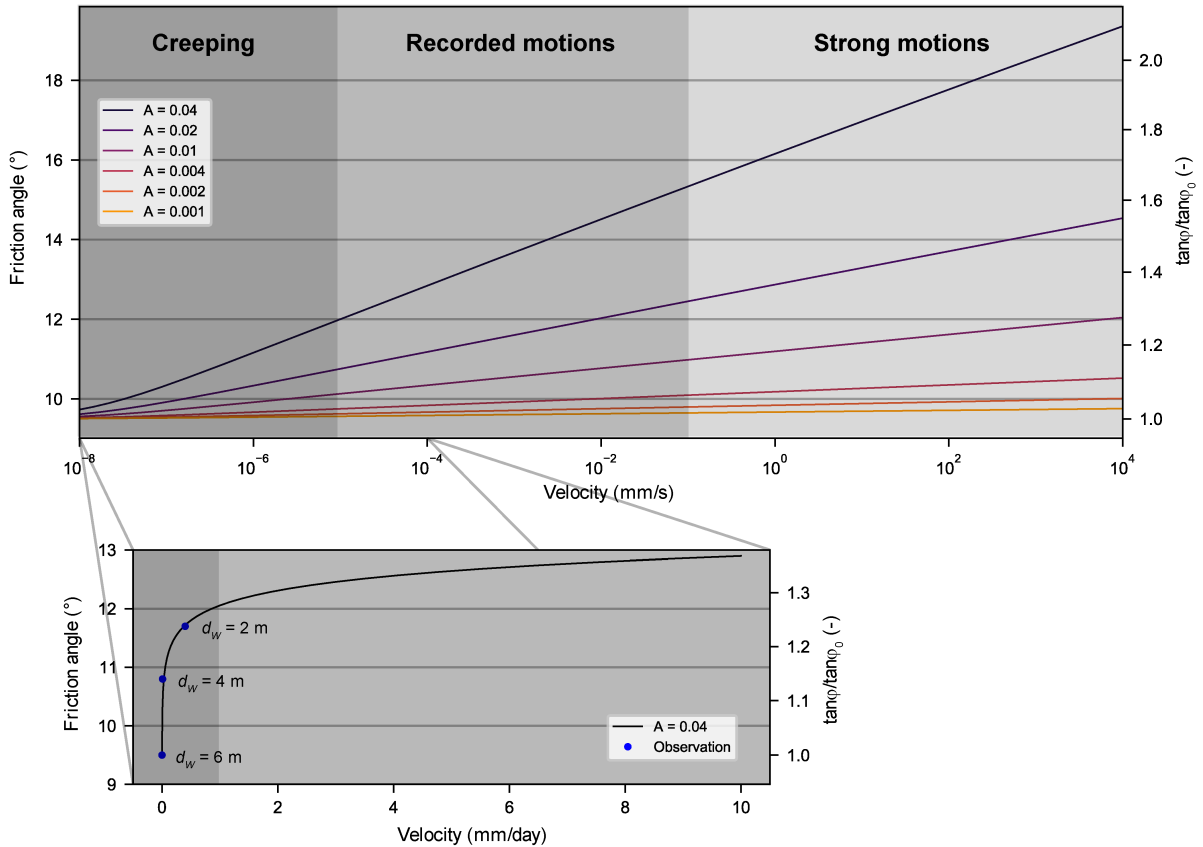
Figure 3.5: Illustration of the logarithmic rate-dependent friction law for different parameters A (top) and for the calibrated model including the observed data. For groundwater levels d_w of 2 m, 4 m and 6 m, corresponding critical friction angles, ensuring a quasi-static equilibrium, of 9.5°, 10.8° and 11.8° were calculated by using a strength reduction analysis.

The seismic analysis is carried out for different groundwater levels because the exact depth at the time of seismic events is unknown. This also allows the influence of the pre-seismic conditions on the co-seismic behaviour to be investigated. The results illustrated in Figure 3.6 clearly show that displacements can be modelled more accurately by taking into account rate effects in the shear zone. While for the Norcia event the prediction based on the medium groundwater depth of 4 m provided an excellent fit to the observed permanent deformations, for the Accumoli event the best fit is obtained by assuming $d_w = 6$ m, and for Visso by assuming $d_w = 3$ m. This is consistent with the pre-seismic landslide conditions given by the creeping velocity and the precipitation (Figure 3.1c). The Visso earthquake took place after a rather wet period characterized by increased creeping velocities of around 0.5 mm/day, indicating a higher groundwater level. On the other hand, prior to the Accumoli event, the landslide was moving at a very slower rate, suggesting a lower level of the groundwater.

Another important insight can be obtained by looking at the displacements (1.3 mm) for a groundwater depth of 2 m during the Norcia event. The seasonal fluctuation in the creeping velocity and the measurements of the groundwater level (Ruggeri et al., 2020) suggest that this is what can be expected when a similar earthquake takes place during a period of increased landslide movements.
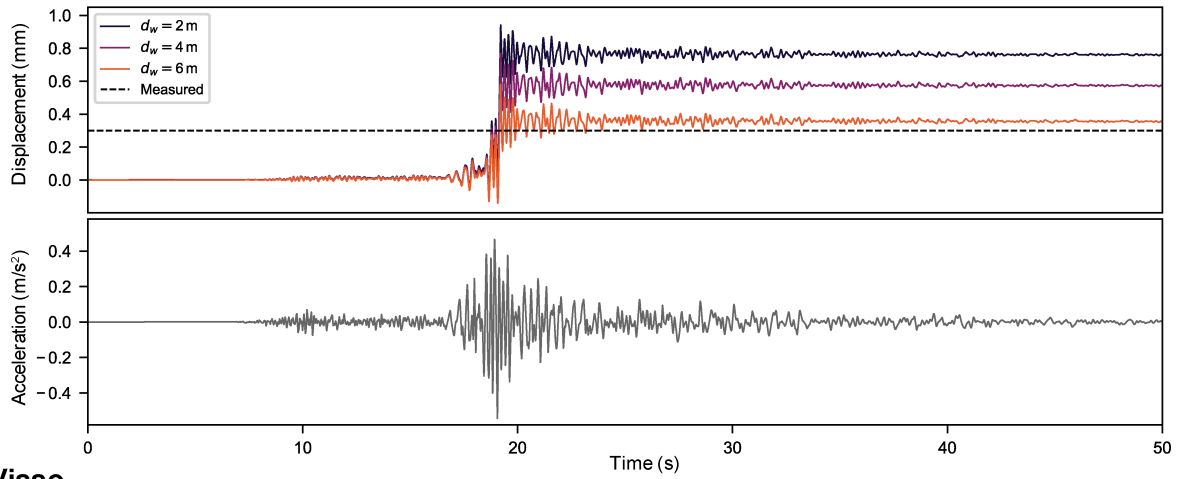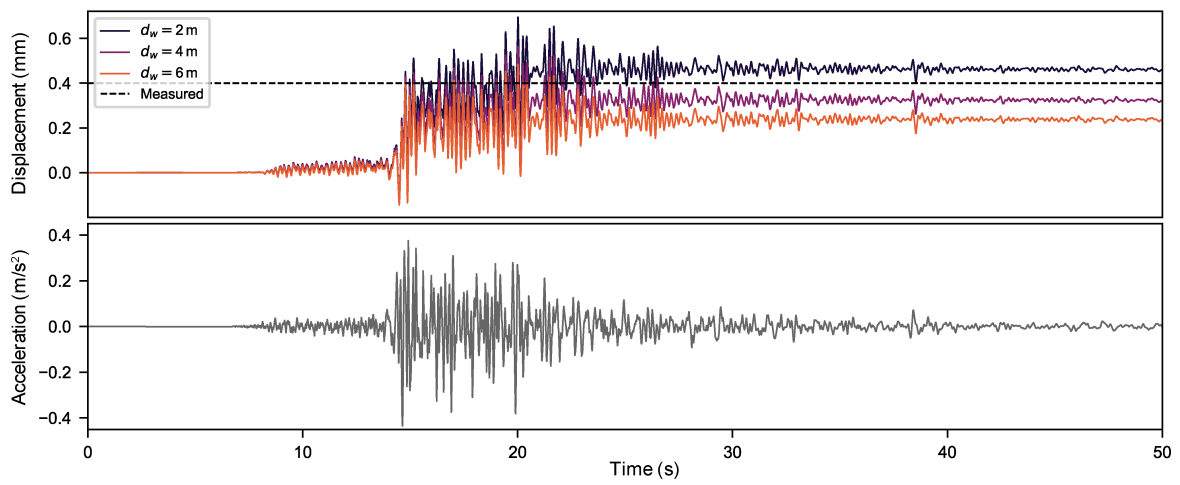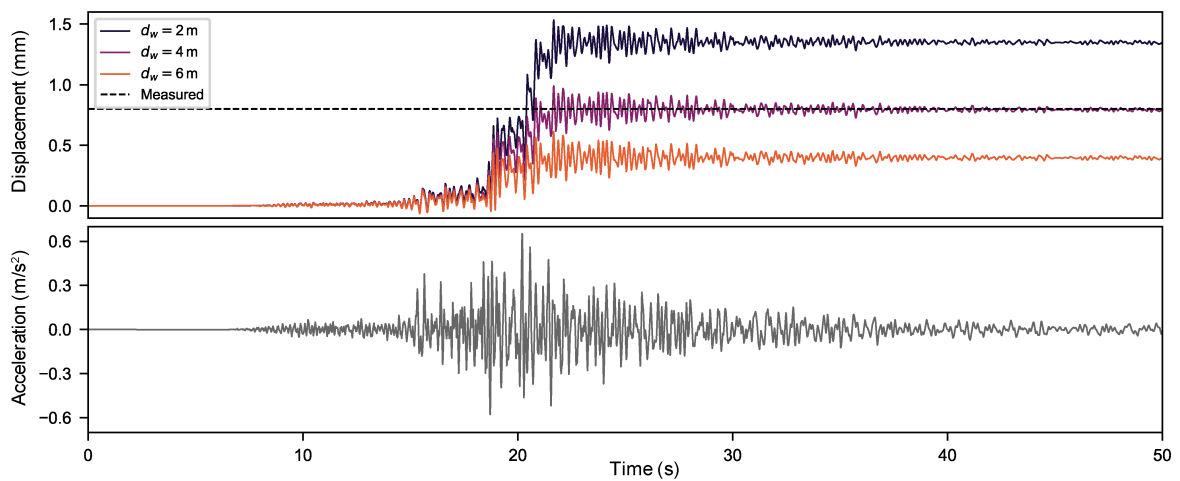
Figure 3.6: Ground motion and evolution of the landslide displacements at AI11 from the MPM analysis for the recorded earthquakes. The displacements are calculated by the difference of the position from a material point above and below the shear zone. The oscillations arise from the elastic waves, which can only be seen because of the small displacements.

3.4.4. Assessment of possible site effects

In the previous analyses, the ground motions recorded at the IT-VAL station have been directly applied to the landslide model, as the station is nearby and has similar site characteristics. Ideally, the input motion at the bedrock should be back-calculated using deconvolution from the recorded surface motion for the geophysical profile (defined by e.g. cross- or downhole tests) at the seismic station (Mejia & Dawson, 2006). Such data are not available for the IT-VAL station. However, the Accumoli earthquake was also recorded by two additional seismic stations in the vicinity of the landslide: IT-ASS and IV-ATCC (Russo et al., 2022). The locations of the seismic stations are shown in Figure 3.1a, and the horizontal ground accelerations (in the direction of the landslide movement) as well as their Fourier spectra in Figure 3.7a. The IT-ASS station is located on ground type A (rock) according to Eurocode 8 (Comité Européen de Normalisation, 2004), and the shear wave velocity is estimated as $v_{s,30} = 1^{'}070$ m/s (Russo et al., 2022). This makes the IT-ASS record suitable as the input at the bedrock of the La Sorbella model. However, it can be observed that both the horizontal ground accelerations and the Fourier spectra are remarkably similar for the IT-VAL and IT-ASS stations, indicating a lack of significant amplification in the vicinity of La Sorbella landslide. Slightly higher accelerations at the IT-VAL station do not necessarily indicate an amplification: they could also be attributed to the different epicentral distance and topography. In contrast, the IV-ATCC is located on a 10 m soft layer on top of a stiffer material and is, therefore, classified as ground type E (soft soil) according to Eurocode 8 (Comité Européen de Normalisation, 2004), which is clearly reflected in the signal and its Fourier spectrum (Figure 3.7a).

The comparison of landslide displacements for the MPM model subjected to the input signals from all the three stations is presented in Figure 3.7b. Although the final displacements are clearly different, the order of magnitude stays the same and confirms the previous results. One could even conclude that the application of the rock outcrop signal recorded at station IT-ASS leads to a more accurate result, when compared to the measured displacement. The uncertainty in groundwater level, however, makes this conclusion not justified.
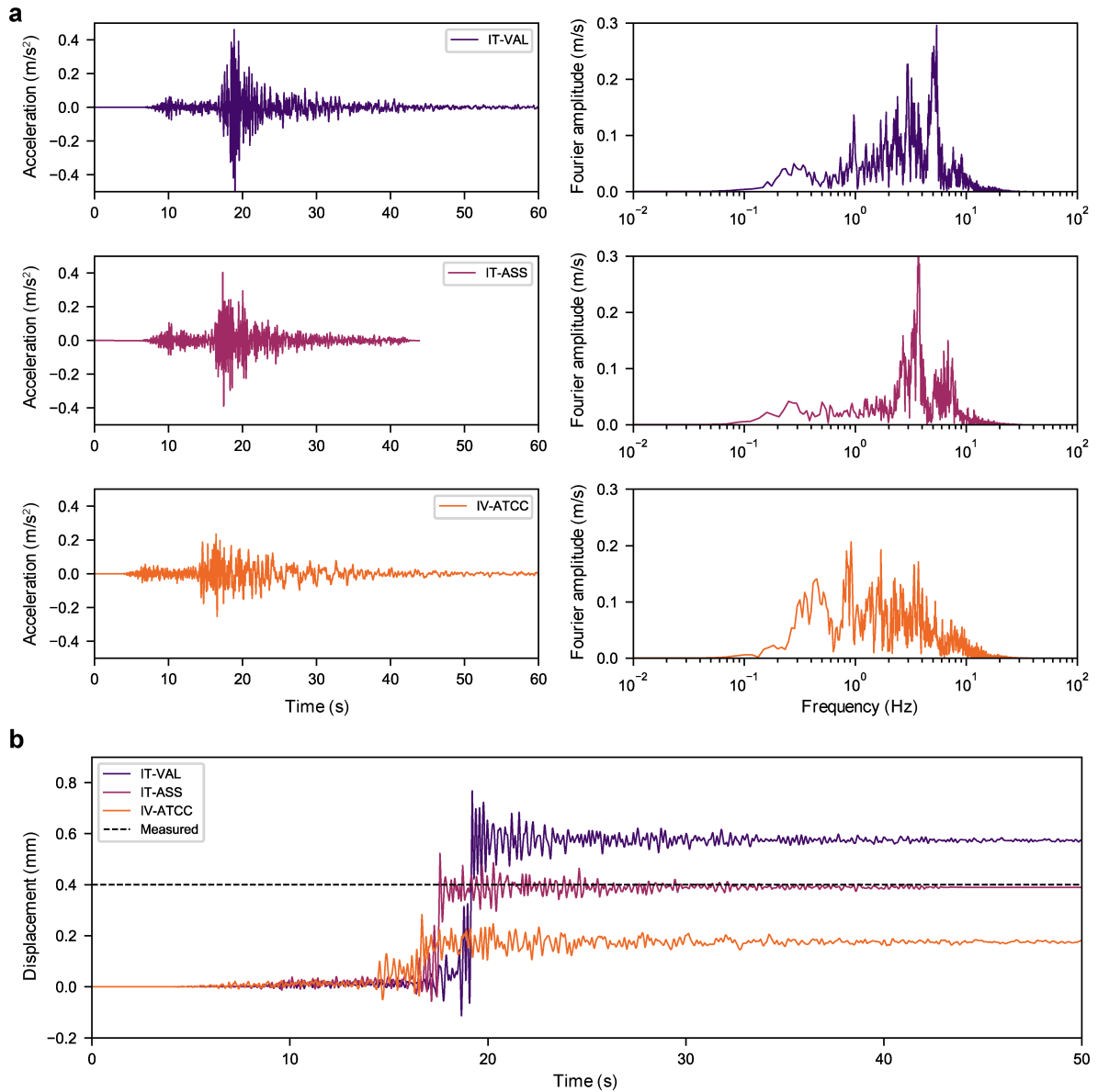
Figure 3.7: Assessment of possible site effects. (a) Horizontal ground acceleration (in landslide direction) and Fourier spectrum of the Accumoli earthquake event at different seismic stations. IT-VAL: Distance to site $d = 1.4$ km, ground type B and estimated $v_{s,30} = 550$ m/s. IT-ASS: Distance to the site $d = 12.9$ km, ground type A and estimated $v_{s,30} = 1'070$ m/s. IV-ATCC: Distance to the site $d = 5.8$ km, ground type E and measured $v_{s,30} = 650$ m/s. (b) Evolution of landslide displacements for the parameters in Table 3.4 and the measured displacement in borehole AI11.

3.5. Predicting La Sorbella landslide response to a strong motion

3.5.1. Predicted displacements

The preceding analyses using the ground motions recorded in 2016 allow quantification of the relative effects of geometry and rate dependency on La Sorbella landslide behaviour during moderate earthquakes. They also serve as a calibration and demonstration of the presented methodology. Based on this, the behaviour for other and especially stronger earthquakes can now be investigated by subjecting the landslide model to a set of recorded ground motions presented in Table 3.5 (Ancheta et al., 2014), using the same soil parameters as in the previous section. Note that this does not represent a risk assessment for this specific landslide, which would require choosing a representative set of input motions for a defined return period. The goal of this analysis is to get an idea about the order of magnitude for the corresponding landslide displacements, as well as the main factors influencing them.

The evolution of the displacements and the final displacements are shown in Figure 3.8. As expected, stronger input motions lead to considerably larger displacements which could cause severe damage to local infrastructure, such as the highway in the case of La Sorbella landslide. However, the landslide decelerates quickly and returns to the state of slow motion, as could be expected from the geometrical effects and the rate-hardening constitutive model. Furthermore, since these displacements can be considered as medium to large, geometrical hardening can also contribute to the deceleration, because some weight is transferred from the unstable to the stable part of the slope.

The largest displacements occurred at the toe of the landslide again for all three earthquakes, which can be expected from the unrestrained front due to release of elastic strain energy in the compression zone. However, for the Kocaeli motion the displacement field looks more uniform, which could be due to the impulse-like characteristics of the input signal (Figure 3.8b).

Table 3.5: Earthquake data for strong motions.

Earthquake	**Chichi**	**Irpinia**	**Kocaeli**
Date	21-09-1999	23-11-1980	17-08-1999
Magnitude M_w	7.6	6.9	7.5
RSN	1182	292	1158
Closest distance to rupture plane R_{rup} (km)	9.8	10.8	15.4
Joyner–Boore distance R_{JB} (km)	9.8	6.8	13.6
Arias intensity (m/s)	2.0	1.4	1.3
Peak ground acceleration (East–West) PGA_h (m/s^2)	3.48	3.14	3.57
Peak ground acceleration (vertical) PGA_v (m/s^2)	2.11	2.30	2.02

a Irpinia

b Kocaeli

c Chichi
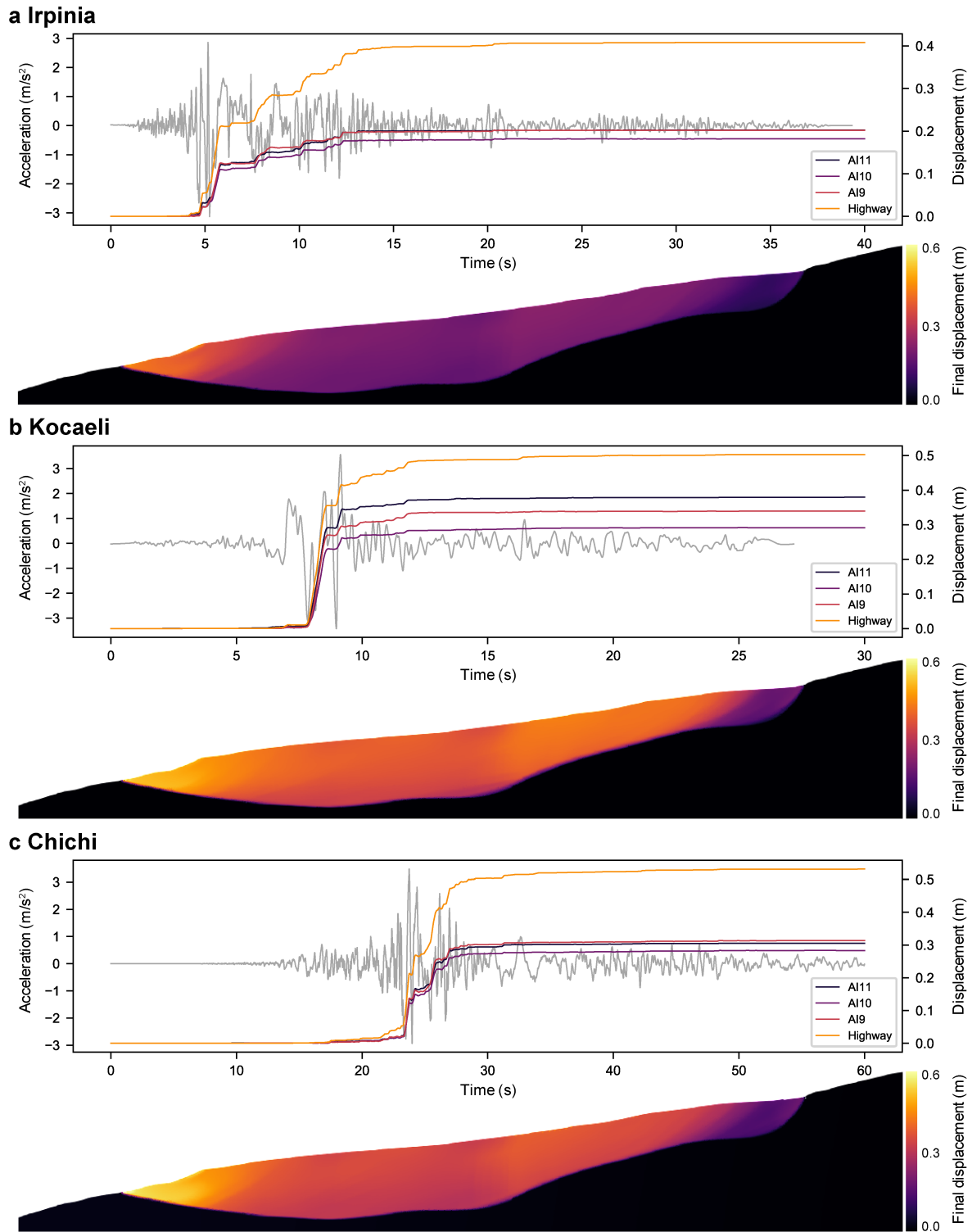
Figure 3.8: Results from the MPM simulation of La Sorbella landslide subjected to three strong input motions. The evolution of the displacements is shown for different locations alongside the ground motion. For each earthquake, the final co-seismic displacements are presented directly underneath.

3.5.2. Influence of rate dependency of shear strength

So far, the parameters of the shear zone have been calibrated based on the annual creeping behaviour of the landslide. This set of parameters also leads to reasonable co-seismic displacements for the recorded input motions. However, these parameters must be applied with caution to stronger earthquakes since the associated displacement rates might be several orders of magnitudes higher. The corresponding constitutive relationship should be calibrated for this range of velocities using appropriate experimental tests instead. The influence of this rate-dependent behaviour is investigated by performing the seismic analysis for different viscosity parameters A, using the Irpinia earthquake motion (Table 3.5). To ensure quasi-static equilibrium in the pre-seismic state for low viscosities, the reference friction angle is set slightly higher than the critical friction angle ($\varphi_0 = 11.0°$, $\varphi_{crit} = 10.8°$).

In Figure 3.9a, the evolution of the landslide displacements is presented for both rate-hardening ($A > 0$) and rate-softening ($A < 0$) behaviour (Duong et al., 2018; Lemos, 2004; Scaringi & Di Maio, 2016; Tika et al., 1996). Although a higher viscosity significantly reduces the displacements compared with the rate-independent case ($A = 0$), for the strong Irpinia motion they remain within the same order of magnitude for a reasonable choice of parameter A. In contrast, the simulations for the recorded input motions (which were significantly weaker, see Sections 3.4.3 and 3.4.4) show a reduction of two orders of magnitude when considering viscosity. This highlights the influence of geometrical effects, which reduce the role of rate effects and are more pronounced for larger displacements. In the case of rate-softening, these effects act against each other, and geometrical hardening prevents the landslide from accelerating into catastrophic failure. The limit case without any geometrical hardening is given by the Newmark's sliding block analysis for an average inclination ($\beta = 8°$) and the corresponding material model with the same factor of safety ($\varphi_0 = 8.15°$, $\varphi_{crit} = \beta = 10.8°$). The comparison of the final displacement for different viscosity parameters A clearly shows that in the absence of geometrical hardening the influence of the rate-dependent behaviour is much larger (Figure 3.9b).
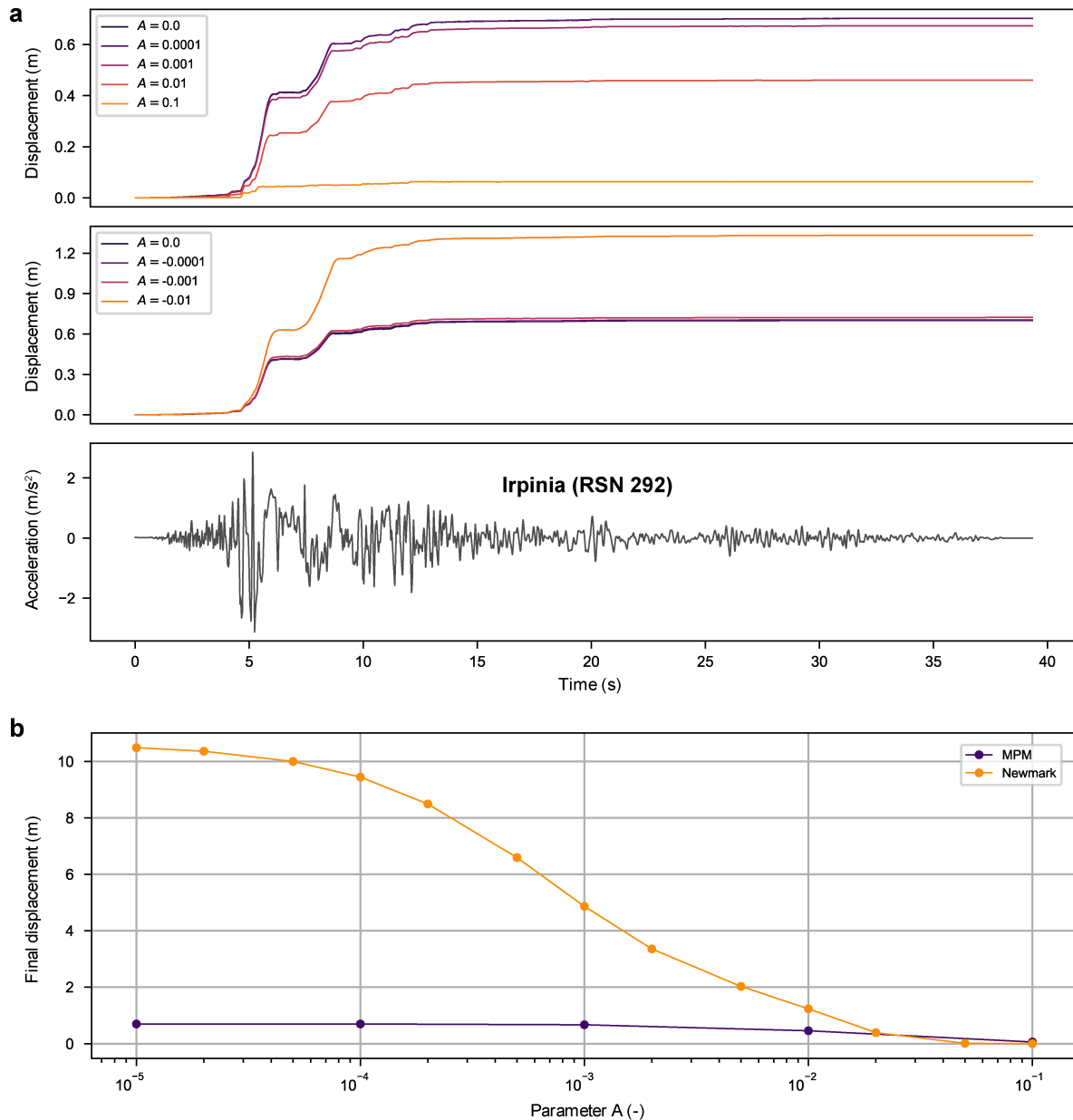
Figure 3.9: Results from the sensitivity analysis for the rate parameter *A*. (a) Evolution of the landslide displacements at location AI11 for different parameters *A*, and the applied ground motion below. (b) Comparison of the final co-seismic displacements from the MPM analysis and a corresponding Newmark's sliding block analysis for different parameters *A*.

3.5.3. Influence of potential softening in the soil mass

Little attention has been paid so far to the material of the landslide body and the surrounding soil masses at the bottom and top of the slope. For older active landslides, it is often assumed that the behaviour is mainly controlled by the sliding surface where most of the shearing is concentrated. However, a potential strength reduction in the soil mass could counteract the geometrical hardening and might lead to larger landslide deformations. This possibility and its consequences are investigated for La Sorbella landslide, assuming, for stronger motions, linear isotropic softening of the soil mass, where the initial friction angle

($\varphi = 30°$) can reduce to a residual value ($\varphi_r = 16°$) based on laboratory tests (Ruggeri et al., 2020). The seismic simulation is performed using the Irpinia input motion for two scenarios: (a) calibrated rate-hardening behaviour of the shear zone analogous to Section 3.4.3 ($A = 0.04$) and (b) rate-softening behaviour of the shear zone ($A = -0.01$). The comparison of the displacements for both scenarios and the corresponding results for a constant strength are presented in Figure 3.10. The consideration of a softening soil mass obviously leads to larger deformations and especially affects the landslide toe. Although the displacements in scenario (a) are significantly higher than for the non-softening analysis, they remain within a certain limit. However, when a rate-softening shear zone is combined with a softening in the soil mass, geometrical hardening does not counterbalance the loss of strength in the shear zone due to the co-seismic acceleration, and the landslide catastrophically fails (Figure 3.10b).
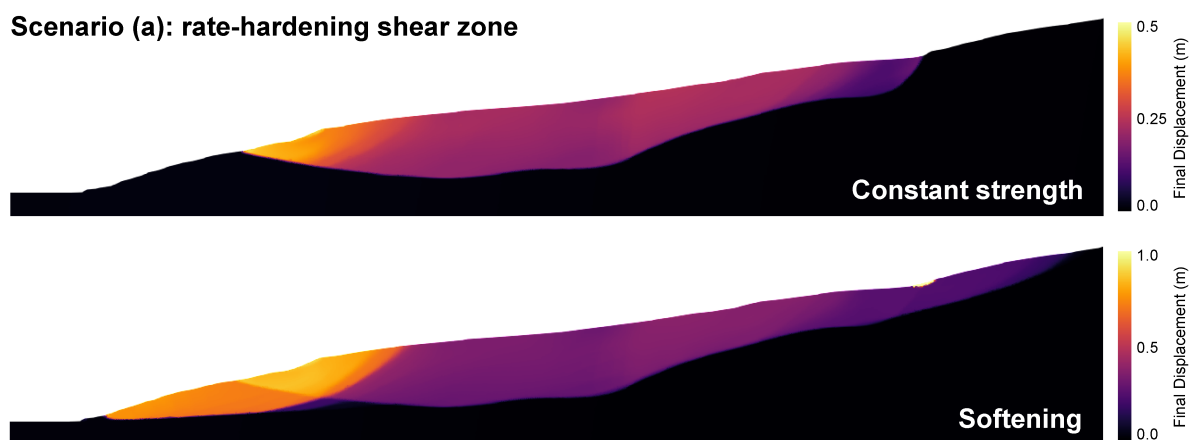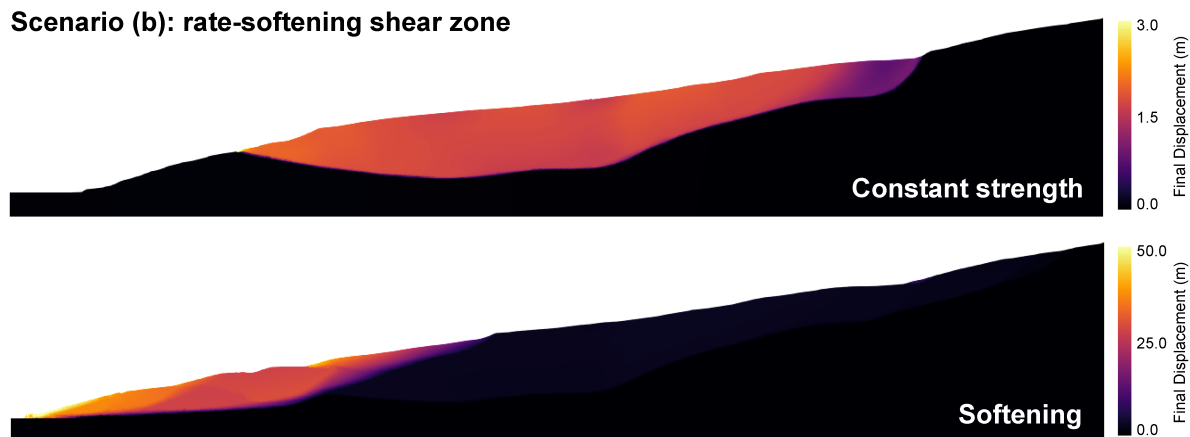
Figure 3.10: Comparison of the final co-seismic displacements for two scenarios: (a) calibrated rate-hardening behaviour of the shear zone for the annual creeping behaviour ($A = 0.04$) and (b) rate-softening behaviour of the shear zone ($A = -0.01$). For both scenarios, the results are presented for analyses where the landslide mass is modelled with a constant strength (top) and where an isotropic softening is considered (bottom).

3.6. Discussion

3.6.1. Geometry and kinematics

The case study of La Sorbella landslide suggests that the effects of geometry cannot be neglected for calculating accurate co-seismic landslide displacements. This is shown in particular by the rate-independent analysis for different pre-seismic safety factors where, in contrast to the Newmark sliding block analysis, displacements calculated using real geometry do not tend to infinity when the landslide is exactly at equilibrium. However, the extent of these effects is likely to depend strongly on the geometry. La Sorbella seems to be particularly influenced, as the steeper top part is stabilized by a more massive bottom part. This becomes even more evident during strong motions for a rate-softening material in the shear zone, where the transfer of mass from the unstable to the stable part prevents the landslide from accelerating into a catastrophic failure. This effect is likely to be less pronounced in a long landslide that has a more constant inclination of the shear zone.

Based on the monitoring results, Ruggeri et al. (2020) concluded that displacement pattern of the landslide shows only small rotation and very small internal deformations. The inclinometer measurements show a tendency for the upper part to move slightly faster than the landslide's toe. This behaviour is observed in constrained landslides to a much greater extent (Oberender & Puzrin, 2016; Puzrin & Schmid, 2012) and is most likely due to the stabilization of the unstable top portion by the stable bottom part. The associated internal deformations are distributed over the entire landslide in the form of elastic deformations leading to increased horizontal stresses in the landslide (Schwager & Puzrin, 2014). In the simulated co-seismic displacements, only small diffusive internal deformation can be observed for large portions of the landslide, even for the stronger motions (Figure 3.8), which is in agreement with the non-seismic behaviour. However, the bottom and top boundaries deform more and for some cases even show distinct internal shearing. The deformation pattern at the top indicates that the location of the shear zone in reality might be different and less localized, with a more complex scarp than the assumed one. In all simulations, the displacements were largest at the toe, which can be explained by the lack of constraint and the seismically induced release of elastic energy stored in this compression zone. Whereas simulations without considering any rate effects (Figure 3.4b) show distinct deformations at the toe, more realistic simulations including a rate-hardening shear zone result in a more diffuse pattern, similar to the non-seismic behaviour.

3.6.2. Shear zone behaviour

Based on the yearly displacements and old history of the slide, the total accumulated displacements are likely to be from tens of centimetres to metres. In combination with the sliding in a distinct shear zone, the shear zone is assumed to have not only reached critical state but also the residual shear strength typical for clayey material, undergoing large deformations (Skempton, 1985). Therefore, shearing is

expected to occur at constant volume, and the effective pressure can be kept constant during the seismic analysis. Impulsive shearing at fast rates could lead to an increase in void ratio due to a turbulent shear mode (Tika et al., 1996) and lead to a change in pore water pressure. Such behaviour would presumably change the post-seismic behaviour due to the low permeability as the shear zone contracted, and excess pore pressures would build up. This behaviour would be then associated with increased post-seismic displacement rates, which have not been observed for this landslide.

The analysis of La Sorbella landslide also shows that neglecting viscous effects leads to overestimation of co-seismic displacements by two orders of magnitude. Therefore, a logarithmic rate-dependent friction law, calibrated based on the yearly creeping behaviour, had to be introduced in the shear zone. This allows an accurate simulation of co-seismic displacements for all three earthquake events recorded in 2016. The presented model can also be used for a risk assessment by subjecting the landslide to other and especially stronger input motions. Therefore, a representative set of earthquake signals for the specific site should be chosen, and the rate-dependent behaviour of the shear zone should be calibrated using appropriate experimental testing (e.g. in a ring shear apparatus) for the expected range of velocities. Since proper experimental data are often unavailable, the risk assessment can be carried out in the form of a parameter study to get an idea of the sensitivity and the maximal expected displacement. Whether a proper consideration of rate effects is important for strong input motions depends on how much the landslide is affected by geometrical hardening.

3.6.3. Assessment of potential scenarios and catastrophic failure

The results presented here suggest that it is unlikely for the active La Sorbella landslide, which is strongly influenced by geometrical hardening, to fail catastrophically. Even a rate-weakening behaviour of the shear zone leads to relatively small displacements, and the landslide decelerates back towards a stable state. As this obviously represents a slightly more stable state due to the mass transfer, one might therefore assume that such co-seismic displacements have not happened in the history of the landslide and are less likely to happen again multiple times. However, the upper part of the slide will remain unstable even after several metres of displacement and will still be prone to earthquake-induced displacements. It should be kept in mind that even stable slopes can experience co-seismic displacements (Figure 3.4).

One of the limitations of the rate-weakening analysis presented here is that it requires the landslide to be in a stable state before the earthquake. Otherwise, the landslide would accelerate without any external influence and would especially not remain in a quasi-static state for a groundwater level varying by 4 m. Therefore, it is not possible to draw any conclusions regarding the landslide's susceptibility to rainfall-induced displacements. In order to investigate this topic, a more sophisticated type of rate-dependent behaviour needs to be used to maintain a quasi-static equilibrium and only exhibit softening for higher velocities.

Depending on the pre-seismic conditions and the landslide history, the soil mass downslope from the sliding layer can also be affected by some type of softening such as excess pore pressures and strain localization (Lacroix et al., 2020). The presented analysis based on the example of La Sorbella shows that the co-seismic behaviour might be influenced by such a loss in strength and could even fail catastrophically. Considering that La Sorbella landslide was already documented more than 30 years ago and was probably triggered prehistorically in a different topographic situation (Ruggeri et al., 2020), the landslide has most likely experienced large deformations and intensive internal shearing where a part of the potential softening has already occurred. Therefore, catastrophic failure seems rather unlikely, and even for a pessimistic assessment the expected strength loss might be less than in the simulation. The only scenario that leads to a catastrophic failure requires the combination of softening in the landslide mass and in the shear zone. To make a definitive statement on whether such a scenario is plausible, a detailed investigation of the in-situ conditions and experimental testing on undisturbed samples is required.

3.6.4. Application of the proposed methodology to other landslides

Ideally, the proposed procedure should be tested on further case studies to assess its reliability. Unfortunately, the co-seismic behaviour of creeping landslides is sparsely reported, and the required data are mostly unavailable (Bontemps et al., 2020; Lacroix et al., 2015, 2014), but we hope that more studies will focus on this important aspect in the future. Accurate simulation of co-seismic landslide displacements also requires high-quality geological and geotechnical models (e.g. geometry, lithological units, constitutive models and the necessary parameters). The proposed methodology is currently limited to plane strain problems, but can be extended to a three-dimensional framework in order to tackle problems with more complex geometry, which, however, will be computationally very expensive.

In order to apply this procedure as a risk assessment to other landslides, the geometry should be reasonably known but can be more complex and incorporate multiple layers and shear zones, since any desired constitutive model can be assigned to each material point. Additionally, an estimate of the geophysical and geotechnical properties of the lithological units is necessary. Based on that, a risk assessment can be made by looking into different scenarios such as different input motions, material models and the corresponding parameters. This will allow identification of the sensitivity to different factors, a probable range of displacements and potential scenarios of catastrophic failure. In cases where experimental data from the shear zone are available, more accurate and sophisticated material models (e.g. Handwerger et al., 2016; Marone, 1998; Ruina, 1983; Scholz, 1998) can be applied, allowing for a more reliable risk assessment. Pore pressure changes controlled by material dilatancy (Iverson, 2005; Iverson et al., 2000), excess pore pressures due to cyclic loading and effects due to frictional heating (Alonso et al., 2016; Vardoulakis, 2000) can also be incorporated. Accounting for these effects would require a hydro-thermo-mechanically coupled MPM, which has been recently applied to a non-seismic

landslide simulation by Alvarado et al. (2019), and can be extended to incorporate rigorous seismic boundary conditions. If the coupled approach appears to be computationally too expensive, these effects can be included through the use of phenomenological constitutive models, which account in a simplified manner for the complex underlying physical mechanisms.

3.7. Conclusions

An attempt has been made to understand the mechanisms behind the extremely small co-seismic displacements of La Sorbella landslide in Italy during recorded moderate earthquake events, and to investigate implications of these mechanisms for the future landslide behaviour during potential strong motions. To achieve this goal, an MPM model is proposed, which includes an accurate representation of the seismic boundaries, ensuring that outgoing waves are not reflected back into the model. Because of the importance of the shear zone and the associated large deformations, a generic large-strain frictional constitutive model for rate-dependent behaviour is introduced. The application of MPM brings the advantage that the analysis can be performed regardless of the deformation magnitude. Therefore, the same model can be applied for both moderate earthquakes and stronger motions, which could cause softening and large displacements.

Applying this model to La Sorbella landslide provides several insights:

 (i)   While effects of the rate hardening and of lower groundwater levels on reducing co-seismic displacements are well appreciated, they are not sufficient to explain how the landslide, which was moving up to 0.5 mm/day during certain periods of the year, could experience only 0.4 mm of co-seismic displacement.

 (ii) The answer lies in the geometric effects: weaker ground motions have difficulty in displacing the massive stable middle portion of the sliding body. Note that, owing to the small magnitude of displacements, these favourable geometric effects have nothing to do with the so-called geometric hardening, where soil weight is transferred from the unstable portion into the stable one, which is often the case for stronger motions.

 (iii) Interestingly, the toe of the landslide, which is supposed to be the most stable part because of the upward inclined sliding surface, experiences the largest displacements. This, we believe, is due to the unidirectional unrestraint and the release of elastic energy stored in this compression zone.

 (iv) Rate dependency of strength plays a larger role during light-to-moderate earthquakes. Calibration of the rate-dependent constitutive relationship requires lab tests. However, it has been shown that for weaker ground motions this relationship can also be successfully calibrated based on the observed velocity fluctuations for various groundwater levels during the creeping stage.

(v)   For stronger motions, co-seismic displacements become larger, causing a weight transfer between unstable and stable parts, and activating geometric hardening. As a result, even the rate-softening of strength sometimes observed in the shear zone would not bring the landslide to catastrophic failure. Such a failure would become possible only if the soil mass in the sliding body and further downhill experienced strain softening, which is unlikely in the case of La Sorbella landslide.

The study presented here demonstrates that the co-seismic behaviour of La Sorbella landslide is strongly influenced by the interplay of geometrical and viscous effects, as well as potential softening in the shear zone and the surrounding soil mass. As a next step, it would be useful to investigate effects of some typical slide geometries on the seismic behaviour of slow-moving landslides. As a possible broader impact, we hope that the proposed approach could pave a way towards more reliable risk assessment for slow-moving landslides.

Acknowledgments

Notations

Small Latin letters

base	elastic base	s	deviatoric stress tensor
c	cohesion	shear	shear zone
d_w	depth of groundwater level	slide	landslide mass
$f(\tau)$	failure surface	sym[•]	symmetric part of tensor
$g(\tau)$	plastic potential	tr(•)	trace of tensor
h	grid size (MPM)	v_0	reference velocity
$h(\alpha, \dot\alpha)$	function for friction coefficient	v_p	pressure wave velocity
h_{el}	element size (FEM)	v_s	shear wave velocity
h_{slide}	landslide height (benchmark)	$v_{s,30}$	average shear wave velocity in top 30m
n_{MP}	number of MPs per grid cell		

Capital Latin letters

A	viscosity parameter	$\mathcal{L}_v$	Lie derivative
B^e	elastic left Cauchy-Green strain tensor	M_W	earthquake magnitude
D^p	rate of plastic deformation tensor	PGA_h	horizontal peak ground acceleration
$\overline{D^p}$	spatially rotated rate of plastic deformation tensor	PGA_v	vertical peak ground acceleration
F	deformation gradient	R^e	elastic rotation tensor
F^e	elastic deformation gradient	R_{epi}	epicentral distance
F^p	plastic deformation gradient	R_{JB}	Joyner-Boore distance
I	identity tensor	R_{rup}	closes distance to rupture plane
$J_1(•)$	first invariant of tensor	RSN	Record Sequence Number (PEER)
$J_2(•)$	second invariant of tensor	SF	safety factor
L^p	plastic velocity gradient		

Small Greek letters

α	plastic strain	μ	second Lamé constant
$\dot\alpha$	rate of plastic strain	ρ	density
$\dot\alpha_0$	reference strain rate	τ	Kirchhoff stress tensor
β	slope inclination (benchmark)	φ	friction angle
$\dot\gamma$	plastic multiplier	φ_0	reference friction angle
δ_s	shear zone thickness	φ_{crit}	critical friction angle
ε	Hencky strain tensor	φ_r	residual friction angle
λ	first Lamé constant		

Capital Greek letters

Ψ	energy density

References

Al-Homoud, A. S. & Tahtamoni, W. (2000). Comparison between predictions using different simplified Newmarks' block-on-plane models and field values of earthquake induced displacements. *Soil Dynamics and Earthquake Engineering*, *19*(2), 73–90. https://doi.org/10.1016/S0267-7261(99)00033-0

Alonso, E. E., Zervos, A. & Pinyol, N. M. (2016). Thermo-poro-mechanical analysis of landslides: from creeping behaviour to catastrophic failure. *Géotechnique*, *66*(3), 202–219. https://doi.org/10.1680/jgeot.15.LM.006

Alsardi, A. & Yerro, A. (2021). Runout Modeling of Earthquake-Triggered Landslides with the Material Point Method. In *International Foundations Congress and Equipment Expo 2021* (pp. 21–31). American Society of Civil Engineers. https://doi.org/10.1061/9780784483428.003

Alvarado, M., Pinyol, N. M. & Alonso, E. E. (2019). Landslide motion assessment including rate effects and thermal interactions: Revisiting the canelles landslide. *Canadian Geotechnical Journal*, *56*(9), 1338–1350. https://doi.org/10.1139/cgj-2018-0779

Ancheta, T. D., Darragh, R. B., Stewart, J. P., Seyhan, E., Silva, W. J., Chiou, B. S. J., … Donahue, J. L. (2014). NGA-West2 database. *Earthquake Spectra*, *30*(3), 989–1005. https://doi.org/10.1193/070913EQS197M

Assefa, S., Graziani, A. & Lembo-Fazio, A. (2017). A slope movement in a complex rock formation: Deformation measurements and DEM modelling. *Engineering Geology*, *219*, 74–91. https://doi.org/10.1016/J.ENGGEO.2016.10.014

Bardenhagen, S. G. & Kober, E. M. (2004). The generalized interpolation material point method. *CMES - Computer Modeling in Engineering and Sciences*, *5*(6), 477–495. https://doi.org/10.3970/cmes.2004.005.477

Bažant, Z. P., Gattu, M. & Vorel, J. (2012). Work conjugacy error in commercial finite-element codes: its magnitude and how to compensate for it. *Proceedings of the Royal Society A: Mathematical, Physical and Engineering Sciences*, *468*(2146), 3047–3058. https://doi.org/10.1098/rspa.2012.0167

Bhandari, T., Hamad, F., Moormann, C., Sharma, K. G. & Westrich, B. (2016). Numerical modelling of seismic slope failure using MPM. *Computers and Geotechnics*, *75*, 126–134. https://doi.org/10.1016/j.compgeo.2016.01.017

Bontemps, N., Lacroix, P., Larose, E., Jara, J. & Taipe, E. (2020). Rain and small earthquakes maintain a slow-moving landslide in a persistent critical state. *Nature Communications*, *11*(1), 1–10. https://doi.org/10.1038/s41467-020-14445-3

Comité Européen de Normalisation. (2004). *EN 1998-1 Eurocode 8: design of structures for earthquake resistance, part 1: general rules, seismic actions and rules for buildings*. European Committee for Standardization.

Dai, F. C., Xu, C., Yao, X., Xu, L., Tu, X. B. & Gong, Q. M. (2011). Spatial distribution of landslides triggered by the 2008 Ms 8.0 Wenchuan earthquake, China. *Journal of Asian Earth Sciences*, *40*(4), 883–895. https://doi.org/10.1016/J.JSEAES.2010.04.010

Dassault Système Simulia. (2019). ABAQUS/Standart [software].

De Souza Neto, E. A., Perić, D. & Owen, D. R. J. (2008). Computational Methods for Plasticity: Theory and Applications. *Computational Methods for Plasticity: Theory and Applications*, 1–791. https://doi.org/10.1002/9780470694626

Duong, N. T., Suzuki, M. & Van Hai, N. (2018). Rate and acceleration effects on residual strength of kaolin and kaolin–bentonite mixtures in ring shearing. *Soils and Foundations*, *58*(5), 1153–1172.

https://doi.org/10.1016/J.SANDF.2018.05.011

Ering, P. & Sivakumar Babu, G. L. (2020). Effect of spatial variability of earthquake ground motions on the reliability of road system. *Soil Dynamics and Earthquake Engineering*, *136*, 106207. https://doi.org/10.1016/J.SOILDYN.2020.106207

European Commission. (2004). Guidelines for the implementation of the H/V spectral ratio technique on ambient vibrations. *SESAME Europeach Research Project WP12*.

Ferretti, A., Fruzzetti, V. M. E., Ruggeri, P. & Scarpelli, G. (2019). Seismic induced displacements of "La Sorbella" landslide (Italy).

Froude, M. J. & Petley, D. N. (2018). Global fatal landslide occurrence from 2004 to 2016. *Natural Hazards and Earth System Sciences*, *18*(8), 2161–2181. https://doi.org/10.5194/NHESS-18-2161-2018

Guerrera, F., Tramontana, M., Donatelli, U. & Serrano, F. (2012). Space/time tectono-sedimentary evolution of the Umbria-Romagna-Marche Miocene Basin (Northern Apennines, Italy): A foredeep model. *Swiss Journal of Geosciences*, *105*(3), 325–341. https://doi.org/10.1007/s00015-012-0118-0

Guzzetti, F. & Cardinali, M. (1989). Carta Inventario dei Movimenti Franosi della Regione dell'Umbria ed aree limitrofe [map]. *Pubblicazione CNR GNDCI*, *204*.

Handwerger, A. L., Rempel, A. W., Skarbek, R. M., Roering, J. J. & Hilley, G. E. (2016). Rate-weakening friction characterizes both slow sliding and catastrophic failure of landslides. *Proceedings of the National Academy of Sciences*, *113*(37), 10281–10286. https://doi.org/10.1073/pnas.1607009113

Hashash, Y. M. & Groholski, D. R. (2010). Recent advances in non-linear site response analysis. *Fifth Interantional Conference on Recent Advances in Geotechnical Earthquake Engineering and Soil Dynamics and Symposium in Honor of Professor I.M. Idriss*, *29*(6), 1–22.

He, M., Ribeiro e Sousa, L., Müller, A., Vargas, E., Sousa, R. L., Oliveira, C. S. & Gong, W. (2019). Numerical and safety considerations about the Daguangbao landslide induced by the 2008 Wenchuan earthquake. *Journal of Rock Mechanics and Geotechnical Engineering*, *11*(5), 1019–1035. https://doi.org/10.1016/J.JRMGE.2019.05.004

Hencky, H. (1928). Über die Form des Elastizitätsgesetzes bei ideal elastischen Stoffen. *Zeitschrift Für Technische Physik*, *6*.

Iverson, R. M. (2005). Regulation of landslide motion by dilatancy and pore pressure feedback. *Journal of Geophysical Research: Earth Surface*, *110*(2), 2015. https://doi.org/10.1029/2004JF000268

Iverson, R. M., Reid, M. E., Iverson, N. R., LaHusen, R. G., Logan, M., Mann, J. E. & Brien, D. L. (2000). Acute sensitivity of landslide rates to initial soil porosity. *Science*, *290*(5491), 513–516. https://doi.org/10.1126/science.290.5491.513

Jiang, C. (2015). The Material Point Method for the Physics-Based Simulation of Solids and Fluids. *University of California Los Angeles*.

Jiang, C., Selle, A., Teran, J. & Stomakhin, A. (2015). The Affine Particle-In-Cell Method. *ACM Transactions on Graphics*, *34*(4).

Jibson, R. W. (2011). Methods for assessing the stability of slopes during earthquakes-A retrospective. *Engineering Geology*, *122*(1–2), 43–50. https://doi.org/10.1016/j.enggeo.2010.09.017

Jibson, R. W., Prentice, C. S., Borissoff, B. A., Rogozhin, E. A. & Langer, C. J. (1994). Some observations of landslides triggered by the 29 April 1991 Racha earthquake, Republic of Georgia. *Bulletin Seismological Society of America*, *84*(4), 963–973.

Keefer, D. K. (2002). Investigating landslides caused by earthquakes - A historical review. *Surveys in*

Geophysics, *23*(6), 473–510. https://doi.org/10.1023/A:1021274710840

Kohler, M., Stoecklin, A. & Puzrin, A. M. (2021). A MPM framework for large deformation seismic response analysis. *Canadian Geotechnical Journal*. https://doi.org/10.1139/cgj-2021-0252

Kramer, S. L. (1996). *Geotechnical Earthquake Engineering*. *Engineering* (Vol. 6). https://doi.org/10.1007/978-3-540-35783-4

Kramer, S. L. & Smith, M. W. (1997). Modified Newmark Model for Seismic Displacements of Compliant Slopes. *Journal of Geotechnical & Geoenvironmental Engineering*, *123*, 635–644. https://doi.org/10.1061/(ASCE)1090-0241(1997)123:7(635)

Lacroix, P., Berthier, E. & Maquerhua, E. T. (2015). Earthquake-driven acceleration of slow-moving landslides in the Colca valley, Peru, detected from Pléiades images. *Remote Sensing of Environment*, *165*, 148–158. https://doi.org/10.1016/J.RSE.2015.05.010

Lacroix, P., Handwerger, A. L. & Bièvre, G. (2020). Life and death of slow-moving landslides. *Nature Reviews Earth and Environment*, *1*(8), 404–419. https://doi.org/10.1038/S43017-020-0072-8

Lacroix, P., Perfettini, H., Taipe, E. & Guillier, B. (2014). Coseismic and postseismic motion of a landslide: observations, modelling, and analogy with tectonic faults. *Geophysical Research Letters*, *41*, 6676–6680. https://doi.org/10.1002/2014GL061170

Lee, E. H. (1969). Elastic-Plastic Deformation at Finite Strains. *Journal of Applied Mechanics*, *36*(1), 1–6. https://doi.org/10.1115/1.3564580

Lemos, L. J. (2004). Shear Behaviour of Pre-Existing Shear Zones Under Fast Loading. *Advances in Geotechnical Engineering: The Skempton Conference*.

Lysmer, J. & Kuhlemeyer, R. L. (1969). Finite Difference Model for Infinite Media. *Journal of Engineering Mechanics*, *95*, 859–877.

Marone, C. (1998). Laboratory-Derived Friction Laws and Their Application To Seismic Faulting. *Annual Review of Earth and Planetary Sciences*, *26*(1), 643–696. https://doi.org/10.1146/annurev.earth.26.1.643

Mejia, L. H. & Dawson, E. M. (2006). Earthquake deconvolution for FLAC. *Proceedings of the 4th International FLAC Symposium on Numerical Modeling in Geomechanics*, 1–9.

Ministero dell'Ambiente e della Tutela del Territorio e del Mare. (2013). DTM LIDAR con risoluzione a terra 1 metro - regione umbria. Retrieved from http://www.pcn.minambiente.it/mattm/

Newmark, N. M. (1965). Effects of Earthquakes on Dams and Embankments. *Géotechnique*, *15*(2), 139–160. https://doi.org/10.1680/geot.1965.15.2.139

Nielsen, A. H. (2014). Towards a complete framework for seismic analysis in Abaqus. *Proceedings of the Institution of Civil Engineers - Engineering and Computational Mechanics*, *167*(1), 3–12. https://doi.org/10.1680/eacm.12.00004

Oberender, P. W. & Puzrin, A. M. (2016). Observation-guided constitutive modelling for creeping landslides. *Géotechnique*, *66*(3), 232–247. https://doi.org/10.1680/jgeot.15.LM.003

Perić, D., Owen, D. R. J. & Honnor, M. E. (1992). A model for finite strain elasto-plasticity based on logarithmic strains: Computational issues. *Computer Methods in Applied Mechanics and Engineering*, *94*(1), 35–61. https://doi.org/10.1016/0045-7825(92)90156-E

Puzrin, A. M. & Schmid, A. (2011). Progressive failure of a constrained creeping landslide. *Proceedings of the Royal Society A: Mathematical, Physical and Engineering Sciences*, *467*(2133), 2444–2461. https://doi.org/10.1098/rspa.2011.0063

Puzrin, A. M. & Schmid, A. (2012). Evolution of stabilised creeping landslides. *Géotechnique*, *62*(6), 491–501. https://doi.org/10.1680/geot.11.P.041

Rathje, E. M. & Bray, J. D. (1999). An examination of simplified earthquake-induced displacement procedures for earth structures. *Canadian Geotechnical Journal*, *37*(3), 731–732. https://doi.org/10.1139/cgj-37-3-731

Rodríguez, C. E., Bommer, J. J. & Chandler, R. J. (1999). Earthquake-induced landslides: 1980-1997. *Soil Dynamics and Earthquake Engineering*, *18*(5), 325–346. https://doi.org/10.1016/S0267-7261(99)00012-3

Rots, J. G., Nauta, P., Kusters, G. M. A. & Blaauwendraad, J. (1985). Smeared Crack Approach and Fracture Localization in Concrete. *Heron*, *30*(1).

Ruggeri, P., Fruzzetti, V. M. E., Ferretti, A. & Scarpelli, G. (2020). Seismic and Rainfall Induced Displacements of an Existing Landslide: Findings from the Continuous Monitoring. *Geosciences 2020, Vol. 10, Page 90*, *10*(3), 90. https://doi.org/10.3390/GEOSCIENCES10030090

Ruina, A. (1983). Slip Instability and State Variable Friction Laws. *Journal of Geophysical Research*.

Russo, E., Felicetta, C., D. Amico, M., Sgobba, S., Lanzano, G., Mascandola, C., … Luzi, L. (2022). *Italian Accelerometric Archive v3.2*. Instituto Nazionale di Geofisica e Vulcanologia, Dipartimento della Protezione Civile Nazionale. https://doi.org/10.13127/itaca.3.2

Scaringi, G. & Di Maio, C. (2016). Influence of Displacement Rate on Residual Shear Strength of Clays. *Procedia Earth and Planetary Science*, *16*, 137–145. https://doi.org/10.1016/j.proeps.2016.10.015

Scaringi, G., Hu, W., Xu, Q. & Huang, R. (2018). Shear-Rate-Dependent Behavior of Clayey Bimaterial Interfaces at Landslide Stress Levels. *Geophysical Research Letters*, *45*(2), 766–777. https://doi.org/10.1002/2017GL076214

Scholz, C. H. (1998). Earthquakes and friction laws. *Nature*, *391*(6662), 37–42. https://doi.org/10.1038/34097

Schulz, W. H. & Wang, G. (2014). Residual shear strength variability as a primary control on movement of landslides reactivated by earthquake-induced ground motion: Implications for coastal Oregon, U.S. *Journal of Geophysical Research: Earth Surface*, *119*(7), 1617–1635. https://doi.org/10.1002/2014JF003088

Schwager, M. V. & Puzrin, A. M. (2014). Inclinodeformeter pressure measurements in creeping landslides: Analytical solutions and field applications. *Geotechnique*, *64*(6), 447–462. https://doi.org/10.1680/geot.13.P.185

Servizio Idrografico Regione Umbria. (2016). Servizio Risorse Idriche e Rischio Idraulico. Retrieved April 5, 2022, from https://annali.regione.umbria.it

Simo, J. C. & Meschke, G. (1993). A new class of algorithms for classical plasticity extended to finite strains. Application to geomaterials. *Computational Mechanics 1993 11:4*, *11*(4), 253–278. https://doi.org/10.1007/BF00371865

Simo, J. C. & Miehe, C. (1992). Associative coupled thermoplasticity at finite strains: Formulation, numerical analysis and implementation. *Computer Methods in Applied Mechanics and Engineering*, *98*(1), 41–104. https://doi.org/10.1016/0045-7825(92)90170-O

Simo, J. C. & Pister, K. S. (1984). Remarks on rate constitutive equations for finite deformation problems: computational implications. *Computer Methods in Applied Mechanics and Engineering*, *46*(2), 201–215. https://doi.org/10.1016/0045-7825(84)90062-8

Skempton, A. W. (1985). Residual strength of clays in landslides, folded strata and the laboratory. *Géotechnique*, *35*(1), 3–18. https://doi.org/10.1680/geot.1985.35.1.3

Soga, K., Alonso, E., Yerro, A., Kumar, K. & Bandara, S. (2016). Trends in large-deformation analysis of landslide mass movements with particular emphasis on the material point method. *Géotechnique*, *66*(3), 248–273. https://doi.org/10.1680/jgeot.15.LM.005

Steffen, M., Kirby, R. M. & Berzins, M. (2008). Analysis and reduction of quadrature errors in the material point method (MPM). *International Journal for Numerical Methods in Engineering*, *76*(6), 922–948. https://doi.org/10.1002/nme.2360

Stoecklin, A., Trapper, P. & Puzrin, A. M. (2021). Controlling factors for post-failure evolution of subaqueous landslides. *Géotechnique*, *71*(10), 879–892. https://doi.org/10.1680/jgeot.19.p.230

Stomakhin, A., Schroeder, C., Chai, L., Teran, J. & Selle, A. (2013). A material point method for snow simulation. *ACM Transactions on Graphics*, *32*(4), 1. https://doi.org/10.1145/2461912.2461948

Sulsky, D., Chen, Z. & Schreyer, H. L. (1994). A particle method for history-dependent materials. *Computer Methods in Applied Mechanics and Engineering*, *118*(1–2), 179–196. https://doi.org/10.1016/0045-7825(94)90112-0

Tika, T. E., Vaughan, P. R. & Lemos, L. J. (1996). Fast shearing of pre-existing shear zones in soil. *Géotechnique*, *46*(2), 197–233. https://doi.org/10.1680/geot.1996.46.2.197

Vardoulakis, I. (2000). Catastrophic landslides due to frictional heating of the failure plane. *Mechanics of Cohesive-Frictional Materials*, *5*(6), 443–467. https://doi.org/10.1002/1099-1484(200008)5:6<443::AID-CFM104>3.0.CO;2-W

Wang, C., Hawlader, B., Islam, N. & Soga, K. (2019). Implementation of a large deformation finite element modelling technique for seismic slope stability analyses. *Soil Dynamics and Earthquake Engineering*, *127*, 105824. https://doi.org/10.1016/J.SOILDYN.2019.105824

Wang, W. M., Sluys, L. J. & De Borst, R. (1997). Viscoplasticity for instabilities due to strain softening and strain-rate softening. *International Journal for Numerical Methods in Engineering*, *40*(20), 3839–3864. https://doi.org/10.1002/(SICI)1097-0207(19971030)40:20<3839::AID-NME245>3.0.CO;2-6

Wedage, A. M. P., Morgenstern, N. R. & Chan, D. H. (1998). A strain rate dependent constitutive model for clays at residual strength. *Canadian Geotechnical Journal*, *35*(2), 364–373. https://doi.org/10.1139/t97-085

Wolf, J. P. (1989). Soil-structure-interaction analysis in time domain. *Nuclear Engineering and Design*, *111*(3), 381–393. https://doi.org/10.1016/0029-5493(89)90249-5

Wriggers, P. (1995). Finite element algorithms for contact problems. *Archives of Computational Methods in Engineering 1995 2:4*, *2*(4), 1–49. https://doi.org/10.1007/BF02736195

Yerro, A. (2015). *MPM modelling of landslides in brittle and unsaturated soils*. Universitat Politècnica de Catalunya (UPC).

Zheng, H., Liu, D. F. & Li, C. G. (2005). Slope stability analysis based on elasto-plastic finite element method. *International Journal for Numerical Methods in Engineering*, *64*(14), 1871–1888. https://doi.org/10.1002/NME.1406

Zienkiewicz, O. C., Bicanic, N. & Shen, F. Q. (1989). Earthquake Input Definition and the Trasmitting Boundary Conditions. In *Advances in Computational Nonlinear Mechanics* (pp. 109–138). Vienna: Springer Vienna. https://doi.org/10.1007/978-3-7091-2828-2_3

Appendix 3.1 – Implementation of constitutive model for shear zones

The presented model is implemented as a fully implicit exponential return mapping algorithm (Simo & Meschke, 1993). By using the logarithmic strain as measure for the material deformation, the return mapping can be written analogously to the small strain format (Perić, Owen, & Honnor, 1992). In the following the implementation presented, however, for details explanations and derivations the reader is referred to (De Souza Neto, Perić, & Owen, 2008). The algorithm start from the previous converged iteration step n and the velocity gradient $\boldsymbol{L}_{n+1}$ of the current step $n+1$. The incremental deformation gradient and the deformation gradient from the current step can be calculated as

$$\boldsymbol{F}_\Delta = \boldsymbol{I} + \Delta t \, \boldsymbol{L}_{n+1} \tag{3.16}$$

$$\boldsymbol{F}_{n+1} = \boldsymbol{F}_\Delta \boldsymbol{F}_n \tag{3.17}$$

where $\boldsymbol{I}$ represent the identity tensor and $\Delta t = t_{n+1} - t_n$ the time increment. Analogously to the small train return mapping algorithm, an elastic trial state is assumed. The left Cauchy-Green strain tensor for the trial state is given as

$$\boldsymbol{B}^e_{trial} = \boldsymbol{F}_\Delta \boldsymbol{B}^e_n (\boldsymbol{F}_\Delta)^T \tag{3.18}$$

where $\boldsymbol{B}^e_n$ is the left Cauchy-Green strain tensor from the previous step. Using the definition of the logarithmic strain, the trial for the elastic strain, internal variable (equivalent plastic strain) and the Kirchhoff stress follow as

$$\boldsymbol{\varepsilon}^e_{trial} = \frac{1}{2} \ln \boldsymbol{B}^e_{trial} \tag{3.19}$$

$$\alpha_{trial} = \alpha_n \tag{3.20}$$

$$\boldsymbol{\tau}_{trial} = 2\mu \boldsymbol{\varepsilon}^e_{trial} + \lambda \text{tr}\left(\boldsymbol{\varepsilon}^e_{trial}\right)\boldsymbol{I} \tag{3.21}$$

Using this trial state, the rate-independent yield condition is checked

$$f_{trial} = f(\boldsymbol{\tau}_{trial}, \alpha_{trial}, \dot{\alpha} = 0) = \sqrt{J_2(s_{trial})} + \frac{1}{3} J_1(\boldsymbol{\tau}_{trial}) \sin(\varphi(\alpha_{trial}, \dot{\alpha} = 0)) \leq 0 \tag{3.22}$$

If this condition is fulfilled there is no yielding an the trial state is accepted

$$(\bullet)_{n+1} := (\bullet)_{trial} \tag{3.23}$$

Otherwise the return mapping has to be performed. In case $J_1(\boldsymbol{\tau}_{trial})$ is positive, the new stress point lies in the apex of the Drucker-Prager cone and the new state is given as

$$\boldsymbol{\varepsilon}^e_{n+1} = \boldsymbol{0} \tag{3.24}$$

$$\alpha_{n+1} = \alpha_{trial} \tag{3.25}$$

$$\tau_{n+1} = 0 \tag{3.26}$$

Otherwise the new stress point lies on the smooth part of the cone. In that case, the return mapping equations are given in the same functional format as the small strain format (De Souza Neto et al., 2008)

$$\boldsymbol{\varepsilon}_{n+1}^e = \boldsymbol{\varepsilon}_{trial}^e - \Delta\gamma \left.\frac{\partial g(\boldsymbol{\tau})}{\partial \boldsymbol{\tau}}\right|_{n+1} = \boldsymbol{\varepsilon}_{trial}^e - \Delta\gamma \frac{1}{2\sqrt{J_2(\boldsymbol{s}_{n+1})}} \boldsymbol{s}_{n+1} \tag{3.27}$$

$$\alpha_{n+1} = \alpha_{trial} + \Delta\alpha = \alpha_{trial} + \frac{\Delta\gamma}{\sqrt{3}} \tag{3.28}$$

$$f\left(\boldsymbol{\tau}_{n+1}, \alpha_{n+1}, \dot{\alpha}_{n+1}\right) = 0 \tag{3.29}$$

$$\boldsymbol{\tau}_{n+1} = 2\mu\boldsymbol{\varepsilon}_{n+1}^e + \lambda\mathrm{tr}\left(\boldsymbol{\varepsilon}_{n+1}^e\right)\boldsymbol{I} \tag{3.30}$$

$$\dot{\alpha}_{n+1} = \frac{\Delta\alpha}{\Delta t} = \frac{\Delta\gamma}{\sqrt{3}\Delta t} \tag{3.31}$$

where the flow rule (eq. 3.11) and the evolution law for the internal variable (eq. 3.12) have been inserted. This system of equations has to be solve for $\boldsymbol{\varepsilon}_{n+1}^e$, α_{n+1}, $\Delta\gamma$. However, it is more convenient to transform this system of equations in one single nonlinear equation in $\Delta\gamma$. Therefore, the updated elastic strain (eq. 3.27) is inserted the elastic constitutive law (eq. 3.30)

$$\boldsymbol{\tau}_{n+1} = \boldsymbol{\tau}_{trial} - \Delta\gamma\mu \frac{1}{\sqrt{J_2(\boldsymbol{s}_{n+1})}} \boldsymbol{s}_{n+1} \tag{3.32}$$

Using the following identity

$$\frac{\boldsymbol{s}_{n+1}}{\sqrt{J_2(\boldsymbol{s}_{n+1})}} = \frac{\boldsymbol{s}_{trial}}{\sqrt{J_2(\boldsymbol{s}_{trial})}} \tag{3.33}$$

The update Kirchhoff stress and the corresponding deviatoric stress can be written as

$$\boldsymbol{\tau}_{n+1} = \boldsymbol{\tau}_{trial} - \frac{\Delta\gamma\mu}{\sqrt{J_2(\boldsymbol{s}_{trial})}} \boldsymbol{s}_{trial} \tag{3.34}$$

$$\boldsymbol{s}_{n+1} = \left(1 - \frac{\Delta\gamma\mu}{\sqrt{J_2(\boldsymbol{s}_{trial})}}\right) \boldsymbol{s}_{trial} \tag{3.35}$$

inserting into the yield condition

$$f_{n+1} = \sqrt{J_2(\boldsymbol{s}_{trial})} + \frac{1}{3} J_1(\boldsymbol{\tau}_{trial}) \sin(\varphi(\alpha_{n+1}, \dot{\alpha}_{n+1})) - \Delta\gamma\mu = 0 \tag{3.36}$$

The friction angle φ can be written as function of $\Delta\gamma$ as

$$\varphi(\Delta\gamma) = \arctan(h(\Delta\gamma)) \tag{3.37}$$

where $h(\Delta\gamma) = \tan\varphi$ given by equation 3.6 or any other model for the friction. Using the trigonometric identity

$$\sin(\arctan(x)) = \frac{x}{\sqrt{1+x^2}} \tag{3.38}$$

the yield condition can be written as

$$f_{n+1}(\Delta\gamma) = \sqrt{J_2(s_{trial})} + \frac{1}{3}J_1(\tau_{trial})\frac{h(\Delta\gamma)}{\sqrt{1+(h(\Delta\gamma))^2}} - \Delta\gamma\mu = 0 \tag{3.39}$$

This nonlinear equation can be solved using a Newton-Raphson algorithm. Denoting the iteration step i with $(\bullet)^{(i)}$, the initial guess and the corresponding yield condition are given as

$$\Delta\gamma^{(0)} = 0 \tag{3.40}$$

$$f^{(0)} = f_{n+1}\left(\Delta\gamma^{(0)}\right) = f_{trial} \tag{3.41}$$

and for iteration step i the yield condition is given by inserting the current value of $\Delta\gamma$ into equation 3.39

$$f^{(n)} = f_{n+1}(\Delta\gamma^{(n)}) = \sqrt{J_2(s_{trial})} + \frac{1}{3}J_1(\tau_{trial})\frac{h\left(\Delta\gamma^{(n)}\right)}{\sqrt{1+(h(\Delta\gamma^{(n)}))^2}} - \Delta\gamma^{(n)}\mu = 0 \tag{3.42}$$

The Newton-Raphson update follows as

$$\Delta\gamma^{(n+1)} = \Delta\gamma^{(n)} - \frac{f^{(n)}}{f'^{(n)}} \tag{3.43}$$

where

$$f'^{(n)} = \left.\frac{\partial f_{n+1}}{\partial\Delta\gamma}\right|_{\Delta\gamma^{(n)}} = \frac{1}{3}J_1(\tau_{trial})\frac{1}{\left[1+\left(h(\Delta\gamma^{(n)})\right)^2\right]^{\frac{3}{2}}}\left.\frac{\partial h(\Delta\gamma)}{\partial\Delta\gamma}\right|_{\Delta\gamma^{(n)}} - \mu \tag{3.44}$$

The iteration is repeated until the yield condition remains under certain tolerance ϵ_{tol}

$$|f^{(n+1)}| \leq \epsilon_{tol} \tag{3.45}$$

Afterwards, the state can be updated according to equations 3.27-3.31. The elastic left Cauchy-Green is also updated

$$\boldsymbol{B}^e_{n+1} = \exp\left[2\boldsymbol{\varepsilon}^e_{n+1}\right] \tag{3.46}$$

Finally, for the MPM algorithm the updated Kirchhoff stress has to be transformed to the Cauchy stress

$$\sigma_{n+1} = \det\left[\mathbf{F}_{n+1}\right]^{-1} \tau_{n+1} \tag{3.47}$$

4 Mechanics of coseismic and postseismic acceleration of active landslides

This chapter consists of the post-print version of the following published article, differing from the original only in terms of layout and formatting and the correction of an erratum[2]: Kohler, M. & Puzrin, A.M. (2023). Mechanics of coseismic and postseismic[3] acceleration of active landslides. *Nature Communications Earth & Environment*. Available at: https://doi.org/10.1038/s43247-023-00797-3

Abstract

Active slow-moving landslides exhibit very different coseismic and postseismic behaviour. Whereas some landslides do not show any postseismic acceleration, there are many that experience an increased motion in the days to weeks following an earthquake. The reason for this behaviour remains debated and the underlying mechanisms are only partially understood. In recent years, it has been suggested that postseismic acceleration is caused by excess pore water pressures generated outside of the shear zone during seismic shaking, with their subsequent diffusion into the shear zone. Here we show that this hypothesis is indeed plausible and hydro-mechanically consistent by using a basic rate-dependent physical landslide model. Our simulations provide insight into the landslide behaviour in response to seismic shaking and its main controlling parameters: preseismic landslide velocity, rate-dependency of soil strength in the shear zone, hydro-mechanical characteristics of the adjacent soil layers and the earthquake intensity.

---

[2] In the published version, the formula for the characteristic consolidation time is incorrect and a corrigendum has been submitted to the journal. In this post-print version, the formula is footnoted and has been corrected accordingly.

[3] In this chapter, the notations *coseismic* and *postseismic* are used instead of *co-seismic* and *post-seismic* due to the journal's preference.

4.1. Introduction

Landslides are one of the major threats in mountainous regions causing thousands of fatalities every year (Froude & Petley, 2018). Besides precipitation, landslide activity can be strongly influenced by earthquakes (Keefer, 2002; Rodríguez et al., 1999). Of particular interest is the response to seismic shaking of active slow-moving landslides, which pose a serious threat to people and infrastructure (Bonzanigo et al., 2007; Hendron & Patton, 1987; Lacroix et al., 2020; Puzrin & Schmid, 2012; Salcedo, 2009). Observations of such landslides reveal a wide range of earthquake related displacements, with surprisingly poor correlation between coseismic and postseismic motion (Lacroix et al., 2022). For instance, the relatively small co-seismic displacements (1-2 cm) of the Maca landslide (Peru) were followed by periods of increased velocities for about one month, resulting in three times greater cumulative displacements (Bontemps et al., 2020; Lacroix et al., 2014). The Mela-Kabod landslide (Iran), on the other hand, was displaced up to 30m during the Sarpol-e-Zahab earthquake, with subsequent 5-10 mm postseismic movements over the next three weeks (Cheaib et al., 2022). La Sorbella landslide (Italy), in turn, did not show any measurable increase in activity after coseismic displacements of 0.3-0.8 mm recorded during three earthquakes (Ferretti et al., 2019; Ruggeri et al., 2020). This large variation in the ratio between coseismic and postseismic motions has also been observed in various landslides affected by the Gorkha earthquake in Nepal (Lacroix et al., 2022).

The behaviour of a landslide during seismic shaking is assumed to be mainly governed by inertia and the dynamic stress change in the shear zone (Jibson, 2011; Newmark, 1965). Depending on the constitutive properties of the shear zone, the landslide's response can vary from zero to very large displacements. A critical control for a catastrophic coseismic collapse of the slope is the mechanism of strength reduction in the shear zone, such as rate-softening (Scaringi et al., 2018; Tika et al., 1996), grain crushing (Sadrekarimi & Olson, 2010; Sassa et al., 2014) or frictional heating (Vardoulakis, 2000). The coseismic motion of a landslides is further influenced by its geophysical properties, namely the shear wave velocity profile, which could lead to an amplification of the seismic signal (Jibson, 2011). It has also been shown that the landslide geometry can strongly influence the coseismic displacements (Kohler & Puzrin, 2022; Pinyol et al., 2022).

The wide range of different observed time scales suggest that the postseismic activity of landslides can have several underlying mechanisms (Lacroix et al., 2022). At annual scales, both landslide accelerations (Song et al., 2022) and increased landslide rates (Marc et al., 2015) are controlled by the combined effect of earthquakes and precipitation. These observations can be explained by damage to the landslide material due to earthquake shaking in the form of micro- and macrofractures, which increase permeability and generate preferential paths for water infiltration (Bontemps et al., 2020). The closure of these cracks, often referred to as healing, can take from months to several years, making a landslide more susceptible to precipitation driven movements. Another time scale of postseismic landslide activity, observed in different studies (Bontemps et al., 2020; Cheaib et al., 2022; Lacroix et

al., 2022, 2014), ranges from weeks to months. In contrast to the annual scale, this acceleration was observed even in the absence of rainfall, which is why another underlying mechanism is suspected. In a recent study, it was suggested that excess pore water pressures (PWP) are generated outside of the shear zone during seismic shaking and later migrate into this zone by seepage, causing an acceleration of the landslide motion (Lacroix et al., 2022). Depending on the origin of the excess pore water pressures and the soil permeability, this could lead to a time-lag of up to several days between the earthquake and the increased landslide mobility and therefore provides a possible reason for delayed landslide failures (Agnesi et al., 2005; Jibson et al., 1994; Keefer, 2002). Although this hypothesis seems to be conceptually reasonable, it has been lacking so far both direct measurements and a quantifiable model for its validation.

According to the fundamental concept of critical state soil mechanics (Roscoe et al., 1958), soils that are continuously sheared will come to the so-called critical state. This state is often described as continuous flow at which the volume and porosity of the soils stay constant with increasing shear deformation (Schofield & Wroth, 1968). Shear zones that have experienced a long history of localized shearing are assumed to have reached this critical state and no or only negligible excess pressures will be generated during further shearing (Lemos, 2004; Schulz & Wang, 2014; Skempton, 1985). Hence, a seismic event cannot lead to a direct weakening of the material in such shear zone. However, layers of fine-grained soils of relatively low permeability can be often found around or close to the shear zone of active landslides (Lacroix et al., 2020; Oberender, 2018; Zerathe et al., 2016). Under cyclic loading (e.g. earthquake shaking) these soils show a strong contractive behaviour if the initial void radio is larger than the critical state void ratio (Boulanger & Idriss, 2006; Kramer, 1996). During the fast process of earthquake shaking in saturated soils, this contraction is impeded because the water cannot be displaced from the pores fast enough. This leads to generation of excess PWP, which means a reduction in effective stresses. For large cyclic stress amplitudes and loosely packed, water-saturated soils, the effective stresses can reduce close to zero causing the well-known phenomena of cyclic liquefaction (Kramer, 1996). Although this phenomena of seismic liquefaction is mostly relevant for the coseismic triggering of debris flows (Islam et al., 2019), the behaviour of active landslides can already be influenced by relatively small reduction in effective stresses (Schulz et al., 2009), caused by lower excess PWP, which can migrate into the shear zone and perturb the quasi-static state of the landslide.

In this paper, we propose a dynamic hydro-mechanical model to study the generation of excess PWP during earthquake shaking and the following diffusion process. This model combines the well-known mechanism of generation of excess PWP as a result of cyclic shearing during an earthquake (Kramer, 1996) and the rate-dependent behaviour of shear zones (Tika et al., 1996). By applying it to parametric and case studies, we attempt to understand the underlying mechanism and to assess the plausibility of the hypothesis that excess PWP, generated outside of the slip surface, can be the main source of post-seismic landslide activity. This will also provide an insight into why the observed coseismic and postseismic landslide movements are that poorly correlated.

4.2. Results

4.2.1. Landslide model

In order to investigate the hydro-mechanical behaviour of active landslides during earthquakes, we propose a simplified model assuming infinite slope conditions (Figure 4.1). The landslide is reduced to slope parallel layers including a base, stable soil and landslide mass, where the latter are separated by the shear zone (slip surfaces). The local stratigraphy can be accurately represented by splitting the soil above and below the shear zone into a number of sublayers with different constitutive models and parameters. The landslide model is based on the theory of saturated porous solids und dynamic conditions introduced by Biot (1956, 1962), which is solved using a finite element discretization. This represents a unified framework, where the mechanism of seismic wave propagation, landslide movements and PWP dissipation are included. However, to get an accurate representation of the landslide behaviour it is crucial to select appropriate constitutive models for the shear zone and the adjacent soil.
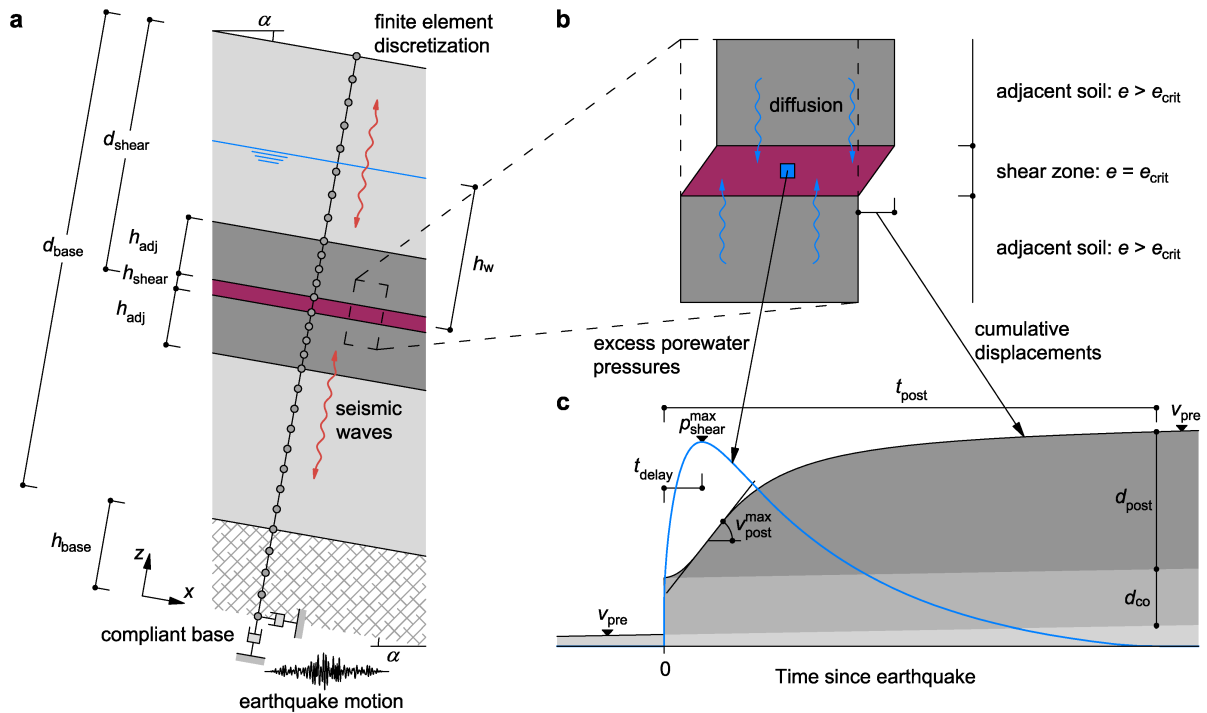
Figure 4.1: Landslide model. (a) The landslide model including the finite element discretization for displacements and pore pressures (considerably more elements are used in the simulations to have a proper representation). (b) Schematic representation of the diffusion of excess pore water pressure from the adjacent soil into the shear zone. The shear zone is assumed to have reached the critical state porosity e_{crit}, whereas the adjacent layers have a higher porosity. (c) Schematic representation of the seismic behaviour of landslides: Starting from an preseismic velocity v_{pre}, the landslide is hit by an earthquake leading to coseismic displacements d_{co}. Excess pore water pressures generated in adjacent soil layers can propagate into the shear zone (blue curve) and lead to a post-seismic activity. Depending on the permeability and the thickness of the layers, this effect can last over a period t_{post} lasting from hours and days to several months. The maximal postseismic velocity v_{max}^{post} is achieved when the excess pore pressures in the shear zone reach the maximal value, which can be delayed by the time t_{delay}, while also depending on the permeability and thickness of the layers.

The shear zone is assumed to have experienced a long history of localized shearing and therefore remains in the critical state, where no or only negligible excess pressure will be generated (Lemos, 2004; Schulz & Wang, 2014; Skempton, 1985) during seismic loading. To model shearing rates over several orders of magnitudes during the pre-, co- and postseismic periods of landslide evolution, a conventional logarithmic rate-hardening friction law is used for the shear zone (Alonso et al., 2016; Handwerger et al., 2016; Wedage et al., 1998). The corresponding relationship between the friction coefficient μ and the shearing rate v and can be written as

$$\mu = \mu_0 \left(1 + A \bullet \ln \left(\frac{v}{v_0} \right) \right) \tag{4.1}$$

where μ_0, A and v_0 are material parameters.

Adjacent to the shear zone, above and below it, two identical layers of fine-grained soils of relatively low permeability are assumed. As pointed out in the introduction, these soils have not yet reached the critical state and, therefore, can experience an accumulation of excess PWP along with the stiffness and strength degradation (Boulanger & Idriss, 2006; Kramer, 1996). Therefore, a multi-surface plasticity model following the framework developed by Prevost (1985) is applied in this work. The basic idea is that for each yield surface the volumetric behaviour is defined to control whether the soil shows a contractive or dilative behaviour. In case of undrained cyclic loading during earthquake shaking, this can result in generation of excess PWP depending on the stress amplitudes and number of cycles. It should be emphasized that the adjacent layers can be interpreted either as homogenous or as homogenized sequence of different sublayers, representing soil susceptible to the generation of excess PWP near the shear zone. The shear zone is likely to be less permeable than the adjacent layers due to its compacted state (Comegna et al., 2007). There is, however, some field evidence showing that it can also be more permeable (Di Maio et al., 2020). In this study they are modelled with the same permeability, which allows for reduction in the number of model parameters. This simplification is justified because the thickness of shear zones, typically ranging from millimeters to decimeters (Corominas et al., 2005; Miao & Wang, 2022; Oberender & Puzrin, 2016; van Asch et al., 2007), is orders of magnitude smaller than that to the adjacent layers. Consequently, the shear zone contribution to seepage is small and not sensitive to its permeability. The stable soil and the landslide mass above the adjacent layers are modelled as linear elastic with a considerably higher permeability and can, therefore, be seen as drainage layers. Whether this corresponds to the actual stratigraphy or whether, for example, this is just a layer of sand or gravel bounding the fine-graded soils is less relevant. Even if there are additional layers susceptible to the generation of excess PWP within the stable soil or the landslide mass, in reality they will hardly influence the shear zone since for landslides of finite lengths the drainage layers will predominantly dissipate excess PWP along the slope. This model should be seen as a generalization of typical landslide conditions (Hungr et al., 2014; Lacroix et al., 2020; Oberender & Puzrin, 2016; Zerathe et al., 2016) to investigate the underlying mechanism. More details on the

landslide model, the applied constitutive models and the corresponding parameters are presented in the Methods section.

4.2.2. Conceptual model response

The conceptual response of the proposed model and some fundamental mechanisms are explained in Figure 4.2. The initial state of the model is given by the quasi-static equilibrium, where the landslide is slowly moving at the preseismic velocity v_{pre} sufficient to counterbalance driving forces by the rate-dependent shear strength. If this model is subjected to an earthquake ground motion, the shear zone and the adjacent soil will show different responses, which in cases of low permeability do not interfere with each other. The seismic shear stress amplitude can occasionally exceed the strength of the shear zone leading to a temporary stepwise acceleration of the landslide. Due to the large scale of the horizontal axis in Figure 4.1c, these steps are indistinguishable and show up as a single step of coseismic displacement d_{co}. The increase in velocity will simultaneously mobilize a higher shear strength according to the logarithmic rate-dependency and counteract the acceleration to some extent. Consequently, smaller coseismic displacements are expected for a higher rate-dependency parameter A. Since the shear zone remains at critical state, no excess PWP are generated in it and the effective normal stress stays constant during seismic shaking. This is illustrated by the vertical coseismic effective stress-path in Figure 4.2a. In contrast, in the adjacent layers excess PWP are generated during cyclic shaking, which is shown by the reduction in effective stresses in Figure 4.2b. While for a high permeability, the response of the shear zone and the adjacent soil cannot be separated and they interfere with each other, the hydro-mechanically coupled dynamic approach used here correctly handles this interaction.

After the earthquake, the diffusion process will start and continue over a longer time scale. The excess PWP in the adjacent layers will propagate into the layers above and below as well as into the shear zone, where this reduction of the effective stress causes a drop in shear strength, resulting in landslide acceleration. Due to the rate dependency of strength, however, this acceleration will cause an increase in strength, compensating for the reduction in effective stresses and allowing the landslide to find a new equilibrium, but at a higher velocity. It follows, that for the same excess PWPs, the higher is the rate dependency, the lower will be the new elevated velocity. As the PWPs gradually dissipate after the earthquake, a progressively smaller velocity will be sufficient to compensate for the strength drop, until all the excess PWP fully dissipate and the landslide returns to its preseismic velocity.
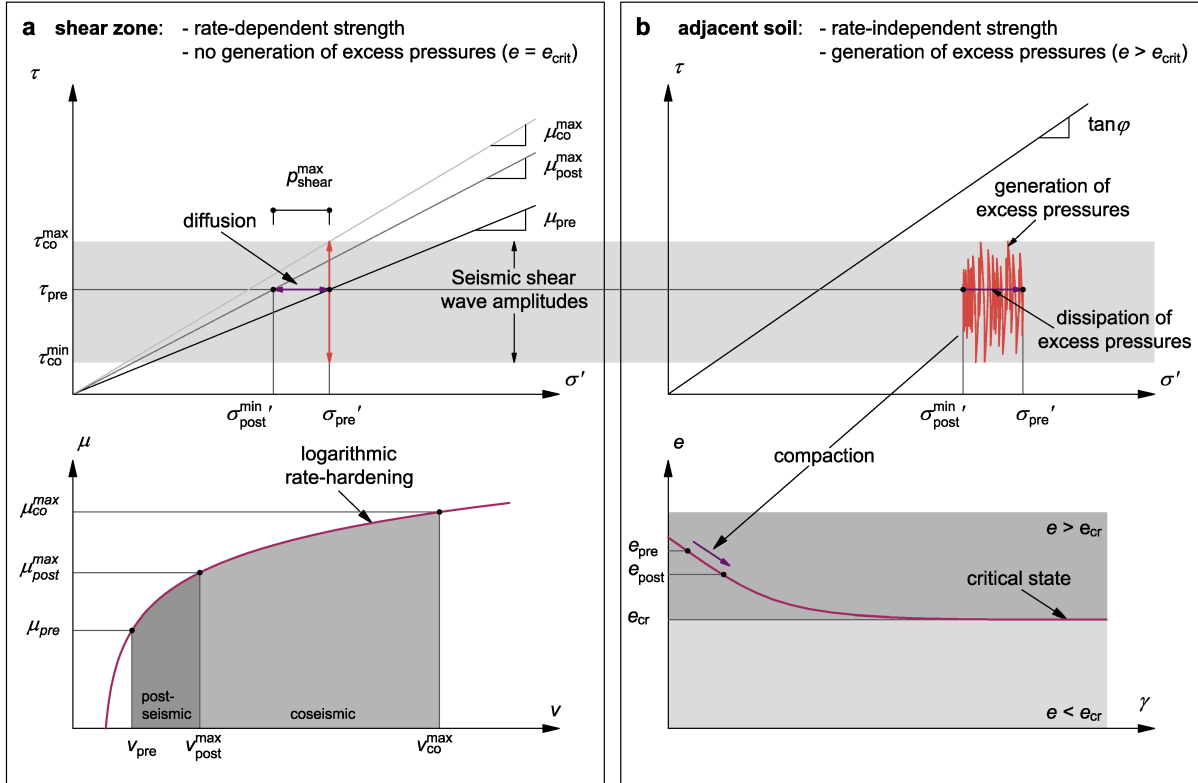
Figure 4.2: Conceptual model response. (a) Stress-path in the space of effectiv normal stress σ' and shear stress τ (top) and rate-dependent friction law (bottom) inside the shear zone. During the seismic shaking, no excess pressures as generated and a higher friction can be mobilized due to the increased coseismic velocity. After the earthquake the diffusion of excess PWP into the shear zone leads to a reduction of the normal effective stress until the minimal value σ'^{min}_{post}. This reduction in effective stress leads to a reduction in the shear resistance accelerating the landslides to a maximal postseismic velocity v^{max}_{post}. Therefore, the reduction in the shear resistance is counterbalanced by the rate dependency leading to a new quasi-static state. During the further diffusion process, the landslide is continuously decelerated to the preseismic velocity v_{pre}. (b) Stress-path (top) and compaction (bottom) in the adjacent soil layers. The cyclic shaking with maximal and minimal shear stress amplitudes of τ^{max}_{co} and τ^{min}_{co} leads to a generation of excess PWP shown by reduction in the effective normal stress from σ'_{pre} to σ'^{min}_{post}. During the following postseismic dissipation process the soil in the adjacent layers starts to compact shown by the reduction of the void radio from e_{pre} to e_{pos}.

4.2.3. Simulation example

The first simulation of an example case, based on the Maca landslide (Zerathe et al., 2016) and the typical range of parameters (e.g. thickness, slope inclination, landslide velocity) (Lacroix et al., 2020), aims to show the capability of the presented model and reveals effects of different phenomena on the seismic acceleration of landslides. The applied parameters are presented in Table 4.1 in the methods section. Rather different patterns can be observed for pre-, co- and postseismic displacements (Figure 4.3a). The initial state of slow movements is interrupted by a short period of distinct displacement steps induced by the earthquake impulses (Figure 4.3b), which is similar to the results from a traditional Newmark's sliding block analysis (Newmark, 1965). After the earthquake, the landslide shows a one day-long acceleration followed by a deceleration over several days reverting to the pre-seismic velocity.
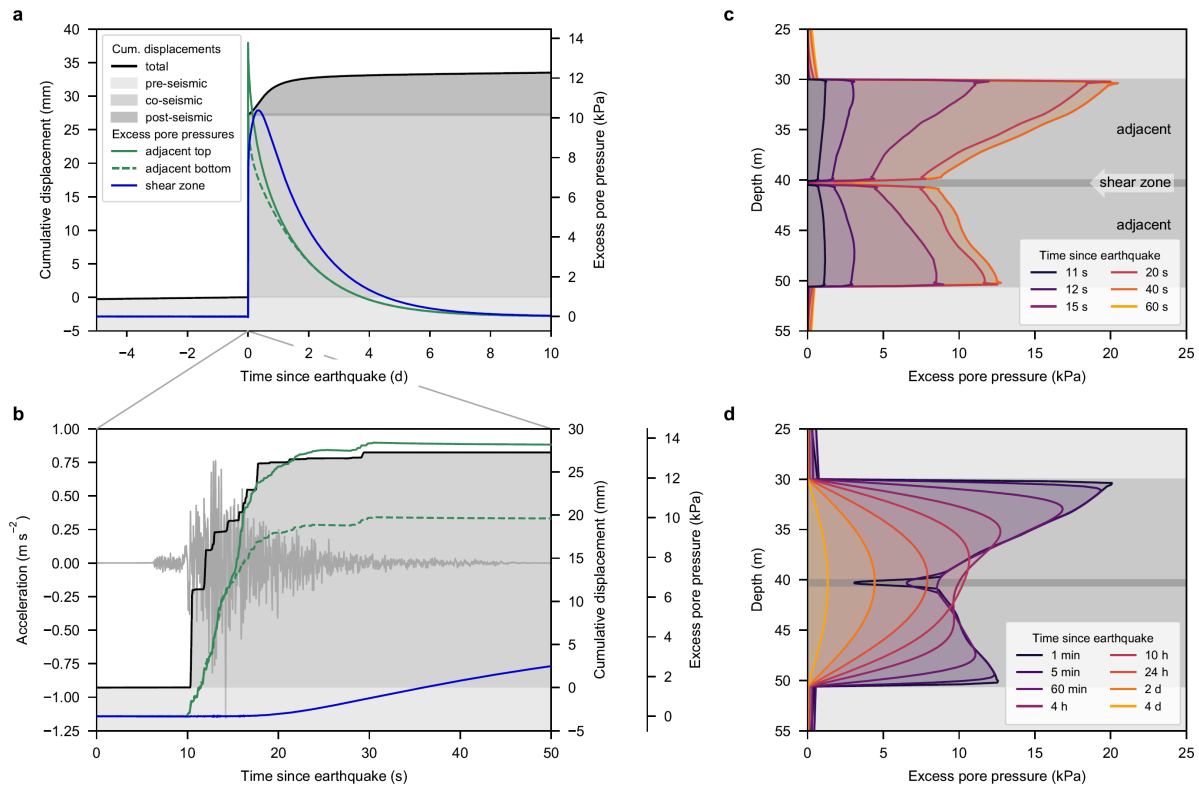
Figure 4.3: Example simulation. (a) Cumulative displacements split into pre-, co- and postseismic contributions and the evolution of excess pore water pressures in the shear zone and the adjacent layers (average). (b) Zoom of the co-seismic behaviour showing the input ground motion (Engineering Strong Motion (ESM) database signal ID: IT-MNF-EMSC-20161030_0000029-HE (Luzi et al., 2020)), cumulative displacements and the evolution of excess pore water pressures in the shear zone and the adjacent layers. (c) Generation of excess pore water pressures in the adjacent soil layers during the earthquake (shear zone marked in dark grey). (d) Dissipation of excess pore water pressures during the postseismic period (shear zone marked in dark grey).

The generation of excess PWP in the adjacent soil layers during the earthquake and the following diffusion into the shear zone are presented in Figure 4.3c and d, respectively. The spatial distribution of excess PWP provides several important insights: (*i*) generation of excess PWP is considerably reduced in the vicinity of the shear zone due to the smaller amplitude of shear stresses, limited by the residual shear strength in the shear zone; (*ii*) since no excess pressures are generated in the shear zone, the only source of their increase is the diffusion from the adjacent soil; (*iii*) the maximal excess PWP reached inside the shear zone is considerably smaller than those in the adjacent soil. The excess PWP in the adjacent soil and the corresponding degradation of strength could theoretically lead to the formation of new shear zones. While the proposed mechanism can capture this effect automatically via the strain softening model used for the adjacent soil, it has not been observed in simulations due to the large difference between the residual strength of the shear zone and the peak strength of the adjacent soil. If the shear zone and the adjacent layers are identical soils of low clay content, these strengths are closer together since the phenomena of particle reorientation leading to a low residual strength (Skempton, 1985) is less dominant. In such a scenario, however, the adjacent layers would be already close to fully

mobilized strength and the critical state. Therefore, the excess PWP generated during an earthquake cannot be substantial, making a postseismic acceleration less likely.

The initial increase and the following dissipation of excess pressures in the shear zone explain the observed post-seismic landslide acceleration and deceleration due to the associated reduction of effective stresses and hence change in the shear resistance. While the geometry, material parameters and seismic loading chosen for this demonstration example are realistic and produce a possible co- and postseismic slope behaviour, this alone does not provide an insight into relative effects of individual parameters and corresponding mechanisms.

4.2.4. Interplay between rate dependency and excess PWP

The parametric study in Figure 4.4. investigates the influence of the most important factors and assesses the potential patterns of between coseismic and postseismic landslide activity. The basis for this simulations is again the Maca landslide (Zerathe et al., 2016) with the ranges for landslide parameters given in Lacroix et al. (2020). It is important to recognize the analogy between the dissipation of excess PWP from the adjacent soil and the one-dimensional consolidation theory (von Terzaghi, 1925), which describes the consolidation process in soils where only unidirectional seepage flow is taking place. A key finding of this theory is that the time until a certain percentage of the excess PWP is dissipated is proportional to the characteristic consolidation time[4] $T = h^2 \gamma_w / (kM)$. Applying this concept to the dissipation of excess PWP in the adjacent layers, the results are plotted with respect to this characteristic time, where $h = h_{adj}$ is the thickness, k the permeability; M the average constrained modulus of the adjacent layers and γ_w is the specific weight of water. The linear dependency of the duration of postseismic motion on the characteristic time (Figure 4.4a) confirms the consolidation analogy. Therefore, the characteristic time can be interpreted as an important landslide-specific parameter, uniquely defining the postseismic duration, regardless of the rate-dependent characteristics of the shear zone material or earthquake intensity. The latter finding is confirmed by observations of the Maca landslide, where two earthquakes of different intensities resulted in almost identical postseismic durations (Lacroix et al., 2022). The chosen range of permeability is typical for fine-grained soils found in landslides (Picarelli et al., 2008; Rosone et al., 2018; van Asch et al., 2007). For more clayey layers, a smaller permeability is locally possible, but the comparison of lab and field tests has shown (Comegna et al., 2007) that the field permeability is usually larger due to in homogeneities. It is rather questionable whether a homogeneous clayey layer of 30 m thickness with a permeability of $k = 10^{-10}$ m/s can be encountered in a real landslide. However, thinner layers with such a permeability are indeed realistic (Comegna et al., 2007; Di Maio et al., 2020), and can lead to postseismic movements over a period of several years.

---

[4] In the published version, the formula for the characteristic consolidation time is incorrect and a corrigendum has been submitted to the journal.
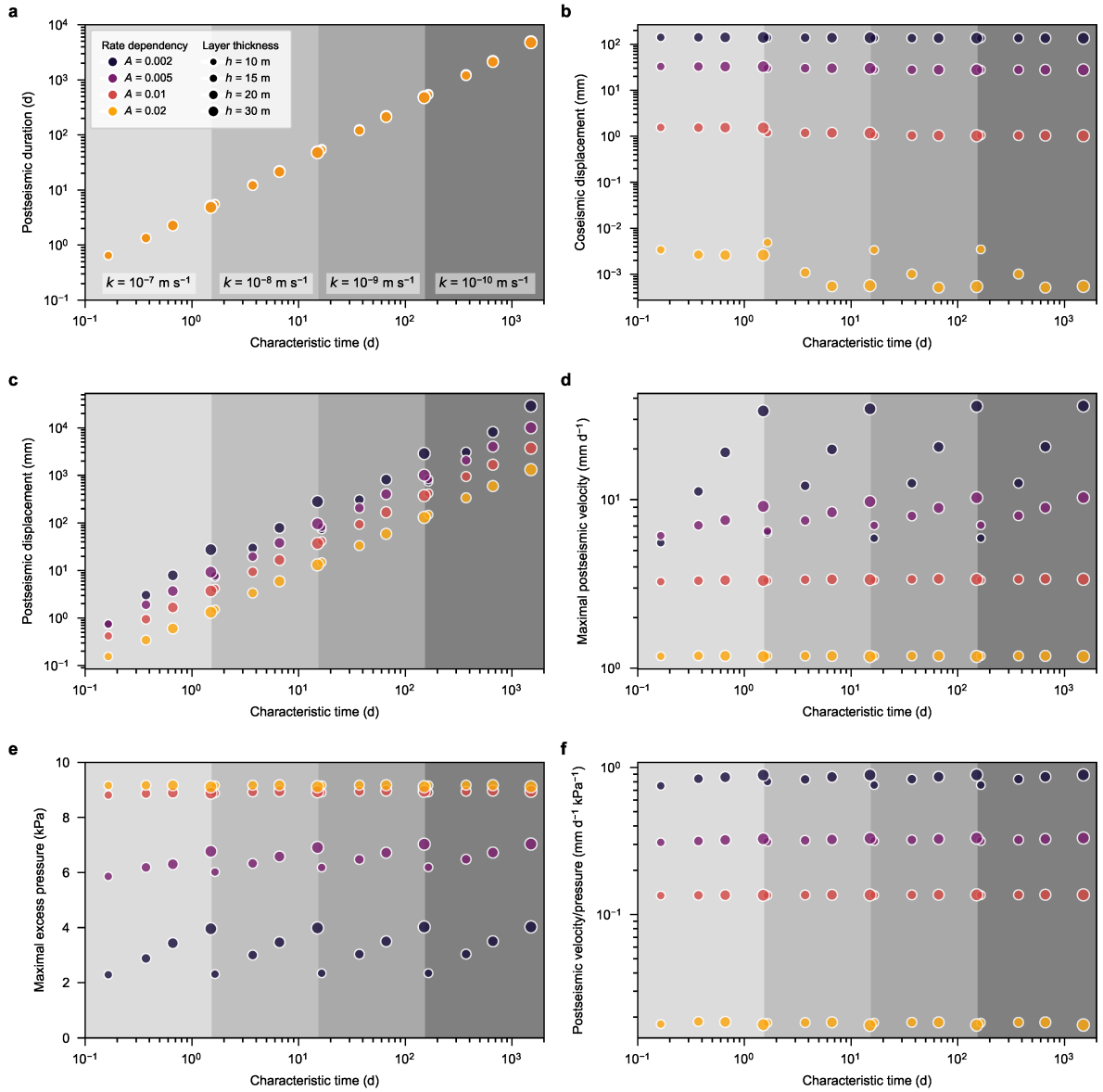
Figure 4.4: Parametric study of co- and post-seismic landslide activity. Simulation results showing the influence of the rate dependency of the shear zone (parameter *A*), thickness of the soil layers adjacent to the shear zone ($h = h_{adj}$) and the permeability of the shear zone and the adjacent soil layers *k*. The results are plotted on the horizontal axis using the characteristic time[5] $T = h^2 \gamma_w/(kM)$, where γ_w is the specific weight of water and *M* the average constrained modulus of the adjacent soil layers, for: (a) Duration of the postseismic period of increased landslide activity, starting after the earthquake and ending once 95% of the excess PWP has been dissipated. The markers for different rate dependencies lie exactly on top of each other and are therefore not visible. (b) Coseismic displacements. (c) Postseismic displacement. (d) Maximal postseismic velocity. (e) Maximal excess pore pressure inside the shear zone. (f) Ratio of the maximal postseismic velocity and the maximal excess pressure. The earthquake motion was retrieved from the ESM database (ESM signal ID: IT-MNF-EMSC-20161030_0000029-HE (Luzi et al., 2020)). The parameters used for the simulations are presented in Table 4.1.

---

[5] In the published version, the formula for the characteristic consolidation time is incorrect and a corrigendum has been submitted to the journal.

The coseismic displacements (Figure 4.4b) are mainly governed by the rate dependency of the shear strength in the shear zone and can vary over several orders of magnitudes for a typical range of observed rate dependencies (Tika et al., 1996). In contrast, the postseismic displacement (Figure 4.4c) is controlled by both the rate dependency and the characteristic time. Dependency on the characteristic time (i.e., duration) is straightforward, because for the same postseismic velocity, a longer duration naturally leads to a larger postseismic displacement. The effects of rate dependency of strength are, however, more complicated. As expected, the postseismic displacement grows with the maximal postseismic landslide velocity, which in turn increases with the maximal excess PWP in the shear zone. The complication arises from the fact that rate dependency has two opposite effects on the pore pressures and the velocity. While on one hand, similar to the preseismic state, a higher rate dependency of the shear zone leads to a lower postseismic velocity (Figure 4.4d); on the other hand it results in higher coseismic excess PWP (Figure 4.4e). The latter can be explained by the isolating effect of the shear zone, which for a low rate dependency can sustain and transfer only limited shear stress amplitudes, resulting in lower excess PWP in the adjacent layers. For higher rate dependency, however, this isolating effect becomes less prominent, because the shear zone behavior remains practically elastic, transferring shear waves of higher amplitudes and causing higher excess PWP. These counteracting effects of rate dependency can be separated by using the ratio between the maximal postseismic velocity and excess PWP (Figure 4.4f), which can be interpreted as a pressure-normalized postseismic velocity. This establishes rate dependency as the main influencing factor for both the velocity and PWP, and highlights the decoupled nature of the two different time-dependent mechanisms affecting the postseismic acceleration: consolidation/seepage (affecting duration) and rate dependency (affecting velocity and PWP) and their relative contributions to the post-seismic displacements. Unravelling this elegant interplay between rate dependency and excess PWP has been critical for understanding the between coseismic and postseismic landslide behaviour. This understanding would, however, be incomplete without an insight into effects of another critical factor – seismic loading.

4.2.5. Influence of earthquake intensity vs the field evidence

The influence of the earthquake intensity on the landslide activity has been investigated by subjecting the landslide model to a large set of variable input signals (Table 4.3 in Appendix 4.1). The comparison of the results with the measurements from different case studies (Bontemps et al., 2020; Cheaib et al., 2022; Lacroix et al., 2022, 2014; Ruggeri et al., 2020; Song et al., 2022) is presented in Figure 4.5. Amongst the most popular intensity measures the peak ground velocity (PGV) was found to provide the best correlation between coseismic and postseismic landslide activity and the earthquake intensity. The postseismic motion is plotted as a displacement ratio, where the post-seismic displacement is normalized by a yearly reference displacement resulting from a constant preseismic velocity. In the preseismic state, the equilibrium is maintained because the reduction in shear resistance caused by a precipitation-driven increase in PWP is counterbalanced by rate-hardening of the shear zone due to an increased landslide

velocity. The postseismic motion can be viewed as a perturbation of the preseismic state by a coseismic increase in PWP, suggesting that the postseismic landslide velocity should directly correlate with the preseismic velocity, as confirmed by a parametric study in Figure 4.9 (Appendix 4.2). Additionally, the comparison of the results shown in Figure 4.5 is provided in non-normalized form in Figure 4.10 (Appendix 4.3).
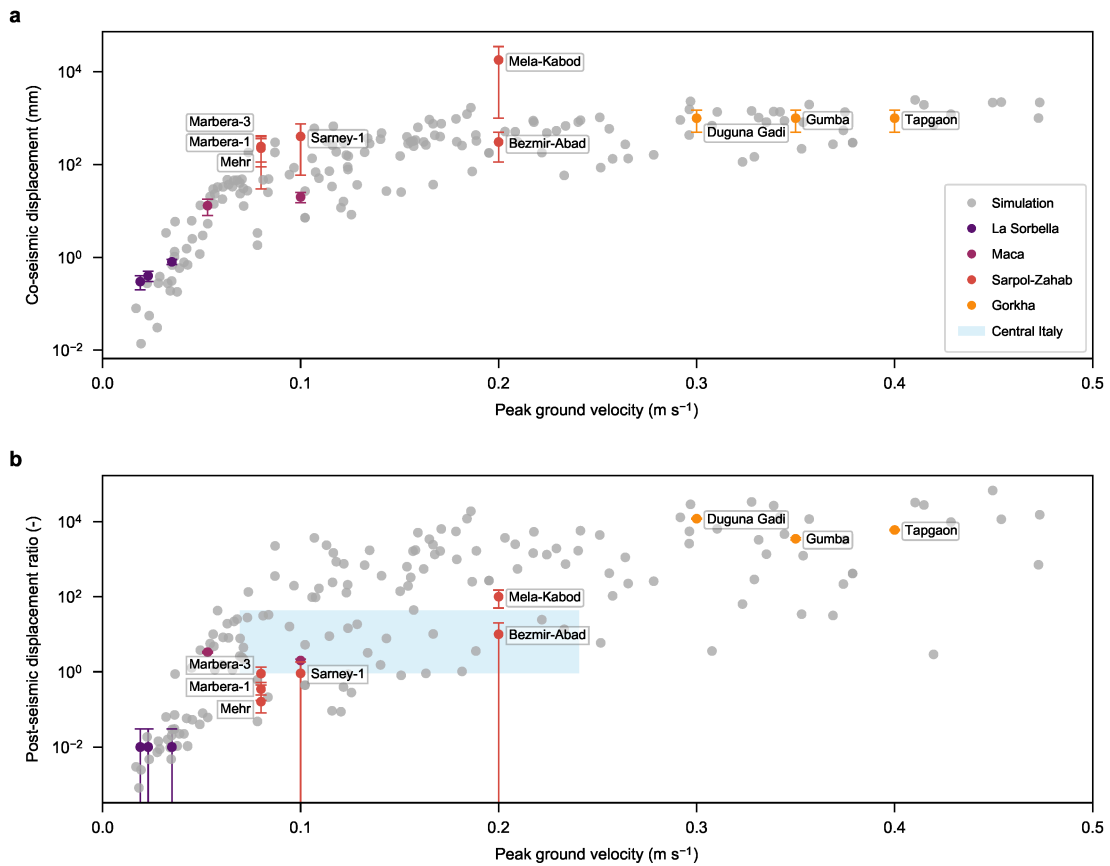
Figure 4.5: Influence of the earthquake intensity on the landslide motion. Comparison of simulations to measurements from case studies for a large set of earthquake signals. (a) coseismic displacements and (b) postseismic displacement ratio given by normalizing the postseismic displacement with a yearly reference displacement resulting from a constant preseismic velocity. The input signals from rock or stiff soil sites were retrieved from the ESM database (Luzi et al., 2020) and are listed in the Table 4.3. The case studies considered are: La Sorbella landslide (Ruggeri et al., 2020), Maca landslide (Bontemps et al., 2020; Lacroix et al., 2014), Sarpol-Zahab earthquake (Cheaib et al., 2022) (Slides: Marbera-1, Marbera-3, Mehr, Sarney-1, Mela-Kabod, Bezmir-Abad), Gorkha earthquake (Lacroix et al., 2022) (Slides: Duguna Gadi, Gumba, Tapgaon) and landslides in Central Italy (Song et al., 2022). The landslides from the Gorkha study show almost no preseismic motion and the reference velocity for the normalization is assumed to be 2 cm/year based on landslide velocity detected in a nearby valley (Bekaert et al., 2020). Error bars represent the measurement error reported in the respective publications. Except for La Sorbella, the input signals are not available and the peak ground acceleration was estimated based on the USGS shakemap (https://earthquake.usgs.gov/data/shakemap/). The parameters used for the simulations are presented in Table 4.1.

Both coseismic and postseismic displacements clearly increase with increasing ground motion intensity, where the fastest logarithmic increase takes place at lowest intensities and a saturation can be observed for intensities at PGV > 0.1. This observation can be explained by the isolating effect of the shear zone, hindering the transfer of large amplitude impulsive shear waves from stronger earthquake motions. Although the postseismic displacement ratio shows a larger scatter, it can still be observed that the post-seismic activity decays slightly faster with the decreasing intensity. This trend has already been detected in real landslides (Lacroix et al., 2022). In general, the simulation results are in good agreement with the measurements from the case studies. In cases where no postseismic motion was measured, it is assumed to be within the order of the accuracy of the measurements.

In case of La Sorbella landslide only very small coseismic and no postseismic displacement were measured during three moderate earthquakes (Ferretti et al., 2019; Ruggeri et al., 2020). The latter is not surprising given the direct relation between the preseismic and postseismic velocity and the fact that La Sorbella is very slow moving. The simulation seems to slightly underestimate the coseismic motion, which can be explained by the strong influence of the rate dependency. This is confirmed by the simulation results in Figure 4.11 (Appendix 4.4), where the model parameters are adjusted for the specific case of La Sorbella slide and the corresponding earthquake signal recorded near the landslide is applied. Firstly, the results suggest a higher rate dependency of the shear zone to accurately match the coseismic displacement, which also means that a smaller postseismic velocity is expected for a given excess pressure. Secondly, the lithology of La Sorbella landslide is different from the proposed landslide model and only shows soil susceptible to excess PWP above the shear zone. This is considered in the case specific simulation (Figure 4.11) leading to less excess PWP and faster dissipation, which could further explain the missing postseismic movements.

The landslides observed in connection with the Sarpol Zahab earthquake in Iran are described as deep-seated sliding mass of limestone blocks, entrained within clayey and debris material (Cheaib et al., 2022). They are all considered pre-existing landslides, either dormant or active, with velocities ranging from 0 to 43 mm/year. All of them showed clear coseismic displacements, which in general lie within the simulated range, except for the Mela-Kabod slide, where a displacement of around 30 m represents an outlier. Considering the strong influence of the rate dependency (see Figure 4.4b), such large displacements could result from a lower rate-hardening. Also other factors decreasing the shear resistance, such as a change from rate-hardening to rate-softening shear behaviour (Lacroix et al., 2020), softening in the landslide mass (Kohler & Puzrin, 2022) or grain crushing (G. Wang & Sassa, 2002) could explain the excessive observed displacements. Some of these landslides (Mela-Kabod, Marbera-1, Marbera 3 and Mehr) showed a postseismic transient motion over 20 days, which fits into the lower range given by the simulation results. Given the insufficient knowledge of the lithology of these slides and that they contain rock as well as soil, they might be less susceptible to excess PWP.

The landslides in Nepal are describe as reactivation of paleo-landslide deposit of breccia material in a silty matrix (Gumba and Duguna Gadi) and a thick rockslide of deformed regolith and weathered bedrock (Tapgaon) (Lacroix et al., 2022). They all share a coseismic displacement of around 1 m, followed by an acceleration during few days after the Gorkha earthquake (with the moment magnitude M_w 7.8) and a similar progressive deceleration for two months. Two interesting observation should be emphasized. Firstly, the Tapgaon slide clearly showed a delay of at least 4 days for the postseismic motion, which may indicate a larger distance between the shear zone and the layers susceptible to generation of excess PWP. Secondly, the Dolakha earthquake (M_w 7.3), an aftershock of the Gorkha event, showed no effect on the postseismic activity of these landslides. An explanation could be that during the strong main shock the contraction potential of the susceptible soil layers has been greatly reduced. Therefore, no or only little PWP were generated during the aftershock.

In a recent study, a large inventory of landslides accelerated by the 2016-2017 Central Italy earthquake sequence was presented (Song et al., 2022). They have reported an average acceleration phase of around one year followed by a stabilization and recovery phase for two years of theses landslides. This falls within the annual time scale of postseismic activity and is usually explained by different mechanisms (Bontemps et al., 2020; Lacroix et al., 2022; Marc et al., 2015). However, these landslides are still illustrated in Figure 4.5 by a shaded area showing their predominant occurrence. Unfortunately, the coseismic displacement of these landslides was not reported and is therefore not shown.

The motion of the Maca landslide (Bontemps et al., 2020; Lacroix et al., 2014) very well fits the general simulation results, which was expected since this slide formed the basis study case for the proposed model. While this analysis allows for quantifying the main effects of seismic loading on landslide activity, the large range of possible responses to different events of similar intensity is, on its own, an important outcome requiring a better understanding. Towards this goal, the proposed methodology is applied to the Maca landslide in Peru (Zerathe et al., 2016) in the following section.

4.2.6. Application to the Maca landslide

Located in a seismically active zone in Peru, the Maca landslide is in a persistent state of slow movements driven by rain and small earthquakes (Bontemps et al., 2020). In 2013, this region was hit by a shallow M_w 6.0 earthquake located 20 km away from the landslide. By means of a permanent GPS station, both the co- and post-seismic displacements could be recorded (Lacroix et al., 2014). Since no appropriate ground motion records are available for this event, the simulation was performed using four different accelerogramms (for rock or stiff soil sites) from earthquakes in other locations (Umbria, Central Italy, Attica, Visso) with similar magnitudes, epicentral distances and PGVs (Figure 4.6). The earthquake signals were retrieved from the Engineering Strong Motion (ESM) database (Luzi et al., 2020). The GPS measurements indicate a post-seismic period of around 50 days. Based on the direct relationship between post-seismic duration and the characteristic consolidation time, the main unknown - permeability - can be adjusted to accurately match the observed duration. The Attica event provides the best fit and is, therefore, used to determine the rate dependency by matching the coseismic displacements. The same rate-hardening parameter is then used for all four input signals to investigate the variability of the landslide behaviour. The results highlight the strong influence of the input motion, which was already observed in Figure 4.5. Whereas the Umbria and Attica events give almost identical coseismic displacements, they generate considerably different pore water pressures, leading to different postseismic accelerations. On the other hand, the Attica and Central Italy records produce quite different coseismic displacements but almost identical pore water pressures and postseismic displacements. These findings might explain why a weaker earthquake led to larger postseismic displacements for the Maca landslide (Bontemps et al., 2020), likely enhanced by a higher preseismic velocity prior to the weaker earthquake.

It can also be noted that the simulation predicts an acceleration of the landslide over several days, whereas this is not evident in the measured data. However, this acceleration is extremely small in the simulation for the Attica event and is hardly visible. The duration of this acceleration depends in particular on the thickness of the shear zone, and for a thinner zone, this effect would disappear.

It follows that for a hydrologically sensitive landslide, seismic events of similar intensity can produce different (albeit relatively modest) excess PWP resulting in a wide range of postseismic displacements. This variation is due to other earthquake characteristics, but no direct correlation or simple explanation could be identified. Most likely, this is a result of various effects interfering with each other and goes beyond the scope of this work. As expected, the corresponding variation in coseismic displacements is less prominent because it is mainly controlled by rate dependency. This explains the different magnitude of scatter in Figure 4.5a and b, and provides additional insight into the observed lack of correlation between coseismic and postseismic displacements.
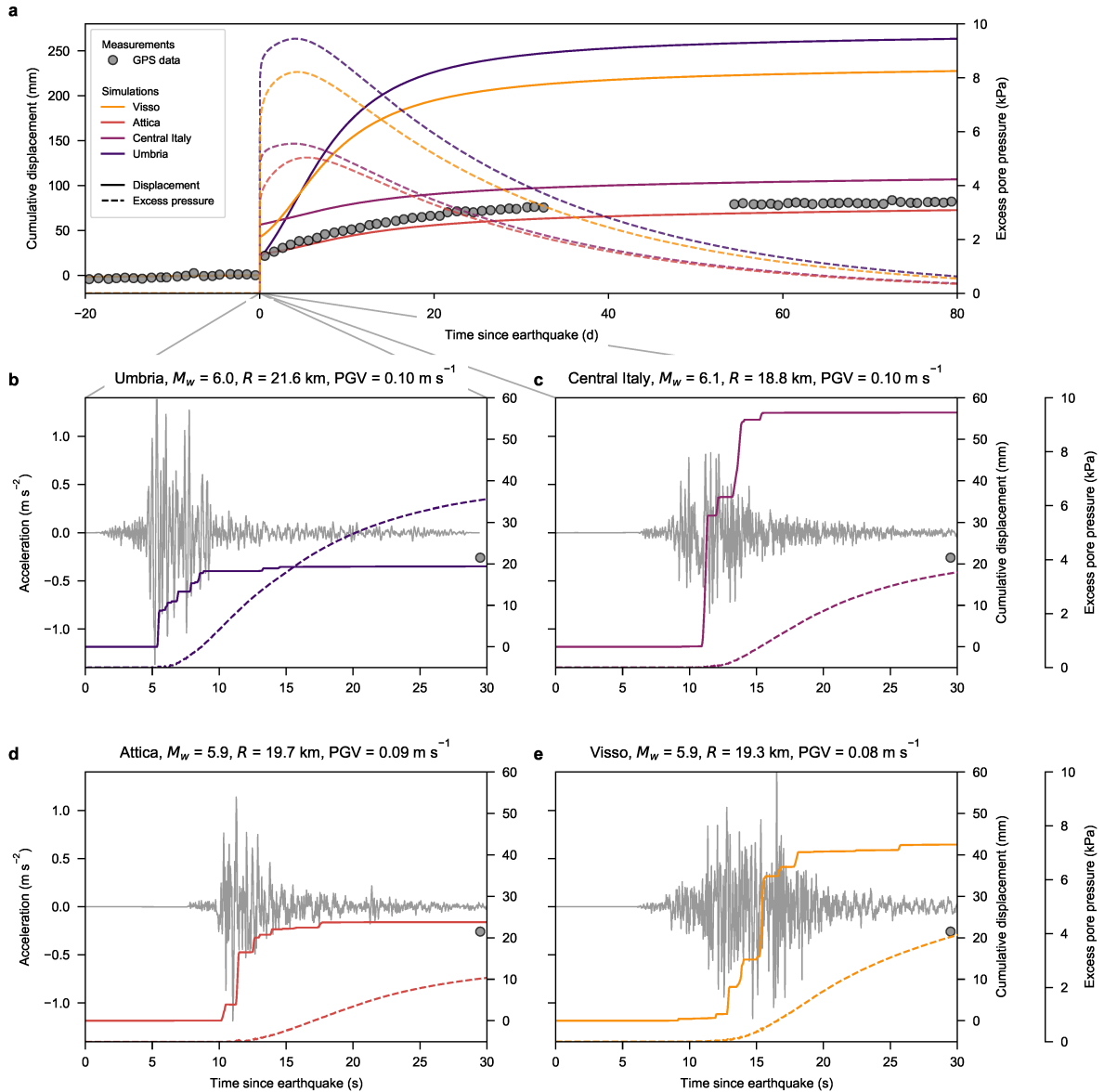
Figure 4.6: Application to the Maca landslide in Peru. (a) Comparison of the GPS measurements (adapted from Lacroix et al. (2014)) and the simulation results for the Maca landslide in Peru. (b)-(e) Zoom into the behaviour during earthquake shaking showing the input ground motion, cumulative displacements and the evolution of excess pore water pressures in the shear zone. The simulation was performed for 4 ground motion signals (rock or stiff soil sites) from earthquakes with similar magnitudes M_w, epicentral distances R and PGVs and were retrieved from the ESM database (Luzi et al., 2020). The parameters and geometry are based on the morphology of the landslide (Zerathe et al., 2016) and are presented in Table 4.1. The permeability of the shear zone and the adjacent soil are calibrated to accurately match the duration of the postseismic period shown by the GPS measurements.

4.3.   Discussion

We proposed a hydro-mechanically coupled finite element landslide model with appropriate constitutive models for shear zones and fine-grained soils under cyclic loading. This allowed us to investigate the potential generation of excess PWP during earthquake shaking and the following diffusion process suggested in various studies as the source of postseismic landslide activity (Bontemps et al., 2020; Lacroix et al., 2022, 2020; Marc et al., 2015; C. Y. Wang & Chia, 2008). In this study, we provide a hydro-mechanical model in support of this hypothesis and show that, for a reasonable choice of parameters, the often-observed postseismic landslide activity can be explained both qualitatively and quantitatively, in spite of the large variation in observed displacements and apparent lack of correlation between their co- and post-seismic components. In an in-depth parametric study, we investigate the underlying mechanisms and identify the most important factors controlling both the coseismic and postseismic motion, which are summarized schematically in Figure 4.7.
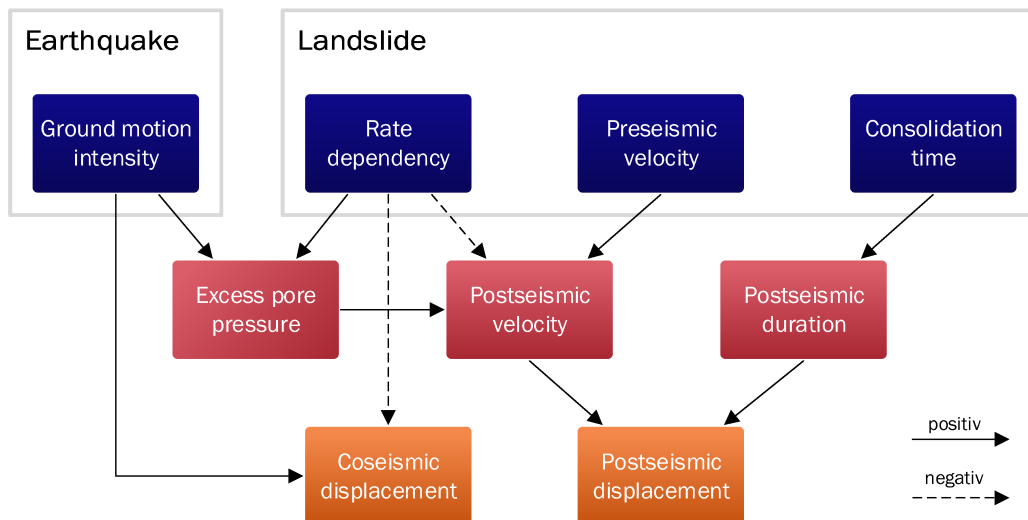
Figure 4.7: Schematic representation of the dependencies for coseismic and postseismic motion. Blue: Input quantities/parameters. Red: Intermediate quantities. Orange: Accumulated coseismic and postseismic displacements. Relations, where an increase of the first parameter/quantity leads to an increase of the second, are marked with a solid line and the opposite with a dashed line.

The comparison with field observation clearly shows that this model can represent the realistic behaviour of active landslides during and after an earthquake. In fact, for the well-documented Maca landslide the model can accurately reproduce the observed evolution of the postseismic motion. A similar trend was also reported for the landslides in Nepal in the weeks following the Gorkha earthquake (Lacroix et al., 2022), which supports the proposed model. However, for a better assessment and validation, more information about the geology and hydrology of the slides in Nepal and Iran is necessary. The presented model can be adapted to various conditions and therefore, the simplified assumptions of a shear zone and the adjacent layers should be seen as a generalization in order to investigate the controlling mechanisms.

The presented model can also explain the observed phenomena of delayed landslides response, which has been mentioned for the Tapgaon slide in Nepal (Lacroix et al., 2022), but has also been observed for other landslide (Agnesi et al., 2005; Jibson et al., 1994; Keefer, 2002). In case of low permeability, the excess PWP developed in the adjacent layers slowly propagates to the shear zone, leading to a delay and a following phase during which the landslide accelerates to the maximal postseismic velocity. This has been shown qualitatively in Figure 4.1 and is somewhat evident in two of the Maca landslide simulations (Figure 4.6a). A longer delay can be expected for a thicker or less permeable shear zone or an additional layer in between the shear zone and the adjacent layer, which is not susceptible for generating excess PWP and simply elongated the propagation distance.

The increased landslide activity over several years after the Central Italy earthquake (Song et al., 2022) is typically attributed to the annual time scale, where other mechanisms are discussed. However, the long-term postseismic duration of several years for less permeable soils, which was shown by the parametric study (Figure 4.4), suggests a possibility of the same mechanism of excess PWP generation. This is supported by the fact that these landslides show the dominant lithology of sandstones and claystones (Song et al., 2022), which are likely to be heavily sheared and fractured around the shear zone and therefore could be susceptible to generating excess PWP. A major finding of this study is that landslides covering a larger area are more likely to accelerate after an earthquake than smaller ones. In the context of the presented model, one can argue that larger landslides are likely to be deeper seated and therefore consist of thicker layers susceptible to generating excess PWP. The same trend has been reported for the size and the runout of the landside and is assumed to be also controlled by pore water pressures (Legros, 2002). In addition, smaller landslides are more prone to boundary effects, such as a faster dissipation of excess PWP in the horizontal direction. To assess whether this scenario is plausible or if this mechanism can at least partially contribute to the observed behaviour, more detailed and specific information on these slides is necessary. Another important factor is the inclination of the landslide, which has not been addressed in this study since a change in slope cannot be performed without simultaneously changing other important parameters. In fact, to keep a steeper landslide in a state of mobile quasi-static equilibrium, a higher friction angle is needed. However, a steeper slide with a higher friction angle occurs in soils with higher content of sand and gravel, which usually show lower rate dependency (Tika et al., 1996). Therefore, it is difficult to compare different inclinations with each other within the limited scope of this paper, presenting, however, an interesting and important topic for the further research.

The landslide model and the gained insight into the underlying physical mechanisms also provide a possibility to investigate the seasonal response of a landslide. Typically, a strong seasonal dependency in the motion of landslides is observed, which is driven by the effect of rainfall and groundwater changes (Alvarado et al., 2019; Bontemps et al., 2020; Handwerger et al., 2019, 2016). The model reaction to a change in the groundwater level could be directly simulated using the proposed model and would even

provide an observation-guided calibration of the model parameters (e.g. rate dependency in the shear zone) (Oberender & Puzrin, 2016). Subjecting the model to earthquake shaking in different seasonal states would then allow for a multi-hazard analysis. Given the identified dependency on the preseismic velocity, the model predicts a larger postseismic velocity and displacement for an earthquake during a more active period of the landslide movements. This is due to the logarithmic rate dependent law applied in the shear zone, where for a larger preseismic velocity, a larger absolute increase in the landslide velocity is necessary to compensate for the same excess PWP in the shear zone. Moreover, this makes a landslide more susceptible to acceleration due to rainfall events after an earthquake, when its velocity is still elevated. This behaviour has been reported in different studies (Bontemps et al., 2020; Song et al., 2022).

Even though not discussed in detail, several related phenomena can be explained by the generation and diffusion of excess PWP outside of the shear zone: reactivation of existing landslides (Keefer, 2002; Lacroix et al., 2022), initiation of new landslides during and after an earthquake (Cheaib et al., 2022; Zhang & Zhang, 2017). These phenomena are analogous to the presented simulations with the subtle difference of starting at a stable state before the earthquake. Once a new landslide is initiated due to generated excess PWP, a state of slow-moving can be reached in case of rate-hardening shear zones (Tika et al., 1996) or other factors increasing the resistance, such as geometrical hardening (Kohler & Puzrin, 2022) or dilative behaviour of the shear zone (Iverson, 2005; Iverson et al., 2000). However, if rate dependent shear strength cannot counterbalance the effect of excess pore water pressures or, even worse, if other softening mechanisms, such as a softening shear zone (Lemos & Vaughan, 2000; Skempton, 1985; G. Wang & Sassa, 2002), rate softening (Tika et al., 1996) or grain crushing (Sadrekarimi & Olson, 2010; Sassa et al., 2014) are caused by intensive shearing, a catastrophic failure could be triggered.

Due to the simplifications of infinite slope conditions, 2- or 3-dimensional effects such as multidirectional flow, geometrical effects (e.g. different behaviour of steeper and flatter parts of the landslide, material accumulation or erosion of the landslide's foot) and landslide runout have not been considered in this study and should be investigated in the future. In addition, the presented methodology should be refined and tested by applying it to further case studies. An ideal measurement setup would be an automated inclinometer (with a high measurement frequency to capture coseismic displacements accurately) in combination with several PWP sensors (close to and around the shear zone). This would allow measuring both the evolution of displacements and PWP during and after an earthquake. Finding a suitable landslide in a seismic active area, installing such a measurement system and capturing a strong enough earthquake, seems, however rather unlikely. Therefore, this topic can be further investigated indirectly by collecting more displacement data from active landslides in seismically active areas using accurate measurement systems (e.g. GNSS, geodetic, extensometers or inclinometers). The lithology of such landslides should be known in order to be able to choose suitable model parameters. Ideally, an

extensive experimental investigation (e.g. cyclic triaxial or simple shear tests) on the soil material from the shear zone and the adjacent layers should be carried out. This would provide an assessment for the potential of generating excess PWP in the adjacent layers. In spite of an acute need for reliable risk assessment, surprisingly few such case studies including a proper site investigation have been reported in the literature. We hope that the proposed physical framework can serve as a basis for future site investigations and field monitoring.

4.4. Methods

4.4.1. Coupled FE model for infinite slope conditions

The basis for the presented methodology is the theory of saturated porous solids under dynamic conditions introduced by Biot (1956, 1962). For earthquake analysis the *u-p*-formulation provides a convenient approximation where the set of equations is written in terms of the soil skeleton deformation $\boldsymbol{u}$ and the pore water pressure *p* (Zienkiewicz, 1984; Zienkiewicz et al., 1980). Assuming infinite slope conditions (Figure 4.1), the governing equations can be considerably simplified since only derivatives with respect to the z-coordinate (perpendicular to the slope inclination) must be considered. The conservation of linear momentum is given as (time derivatives are denoted as $\dot{u} = \frac{\partial u}{\partial t}$ and $\ddot{u} = \frac{\partial^2 u}{\partial t^2}$)

$$\frac{\partial \boldsymbol{\sigma}}{\partial z} + \rho \boldsymbol{b} = \rho \ddot{\boldsymbol{u}} \qquad (4.2)$$

where $\boldsymbol{b}$ is a body force (usually gravity) and ρ the total density. The stress tensor $\boldsymbol{\sigma} = \begin{pmatrix} \sigma \\ \tau \end{pmatrix}$ consists of the normal stress σ and the shear stress τ. The other components of the stress tensors are considered under the assumption of infinite slope condition. The balance of mass is given as

$$\frac{n}{K_w} \dot{p} + \dot{\varepsilon} - \frac{k}{\rho_w g} \frac{\partial^2 p}{\partial z^2} = 0 \qquad (4.3)$$

where *n* is the soil porosity, K_w the bulk modulus of water, *k* the permeability, ρ_w the water density and *g* the gravitational acceleration. The volumetric strain rate of the soil skeleton $\dot{\varepsilon}$ results from the strain tensor for infinite slope conditions (plane strain with a vanishing strain in direction of the slope)

$$\boldsymbol{\varepsilon} = \frac{\partial \boldsymbol{u}}{\partial z} = \begin{pmatrix} \varepsilon \\ \gamma \end{pmatrix} \rightarrow \dot{\boldsymbol{\varepsilon}} = \frac{\partial \dot{\boldsymbol{u}}}{\partial z} = \begin{pmatrix} \dot{\varepsilon} \\ \dot{\gamma} \end{pmatrix} \qquad (4.4)$$

The behaviour of the soil skeleton is introduced by any constitutive model which relates any strain ε to the corresponding effective stresses (von Terzaghi, 1925)

$$\sigma' = \begin{pmatrix} \sigma' \\ \tau \end{pmatrix} = \sigma - p\begin{pmatrix} 1 \\ 0 \end{pmatrix} \tag{4.5}$$

This system of equations (4.2-4.5) is solved by applying a fully implicit dynamic finite element method similar to one-dimensional ground response analyses (Kramer, 1996). The landslide is discretized in finite elements perpendicular to the slope inclination as presented in Figure 4.1, which allows the accurate representation of different soil and rock layers. To minimize the problem of instabilities in the finite element solution of Biot's equations, displacements are approximated with quadratic and pore pressures with linear shape functions (Reed, 1984; Sandhu et al., 1977).

Aside from the gravitational body force, the landslide is subjected to a dynamic earthquake input motion. To prevent downwards propagating waves from being reflected back into the model, the concept of a compliant base boundary is applied (Zienkiewicz et al., 1989). Therefore, viscous dashpot elements are connected at the base of the model to absorb outgoing waves (Lysmer & Kuhlemeyer, 1969). In addition, instead of applying the acceleration time history, the input motion is transformed into a boundary traction in slope parallel direction given by

$$t_s(t) = 2v_{su}(t)\sqrt{\rho G} \tag{4.6}$$

where ρ and G are the density and shear modulus of the base material. v_{su} is the particle velocity of the upwards propagating wave, i.e. half the outcrop motion (Mejia & Dawson, 2006). The parameters used for the different simulations are listed in Table 4.1.

4.4.2. Rate dependent shear zone

The shear zone is modelled by a rate dependent constitutive model. Based on results from ring shear tests on shear zone material (Duong et al., 2018; Scaringi et al., 2018; Tika et al., 1996), the following logarithmic law for the friction coefficient μ is applied

$$\mu = \tan \varphi = \tan \varphi_0 \left(1 + A \bullet \ln \left(\frac{\dot{\gamma} + \dot{\gamma}_0}{\dot{\gamma}_0} \right) \right) \tag{4.7}$$

where φ_0, A and $\dot{\gamma}_0$ are material parameters. This type of relation is often chosen for shear zones in active landslides (Alonso et al., 2016; Handwerger et al., 2016; Puzrin & Schmid, 2011; Wedage et al., 1998), but the reference strain rate $\dot{\gamma}_0$ is also added in the numerator to avoid the singularity in the logarithm (Kohler & Puzrin, 2022).

The strain rate in the shear zone $\dot{\gamma}$ can be linked to the landslide velocity v for a given shear zone thickness h_{shear} as

$$\dot{\gamma} = \frac{\upsilon}{h_{\text{shear}}} \tag{4.8}$$

Based on a given landslide inclination and a reference velocity $\upsilon_0 = \dot{\gamma}_0 h_{\text{shear}}$, the associated reference friction angle φ_0 can be calibrated.

Table 4.1: Parameters used for the simulations.

Parameter	Symbol	Demo (Fig. 4.3)	Study 1 (Fig. 4.4)	Study 2 (Fig. 4.5)	Maca (Fig. 4.6)
Geometry					
Inclination	α		$12°$		
Base thickness	h_{base}		10 m		
Base depth	d_{base}		100 m		
Shear zone depth	d_{shear}		40 m		
Adjacent soil thickness	$h_{\text{adj}} = h$	10 m	var.	20 m	30 m
Shear zone thickness	h_{shear}		0.1 m		
Water table height	h_{w}		30 m		
Mechanical parameters					
P-wave modulus base	M_{base}		15 GPa		
S-wave modulus base	G_{base}		5 GPa		
Density base	ρ_{base}		2700 kg/m^3		
P-wave modulus soil (Hardin & Richart Jr., 1963)	M_{soil}		320 MPa $\bullet (\sigma_0/100kPa)^{0.5}$		
S-wave modulus soil (Hardin & Richart Jr., 1963)	G_{soil}		80 MPa $\bullet (\sigma_0/100kPa)^{0.5}$		
Density soil	ρ_{soil}		2000 kg/m^3		
Permeability					
Permeability base	k_{base}		10^{-6} m/s		
Permeability stable soil and top soil	k_{soil}		10^{-6} m/s		
Permeability shear zone and adjacent soil	k	$0.5 \bullet 10^{-8}$ m/s	var.	10^{-8} m/s	$0.5 \bullet 10^{-8}$ m/s
Shear zone					
Reference velocity	υ_0	1.0 cm/y	0.1 m/y	0.1 m/y	3.1 cm/y
Rate dependency parameter	A	0.01	var.	0.01	0.0043

4.4.3. Constitutive model for cyclic loading of fine-grained soils

In this work, the multisurface model developed by Stoecklin et al. (2020) is applied. For the integration in the presented numerical framework, the model is simplified by a two-dimensional formulation for the applied infinite landslide conditions, but can easily be transferred to the application of finite slope geometries using the implementation presented by Stoecklin et al. (2020). In the following, the basic equations of the model are presented with an emphasis on the two-dimensional formulation and a slight change in the original formulation also allowing for dilative behaviour. For more details on the model and its implementation the reader is referred to Stoecklin et al. (2020).

Based on the general multisurface framework developed by Prevost (1985) with n_y-nested yield surfaces $f^1, \ldots, f^k, \ldots, f^{n_y}$ with frictional, linear, kinematic hardening (Figure 4.8a) the yield function for the kth surface has the form

$$f^k = |\tau - \alpha^k \sigma'| - \mu^k \sigma' = 0 \tag{4.9}$$

where, for a two dimensional formulation, the backstress tensor is reduced to the scalar kinematic hardening variable α^k. The size of the yield surface μ^k is given by

$$\mu^k = \eta^k \mu = \eta^k \tan \varphi \tag{4.10}$$

where $\mu = \tan \varphi$ defines the failure surface by the friction angle φ. The internal coordinate η^k is linearly spaced between the innermost surface ($\eta^1 > 0$), bounding the elastic region, and the failure surface ($\eta^{n_y} = 1$). Both the volumetric strain rate $\dot{\varepsilon}$ and the shear strain rate $\dot{\gamma}$ are assumed to be decomposable into an elastic and plastic contribution

$$\dot{\varepsilon} = \dot{\varepsilon}^e + \dot{\varepsilon}^p \tag{4.11}$$

$$\dot{\gamma} = \dot{\gamma}^e + \dot{\gamma}^p \tag{4.12}$$

where the superscripts e and p denote the elastic and the plastic part. The elastic contribution is described by linear and isotropic elasticity. The normal and shear stresses hence follow as

$$\sigma = M\varepsilon \tag{4.13}$$

$$\tau = G\gamma \tag{4.14}$$

where M and G denote the constrained or P-wave modulus and the shear or S-wave modulus respectively. Following the approach by Elgamal et al. (2003), the flow rule on each surface has an associative deviatoric and a nonassociative volumetric component

$$\dot{\gamma}^{p,k} = \lambda^k \hat{n} \tag{4.15}$$

$$\dot{\varepsilon}^{p,k} = -\beta^k \lambda^k \tag{4.16}$$

where $\dot{\lambda}^k$ is the plastic multiplier and $\hat{n}$ is equal 1 or -1 for flow at the top or bottom yield surface respectively. The shear-volumetric coupling is controlled by the flow variable β^k, where a negative value results in contractive and a positive in dilative plastic strains on the corresponding yield surface. The total strain increment is given by the sum of the elastic increment and the contribution of all active surfaces

$$\dot{\varepsilon} = \dot{\varepsilon}^e + \sum_k \dot{\varepsilon}^{p,k} = \dot{\varepsilon}^e - \sum_k \beta^k \dot{\lambda}^k \tag{4.17}$$

$$\dot{\gamma} = \dot{\gamma}^e + \sum_k \dot{\gamma}^{p,k} = \dot{\gamma}^e + \sum_k \dot{\lambda}^k \hat{n} \tag{4.18}$$

The hardening is governed by a purely deviatoric, linear hardening rule

$$\dot{\alpha}^k = h^k \dot{\lambda}^k \hat{n} \tag{4.19}$$

where h^k is the hardening modulus. To control the behaviour of the model, both the flow variable β^k and the hardening modulus h^k can be defined for each yield surface independently. The latter is defined according to Stoecklin et al. (2020) by the hardening function

$$h^k = h_0 n_y \left(1 - \eta^k\right)^b \tag{4.20}$$

where h_0 and b are hardening parameters. The total number of yield surfaces n_y is included to avoid a dependency of the hardening parameters on the chosen number of surfaces. As shown by Stoecklin et al. (2020) the hardening parameters allow to match the model response to stress-strain curves from simple shear tests or to modulus reduction and material damping curves. The flow variable is defined slightly differently as originally proposed to also account for the dilative behaviour often observed in fine-grained soils

$$\beta^k = \begin{cases} \beta_c \bullet \max \left(\dfrac{\varepsilon_f^p - \varepsilon^p}{\varepsilon_f^p}, \left(\zeta_f\right)^{1/c} \right)^c - \dfrac{\hat{\varepsilon}^p}{\hat{\varepsilon}_{ref}^p} & \eta^k \leq \eta_p \\ \beta_d & \eta^k > \eta_p \end{cases} \tag{4.21}$$

where $\beta_c < 0$ defines the contraction associated with the initial state of the material for the yield surface with an internal coordinate below η_p and $\beta_d > 0$ controls the dilation for the surfaces above. The dependency on the accumulated plastic volumetric strain $\hat{\varepsilon}^p$ leads to a diminishing of an initial contraction β_c to residual contraction of $\zeta_f \beta_c$ at the accumulated plastic volumetric strain ε_f^p and can be controlled by parameter c. Additionally, the cyclic contraction potential $\hat{\varepsilon}^p$ is introduced as

$$\hat{\varepsilon}^p = \int \dot{\alpha}^p dt \quad \text{with} \quad \dot{\alpha}^p = \begin{cases} \dot{\varepsilon}^p & \text{if } \dot{\hat{\varepsilon}}^p \geq 0 \\ 0 & \text{else} \end{cases} \tag{4.22}$$

Hence the cyclic contraction potential grows if the material is dilating and decreases to a minimal value of zero in case of contraction. Including this contraction potential into equation 4.21 results in the butterfly-like shape for undrained cyclic tests and can be controlled by the parameter $\hat{\varepsilon}^{p}_{ref}$.
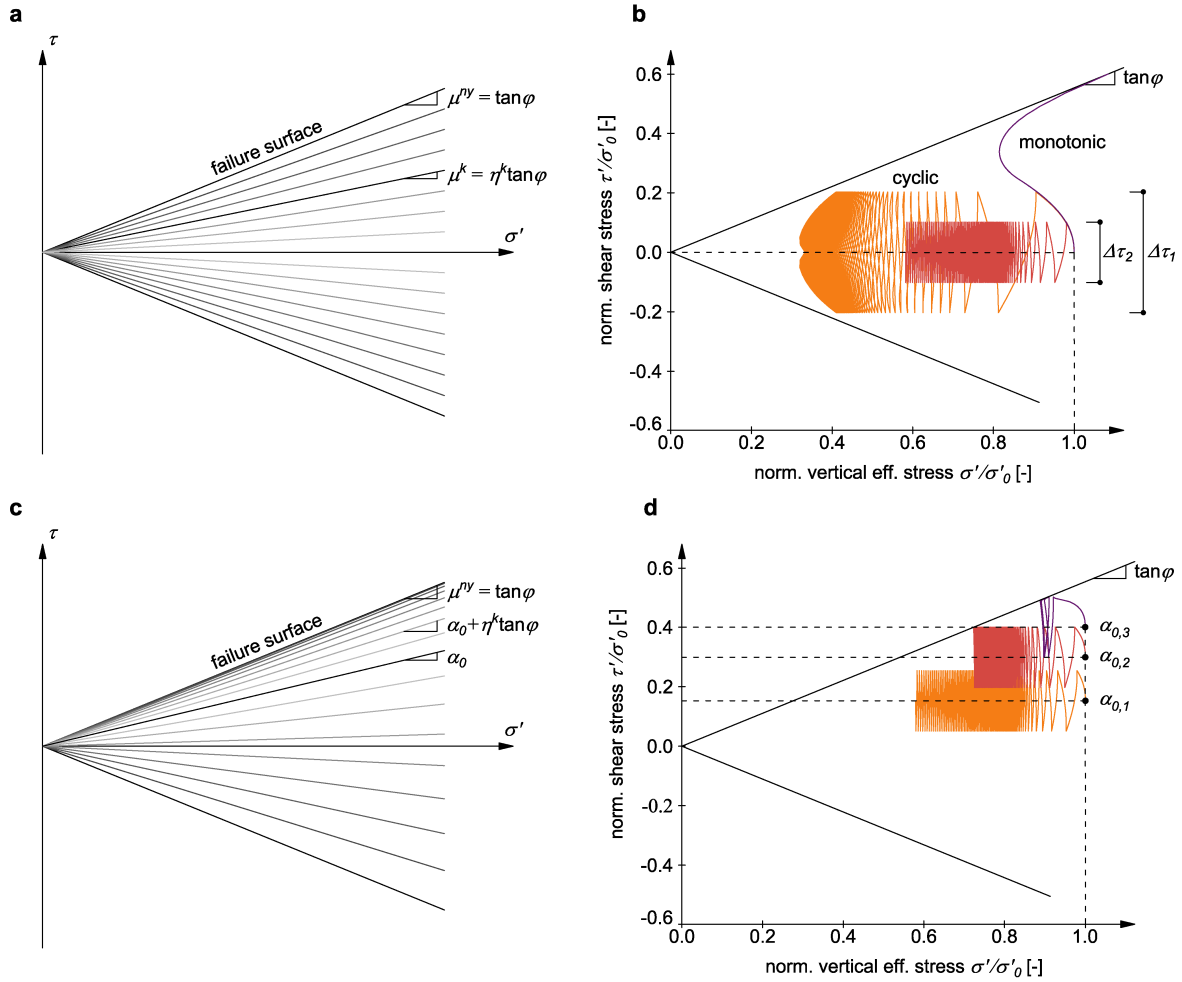
Figure 4.8: Constitutive model for cyclic loading of fine-grained soils. (a) Illustration of the multi-yield surface model. (b) Model response for a monotonic and two cyclic undrained tests with different stress amplitudes (80 cylices). (c) Illustration of the initial arrangement of the yield surfaces after anisotropic consolidation. (d) Model response for cyclic undrained tests for different anisotropic consolidation stresses (80 cycles).

Figure 4.8b shows the model response for a monotonic and two cyclic undrained tests with different stress amplitudes using the parameters presented in Table 4.2. To take into account the effect of anisotropic consolidation, the yield surfaces are rotated by specifying an initial value of the corresponding hardening variable α_0^k (Figure 4.8c), which is often referred to as a "memory" variable (Prevost, 1985) and given as

$$\alpha_0^k = \alpha_0 \left(1 - \left(\eta^k \right)^{\frac{\tan\varphi}{\alpha_0}} \right) \tag{4.23}$$

113

where the consolidation stress ratio is given as $\alpha_0 = \tau_0/\sigma_0'$. The model response for cyclic undrained tests for different anisotropic consolidation stresses is shown in Figure 4.8d using the same parameters presented in Table 4.2. The same set of parameters are used for all the landslide simulations.

Table 4.2: Parameters used for the simulation of fine grained soils

Parameter	Symbol	Value
Elasticity		
Constrained or P-wave modulus	M	320 MPa $\bullet$ $(\sigma_0/100\ kPa)^{0.5}$
Shear or S-wave modulus	G	80 MPa $\bullet$ $(\sigma_0/100\ kPa)^{0.5}$
Hardening		
Hardening parameter	h_0	10.0
Hardening parameter	b	2.1
Volumetric behaviour		
Contraction parameter	β_c	$-22.0 \bullet \sigma_0/M$
Dilation parameter	β_d	$2.2 \bullet \sigma_0/M$
Threshold coordinate	η_p	0.5
Accumulated plastic volumetric strain at full degradation	ε_f^p	$0.44 \bullet \sigma_0/M$
Contraction degradation factor	ζ_f	2%
Contraction degradation parameter	c	3.0
Reference contraction potential	$\hat{\varepsilon}_{ref}^p$	$0.24 \bullet \sigma_0/M$
Failure		
Inclination of failure surface	$\mu = \tan\varphi$	0.55

Acknowledgments

Notations

Small Latin letters

$\boldsymbol{b}$	body force vector	h_w	water table height
b	hardening parameter	k	permeability
c	contraction degradation parameter	$\widehat{n}$	direction of flow
d_base	base depth	n_y	total number of yield surfaces
d_{co}	coseismic displacement	p	pore water pressure
e	porosity	t	time
e_{crit}	critical state porosity	t_{delay}	delay time of maximal postseismic activity
e_{pre}	preseismic porosity	t_{post}	duration of postseismic activity
e_{post}	postseismic porosity	t_s	ground motion traction boundary
f^k	yield function k	$\boldsymbol{u}$	deformation vector
g	gravitational acceleration	υ	velocity
$h = h_{adj}$	thickness of adjacent layers	υ_0	reference velocity
h_0	hardening parameter	υ_{max}^{post}	maximal postseismic velocity
h_base	base thickness	υ_{pre}	preseismic velocity
h^k	hardening modulus of yield surface k	υ_{su}	particle velocity of the upwards propagating shear wave
h_shear	shear zone thickness		

Capital Latin letters

A	rate dependency parameter	M_w	earthquake magnitude
G	S-wave / shear modulus	PGV	peak ground velocity
K_w	bulk modulus of water	R	epicentral distance
M	P-modulus/ constrained modulus	T	characteristic consolidation time

Small Greek letter

α^k	kinematic hardening variable of yield surface k	η_p	threshold coordinate
α_0	consolidation stress ratio	λ^k	plastic multiplier of yield surface k
β_c	contraction parameter	μ	friction coefficient
β_d	dilation parameter	μ_0	reference friction coefficient
β^k	flow variable of yield surface k	ρ	density
γ	shear strain	ρ_w	density of water
$\dot{\gamma}_0$	reference strain rate	$\boldsymbol{\sigma}$	total stress tensor
γ^e, γ^p	elastic / plastic shear strain	σ	normal stress
γ_w	specific weight of water	$\boldsymbol{\sigma}'$	effective stress tensor
$\boldsymbol{\varepsilon}$	strain tensor	σ'	effective normal stress
ε	volumetric strain	$\sigma_{post}^{'min}$	minimal postseismic effective stress
$\varepsilon^e, \varepsilon^p$	elastic / plastic volumetric strain	τ	shear stress
$\widehat{\varepsilon}^\mathrm{p}$	contraction potential	τ_{co}^{max}	maximal coseismic shear stress
$\widehat{\varepsilon}_\mathrm{ref}^\mathrm{p}$	reference contraction potential	φ	friction angle
ζ_f	contraction degradation factor	φ_0	reference friction angle
η^k	internal coordinate of yield surface k		

References

Agnesi, V., Camarda, M., Conoscenti, C., Di Maggio, C., Serena Diliberto, I., Madonia, P. & Rotigliano, E. (2005). A multidisciplinary approach to the evaluation of the mechanism that triggered the Cerda landslide (Sicily, Italy). *Geomorphology*, *65*(1–2), 101–116. https://doi.org/10.1016/J.GEOMORPH.2004.08.003

Alonso, E. E., Zervos, A. & Pinyol, N. M. (2016). Thermo-poro-mechanical analysis of landslides: from creeping behaviour to catastrophic failure. *Géotechnique*, *66*(3), 202–219. https://doi.org/10.1680/jgeot.15.LM.006

Alvarado, M., Pinyol, N. M. & Alonso, E. E. (2019). Landslide motion assessment including rate effects and thermal interactions: Revisiting the canelles landslide. *Canadian Geotechnical Journal*, *56*(9), 1338–1350. https://doi.org/10.1139/cgj-2018-0779

Bekaert, D. P. S., Handwerger, A. L., Agram, P. & Kirschbaum, D. B. (2020). InSAR-based detection method for mapping and monitoring slow-moving landslides in remote regions with steep and mountainous terrain: An application to Nepal. *Remote Sensing of Environment*, *249*, 111983. https://doi.org/10.1016/J.RSE.2020.111983

Biot, M. A. (1956). Theory of Propagation of Elastic Waves in a Fluid-Saturated Porous Solid. *Journal of the Acoustical Society of America*, *28*(2), 168–178. https://doi.org/10.1121/1.1908239

Biot, M. A. (1962). Mechanics of deformation and acoustic propagation in porous media. *Journal of Applied Physics*, *33*(4), 1482–1498. https://doi.org/10.1063/1.1728759

Bontemps, N., Lacroix, P., Larose, E., Jara, J. & Taipe, E. (2020). Rain and small earthquakes maintain a slow-moving landslide in a persistent critical state. *Nature Communications*, *11*(1), 1–10. https://doi.org/10.1038/s41467-020-14445-3

Bonzanigo, L., Eberhardt, E. & Loew, S. (2007). Long-term investigation of a deep-seated creeping landslide in crystalline rock. Part I. Geological and hydromechanical factors controlling the Campo Vallemaggia landslide. *Canadian Geotechnical Journal*, *44*(10), 1157–1180. https://doi.org/10.1139/T07-043

Boulanger, R. W. & Idriss, I. M. (2006). Liquefaction Susceptibility Criteria for Silts and Clays. *Journal of Geotechnical and Geoenvironmental Engineering*, *132*(11), 1413–1426. https://doi.org/10.1061/(ASCE)1090-0241(2006)132:11(1413)

Cheaib, A., Lacroix, P., Zerathe, S., Jongmans, D., Ajorlou, N., Doin, M. P., … Abdallah, C. (2022). Landslides induced by the 2017 Mw7.3 Sarpol Zahab earthquake (Iran). *Landslides*, *19*(3), 603–619. https://doi.org/10.1007/S10346-021-01832-0

Comegna, L., Picarelli, L. & Urciuoli, G. (2007). The mechanics of mudslides as a cyclic undrained-drained process. *Landslides*, *4*(3), 217–232. https://doi.org/10.1007/S10346-007-0083-2

Corominas, J., Moya, J., Ledesma, A., Lloret, A. & Gili, J. A. (2005). Prediction of ground displacements and velocities from groundwater level changes at the Vallcebre landslide (Eastern Pyrenees, Spain). *Landslides*, *2*(2), 83–96. https://doi.org/10.1007/S10346-005-0049-1

Di Maio, C., De Rosa, J., Vassallo, R., Coviello, R. & Macchia, G. (2020). Hydraulic conductivity and pore water pressures in a clayey landslide: Experimental data. *Geosciences (Switzerland)*, *10*(3). https://doi.org/10.3390/GEOSCIENCES10030102

Duong, N. T., Suzuki, M. & Van Hai, N. (2018). Rate and acceleration effects on residual strength of kaolin and kaolin–bentonite mixtures in ring shearing. *Soils and Foundations*, *58*(5), 1153–1172. https://doi.org/10.1016/J.SANDF.2018.05.011

Elgamal, A., Yang, Z., Parra, E. & Ragheb, A. (2003). Modeling of cyclic mobility in saturated cohesionless soils. *International Journal of Plasticity*, *19*(6), 883–905. https://doi.org/10.1016/S0749-6419(02)00010-4

Ferretti, A., Fruzzetti, V. M. E., Ruggeri, P. & Scarpelli, G. (2019). Seismic induced displacements of "La Sorbella" landslide (Italy).

Froude, M. J. & Petley, D. N. (2018). Global fatal landslide occurrence from 2004 to 2016. *Natural Hazards and Earth System Sciences*, *18*(8), 2161–2181. https://doi.org/10.5194/NHESS-18-2161-2018

Handwerger, A. L., Fielding, E. J., Huang, M. H., Bennett, G. L., Liang, C. & Schulz, W. H. (2019). Widespread Initiation, Reactivation, and Acceleration of Landslides in the Northern California Coast Ranges due to Extreme Rainfall. *Journal of Geophysical Research: Earth Surface*, *124*(7), 1782–1797. https://doi.org/10.1029/2019JF005035

Handwerger, A. L., Rempel, A. W., Skarbek, R. M., Roering, J. J. & Hilley, G. E. (2016). Rate-weakening friction characterizes both slow sliding and catastrophic failure of landslides. *Proceedings of the National Academy of Sciences*, *113*(37), 10281–10286. https://doi.org/10.1073/pnas.1607009113

Hardin, B. O. & Richart Jr., F. E. (1963). Elastic Wave Velocities in Granular Soils. *Journal of the Soil Mechanics and Foundations Division*, *89*(1), 33–65. https://doi.org/10.1061/JSFEAQ.0000493

Hendron, A. J. & Patton, F. D. (1987). The vaiont slide — A geotechnical analysis based on new geologic observations of the failure surface. *Engineering Geology*, *24*(1–4), 475–491. https://doi.org/10.1016/0013-7952(87)90080-9

Hungr, O., Leroueil, S. & Picarelli, L. (2014). The Varnes classification of landslide types, an update. *Landslides*, *11*(2), 167–194. https://doi.org/10.1007/S10346-013-0436-Y

Islam, N., Hawlader, B., Wang, C. & Soga, K. (2019). Large-deformation finite-element modelling of earthquake-induced landslides considering strain-softening behaviour of sensitive clay. *Canadian Geotechnical Journal*, *56*(7), 1003–1018. https://doi.org/10.1139/cgj-2018-0250

Iverson, R. M. (2005). Regulation of landslide motion by dilatancy and pore pressure feedback. *Journal of Geophysical Research: Earth Surface*, *110*(2), 2015. https://doi.org/10.1029/2004JF000268

Iverson, R. M., Reid, M. E., Iverson, N. R., LaHusen, R. G., Logan, M., Mann, J. E. & Brien, D. L. (2000). Acute sensitivity of landslide rates to initial soil porosity. *Science*, *290*(5491), 513–516. https://doi.org/10.1126/science.290.5491.513

Jibson, R. W. (2011). Methods for assessing the stability of slopes during earthquakes-A retrospective. *Engineering Geology*, *122*(1–2), 43–50. https://doi.org/10.1016/j.enggeo.2010.09.017

Jibson, R. W., Prentice, C. S., Borissoff, B. A., Rogozhin, E. A. & Langer, C. J. (1994). Some observations of landslides triggered by the 29 April 1991 Racha earthquake, Republic of Georgia. *Bulletin Seismological Society of America*, *84*(4), 963–973.

Keefer, D. K. (2002). Investigating landslides caused by earthquakes - A historical review. *Surveys in Geophysics*, *23*(6), 473–510. https://doi.org/10.1023/A:1021274710840

Kohler, M. & Puzrin, A. M. (2022). Mechanism of Co-Seismic Deformation of the Slow-Moving La Sorbella Landslide in Italy Revealed by MPM Analysis. *Journal of Geophysical Research: Earth Surface*, *127*(7), e2022JF006618. https://doi.org/10.1029/2022JF006618

Kramer, S. L. (1996). *Geotechnical Earthquake Engineering. Engineering* (Vol. 6). https://doi.org/10.1007/978-3-540-35783-4

Lacroix, P., Gavillon, T., Bouchant, C., Lavé, J., Mugnier, J. L., Dhungel, S. & Vernier, F. (2022). SAR and optical images correlation illuminates post-seismic landslide motion after the Mw 7.8 Gorkha earthquake (Nepal). *Scientific Reports*, *12*(1), 1–13. https://doi.org/10.1038/s41598-022-10016-2

Lacroix, P., Handwerger, A. L. & Bièvre, G. (2020). Life and death of slow-moving landslides. *Nature Reviews Earth and Environment*, *1*(8), 404–419. https://doi.org/10.1038/S43017-020-0072-8

Lacroix, P., Perfettini, H., Taipe, E. & Guillier, B. (2014). Coseismic and postseismic motion of a landslide: observations, modelling, and analogy with tectonic faults. *Geophysical Research Letters*, *41*, 6676–6680. https://doi.org/10.1002/2014GL061170

Legros, F. (2002). The mobility of long-runout landslides. *Engineering Geology*, *63*(3–4), 301–331. https://doi.org/10.1016/S0013-7952(01)00090-4

Lemos, L. J. (2004). Shear Behaviour of Pre-Existing Shear Zones Under Fast Loading. *Advances in Geotechnical Engineering: The Skempton Conference*, (1981).

Lemos, L. J. & Vaughan, P. R. (2000). Clay - interface shear resistance. *Géotechnique*, *50*(1), 55–64.

Luzi, L., Lanzano, G., Felicetta, C., D'Amico, C. M., Russo, E., Sgobba, S., … Group, O. W. (2020). Engineering Strong Motion database (ESM) (Version 2.0). https://doi.org/10.13127/ESM.2

Lysmer, J. & Kuhlemeyer, R. L. (1969). Finite Difference Model for Infinite Media. *Journal of Engineering Mechanics*, *95*, 859–877.

Marc, O., Hovius, N., Meunier, P., Uchida, T. & Hayashi, S. (2015). Transient changes of landslide rates after earthquakes. *Geology*, *43*(10), 883–886. https://doi.org/10.1130/G36961.1

Mejia, L. H. & Dawson, E. M. (2006). Earthquake deconvolution for FLAC. *Proceedings of the 4th International FLAC Symposium on Numerical Modeling in Geomechanics*, (1969), 1–9.

Miao, H. & Wang, G. (2022). Shear rate effect on the residual strength of saturated clayey and granular soils under low- to high-rate continuous shearing. *Engineering Geology*, *308*, 106821. https://doi.org/10.1016/J.ENGGEO.2022.106821

Newmark, N. M. (1965). Effects of Earthquakes on Dams and Embankments. *Géotechnique*, *15*(2), 139–160. https://doi.org/10.1680/geot.1965.15.2.139

Oberender, P. W. (2018). *Creeping Constrained Landslides Under Extreme Environmental and Seismic Conditions*. ETH Zurich. https://doi.org/10.3929/ETHZ-B-000275247

Oberender, P. W. & Puzrin, A. M. (2016). Observation-guided constitutive modelling for creeping landslides. *Géotechnique*, *66*(3), 232–247. https://doi.org/10.1680/jgeot.15.LM.003

Picarelli, L., Olivares, L., Comegna, L. & Damiano, E. (2008). Mechanical aspects of flow-like movements in granular and fine grained soils. *Rock Mechanics and Rock Engineering*, *41*(1), 179–197. https://doi.org/10.1007/S00603-007-0135-X

Pinyol, N. M., Di Carluccio, G. & Alonso, E. E. (2022). A slow and complex landslide under static and seismic action. *Engineering Geology*, *297*, 106478. https://doi.org/10.1016/j.enggeo.2021.106478

Prevost, J. H. (1985). A simple plasticity theory for frictional cohesionless soils. *International Journal of Soil Dynamics and Earthquake Engineering*, *4*(1), 9–17. https://doi.org/10.1016/0261-7277(85)90030-0

Puzrin, A. M. & Schmid, A. (2011). Progressive failure of a constrained creeping landslide. *Proceedings of the Royal Society A: Mathematical, Physical and Engineering Sciences*, *467*(2133), 2444–2461. https://doi.org/10.1098/rspa.2011.0063

Puzrin, A. M. & Schmid, A. (2012). Evolution of stabilised creeping landslides. *Géotechnique*, *62*(6), 491–501. https://doi.org/10.1680/geot.11.P.041

Reed, M. B. (1984). An investigation of numerical errors in the analysis of consolidation by finite elements. *International Journal for Numerical and Analytical Methods in Geomechanics*, *8*(3), 243–257. https://doi.org/10.1002/NAG.1610080304

Rodríguez, C. E., Bommer, J. J. & Chandler, R. J. (1999). Earthquake-induced landslides: 1980-1997. *Soil Dynamics and Earthquake Engineering*, *18*(5), 325–346. https://doi.org/10.1016/S0267-7261(99)00012-3

Roscoe, K. H., Schofield, A. N. & Wroth, C. P. (1958). On the yielding of soils. *Geotechnique*, *8*(1), 22–53. https://doi.org/10.1680/geot.1958.8.1.22

Rosone, M., Ziccarelli, M., Ferrari, A. & Farulla, C. A. (2018). On the reactivation of a large landslide induced by rainfall in highly fissured clays. *Engineering Geology*, *235*, 20–38. https://doi.org/10.1016/J.ENGGEO.2018.01.016

Ruggeri, P., Fruzzetti, V. M. E., Ferretti, A. & Scarpelli, G. (2020). Seismic and Rainfall Induced Displacements of an Existing Landslide: Findings from the Continuous Monitoring. *Geosciences 2020, Vol. 10, Page 90*, *10*(3), 90. https://doi.org/10.3390/GEOSCIENCES10030090

Sadrekarimi, A. & Olson, S. M. (2010). Particle damage observed in ring shear tests on sands. *Canadian Geotechnical Journal*, *47*(5), 497–515. https://doi.org/10.1139/T09-117

Salcedo, D. A. (2009). Behavior of a landslide prior to inducing a viaduct failure, Caracas–La Guaira highway, Venezuela. *Engineering Geology*, *109*(1–2), 16–30. https://doi.org/10.1016/J.ENGGEO.2009.02.001

Sandhu, R. S., Liu, H. & Singh, K. J. (1977). Numerical performance of some finite element schemes for analysis of seepage in porous elastic media. *International Journal for Numerical and Analytical Methods in Geomechanics*, *1*(2), 177–194. https://doi.org/10.1002/NAG.1610010205

Sassa, K., Canuti, P. & Yin, Y. (2014). *Landslide science for a safer geoenvironment. Landslide Science for a Safer Geoenvironment* (Vol. 1). https://doi.org/10.1007/978-3-319-04999-1

Scaringi, G., Hu, W., Xu, Q. & Huang, R. (2018). Shear-Rate-Dependent Behavior of Clayey Bimaterial Interfaces at Landslide Stress Levels. *Geophysical Research Letters*, *45*(2), 766–777. https://doi.org/10.1002/2017GL076214

Schofield, A. N. & Wroth, C. P. (1968). *Critical state soil mechanics*. McGraw-Hill.

Schulz, W. H., Kean, J. W. & Wang, G. (2009). Landslide movement in southwest Colorado triggered by atmospheric tides. *Nature Geoscience 2009 2:12*, *2*(12), 863–866. https://doi.org/10.1038/ngeo659

Schulz, W. H. & Wang, G. (2014). Residual shear strength variability as a primary control on movement of landslides reactivated by earthquake-induced ground motion: Implications for coastal Oregon, U.S. *Journal of Geophysical Research: Earth Surface*, *119*(7), 1617–1635. https://doi.org/10.1002/2014JF003088

Skempton, A. W. (1985). Residual strength of clays in landslides, folded strata and the laboratory. *Géotechnique*, *35*(1), 3–18. https://doi.org/10.1680/geot.1985.35.1.3

Song, C., Yu, C., Li, Z., Utili, S., Frattini, P., Crosta, G. & Peng, J. (2022). Triggering and recovery of earthquake accelerated landslides in Central Italy revealed by satellite radar observations. *Nature Communications*, *13*(1), 1–12. https://doi.org/10.1038/s41467-022-35035-5

Stoecklin, A., Friedli, B. & Puzrin, A. M. (2020). A multisurface kinematic hardening model for the behavior of clays under combined static and undrained cyclic loading. *International Journal for Numerical and Analytical Methods in Geomechanics*, nag.3149. https://doi.org/10.1002/nag.3149

Tika, T. E., Vaughan, P. R. & Lemos, L. J. (1996). Fast shearing of pre-existing shear zones in soil. *Géotechnique*, *46*(2), 197–233. https://doi.org/10.1680/geot.1996.46.2.197

van Asch, T. W. J., Van Beek, L. P. H. & Bogaard, T. A. (2007). Problems in predicting the mobility of slow-moving landslides. *Engineering Geology*, *91*(1), 46–55. https://doi.org/10.1016/J.ENGGEO.2006.12.012

Vardoulakis, I. (2000). Catastrophic landslides due to frictional heating of the failure plane. *Mechanics of Cohesive-Frictional Materials*, *5*(6), 443–467. https://doi.org/10.1002/1099-1484(200008)5:6<443::AID-CFM104>3.0.CO;2-W

von Terzaghi, K. (1925). *Erdbaumechanik auf bodenphysikalischer Grundlage*. Leipzig-Wien: Franz Deuticke.

Wang, C. Y. & Chia, Y. (2008). Mechanism of water level changes during earthquakes: Near field versus intermediate field. *Geophysical Research Letters*, *35*(12), 12402. https://doi.org/10.1029/2008GL034227

Wang, G. & Sassa, K. (2002). Post-failure mobility of saturated sands in undrained load-controlled ring shear tests. *Canadian Geotechnical Journal*, *39*(4), 821–837. https://doi.org/10.1139/t02-032

Wedage, A. M. P., Morgenstern, N. R. & Chan, D. H. (1998). A strain rate dependent constitutive model for clays at residual strength. *Canadian Geotechnical Journal*, *35*(2), 364–373. https://doi.org/10.1139/t97-085

Zerathe, S., Lacroix, P., Jongmans, D., Marino, J., Taipe, E., Wathelet, M., … Tatard, L. (2016). Morphology, structure and kinematics of a rainfall controlled slow-moving Andean landslide, Peru. *Earth Surface Processes and Landforms*, *41*(11), 1477–1493. https://doi.org/10.1002/ESP.3913

Zhang, S. & Zhang, L. M. (2017). Impact of the 2008 Wenchuan earthquake in China on subsequent long-term debris flow activities in the epicentral area. *Geomorphology*, *276*, 86–103. https://doi.org/10.1016/J.GEOMORPH.2016.10.009

Zienkiewicz, O. C. (1984). Dynamic behaviour of saturated porous media; The generalized Biot formulation and its numerical solution .pdf. *International Journal for Numerical and Analytical Methods in Geomechanics*.

Zienkiewicz, O. C., Bicanic, N. & Shen, F. Q. (1989). Earthquake Input Definition and the Trasmitting Boundary Conditions. In *Advances in Computational Nonlinear Mechanics* (pp. 109–138). Vienna: Springer Vienna. https://doi.org/10.1007/978-3-7091-2828-2_3

Zienkiewicz, O. C., Chang, C. T. & Bettess, P. (1980). Drained, undrained, consolidating and dynamic behaviour assumptions in soils. *Geotechnique*, *30*(4), 385–395. https://doi.org/10.1680/geot.1980.30.4.385

Appendix 4.1 – Set of input motions used for simulations

Table 4.3: Set of input motions (N and E direction) used in Figure 4.5 (retrieved from Engineering Strong Motion (ESM) datbase (Luzi et al., 2020))

ESM ID	ESM ID	ESM ID
A-A006-INT-UT19990920_174715	A- EHC0-INT-UT19990920_174715	SM-112-IS-2000-0053
A-A007-INT-UT19990920_174715	A-F003-INT-UT19990920_174715	IV-EVRN-EMSC-20181226_0000014
A-A010-INT-UT19990920_174715	A-F006-INT-UT19990920_174715	IT-NRC-EMSC-20161026_0000077
A-A014-INT-UT19990920_174715	A-F020-INT-UT19990920_174715	A-C034-INT-UT19991022_021856
A-A051-INT-UT19990920_174715	A-F022-INT-UT19990920_174715	A-C006-INT-UT19991022_021856
A-A077-INT-UT19990920_174715	A-F023-INT-UT19990920_174715	IT-BGI-IT-1980-0012
A-A098-INT-UT19990920_174715	A-F024-INT-UT19990920_174715	HI-KAL2-GR-1986-0011
A-B017-INT-UT19990920_174715	A-F028-INT-UT19990920_174715	IT-NOR-EMSC-20161026_0000095
A-B018-INT-UT19990920_174715	A-F031-INT-UT19990920_174715	3A-MZ27-EMSC-20161030_0000029
A-B031-INT-UT19990920_174715	A-F033-INT-UT19990920_174715	HI-ARG2-EMSC-20140203_0000008
A-B035-INT-UT19990920_174715	A-F034-INT-UT19990920_174715	IV-T1299-EMSC-20161030_0000029
A-B046-INT-UT19990920_174715	A-F038-INT-UT19990920_174715	A-C034-INT-UT19991022_021856
A-B048-INT-UT19990920_174715	A-F041-INT-UT19990920_174715	3A-MZ11-EMSC-20161030_0000029
A-B057-INT-UT19990920_174715	A-F045-INT-UT19990920_174715	IT-VAL-EMSC-20160824_0000006
A-B060-INT-UT19990920_174715	A-F048-INT-UT19990920_174715	IT-VAL-EMSC-20161030_0000029
A-B081-INT-UT19990920_174715	A-F059-INT-UT19990920_174715	IT-VAL-EMSC-20161026_0000095
A-B094-INT-UT19990920_174715	A-F060-INT-UT19990920_174715	IT-ASS-IT-1997-0006
A-B096-INT-UT19990920_174715	A-G028-INT-UT19990920_174715	HL-MRNA-GR-1995-0047
A-B100-INT-UT19990920_174715	A-G041-INT-UT19990920_174715	IT-ACC-EMSC-20170118_0000034
A-B104-INT-UT19990920_174715	IT-RQT-EMSC-20161026_0000077	A-C081-INT-UT19991022_021856
A-B105-INT-UT19990920_174715	RA-BERA-EMSC-20071129_0000090	HI-ATH4-GR-1999-0001
A-B118-INT-UT19990920_174715	RA-MAZM-EMSC-20071129_0000090	IT-MMO-EMSC-20161026_0000095
A-B128-INT-UT19990920_174715	A-C1059-TK-1999-0415	IT-MNF-EMSC-20161026_0000095
A-C008-INT-UT19990920_174715	A-D0531-TK-1999-0415	
A-C042-INT-UT19990920_174715	TK-4101-TK-1999-0294	
A-C052-INT-UT19990920_174715	RA-ADEA-EMSC-20071129_0000090	
A-C079-INT-UT19990920_174715	RA-JARA-EMSC-20071129_0000090	
A-D054-INT-UT19990920_174715	HI-KRN1-GR-1997-0014	
A-D069-INT-UT19990920_174715	IT-BSC-IT-1980-0012	
A-E066-INT-UT19990920_174715	IT-ASS-IT-1997-0006	

Appendix 4.2 – Influence of preseismic velocity
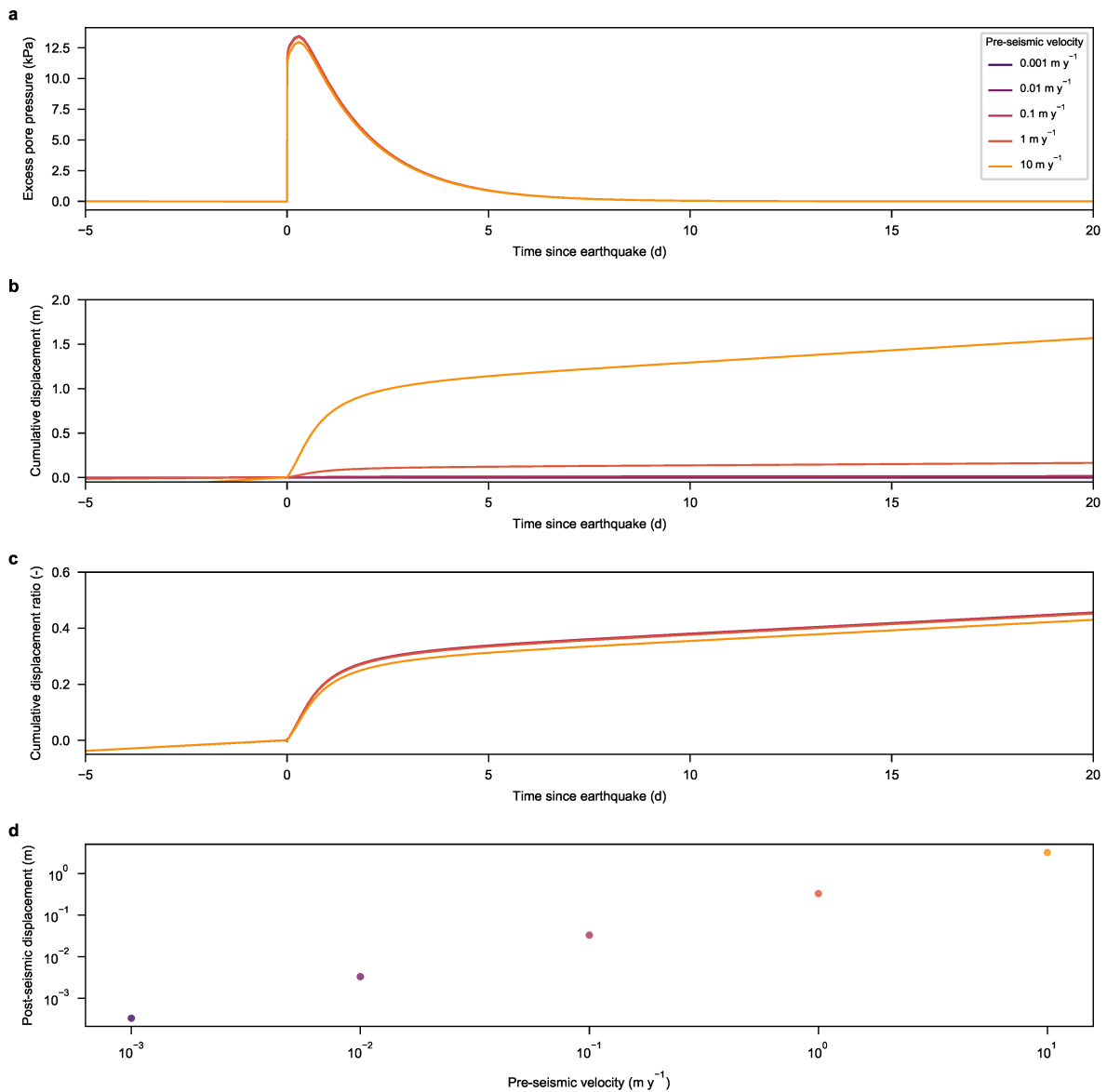
Figure 4.9: Influence of the preseismic landslide velocity. Simulation results showing the influence of the preseismic (or reference velocity) on the postseismic behaviour (for a constant rate dependency A). The evolution of the excess pore water pressures inside the shear zone (a) are almost identical for all preseismic velocities. The cumulative landslide displacement (b) caused by the excess pressures, however, are significantly higher for higher preseismic velocities. When the displacements are normalized by the yearly reference displacement resulting from a constant preseismic velocity (c), the differences between different preseismic velocities become nearly invisible. The linear dependency of the postseismic displacements on the preseismic can be clearly represented by the final postseismic displacement (d). The earthquake motion was retrieved from the ESM database (ESM signal ID: IT-MNF-EMSC-20161030_0000029-HE (Luzi et al., 2020)). The parameters used for the simulations are presented in Table 4.4.

Table 4.4: Parameters used for the simulations of the influence of the preseismic velocity.

Parameter	Symbol	Study pre-seismic velocity (Fig. 4.9)
	Geometry	
Inclination	α	12°
Base thickness	h_{base}	10 m
Base depth	d_{base}	100 m
Shear zone depth	d_{shear}	40 m
Adjacent soil thickness	$h_{\text{adj}} = h$	10 m
Shear zone thickness	h_{shear}	0.1 m
Water table height	h_{w}	30 m
	Mechanical parameters	
P-wave modulus base	M_{base}	15 GPa
S-wave modulus base	G_{base}	5 GPa
Density base	ρ_{base}	2700 kg/m^3
P-wave modulus soil	M_{soil}	320 MPa $\bullet (\sigma_0/100kPa)^{0.5}$
S-wave modulus soil	G_{soil}	80 MPa $\bullet (\sigma_0/100\text{kPa})^{0.5}$
Density soil	ρ_{soil}	2000 kg/m^3
	Permeability	
Permeability base	k_{base}	10^{-6} m/s
Permeability stable soil and top soil	k_{soil}	10^{-6} m/s
Permeability shear zone and adjacent soil	k	10^{-8} m/s
	Shear zone	
Reference velocity	v_0	var.
Rate dependency parameter	A	0.01

Appendix 4.3 – Influence of the earthquake intensity on the landslide motion
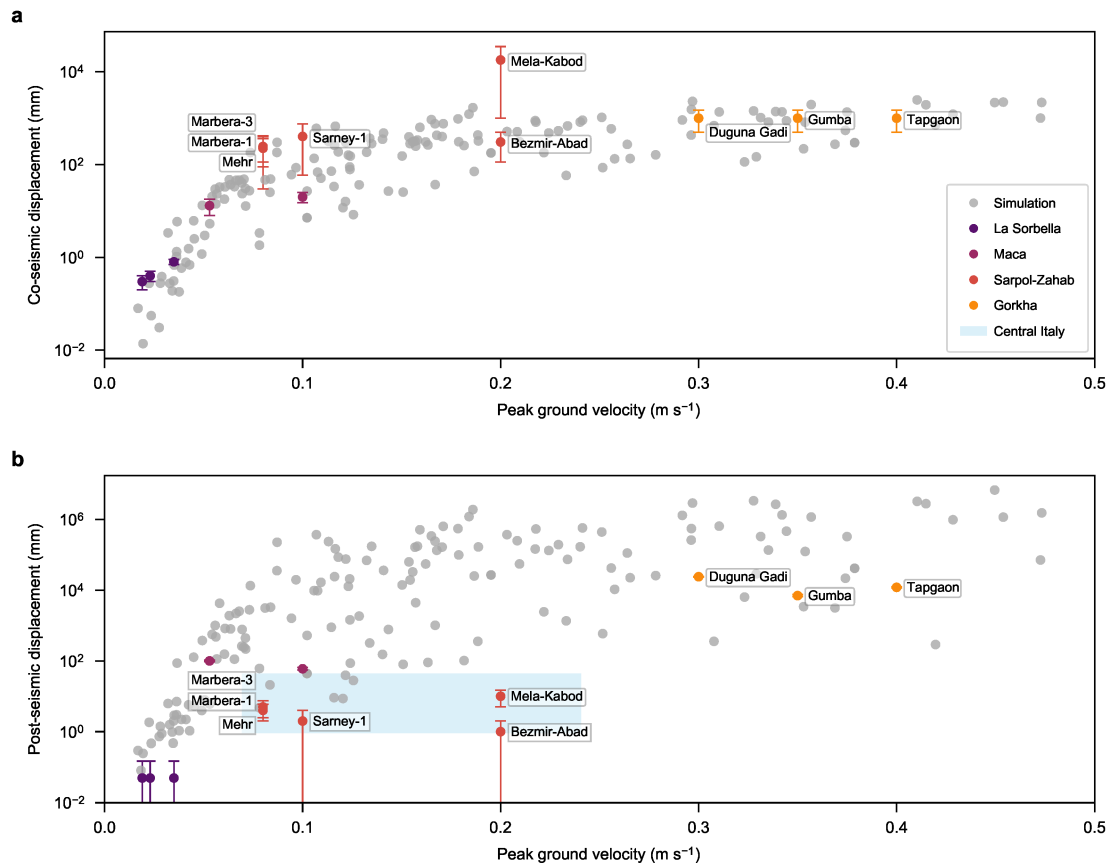
Figure 4.10: Influence of the earthquake intensity on the landslide motion. Comparison of simulations to measurements from case studies for a large set of earthquake signals. (a) coseismic and (b) postseismic displacement. This plot represents the non-normalized form of Figure 4.5 of the main manuscript. The input signals from rock or stiff soil sites were retrieved from the ESM database (Luzi et al., 2020) and are listed in the Table 4.3. The case studies considered are: La Sorbella landslide (Ruggeri et al., 2020), Maca landslide (Bontemps et al., 2020; Lacroix et al., 2014), Sarpol-Zahab earthquake (Cheaib et al., 2022) (Slides: Marbera-1, Marbera-3, Mehr, Sarney-1, Mela-Kabod, Bezmir-Abad), Gorkha earthquake (Lacroix et al., 2022) (Slides: Duguna Gadi, Gumba, Tapgaon) and landslides in Central Italy (Song et al., 2022). The landslides from the Gorkha study show almost no preseismic motion and the reference velocity for the normalization is assumed to be 2 cm/year based on landslide velocity detected in a nearby valley (Bekaert et al., 2020). Error bars represent the measurement error reported in the respective publications. Except for La Sorbella, the input signals are not available and the peak ground acceleration was estimated based on the USGS shakemap (https://earthquake.usgs.gov/data/shakemap/). The parameters used for the simulations are presented in Table 4.1.

Appendix 4.4 – Application to La Sorbella landslide
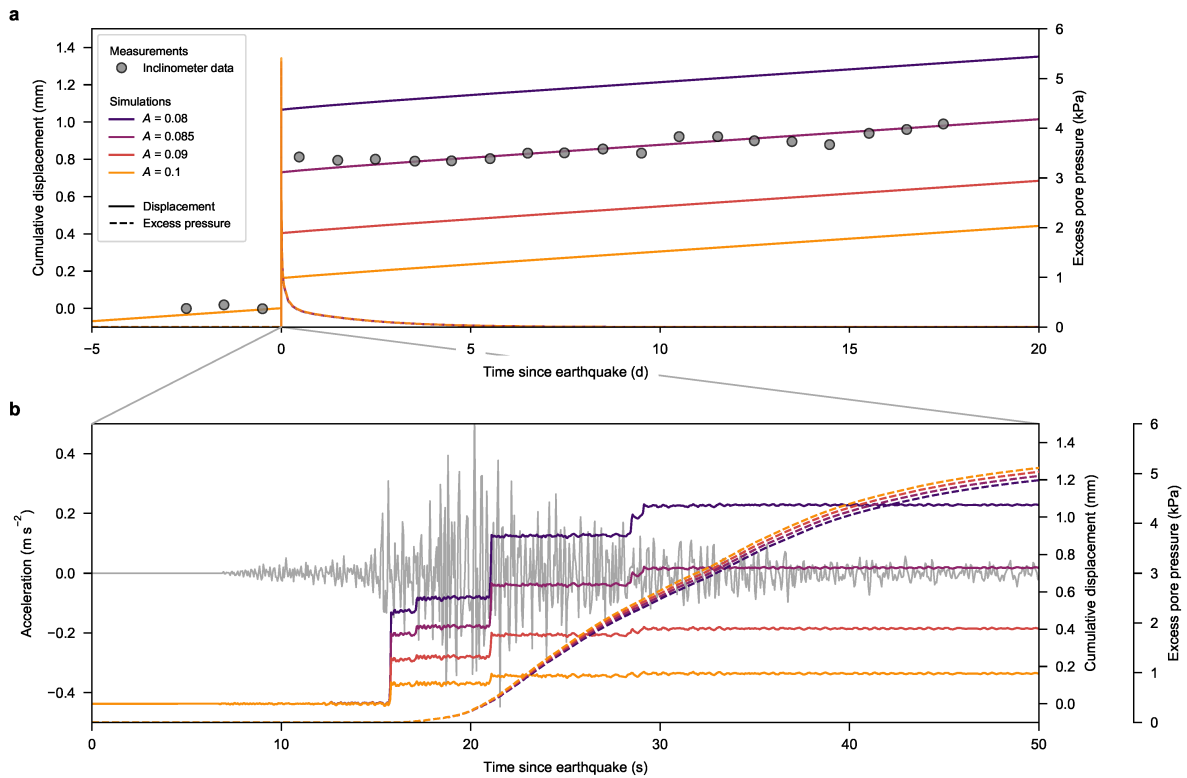
Figure 4.11: Application to La Sorbella landslide. (a) Comparison of the inclinometer measurements (adapted from (Ruggeri et al., 2020)) and the simulation results for La Sorbella landslide during the Norcia earthquake for different rate-dependency parameter A. The postseismic activity in considerably smaller due to the fact that excess PWP are only generated above the shear zone and due to the larger rate-dependency. (b) Zoom into the behaviour during earthquake shaking showing the input motion, cumulative displacements and the evolution of excess pore water pressures in the shear zone. The earthquake motion was retrieved from the ESM database (ESM signal ID: IT-VAL-EMSC-20161030_0000029-HE (Luzi et al., 2020)). The parameters used for the simulations are presented in Table 4.5.

Table 4.5: Parameters used for the simulations of La Sorbella landslide.

Parameter	Symbol	La Sorbella (Fig. 4.11)
Geometry		
Inclination	α	8°
Base thickness	h_{base}	10 m
Base depth	d_{base}	26 m
Shear zone depth	d_{shear}	25 m
Adjacent soil thickness	$h_{\text{adj}} = h$	15 m (only above shear zone)
Shear zone thickness	h_{shear}	0.1 m
Water table height	h_{w}	21 m
Mechanical parameters		
P-wave modulus base	M_{base}	15 GPa
S-wave modulus base	G_{base}	5 GPa
Density base	ρ_{base}	2700 kg/m^3
P-wave modulus soil	M_{soil}	320 MPa $\bullet (\sigma_0/100kPa)^{0.5}$
S-wave modulus soil	G_{soil}	80 MPa $\bullet (\sigma_0/100kPa)^{0.5}$
Density soil	ρ_{soil}	2000 kg/m^3
Permeability		
Permeability base	k_{base}	10^{-6} m/s
Permeability stable soil and top soil	k_{soil}	10^{-6} m/s
Permeability shear zone and adjacent soil	k	$0.5 \bullet 10^{-8}$ m/s
Shear zone		
Reference velocity	v_0	1.0 cm/y
Rate dependency parameter	A	var.

5 Rate, water pressure and temperature effects in landslide shear zones

Abstract

The behaviour of slow-moving landslides is controlled by the residual strength of the shear zone. Despite their mobile state, such slides can often withstand extreme events like heavy rainfalls and earthquakes. A rate-hardening in the shear zone is suspected to be one of the main stabilizing factors and has been well investigated, in particular for clayey soils. Soils from steep alpine landslides, on the other hand, are often dominated by silts and sands with various clay content, and while understanding of their rate dependency is less advanced, it remains critical for the reliable risk assessment. In this article, an improved ring shear apparatus is presented and applied to investigate rate, pore water pressure and temperature effects in landslide shear zones. The testing program on samples from two alpine landslides in Switzerland reveals a moderately positive rate effect explaining their mobile state. An achieved insight into the thermo-hydro-mechanical processes of fast shearing provides physical evidence to the widely debated hypothesis on generation of excess pore water pressure due to frictional heating. However, for the tested materials this effect only occurs after extended shearing and does not lead to a complete loss of shear strength. Based on that and the observed positive rate effects, catastrophic failure seems unlikely for these landslides. At the same time, the results suggest that for less permeable soils, frictional heating may indeed be a source of negative rate effect during very rapid shearing.

5.1. Introduction

5.1.1. Shear rate effects

Shear zones of active landslides are usually characterised by fine-grained soils that are in the residual state of shearing. Depending on the grain size distribution, two general types of residual state can be identified. Granular soils (sands and silts) reach after significant deformation a state of constant shear stress and volume, the so-called critical state. In contrast, soils with a considerable clay fraction show a further decrease in shear strength due to alignment of clay particles, reaching a constant shear stress only after a very extended deformation (Lupini et al., 1981; Skempton, 1985). In both cases, the residual state refers to the asymptotically approached minimal value of strength during continuous slow shearing when a steady state is reached. Because this value is rate dependent it has been termed in the literature as a steady state strength (Scaringi et al., 2018), with the term residual strength usually reserved for very slow steady states (shearing velocity $v \leq 0.01mm/s$). Accelerating shearing from this slow steady state produces three different responses (Figure 5.1): positive, negative and neutral (Lemos, 2003, 2004; Tika et al., 1996). The positive effect is characterised by an increase of resistance with an increasing shearing rate and is typical for high plasticity clays. On the other hand, a negative effect can be found in clays of low or intermediate plasticity and is the most feared type of behaviour. In granular soils, such as silts and sands, with a very small percentage of clay particles ($< 5\%$), usually a neutral effect is observed (e.g. Lemos, 2003). Regardless of the type, a transient behaviour of a fast peak followed by a fast steady state can often be observed during impulsive shearing (Grelle & Guadagno, 2010).
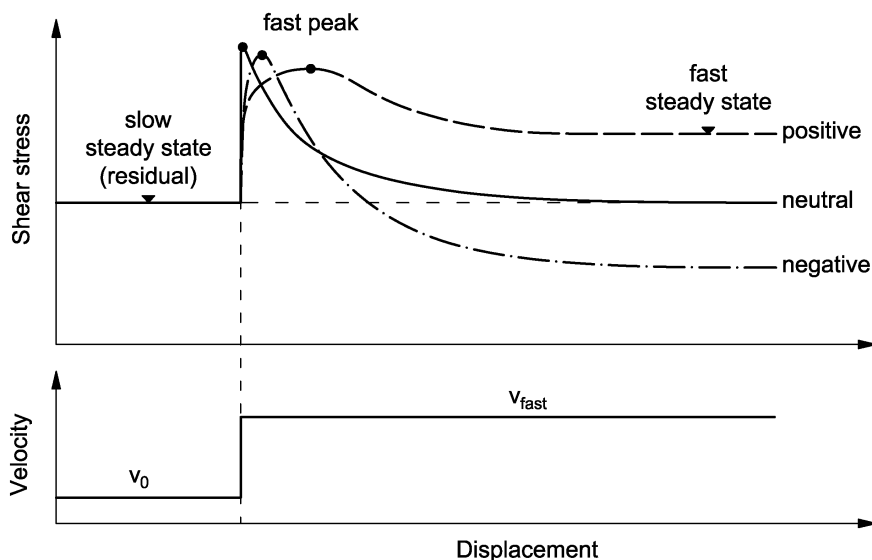
Figure 5.1: Effects of fast shearing in the residual state (after Lemos (2003) and Grelle & Guadagno (2010)). Three different categories of rate effects are differentiated: positive, neutral and negative.

Tika & Hutchinson (1999) suggested that the catastrophic event of 1963 at the Vajont dam in Italy is due to negative rate effects. During filling of the water reservoir, the Vajont landslide was triggered, which resulted in a tsunami waver overtopping the dam. Around 2000 people lost their lives and tremendous damage was caused (Hendron & Patton, 1987). Post-failure simulations indicate that the strength of the Vajont landslide must have dropped to an extremely low value (Alonso & Pinyol, 2010; Crosta et al., 2016). Otherwise the reported velocity of around 25-30 m/s (Caloi, 1966; Müller L, 1964) could not have been reached. This drop in shear strength is commonly attributed to frictional heating on the sliding surface leading to generation of excess pore water pressures (Hendron & Patton, 1987; Romero & Molina, 1974; Vardoulakis, 2002; Voight & Faust, 1982). This mechanism, however, remains debated and has not been proven experimentally. This case illustrates the importance of the shear zone behaviour when investigating landslides and assessing their potential risk. In particular, it must be determined whether negative rate effects are possible or not. Besides thermal pressurization due to frictional heating several other mechanisms have been proposed explained the phenomena of rate weakening during shearing. Particle crushing has been observed in several cases (Fukuoka et al., 2007; Okada et al., 2004; Vafaei et al., 2019), which leads to a higher concentration of fine particles in the shear zone and a decrease in shear strength. Additional to thermal pressurization, frictional heating, or in this respect often called flash heating, can lead to melting, recrystallization and carbonate decomposition (Beutner & Gerbi, 2005; Goldsby & Tullis, 2011; Hu et al., 2019; Lucas et al., 2014; Mitchell et al., 2015). Other mechanisms can be acoustic fluidization (Melosh, 1979) and mechanical fluidization (Davies, 1982).

In mountainous regions such as the Alps or the Himalaya, there are numerous active landslides and many of them are characterised by steep terrain shaped by glacial erosion (Agliardi et al., 2019, 2020; Puzrin & Schmid, 2011; Sterba et al., 2000; Strauhal et al., 2017). Unlike flatter landslides with a clay-dominated shear zone, steep landslides often have a mixture of silt and sand with varying clay content. Although these are classified as granular soils, neutral rate effects cannot be assumed a priori for their residual strength, because of their non-negligible clay content. In fact, various studies have demonstrated both positive and negative rate effects for such soils, depending on the shearing rates and the clay content (Kang et al., 2022; Scaringi & Di Maio, 2016; Scaringi et al., 2018; Tika et al., 1996; Wang et al., 2023). The problem with alpine soils, which are silty sands, is not only that their rate effects are less pronounced and understood, but also that their clay content (> 5%) makes the understanding of rate effects even more complicated, but nevertheless critical for the risk assessment of these landslides.

5.1.2. Ring shear apparatus

The ring shear apparatus was designed to investigate the shear resistance at large displacements and was first proposed by A. Casagrande as reported by Hvorslev (1939). Various forms of this apparatus had been developed in the years before the Second World War by Gruner & Haefeli (1934), Cooling & Smith (1936) and Hvorslev (1939). They all share the principle of a ring-shaped sample which is loaded normally and twisted. This concept was later improved by Bishop et al. (1971) and Bromhead (1979) giving their names to the corresponding apparatus type. The Bishop-type ring shear consists of upper and lower confinement rings with a controllable gap in between. By rotating the lower rings while simultaneously holding the upper rings in place, the shear plane is forced to develop at this gap. While this type is often preferred in research, it is less commonly used in practice due to its complexity. Therefore, the Bromhead-type apparatus is considered more practical due to its design of a single shear box, where the sample is sheared along the top plate. A major disadvantage of the Bishop-type apparatus is the extrusion of soil through the gap between the confinement rings, which becomes even worse at higher shear speeds. It is not clear how this constant leakage of soil influences the observed shear behaviour. Furthermore, the gap leads to an immediate dissipation of potential excess pore water pressure developed during shearing. This might not only affect the shear resistance but also makes it pointless to measure pore the water pressure directly at the shear zone. This issues have been overcome by a series of undrained ring-shear devices developed in the last decades (Sassa, 1984, 1996; Sassa et al., 2004). The central improvement is a rubber edge placed between the lower and upper rings as sealing to prevent leakage of both water and soil. This allowed Sassa et al. (2004) to study the undrained shear behaviour of different soils and investigate the soil liquefaction by means of ring shear tests.

5.1.3. Goal and objectives

In this study, we first present an improved ring shear apparatus incorporating the latest developments in this type of soil testing. The main feature is an improved sealing, which prevents leakage of water and soil, while at the same time allowing the study of rate effects due to its low friction. Furthermore, the integration of both pore water pressure and temperature sensors allows for a better understanding of the mechanisms involved. In the second part, we investigate the effect of shearing rate, pore water pressure and temperature on the residual shear strength of granular soils from two alpine landslides. The main goal is to identify whether these samples exhibit positive, neutral or negative rate effects and to quantify them. For the first time, we investigate experimentally the potential of frictional heating leading to a reduction in shear strength. This will provide an assessment of whether a catastrophic failure of these landslides is a realistic scenario.
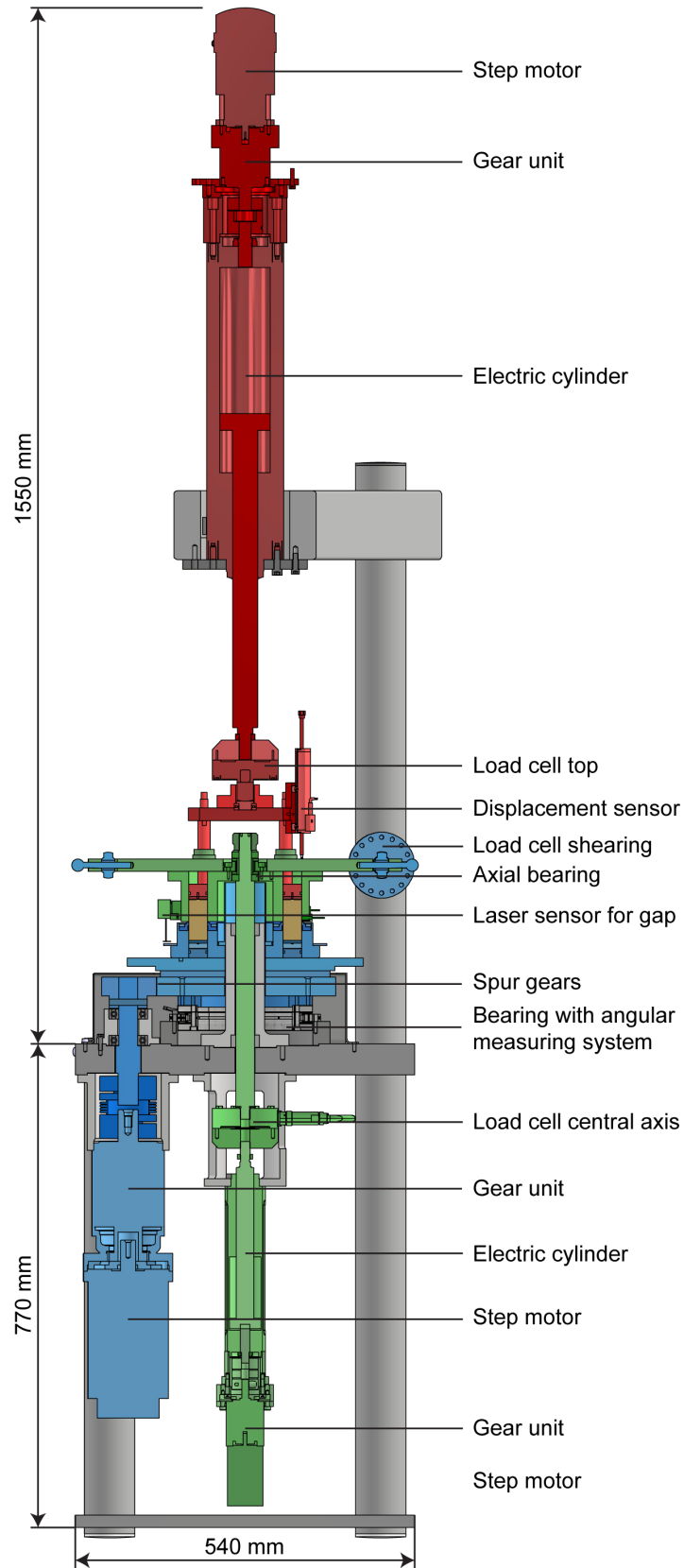
5.2.   Ring shear apparatus

5.2.1. General

The ring shear apparatus developed by the ETH Zurich for this study is of a Bishop-type (Bishop et al., 1971) and incorporates several improvements from Sassa et al. (2004), as well as some new features, which will be described below. The general layout consists of the three main units, each driven by a separate step motor (Figure 5.2):

(i)   The vertical force unit: The force is applied to the sample by the top step motor and electrical cylinder. This force is transferred to the loading plate using a roller bearing in order not to transmit any torque. A load cell in between allows measuring the applied force; a potentiometer provides the vertical displacement of the loading plate.

(ii)   The gap control unit: The second step motor and electrical cylinder underneath the shear box regulate both distance and force at the gap between upper and lower confinement rings. The central axis connects the shaft of the cylinder to the top plate of the shear box by means of an axial bearing to prevent the transition of any torque. The applied force at the axis is measured by a load cell and the distance between upper and lower confinement rings is directly measured at the gap using three laser sensors.

(iii) The torque unit: The rotational shearing of the lower part of the shear box is controlled by the third step motor and a gear unit. These are connected through an axle to a small gear wheel, which drives a larger one directly underneath the shear box. The shear displacement of the sample is obtained from an angular measuring system integrated into the precision bearing below the large gear wheel. The torque transmitted between the lower and upper part of the shear box is derived from the pair of forces measured by two horizontal load cells, which prevent the upper part from rotating as well.

In addition, the apparatus includes separate units for power supply, controlling and logging. The latter are connected to a computer to control and monitor the tests. Furthermore, a water pressure unit allows the pore water pressure in the sample to be set and regulated.

Figure 5.2: Cross section of the ring shear apparatus and its main component. The general layout consists of three main units: the vertical force unit (red), the gap control unit (green) and the torque unit (blue).

5.2.2. **Shear box**

The crucial part of the apparatus is the shear box (Figure 5.3 and Figure 5.4), which consists of a stationary upper part and a rotating lower part separated by a small gap. Both parts are composed of an outer and inner ring confining the soil sample with outer radius $r_A = 90mm$ and inner radius $r_I = 60mm$. The height of the sample can vary within $h = 50 - 85mm$. To prevent the leakage of both water and soil through the gap, PTFE (polytetrafluoroethylene) seals are placed in between the lower and upper confinement rings. PTFE has the advantage of a very low friction coefficient and in particular exhibits an exceptionally steady frictional behaviour over very large shear deformations. In contrast, rubber edges as chosen by Sassa et al. (2004) are less optimal when investigating the subtle rate effects in soils at medium pressures. In contrast, for test at high pressures, PTFE does not properly seal (unless an unreasonably high contact pressure is applied) and rubber edges should be preferred. To maximize the contact pressure for a certain force applied by the gap control unit, the surface area of the PTFE seals is minimized by a trapezoidal cross-section with a width of 1mm at the top (6 mm at the bottom). The reduced width has the additional advantage of a low vertical stiffness of the seals, which means that the contact force changes only marginally in case of a small change of the gap. However, to keep the gap and compression of the seals constant, the distance between lower and upper confinement rings is monitored by laser sensors and regulated by the gap control unit. It should be emphasised that a simple fixing of the position of the gap control unit motor does not guarantee on its own a constant gap due to the deformation of other device components (e.g. central axis, load cell, top plate).
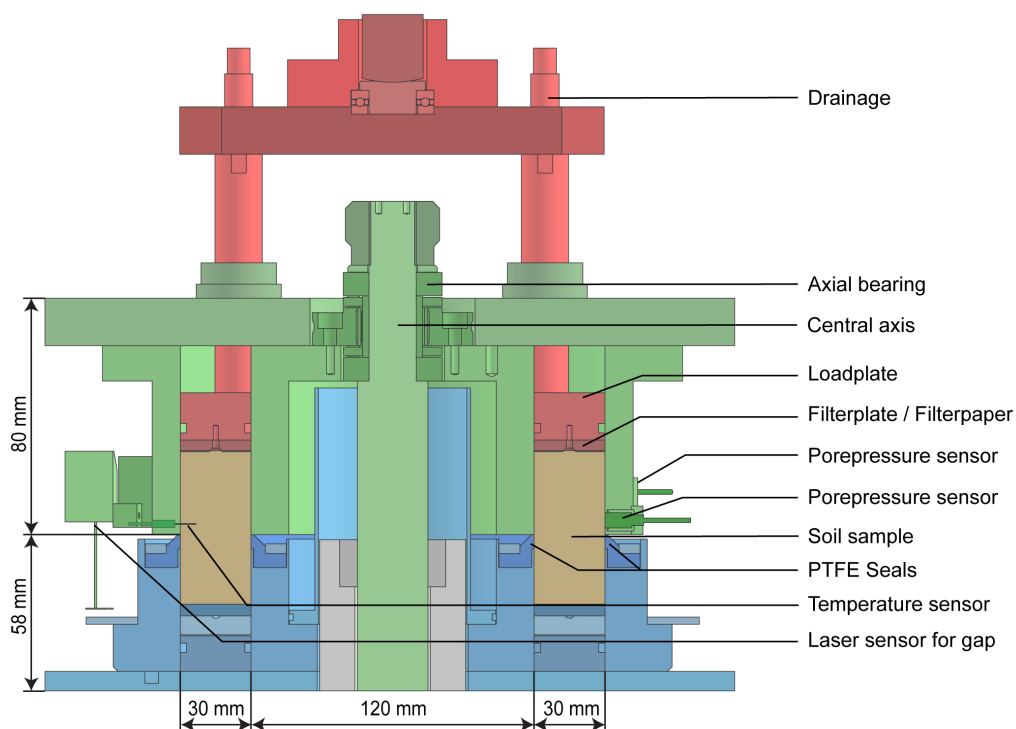
Figure 5.3: Cross section of the ring shear box showing all the main parts and sensors.

The seals do not only prevent the leakage of soil but also that of water, which allows measuring the pore water pressures at or close to the shear zone, since they are not dissipated right away at the gap. For this purpose, multiple pore pressure sensors are mounted at the upper confinement rings. Three pairs of sensors are evenly distributed around the circumference of the ring at 120 degree distances, with sensors in each pair located, at the heights of 6mm and 18mm above the gap. Besides a porous metal filter, the sensors are covered with a filter paper to prevent clogging. In addition, three thermocouple sensors can be inserted into the sample through cable glands slightly above the gap. This allows to measure the temperature close to or even right at the shear zone, since the cables are slightly bent downwards during consolidation. Durable brazed junctions allow the thermocouple to resist the shearing inside the shear zone, but must be inspected after each test and replaced regularly.

Drainage of the sample is enabled by water channels through the bottom and top of the shear box. These channels can also be closed by valves for undrained conditions or connected to the water pressure unit to regulate the pore water pressure. A uniform drainage or pressure distribution is guaranteed by porous metal filter plates at the sample's bottom and top. Filter paper is placed in between to prevent fine contents from entering the filter plates.
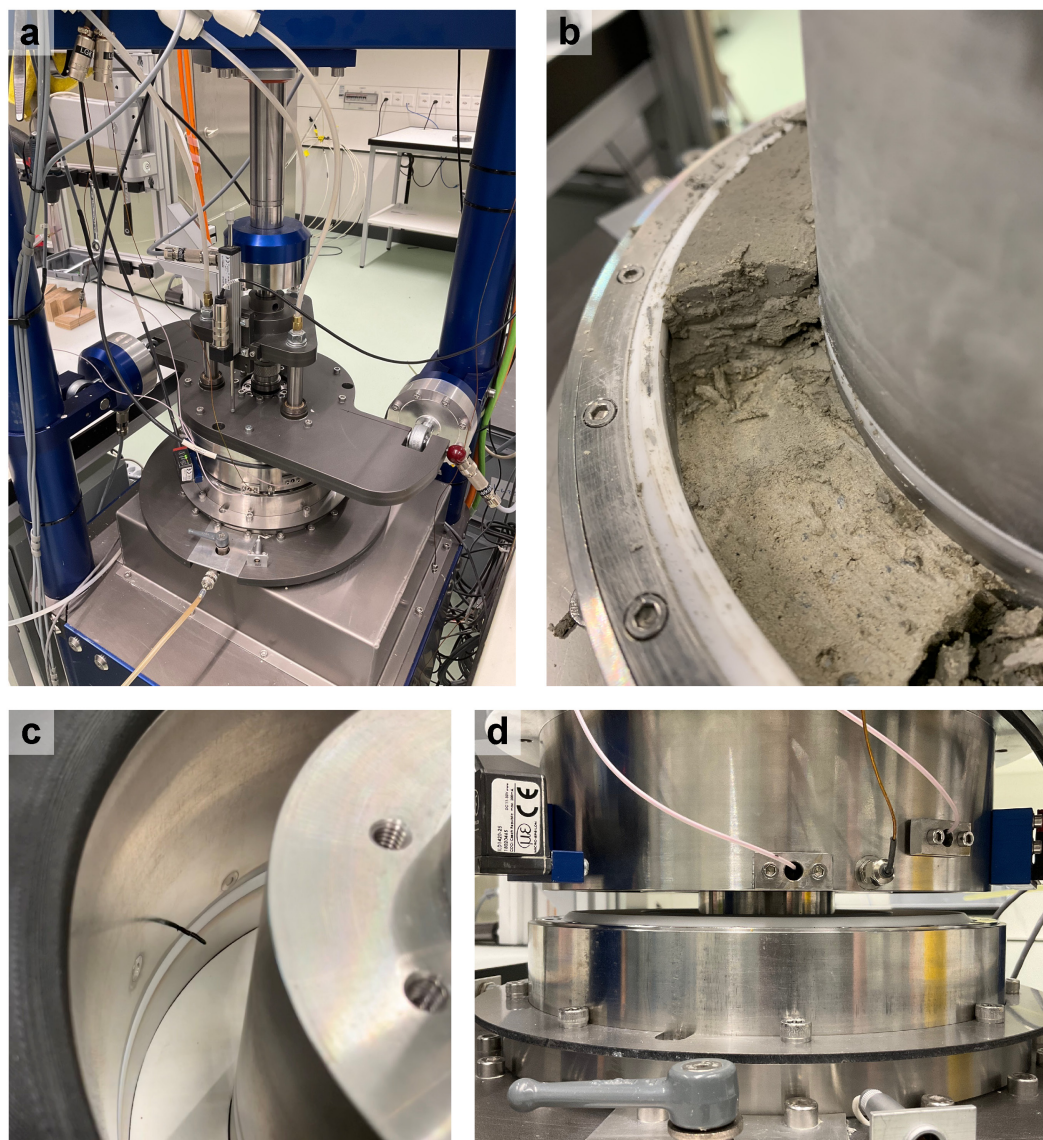
Figure 5.4: Photos of the ring shear apparatus (a), shear zone and PTFE seals (b), inside of the shear box showing the local pore water pressure and temperature sensors (c), outside of the shear box and the open gap (d).

5.3.   Procedures and Materials

5.3.1. Testing procedure

Each test series begins with the installation of new PTFE seals. Due to some minor height irregularities, the shear box is first sheared empty to achieve a smooth and even surface of the inner and outer seals. This procedure is necessary to prevent water and soil leakage during the subsequent tests. Afterwards the force on the seals is adjusted using the central axis. Tests have shown that a central force $F_A = 2$ kN is optimal, which on the one hand keeps the friction small, but is still sufficient to guarantee the sealing. Furthermore, the pore water pressure sensors are pre-saturated with de-aired water, calibrated using an external pressure sensor and installed at the shear box. The same applies to the temperature sensors,

which are positioned so that they reach about 1 cm into the shear box. This choice of depth is slightly less than half the width of the shear zone (3 cm). The aim is to reduce the influence of the confinement rings, but at the same time not to have very long sensors that are bent too much.

Due to the dimensions of the shear box, only the fraction with a grain size smaller than 2 mm is tested. The dry sample is mixed with de-aired water to a slurry with the water content close to its liquid limit. The air is then extracted from the slurry by applying a vacuum. The slurry is then poured into the shear box and evenly dispersed in layers using a stamp. In order to remove air from the upper filter plate and upper drainages, water pressure is applied to the bottom drainage valve generating a flow through the shear box. Subsequently, both the upper and lower drainage valves are closed and the saturation is verified by a B-value test.

The samples are consolidated stepwise until the target normal stress of approximately $\sigma_n = 400$ kPa is reached, which represents the in-situ conditions at which the samples were retrieved from the landslide shear zone. To investigate the influence of the normal stress, several tests were carried out at lower stress values. After the consolidation the shear tests are performed according to the testing program summarized in Table 5.1. During all of the following stages, the lower drainage valves are closed whereas the upper ones remain open. The sample is initially sheared at a slow rate v_{init} until the residual state is reached, which is followed by further shearing at an even lower rate v_0, which represents the slow residual state.

The rate dependency of the soil is examined with two types of tests, performed on the same soil sample. First, a series of single-stage tests is performed with a single velocity step v, which is different for each test. In between these tests, the shearing is stopped for several hours. Secondly, a multi-stage test is carried out where the velocity steps follow one after the other only interrupted by a period of slow shearing. The shearing distance is increased with the velocity to allow the sample to reach a new steady state.

Table 5.1: Testing program

Stage	Shearing velocity (mm/min)	Shear displacement (mm)
Initial shearing	$v_{init} = 0.1$	$d_{init} = 250$
	$v_0 = 0.01$	$d_0 = 10$
Single-stage	$v_0 \rightarrow v \rightarrow v_0$	$d_0 \rightarrow d \rightarrow d_0$
	$v_0 = 0.01$	$d_0 = 2$
	$v = 0.05, 0.2, 0.5, 2, 5, 20, 50, 200$	$d = 50$
Multi-stage	$v_0 \rightarrow v_1 \rightarrow v_0 \rightarrow v_2 \rightarrow \cdots$	$d_0 \rightarrow d_1 \rightarrow d_0 \rightarrow d_2 \rightarrow \cdots$
	$v_0 = 0.01$	$d_0 = 2$
	$v = 0.02, 0.05, 0.2, 0.5, 2, 5, 20,$	$d = 10, 30, 40, 50, 50, 50, 100,$
	$50, 200, 500, 2000, 5000$	$200, 500, 500, 1000, 1000$

5.3.2. Materials

The material tested in this study was extracted from the shear zone of two landslides in Switzerland, the Marsc landslide in Luzzone (Kohler et al. (2023) and Chapter 6) and Brattas landslide in St Moritz (Schluchter, 1988; Sterba et al., 2000). These represent typical alpine landslides, which are characterized by their steep inclination and a disturbed moraine deposit. The soil mass consists of cobbles and boulder embedded in a silty and sandy soil matrix. These landslides are deep-seated slow-moving landslides whose movement are mainly controlled by hydrological conditions and therefore show a seasonal velocity pattern. The Marsc landslide covers an area of almost 0.2 km2 and is moving with a velocity of 0.1-0.3 m/year. The Brattas landslide is considerable larger with an area of around 1 km2 and the velocities are in the range of 0.1-0.5 m/year. In both landslides, the shear zone has been located in an average depth of 20 m by inclinometer measurements in several boreholes and represents a weaker layer of a higher fine content including a clay fraction (Figure 5.5). One sample was available from the Brattas landslide (StM-1502-22) and several from different borehole were extracted from the Marsc landslide (Luz-11-10, Luz-12-13, Luz-12-14). The large scatter in the grain size distribution highlights the variability of the soil mass and even in the shear zones a considerable gravel fraction was found. The soils can be classified as silty sands with gravel. For the preparation of the samples, fractions larger than 2 mm were removed by dry sieving.
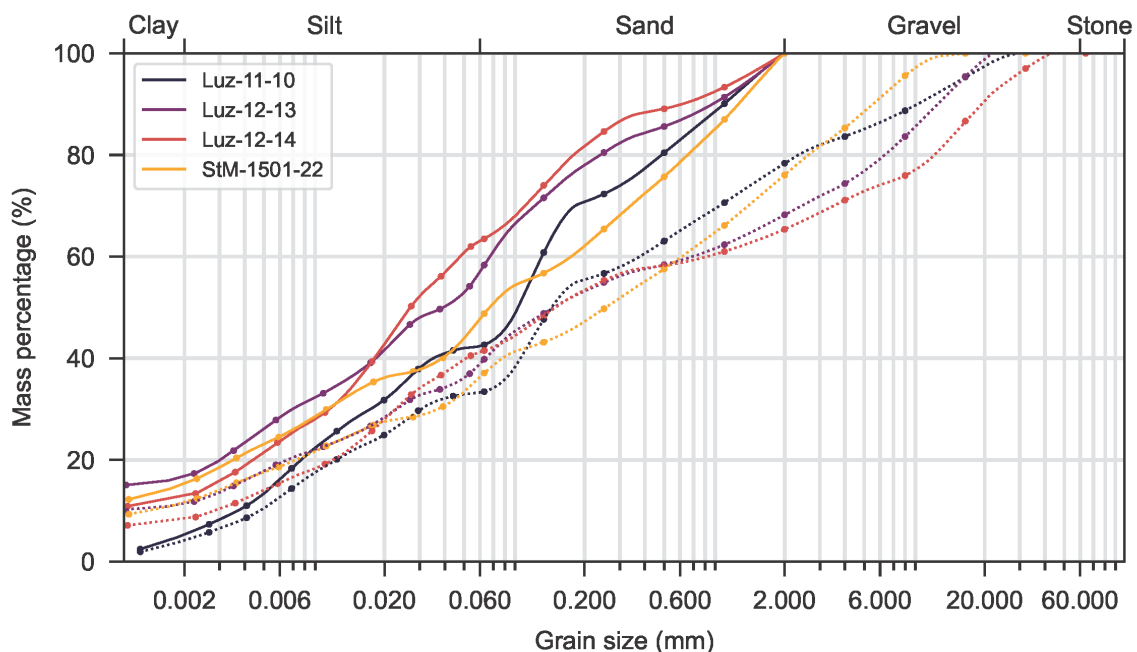
Figure 5.5: Grain size distribution of the tested samples from the Marsc (Luz-11-10, Luz-12-13, Luz-12-14) and the Brattas (StM-1501-22) landslide. The dotted lines represent the original distribution of the retrieved samples and the solid curves represent the distribution of the tested material of the fraction below 2 mm.

The mineral composition of the samples (<2 mm) was determined with an X-Ray diffraction analysis (XRD). All samples from the Marsc landslide consist mainly of quartz (45-50 wt%), mica (35-45 wt%) and minor amounts (<5 wt%) of feldspar, calcite, chlorite, dolomite and hematite. The sample of the Brattas landslide shows a slightly different mineral composition. Although the main components are again quartz (30 wt%) and mica (45 wt%), it has a much higher chlorite content of 13 wt%. Furthermore, some minor amounts (<5 wt%) of feldspar, calcite and dolomite were found.

5.4. Results

### 5.4.1. Rate effects

The results of the single-stage series are presented for two Luzzone samples in Figure 5.6, showing the evolution of the shear resistance in terms of the friction coefficient. The friction coefficient is calculated by the ratio of the shear stress τ and the normal stress σ as $\mu = \tau/\sigma$. Both specimens exhibit an instantaneous increase in shear resistance due to the velocity step, consistent with their granular nature. Afterwards, they behave very differently, although both originate from the sliding surface of the same landslide. The sample Luz-11-10 reveals a fast peak, followed by a slow decline to the new fast steady state. The extent of this decrease depends directly on the shearing velocity and the chosen displacement of 50 mm is not or only barely sufficient to reach a steady state at the highest one. The Luz-12-14, on the other hand, barely shows any fast peak and almost immediately attains the fast steady state. A similar difference in behaviour can be observed at the step back to the slow velocity. One may also note that the steady state friction values of Luz-11-10 are in general slightly higher. Despite all these differences, both samples clearly exhibit a positive rate effect.

The sample Luz-11-10 is characterised by a transient response, which is typical in tectonics for faults and is usually described by rate-and-state friction laws (Dieterich, 1979; Ruina, 1983). This behaviour is even better visible in the results of the multistage tests (Figure 5.7). For all the specimens presented, the evolution of strength shows this transient response, but in different manifestation. Especially the sample from the Brattas landslide (StM-1501-22) shows a clear fast peak at low velocities, but this peak disappears completely at high velocities. Instead, the shear strength is steadily increasing over large shear distances and a steady state is hardly reached. In contrast, even at high velocities, Luz-11-10 exhibits a distinct fast peak, followed by a slow decline, whereas Luz-12-14 lies in between quickly returning to a new steady state in each stage. Another difference can be seen during the stages of slow shearing between the subsequent fast shearing steps (see insets in Figure 5.7). Following the immediate drop in resistance, the shear strength gradually increases to the slow steady state in case of Luz-11-10, whilst other specimens exhibit a further decline. The latter is consistent with the findings of Tika et al. (1996) and can be explained by the disordering of the clay particles during rapid shearing. The shear

resistance is thus above the slow steady state in the beginning of the subsequent slow phase and decreases during further shearing due to the alignment of the particles. In fact, both of the samples Luz-12-14 and StM-1501-22 contain a sizeable clay fraction. The sample Luz-11-10 contains more sand and hardly any clay and thus has a distinctly granular character, which is characterised by a turbulent shear mechanism (Lemos, 2004). Please note that due to an error in the test procedure, the last three slow phases between the fastest velocity steps of Luz-12-14 were too short. This is particularly evident between the two last steps, where only a marginal drop in strength was measured.
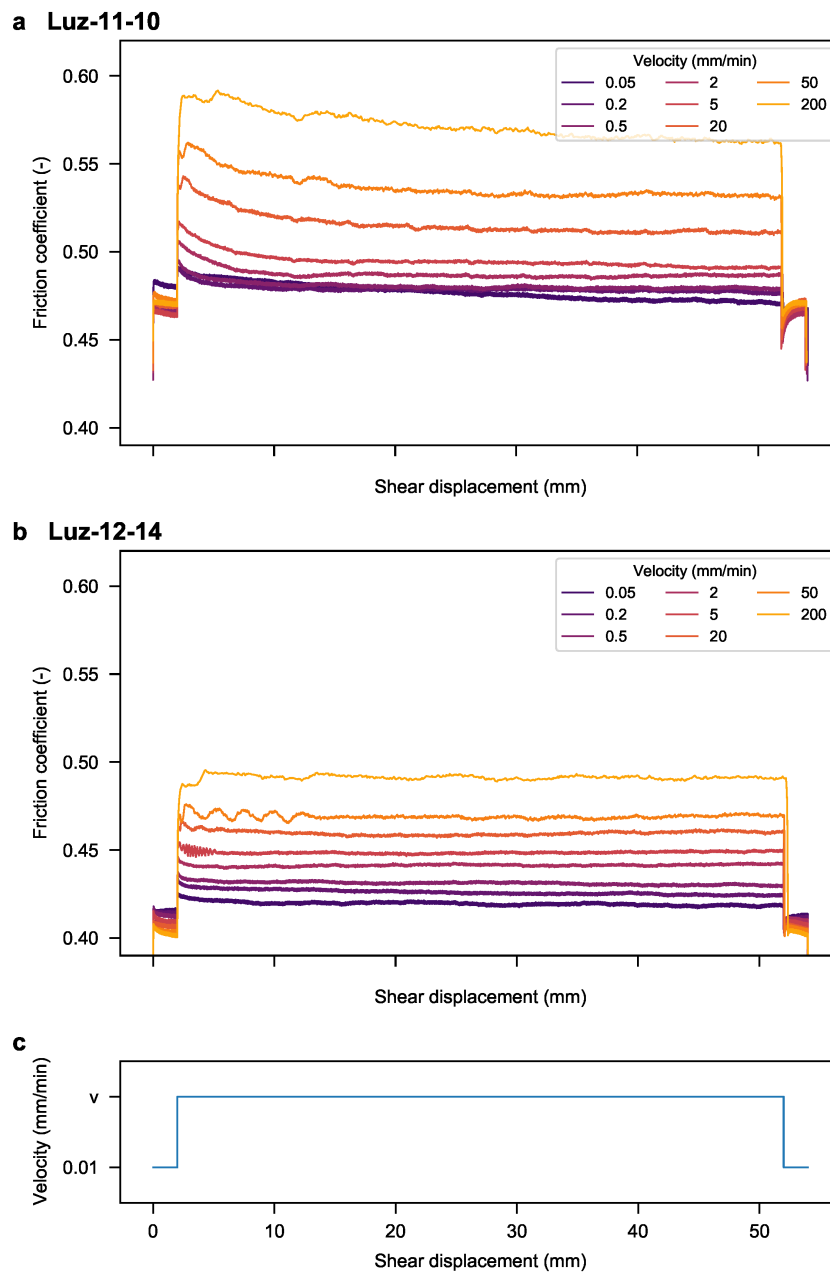
Figure 5.6: Results from the single-stage test series of samples Luz-11-10 and Luz-12-14. Evolution of the mobilized friction coefficient at different velocities (a), (b) for a normal stress of $\sigma_n = 400$ kPa. Applied velocity step (c).
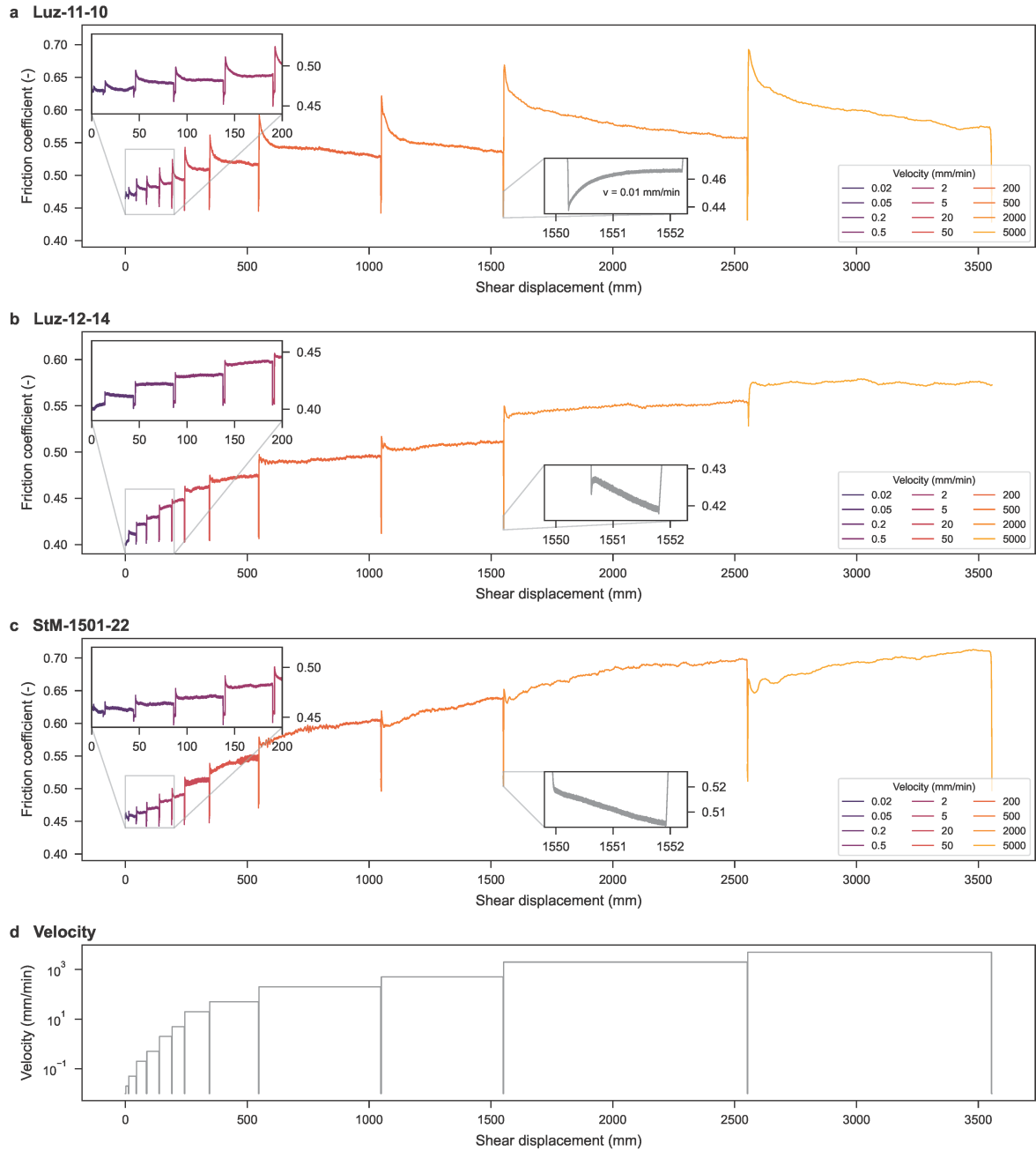
Figure 5.7: Results from the multi-stage test series of samples Luz-11-10 (a), Luz-12-14 (b) and StM-1501-22 (c) for a normal stress of $\sigma_n = 400$ kPa. Shearing velocities of the multi-stage test series (d).

A comprehensive comparison of the soils can be made by plotting steady state strength and fast peak with respect to the shearing velocity (Figure 5.8). The steady state strength was determined by the average friction coefficient of the last 10% of shearing distance per stage. It should be noted that, depending on the sample, a clear steady state has not yet been reached for some of the stages. The shearing distance at each stage was defined by several pre-tests carried out on different samples with the aim of achieving a standardized test procedure, which sometimes, which in some tests turned out to be a slightly too short. All samples exhibit a positive rate effect, although the absolute friction is different. Not surprisingly, the samples with a higher percentage of sand (Luz-11-10 and StM-1501-22) have a higher shear resistance across all velocities. Except for Luz-11-10, which has almost no fines, the differences between the fast steady states and peaks are very small and confirm the above findings. To better represent the rate effect, the fast steady state friction coefficient μ_{ss} is normalised with the slow steady state (or residual) friction coefficient μ_{v0} (at $v_0 = 0.01$ mm/min). Therefore, a ratio $\mu_{ss}/\mu_{v0} > 1$ represents a positive, $\mu_{ss}/\mu_{v0} < 1$ a negative and $\mu_{ss}/\mu_{v0} = 1$ a neutral rate effect (Figure 5.8c). This reveals that the samples differ widely in terms of rate dependency. The smallest rate dependency can be observed for Luz-11-10 and once again is consistent with its purely granular character, where less rate effects are expected (Lemos, 2004; Tika et al., 1996). The other samples show a stronger dependency on the shearing velocity. Soil samples from the Brattas landslide in St. Moritz have been already investigated in a previous study (Puzrin & Schmid, 2011), where a rate dependency of 2 % per logarithmic cyclic was reported and well agrees with the current results.

a Steady state

b Fast peak

c Ratio
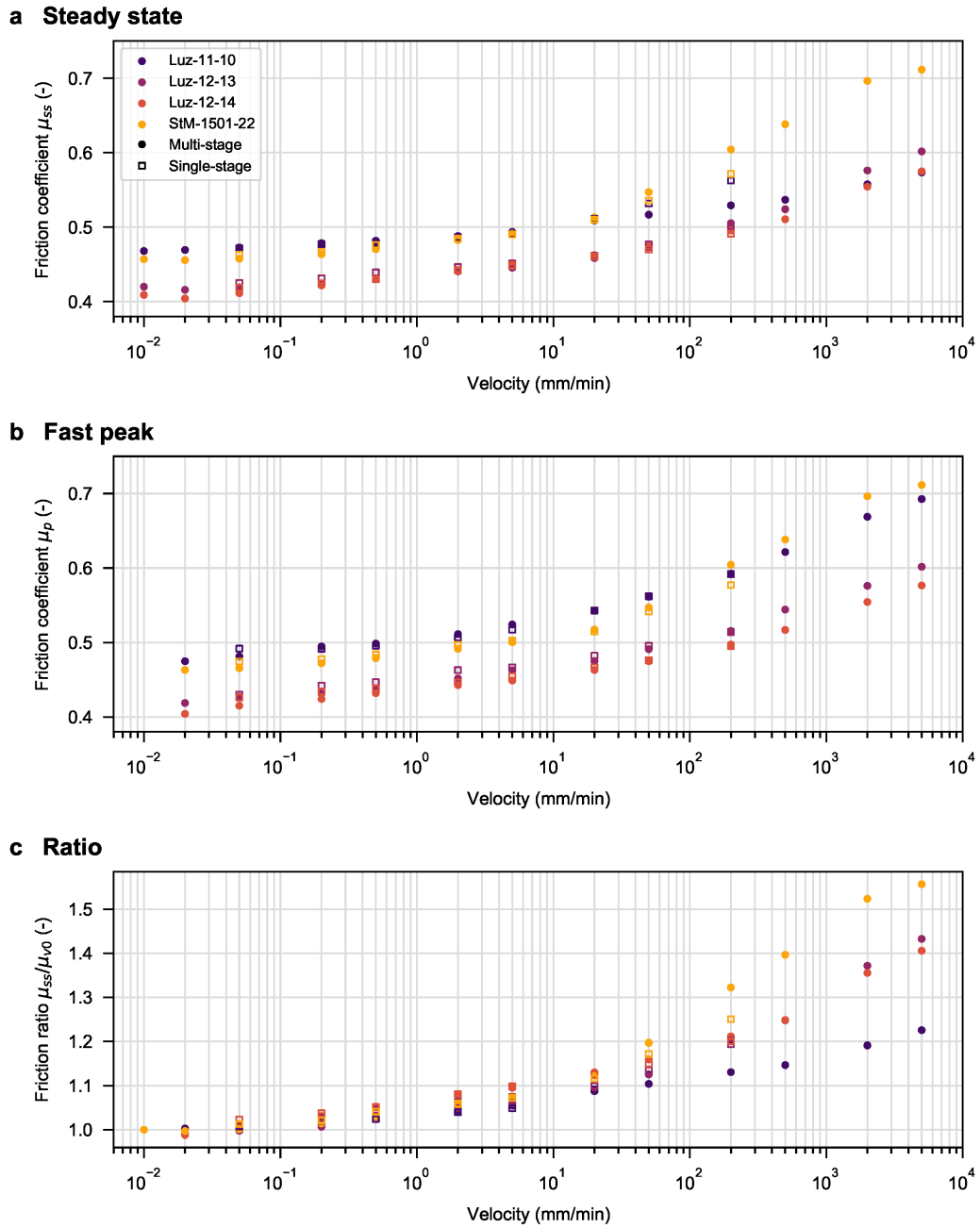
Figure 5.8: Summary plot of the results of the single- and multi-stage tests series on different samples for a normal stress of $\sigma_n = 400$ kPa. (a) Steady state coefficient, (b) fast peak friction coefficient and (c) normalized steady state friction by the slow steady state / residual friction coefficient μ_{v0}.

In addition, some tests were carried out at lower normal stresses to investigate their influence. The corresponding results are presented in Figure 5.9. In general, slightly higher friction can be observed at lower normal stresses. This trend is more evident for the sample from the Marsc landslide. It is particularly noteworthy that there is a slight negative rate effect at low stresses and moderate velocities. At higher velocities, however, the behaviour changes back to a clear rate-hardening. Higher strengths and the slightly negative rate effect at moderate velocities for low normal stresses have already been reported in other studies (Li et al., 2017; Scaringi et al., 2018; Tika et al., 1996). In the case of the large and deep-seated Marsc and Brattas landslide considered in this study, however, such low normal stresses are not representative and thus less relevant.
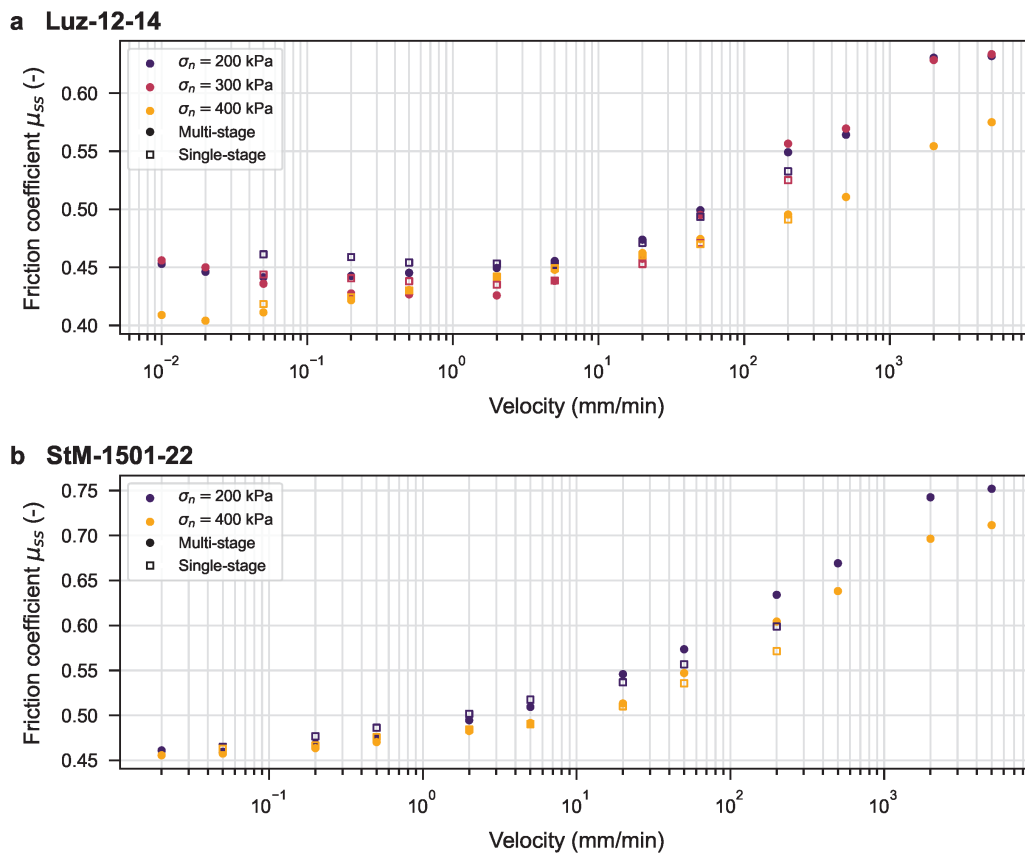
Figure 5.9: Summary plot of the steady state friction of the single- and multi-stage tests series at different normal stresses σ_n for samples Luz-12-14 (a) and StM-1501-22 (b).

5.4.2. Evolution of the pore pressure

The attached sensors allow for investigating the evolution of the pore water pressures during the different stages of shearing. All tests were carried out under drained conditions with the upper valves open. This should reflect the field conditions of a shear zone surrounded by more permeable layers as is the case for these two landslides. The samples have a height of 6-7 cm after shearing to the residual state, but the shear zone formed during the tests measures only 1-2 cm at removal. Therefore, a test with closed valves would not correspond to an undrained test for the shear zone anyway due to the partial drainage by the surrounding material. The results of the single-stage test for two samples are shown in Figure 5.10. In addition to the evolution of pore water pressure (Figure 5.10a, b), the vertical displacements are shown as well (Figure 5.10c, d). Hardly any excess pore water pressure is measured during slow shearing (up to 2 mm/min), confirming that the samples have reached the residual state (Skempton, 1985). At higher velocities, negative pore water pressure (with respect to the atmospheric pressure) is generated in both specimens, and its magnitude is around 10 times higher for Luz-12-14. This difference is mainly attributed to the higher percentage of fines and thus lower permeability, which delays dissipation of water pressure. The negative pressure arises abruptly at the velocity step and the magnitude seems to correlate with the shearing speed. The following rate of dissipation seems to differ between stages, but is only due to the different durations of shearing.

The samples generally show a contractive behaviour in the course of the stages. However, during fast shearing a slight dilation can be observed explaining the negative pore water pressure. The more permeable Luz-11-10 sample allows an almost immediate increase in volume, whereas this is delayed in Luz-12-14. The tendency of granular soils to dilate at high shearing rates has already been observed in previous studies (Hungr & Morgenstern, 1984; Lemos, 2004; Tika et al., 1996). However, a precise conclusion is difficult to draw, because the vertical displacement, and hence the volume change, represents the cumulative behaviour of the shear zone and the surrounding material. Therefore, it is assumed that the general decrease in volume is primarily due to the contraction of the surrounding less sheared material, which is subjected to an increased shear stress due to the positive rate effect (Grelle & Guadagno, 2010). This explain the abrupt volume decrease at the beginning of the fast stages for sample Luz-12-14. Furthermore, shear thickening at higher velocities (Hu et al., 2022) and grain crushing (Sadrekarimi & Olson, 2010; Wang & Sassa, 2002) might also contribute to the decrease in volume.

The behaviour patterns discussed for the single-stage tests can be also observed in the corresponding multi-stage tests (Figure 5.11a, b). Even higher magnitudes and high fluctuations of negative pressures are measured in Luz-12-14 during fast shearing, presumably as a consequence of turbulent shearing. The absence of any negative pressure for Luz-11-10 confirms the granular character of the sample as already observed by the fast peaks (Figure 5.7). For Luz-12-14, on the other hand, the slight peaks observed in Figure 5.8b can be explained by the negative pore water pressures. However, it would be unreasonable to calculate an effective friction coefficient, since the pore water pressure measured at

certain points slightly above the shear zone does not represent the average condition in the shear zone. Due to the high shearing velocities, an equilibrium state is not reached and the pore water pressure can have a large gradient in the vertical direction.
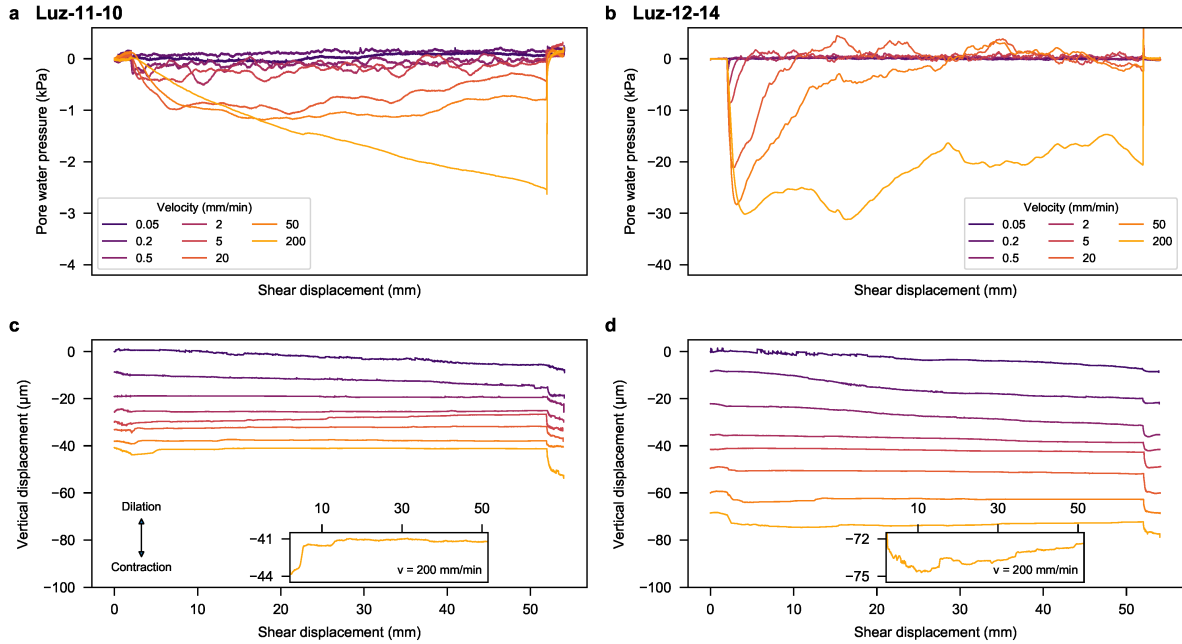
Figure 5.10: Results from single-stage test series of samples Luz-11-10 and Luz-12-14 for a normal stress of $\sigma_n = 400$ kPa. Evolution of pore water pressures (a, b) and vertical displacement (c, d).
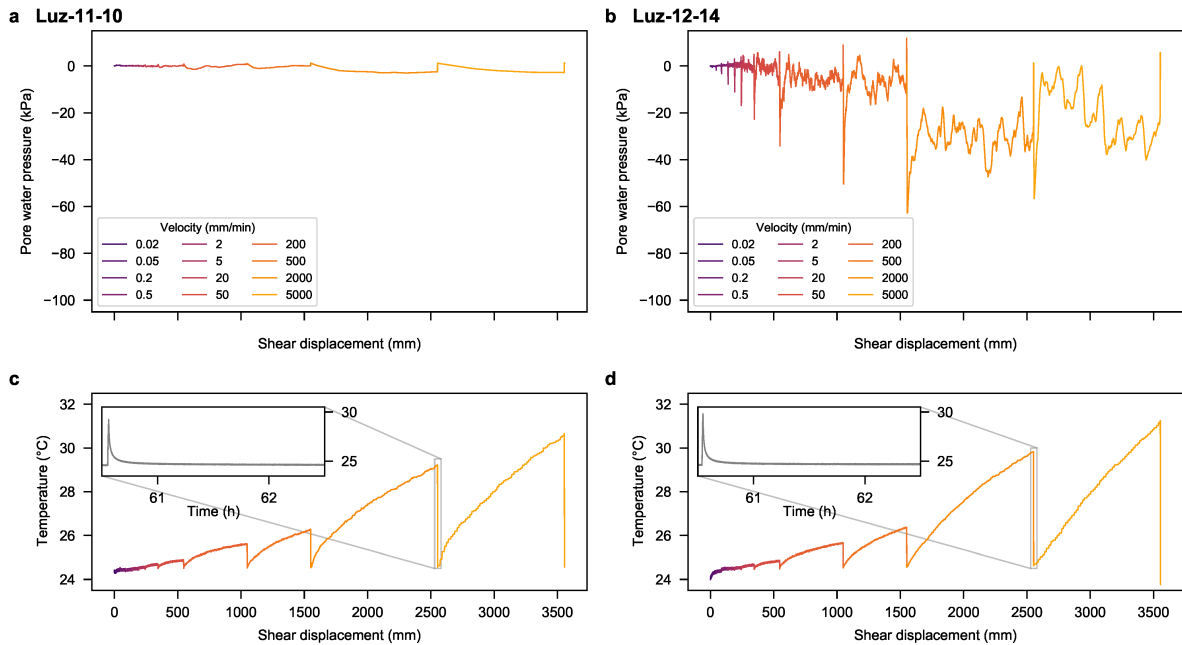
Figure 5.11: Results from multi-stage test series of samples Luz-11-10 and Luz-12-14 for a normal stress of $\sigma_n = 400$ kPa. Evolution of pore water pressures (a, b) and temperature (c, d).

5.4.3. Temperature effects

In order to investigate the effect of frictional heating on the shearing behaviour, the temperature inside the soil has been recorded during most of the tests shown above. While negligible in the single-stage series, a moderate temperature increase was consistently measured during fast shearing in the multi-stage tests (Figure 5.11c, d). In the fastest stage a steady increase of almost 8°C was recorded and the evolution suggests that ongoing shearing would lead to a further increase. Whether this increase does influence shearing or is just a result of it, is difficult to conclude. According to the few studies available on the effect of temperature on the residual strength (Bucher, 1975; Shibasaki et al., 2017; Yavari et al., 2016), a direct dependency for this type of soil is negligible. For soils with a much higher clay content and in particular for active clays, such a direct dependency can certainly be observed (Scaringi & Loche, 2022). An indirect influence by pore water pressure seems unlikely as well, since mainly negative pressure was measured. This is not surprising as the velocities are too low based on the numerical simulations by Pinyol & Alonso (2010). Therefore, specific tests at even higher velocities have been carried out.

In agreement with the findings on rate dependency, a positive rate effect can again be seen at the beginning of the tests (Figure 5.12a-c). However, the further evolution shows a different pattern for the three tested velocities. While the lowest velocity (0.05 m/s) shows a fairly constant resistance, a steady decrease can be observed for the middle velocity (0.1 m/s). At the highest velocity (0.2 m/s), there is a sharp drop in resistance after a peak reached at around 15 m shear displacement. As the shearing continues, a steady decrease similar to that of the middle velocity (0.1 m/s) is obtained. This behaviour can be explained by the generation of positive excess pore water pressures (Figure 5.12d-f). The observed offset between the increase in pore water pressure and the decrease in resistance at higher velocities can be explained by the fact that the water pressure is measured above the shear zone, further confirmed by the different evolution between the lower and upper rows of sensor. In the slowest test, on the other hand, fairly equalized pore water pressure is measured. The generation of excess pore water pressure is assumed to result from frictional heating and the associated faster thermal expansion of the water (Vardoulakis, 2002; Voight & Faust, 1982). This is confirmed in the test by plotting the evolution of the dissipation of mechanical work (Figure 5.12g-i) and the temperature (Figure 5.12j-l). The mechanical dissipation is calculated per unit volume for a shear zone thickness of $\delta_s = 2$ cm as

$$\dot{W} = \frac{\tau \bullet v}{\delta_s} \tag{5.1}$$

where τ denotes the shear stress and v the shearing velocity. If other dissipation mechanisms are neglected (especially acoustic emission), the mechanical dissipation is closely related to the heat rate generated in the shear zone. The drop in resistance can be also observed in the dissipation and explains why the rate of pore water pressure generation decreases with further shearing. The temperatures measured by the three thermocouple sensors differ noticeably, because their position inside the sample

depends on how they are bent during consolidation and shearing. This large temperature gradient has already been demonstrated in numerical calculations (Pinyol & Alonso, 2010; Vardoulakis, 2002). It can therefore be assumed that much higher temperatures are reached directly in the shear zone and even boiling of water seems realistic.
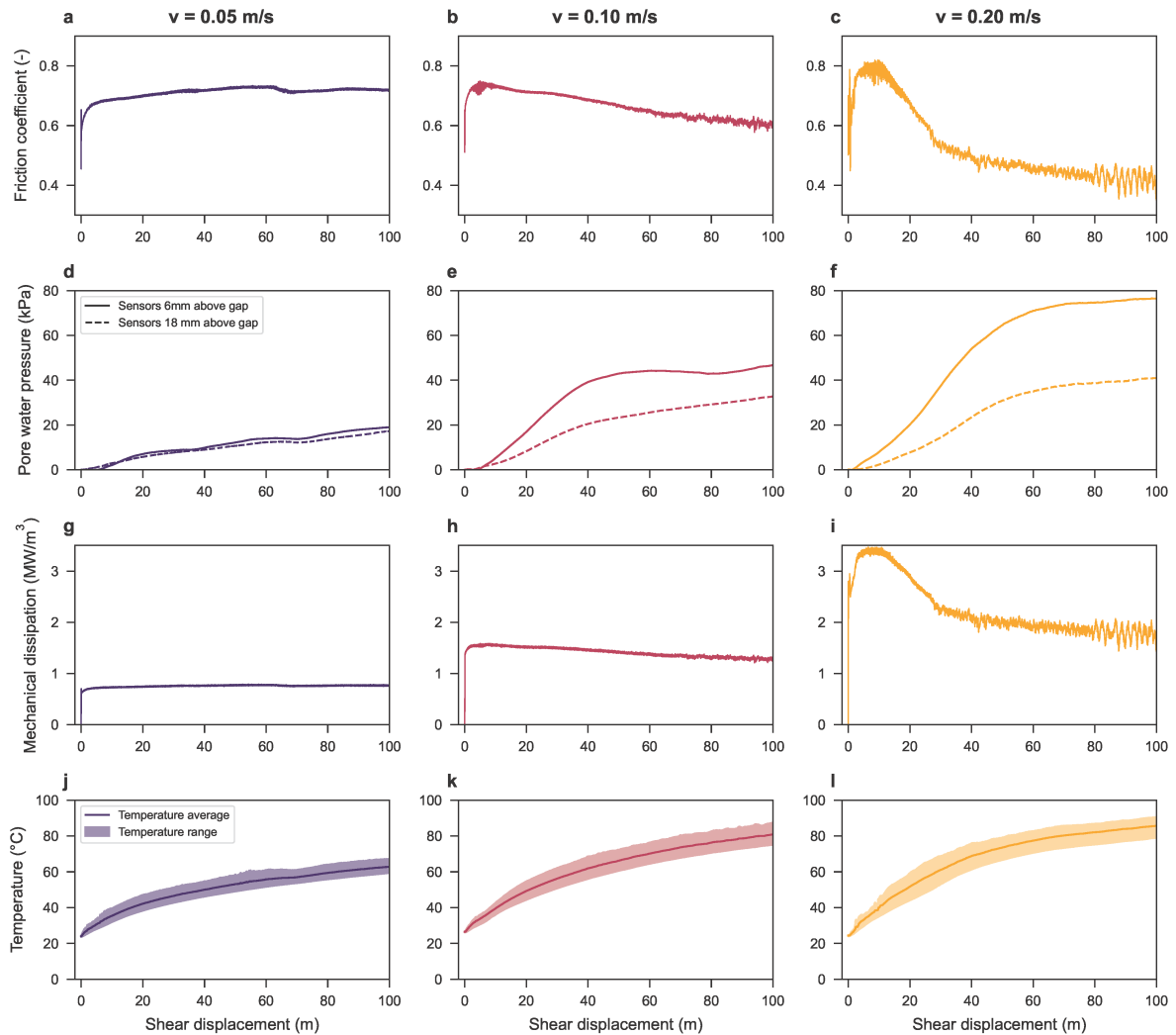

Figure 5.12: Results from the very rapid shearing test series of sample Luz-12-13. Evolution of the friction coefficient (a-c), pore water pressures (d-f), mechanical dissipation (g-i) and temperature (j-l).

5.5. Discussion

5.5.1. Comparison to other landslides

Different phenomena have been observed in the experiments performed in this study. Depending on the sample, typical patterns of the shearing behaviour of granular materials of varying intensity were evident, including a rate-and-state friction behaviour with a more or less pronounced fast peak. However, when the steady state behaviour is considered, the differences are smaller, which is not surprising given the similar grain size distributions. To put this into perspective, the range is shown in Figure 5.13 together with a selection of results from different landslides reported in other studies (Hu et al., 2017; Miao & Wang, 2021, 2022; Miao et al., 2014; Scaringi et al., 2018; Wang et al., 2010). The friction coefficients found in this study are clearly in the upper range (Figure 5.13a), which is consistent with the steep slope inclinations of the Marsc and Brattas landslide and is due to the composition of the soils. The samples from both landslides have a clay fraction of only 5-18 % and also include a high proportion of sand, resulting in such high shear resistance. Therefore, the presented range is in good agreement with other studies.

For landslide, rate effects are of particular importance, which can be shown by the normalisation with the slow residual strength (Figure 5.13b). It is evident that the values found in this study are in the middle of the range of literature data. In general, a mostly neutral to strongly positive rate effect can be observed for all of them. While there is still a slight rate-softening for the Xingfusi (Miao & Wang, 2021, 2022) and Kualiangzi (Scaringi et al., 2018) landslides at moderate velocities, both change to a clear rate-hardening behaviour at higher velocities. A similar trend was observed in this study, but only for low normal stresses, which are not representative of the actual landslide conditions. The comparison reveals that the positive rate effect correlates with the clay fraction (CF). This has been shown in several studies (Duong et al., 2018; Duque et al., 2023; Lemos, 2004; Tika et al., 1996) and is usually explained by the shear mechanisms proposed by Lupini et al. (1981). Granular soils, which are dominated by round grains, show a turbulent shear behaviour that leads to a neutral rate effect. If platy clay particles are present, a sliding mechanism occurs and leads to positive rate effects. This can also be confirmed by the presented results, as the sample with the lowest clay content exhibits the least rate effect. This is particularly evident in the slow periods of the multi-stage tests between the two high velocity steps. The samples with a high clay content show a continuous decrease in strength, which only returns to the slow-residual after a large shearing distance. The sample with hardly any clay, on the other hand, shows a rate-and-state frictional behaviour of an immediate strength drop and a following fast recovery to the slow-residual state. The same behaviour has been reported in other studies (Agliardi et al., 2020; Scaringi et al., 2018; Wang et al., 2023).
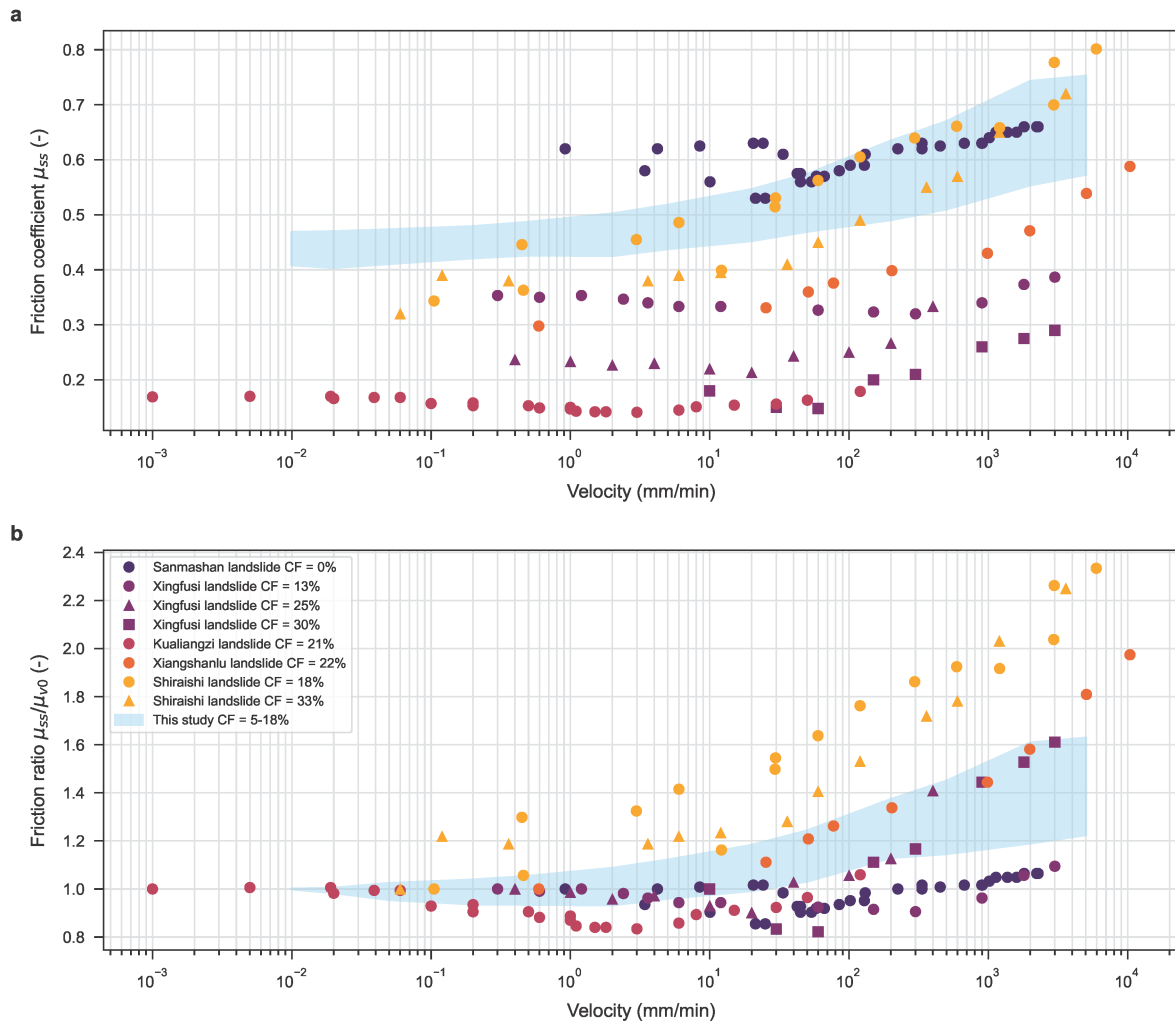
Figure 5.13: Comparison of the results of this study to results from other studies: Sanmashan landslide (Hu et al., 2017), Xingfusi landslides (Miao & Wang, 2021, 2022), Kualiangzi landslide (Scaringi et al., 2018), Xiangshanlu landslide (Miao et al., 2014) and Shiraishi landslide (Wang et al., 2010). CF refers to the clay fraction of the corresponding soils.

5.5.2. Implications on landslide dynamics

The residual strength and its rate dependency is a primary control of landslide motion (Schulz & Wang, 2014). Field observations on slow-moving landslide often show a direct correlation between the velocity and the ground water level (Bonzanigo et al., 2007; Corominas et al., 2005; Van Asch et al., 2009). During rainy periods and the associated rise of the water level, the effective stresses in the shear zone decrease and so does the resistance. Nevertheless, this does usually not lead to a collapse of the landslide, but to a slight acceleration. It is assumed that this behaviour is due to a rate-hardening shear zone. Laboratory tests on corresponding soil samples and the here presented results confirm this (Bhat & Yatabe, 2015; Li et al., 2017; Miao et al., 2014; Scaringi & Di Maio, 2016). The positive rate effect is considered to be the main reason why slow-moving landslide do not fail catastrophically even during extreme events such as heavy precipitation or earthquakes (Lacroix et al., 2020). On the contrary,

surprisingly small co-seismic displacements have been measured on La Sorbella (Ruggeri et al., 2020) and Maca (Lacroix et al., 2014) landslides. Given that these often are several centuries old, it is likely that they have already been exposed to several extreme events, in particular heavy precipitation. The fact that they have withstood these events may indicate that they are controlled by a pronounced rate hardening shear zone, which provides additional resistance at higher velocities and allows the landslide to slow down afterwards. This also applies to the two landslides considered in this study.

The catastrophic event of Vajont (Hendron & Patton, 1987) and other landslides showing a transition from slow-moving to fast acceleration (Carlà et al., 2019; Handwerger et al., 2019; Intrieri et al., 2018) illustrate that such a self-stabilizing behaviour cannot always be assumed. It is therefore important to make an appropriate assessment of potential scenarios for landslides that have a high potential for damage. In addition to field measurements and observations, laboratory tests on the material behaviour of the shear zone are of particular importance (Schulz & Wang, 2014). With the aid of ring shear tests, it has been possible to identify a negative rate effect for a number of failed landslides (Kang et al., 2022; Tika & Hutchinson, 1999; Yin et al., 2017), which is a possible explanation for their behaviour. Although no such effect was observed for the usually investigated range, additional tests were carried out at even higher velocities. At these velocities, an increase in pore water pressure can be measured and is attributed to friction heating. This results in a continuously decreasing resistance and thus a corresponding decrease in the heat rate, allowing a steady state to be reached before the friction drops completely. In order to reach such a high shearing velocity in the first place, an extremely high acceleration of the landslide is required. Due to the rate hardening behaviour, an even higher forcing on the landslide is required for such an acceleration. The results also show that a long shear path with this high velocity is necessary until the drop in resistance begins. It can therefore be assumed that for the two Alpine landslides in this study such a scenario is rather unlikely.

5.5.3. Limitations and further research

From the presented results it cannot be concluded, however, that the phenomenon of frictional heating is not relevant in general. Considering that the permeability of the samples tested was determined to be $k = 0.5 - 1 \cdot 10^{-9}$ *m/s*, these results could have been expected according to the numerical analyses of Pinyol & Alonso (2010). For more impermeable soils, this effect is expected to be much more pronounced, as the generated pore water pressures cannot be dissipated as quickly and thus no steady state can be reached. In fact, ring shear tests on samples from the Vajont slide exhibit a drop in resistance of 50% already at a much lower velocity and smaller shearing distance than the tests performed in this study (Tika & Hutchinson, 1999). Therefore, this phenomenon needs to be further investigated on different soil materials. It would be particularly interesting if this effect is rigorously studied on a set of samples with different permeability. A prediction for the results is difficult to make. Although the pore water pressures won't be dissipated that quickly in impermeable materials, the heat development is lower

due to the lower shear resistance of clayey materials and counteracts the generation of excess pore water pressure due to frictional heating.

It is has already been demonstrated that the residual strength is not affected by the initial structure of the soil and thus should not depend on the procedure for the sample reconstitution (Bishop et al., 1971). During fast shearing, however, the non-sheared material above and below the shear zone can also influence the results due to the effect on dissipation of pore water pressure and heat. In particular, the density, and therefore the permeability, can affect the evolution of excess pore water pressure, resulting in a different shear resistance. How strong this influence is has not yet been investigated.

The behaviour of landslides is an extremely complex process, which is usually determined by various factors and mechanisms. The shear characteristics described here and the findings regarding rate dependence, pore water pressures and temperatures are only part of the picture. Most landslides, like the ones discussed here, have different velocities along the shear zone due to topography and geology. This makes the overall behaviour of the landslide and its susceptibility to catastrophic events difficult to assess and cannot be judged solely on the basis of shear behaviour in the laboratory. The here presented results from the Luzzone landslide together with field measurements and simulations allowed Kohler et al. (2023) to assess the seismic behaviour of the landslide. This type of experimental tests should be carried on sample from other landslides with different kinematics in order to assess the influence and their behaviour.

5.6.   Conclusions

In this study, we present an improved ring shear apparatus to investigate rate, pore water pressure and temperature effects in shear zones. This apparatus incorporates the latest developments of ring shear devices combined with an improved shear box, which allows reducing friction, and simultaneously preventing leakage of water and soil. This allows to reliably assess rate effects over a very wide range of shearing rates and at the same time to provide an insight in the thermo-hydro-mechanical processes by means of local pore water pressure and temperature sensors. The capability of the apparatus is demonstrated by an experimental program on shear zone samples from two alpine landslides in Switzerland. In contrast to clay-dominated landslides materials, less is known about rate effects in these materials characterized by a high content of granular fractions. In this work, we provide insight into the transient behaviour during slow to fast shearing and show that these soils exhibit a moderately positive rate effect. We show that in these soils either zero or negative pore water pressure are generated during fast shearing. Although we measure a temperature increase inside the sample at high velocities, the associated expansion of the water is not sufficient to compensate for the negative pressures. Only at very rapid and extensive shearing, a considerable temperature and pore water pressure increase could be detected. This confirms that the phenomenon of frictional heating can indeed lead to often debated generation of excess pressures. However, we show that for the tested material this effect only occurs after long shearing and does not lead to a complete loss of shear strength. On the contrary, the reduction in shear strength causes a reduction in heat generation, allowing a new steady state to be reached. Based on that and the observed positive rate effects, catastrophic failure seems to be unlikely for these landslides. At the same time, the results suggest that for less permeable soils, frictional heating may indeed be a source of negative rate effect during very rapid shearing.

Data Availability

The data of the grain size distribution (Fig. 5.5), all the performed tests shown and the summary of the data (Fig. 5.8 and 5.9) are available at ETH Research Collection via https://doi.org/10.3929/ethz-b-000607909 licenced under Creative Commons Attribution 4.0 International (Kohler, 2023).

Notations

Small Latin letters

d	shear displacement	r_A	outer sample radius
d_0	shear displacement at slow velocity	r_I	inner sample radius
d_{init}	initial shear displacement	v	shearing velocity
h	sample height	v_0	slow shearing velocity
k	permeability	v_{init}	initial shearing velocity

Capital Latin letters

F_A	force at central axis	$\dot{W}$	mechanical dissipation

Small Greek letter

δ_s	shear zone thickness	σ_n	normal stress
μ_{ss}	steady state friction coefficient	τ	shear stress
μ_{v0}	slow steady state / residual friction coefficient		

References

Agliardi, F., Riva, F., Barbarano, M., Zanchetta, S., Scotti, R. & Zanchi, A. (2019). Effects of tectonic structures and long-term seismicity on paraglacial giant slope deformations: Piz Dora (Switzerland). *Engineering Geology*, *263*, 105353. https://doi.org/10.1016/J.ENGGEO.2019.105353

Agliardi, F., Scuderi, M. M., Fusi, N. & Collettini, C. (2020). Slow-to-fast transition of giant creeping rockslides modulated by undrained loading in basal shear zones. *Nature Communications*, *11*(1), 1–11. https://doi.org/10.1038/s41467-020-15093-3

Alonso, E. E. & Pinyol, N. M. (2010). Criteria for rapid sliding I. A review of Vaiont case. *Engineering Geology*, *114*(3–4), 198–210. https://doi.org/10.1016/J.ENGGEO.2010.04.018

Beutner, E. C. & Gerbi, G. P. (2005). Catastrophic emplacement of the Heart Mountain block slide, Wyoming and Montana, USA. *Bulletin of the Geological Society of America*, *117*(5–6), 724–735. https://doi.org/10.1130/B25451.1

Bhat, D. R. & Yatabe, R. (2015). Effect of shearing rate on residual strength of landslide soils. *Engineering Geology for Society and Territory - Volume 2: Landslide Processes*, 1211–1215. https://doi.org/10.1007/978-3-319-09057-3_212

Bishop, A. W., Green, G. E., Garga, V. K., Andresen, A. & Brown, J. D. (1971). A New Ring Shear Apparatus and Its Application to the Measurement of Residual Strength. *Géotechnique*, *21*(4), 273–328. https://doi.org/10.1680/geot.1971.21.4.273

Bonzanigo, L., Eberhardt, E. & Loew, S. (2007). Long-term investigation of a deep-seated creeping landslide in crystalline rock. Part I. Geological and hydromechanical factors controlling the Campo Vallemaggia landslide. *Canadian Geotechnical Journal*, *44*(10), 1157–1180.

Bromhead, E. N. (1979). A Simple Ring Shear Apparatus. *Ground Engineering*, *12*, 40–44.

Bucher, F. (1975). *Die Restscherfestigkeit natürlicher Böden, ihre Einflussgrössen und Beziehungen als Ergebnis experimenteller Untersuchungen*. ETH Zürich. https://doi.org/10.3929/ETHZ-A-000103428

Caloi, P. (1966). L'evento del Vajont nei suoi aspetti geodinamici. *Annals of Geophysics*, *19*(1), 1–74. https://doi.org/10.4401/ag-5037

Carlà, T., Intrieri, E., Raspini, F., Bardi, F., Farina, P., Ferretti, A., … Casagli, N. (2019). Perspectives on the prediction of catastrophic slope failures from satellite InSAR. *Scientific Reports*, *9*(1), 1–9. https://doi.org/10.1038/s41598-019-50792-y

Cooling, L. F. & Smith, D. B. (1936). The Shearing Reistance of Soils. In *Proceedings of 1st International Conference on Soil Mechanics and Foundation Engineering* (pp. 37–41).

Corominas, J., Moya, J., Ledesma, A., Lloret, A. & Gili, J. A. (2005). Prediction of ground displacements and velocities from groundwater level changes at the Vallcebre landslide (Eastern Pyrenees, Spain). *Landslides*, *2*(2), 83–96. https://doi.org/10.1007/S10346-005-0049-1

Crosta, G. B., Imposimato, S. & Roddeman, D. (2016). Landslide spreading, impulse water waves and modelling of the Vajont rockslide. *Rock Mechanics and Rock Engineering*, *49*(6), 2413–2436. https://doi.org/10.1007/S00603-015-0769-Z

Davies, T. R. H. (1982). Spreading of rock avalanche debris by mechanical fluidization. Rock Mechanics, 15(1), 9–24. https://doi.org/10.1007/BF01239474

Dieterich, J. H. (1979). Modeling of rock friction: 1. Experimental results and constitutive equations. *Journal of Geophysical Research: Solid Earth*, *84*(B5), 2161–2168. https://doi.org/10.1029/JB084IB05P02161

Duong, N. T., Suzuki, M. & Van Hai, N. (2018). Rate and acceleration effects on residual strength of kaolin and kaolin–bentonite mixtures in ring shearing. *Soils and Foundations*, *58*(5), 1153–1172. https://doi.org/10.1016/J.SANDF.2018.05.011

Duque, J., Loche, M. & Scaringi, G. (2023). Rate-dependency of residual shear strength of soils: implications for landslide evolution. Geotechnique Letters, 13(2), 1–8. https://doi.org/10.1680/JGELE.23.00004

Fukuoka, H., Sassa, K. & Wang, G. (2007). Influence of shear speed and normal stress on the shear behavior and shear zone structure of granular materials in naturally drained ring shear tests. In Landslides (Vol. 4, pp. 63–74). https://doi.org/10.1007/s10346-006-0053-0

Goldsby, D. L. & Tullis, T. E. (2011). Flash heating leads to low frictional strength of crustal rocks at earthquake slip rates. Science, 334(6053), 216–218. https://doi.org/10.1126/SCIENCE.1207902

Grelle, G. & Guadagno, F. M. (2010). Shear mechanisms and viscoplastic effects during impulsive shearing. *Géotechnique*, *60*(2), 91–103. https://doi.org/10.1680/geot.8.P.019

Gruner, H. E. & Haefeli, R. (1934). Beitrag zur Untersuchung des physikalischen und statischen Verhaltens kohärenter Bodenarten. *Schweizer Bauzeitung*, *103*, 171–174.

Handwerger, A. L., Huang, M. H., Fielding, E. J., Booth, A. M. & Bürgmann, R. (2019). A shift from drought to extreme rainfall drives a stable landslide to catastrophic failure. *Scientific Reports*, *9*(1), 1–12. https://doi.org/10.1038/s41598-018-38300-0

Hendron, A. J. & Patton, F. D. (1987). The vaiont slide — A geotechnical analysis based on new geologic observations of the failure surface. *Engineering Geology*, *24*(1–4), 475–491. https://doi.org/10.1016/0013-7952(87)90080-9

Hu, W., Huang, R. Q., McSaveney, M., Yao, L., Xu, Q., Feng, M. S. & Zhang, X. H. (2019). Superheated steam, hot CO_2 and dynamic recrystallization from frictional heat jointly lubricated a giant landslide: Field and experimental evidence. Earth and Planetary Science Letters, 510, 85–93. https://doi.org/10.1016/j.epsl.2019.01.005

Hu, W., Li, Y., Xu, Q., Huang, R., McSaveney, M., Wang, G., … Zheng, Y. (2022). Flowslide High Fluidity Induced by Shear Thinning. *Journal of Geophysical Research: Solid Earth*, *127*(12), e2022JB024615. https://doi.org/10.1029/2022JB024615

Hu, W., Xu, Q., Wang, G., Scaringi, G., Mcsaveney, M. & Hicher, P. Y. (2017). Shear Resistance Variations in Experimentally Sheared Mudstone Granules: A Possible Shear-Thinning and Thixotropic Mechanism. *Geophysical Research Letters*, *44*(21), 11,040-11,050. https://doi.org/10.1002/2017GL075261

Hungr, O. & Morgenstern, N. R. (1984). Experiments on the flow behaviour of granular materials at high velocity in an open channel. *Geotechnique*, *34*(3), 405–413. https://doi.org/10.1680/geot.1984.34.3.405

Hvorslev, M. J. (1939). Torsion shear tests and their place in the determination of the shearing resistance of soils. *Proceedings-American Society for Testing and Materials*, *39*, 999–1022.

Intrieri, E., Raspini, F., Fumagalli, A., Lu, P., Del Conte, S., Farina, P., … Casagli, N. (2018). The Maoxian landslide as seen from space: detecting precursors of failure with Sentinel-1 data. *Landslides*, *15*(1), 123–133. https://doi.org/10.1007/S10346-017-0915-7

Kang, X., Wang, S., Wu, W. & Xu, G. (2022). Residual state rate effects of shear-zone soil regulating slow-to-fast transition of catastrophic landslides. *Engineering Geology*, *304*, 106692. https://doi.org/10.1016/J.ENGGEO.2022.106692

Kohler, M. (2023). Ring shear test data on samples from two alpine landslides in Switzerland. https://doi.org/10.3929/ETHZ-B-000607909

Kohler, M., Hodel, D., Keller, L., Molinari, A. & Puzrin, A. M. (2023). Case Study of an Active Landslide at the Flank of a Water Reservoir and its Response During Earthquakes. Engineering Geology. https://doi.org/10.1016/j.enggeo.2023.107243

Lacroix, P., Handwerger, A. L. & Bièvre, G. (2020). Life and death of slow-moving landslides. *Nature Reviews Earth and Environment*, *1*(8), 404–419. https://doi.org/10.1038/S43017-020-0072-8

Lacroix, P., Perfettini, H., Taipe, E. & Guillier, B. (2014). Coseismic and postseismic motion of a landslide: observations, modelling, and analogy with tectonic faults, 38400. https://doi.org/10.1002/2014GL061170

Lemos, L. J. (2003). Shear behaviour of pre-existing shear zones under fast loading–insights on the landslide motion. *Intern. Conf.: Fast Slip Movements Prediction and Prevention for Risk Mitigation, Sorrento, Naples*, (c).

Lemos, L. J. (2004). Shear Behaviour of Pre-Existing Shear Zones Under Fast Loading. *Advances in Geotechnical Engineering: The Skempton Conference*, (1981).

Li, D., Yin, K., Glade, T. & Leo, C. (2017). Effect of over-consolidation and shear rate on the residual strength of soils of silty sand in the Three Gorges Reservoir. *Scientific Reports*, *7*(1), 1–11. https://doi.org/10.1038/s41598-017-05749-4

Lucas, A., Mangeney, A. & Ampuero, J. P. (2014). Frictional velocity-weakening in landslides on Earth and on other planetary bodies. Nature Communications, 5(1), 1–9. https://doi.org/10.1038/ncomms4417

Lupini, J. F., Skinner, A. E. & Vaughan, P. R. (1981). The drained residual strength of cohesive soils. *Géotechnique*, *31*(2), 181–213. https://doi.org/10.1680/geot.1981.31.2.181

Melosh, H. J. (1979). Acoustic fluidization: A new geologic process? Journal of Geophysical Research: Solid Earth, 84(B13), 7513–7520. https://doi.org/10.1029/JB084IB13P07513

Miao, H. & Wang, G. (2021). Effects of clay content on the shear behaviors of sliding zone soil originating from muddy interlayers in the Three Gorges Reservoir, China. *Engineering Geology*, *294*, 106380. https://doi.org/10.1016/J.ENGGEO.2021.106380

Miao, H. & Wang, G. (2022). Shear rate effect on the residual strength of saturated clayey and granular soils under low- to high-rate continuous shearing. *Engineering Geology*, *308*, 106821. https://doi.org/10.1016/J.ENGGEO.2022.106821

Miao, H., Wang, G., Yin, K., Kamai, T. & Li, Y. (2014). Mechanism of the slow-moving landslides in Jurassic red-strata in the Three Gorges Reservoir, China. *Engineering Geology*, *171*, 59–69. https://doi.org/10.1016/J.ENGGEO.2013.12.017

Mitchell, T. M., Smith, S. A. F., Anders, M. H., Di Toro, G., Nielsen, S., Cavallo, A. & Beard, A. D. (2015). Catastrophic emplacement of giant landslides aided by thermal decomposition: Heart Mountain, Wyoming. Earth and Planetary Science Letters, 411, 199–207. https://doi.org/10.1016/j.epsl.2014.10.051

Müller L. (1964). The rock slide in the Vajont Valley. *Rock Mechanics and Engineering Geology*, *2*(3), 148–212.

Okada, Y., Sassa, K. & Fukuoka, H. (2004). Excess pore pressure and grain crushing of sands by means of undrained and naturally drained ring-shear tests. Engineering Geology, 75(3–4), 325–343. https://doi.org/10.1016/j.enggeo.2004.07.001

Pinyol, N. M. & Alonso, E. E. (2010). Criteria for rapid sliding II.: Thermo-hydro-mechanical and scale effects in Vaiont case. *Engineering Geology*, *114*(3–4), 211–227. https://doi.org/10.1016/J.ENGGEO.2010.04.017

Puzrin, A. M. & Schmid, A. (2011). Progressive failure of a constrained creeping landslide. *Proceedings of the Royal Society A: Mathematical, Physical and Engineering Sciences*, *467*(2133), 2444–2461. https://doi.org/10.1098/rspa.2011.0063

Romero, S. U. & Molina, R. (1974). Kinematic aspects of the Vaiont slide. *International Journal of Rock Mechanics and Mining Sciences and Geomechanics Abstracts*, *11*(8), 162.

Ruggeri, P., Fruzzetti, V. M. E., Ferretti, A. & Scarpelli, G. (2020). Seismic and Rainfall Induced Displacements of an Existing Landslide: Findings from the Continuous Monitoring. *Geosciences 2020, Vol. 10, Page 90*, *10*(3), 90. https://doi.org/10.3390/GEOSCIENCES10030090

Ruina, A. (1983). Slip Instability and State Variable Friction Laws. *Jurnal of Geophysical Research*.

Sadrekarimi, A. & Olson, S. M. (2010). Particle damage observed in ring shear tests on sands. *Canadian Geotechnical Journal*, *47*(5), 497–515. https://doi.org/10.1139/T09-117

Sassa, K. (1984). The machanism starting liquefied landslides and debris flows. In *Proceedings of 4th International Symposium on Landslides* (pp. 349–354).

Sassa, K. (1996). Prediction of earthquake induced landslides. In *Proceedings of 7th International Symposium on Landslides* (pp. 114–132).

Sassa, K., Fukuoka, H., Wang, G. & Ishikawa, N. (2004). Undrained dynamic-loading ring-shear apparatus and its application to landslide dynamics. *Landslides*, *1*(1), 7–19. https://doi.org/10.1007/S10346-003-0004-Y

Scaringi, G. & Di Maio, C. (2016). Influence of Displacement Rate on Residual Shear Strength of Clays. *Procedia Earth and Planetary Science*, *16*, 137–145. https://doi.org/10.1016/j.proeps.2016.10.015

Scaringi, G., Hu, W., Xu, Q. & Huang, R. (2018). Shear-Rate-Dependent Behavior of Clayey Bimaterial Interfaces at Landslide Stress Levels. *Geophysical Research Letters*, *45*(2), 766–777. https://doi.org/10.1002/2017GL076214

Scaringi, G. & Loche, M. (2022). A thermo-hydro-mechanical approach to soil slope stability under climate change. Geomorphology, 401, 108108. https://doi.org/10.1016/J.GEOMORPH.2022.108108

Schluchter, C. (1988). Instabilities in the area of St. Moritz, Switzerland - geology, chronology, geotechnology. *Landslides. Proc. 5th Symposium, Lausanne, 1988. Vol 2*, 1375–1380.

Schulz, W. H. & Wang, G. (2014). Residual shear strength variability as a primary control on movement of landslides reactivated by earthquake-induced ground motion: Implications for coastal Oregon, U.S. *Journal of Geophysical Research: Earth Surface*, *119*(7), 1617–1635. https://doi.org/10.1002/2014JF003088

Shibasaki, T., Matsuura, S. & Hasegawa, Y. (2017). Temperature-dependent residual shear strength characteristics of smectite-bearing landslide soils. *Journal of Geophysical Research: Solid Earth*, *122*(2), 1449–1469. https://doi.org/10.1002/2016JB013241

Skempton, A. W. (1985). Residual strength of clays in landslides, folded strata and the laboratory. *Géotechnique*, *35*(1), 3–18. https://doi.org/10.1680/geot.1985.35.1.3

Sterba, I., Lang, H.-J. & Amann, P. (2000, November 19). The Brattas Landslide In St. Moritz. *ISRM International Symposium*.

Strauhal, T., Zangerl, C., Fellin, W., Holzmann, M., Engl, D. A., Brandner, R., … Tessadri, R. (2017). Structure, Mineralogy and Geomechanical Properties of Shear Zones of Deep-Seated Rockslides in Metamorphic Rocks (Tyrol, Austria). *Rock Mechanics and Rock Engineering*, *50*(2), 419–438. https://doi.org/10.1007/S00603-016-1113-Y

Tika, T. E. & Hutchinson, J. N. (1999). Ring shear tests on soil from the Vaiont landslide slip surface. *Géotechnique*, *49*(1), 59–74. https://doi.org/10.1680/geot.1999.49.1.59

Tika, T. E., Vaughan, P. R. & Lemos, L. J. (1996). Fast shearing of pre-existing shear zones in soil. *Géotechnique*, *46*(2), 197–233. https://doi.org/10.1680/geot.1996.46.2.197

Vafaei, N., Fakharian, K. & Sadrekarimi, A. (2019). An Experimental Study on Effect of Boundary Condition on Particle Damage in Shear Zone of Crushed Sand. Journal of Geophysical Research: Solid Earth, 124(9), 9546–9561. https://doi.org/10.1029/2018JB017153

Van Asch, T. W. J., Malet, J. P. & Bogaard, T. A. (2009). The effect of groundwater fluctuations on the velocity pattern of slow-moving landslides. *Natural Hazards and Earth System Sciences*, *9*(3), 739–749. https://doi.org/10.5194/NHESS-9-739-2009

Vardoulakis, I. (2002). Dynamic thermo-poro-mechanical analysis of catastrophic landslides. *Geotechnique*, *52*(3), 157–171. https://doi.org/10.1680/GEOT.2002.52.3.157

Voight, B. & Faust, C. (1982). Frictional heat and strength loss in some rapid landslides. *Geotechnique*, *32*(1), 43–54. https://doi.org/10.1680/geot.1982.32.1.43

Wang, G. & Sassa, K. (2002). Post-failure mobility of saturated sands in undrained load-controlled ring shear tests. *Canadian Geotechnical Journal*, *39*(4), 821–837. https://doi.org/10.1139/t02-032

Wang, G., Suemine, A. & Schulz, W. H. (2010). Shear-rate-dependent strength control on the dynamics of rainfall-triggered landslides, Tokushima Prefecture, Japan. *Earth Surface Processes and Landforms*, *35*(4), 407–416. https://doi.org/10.1002/esp.1937

Wang, G., Watanabe, N., Hoshikawa, K., Furuya, G., Cai, F. & Wu, S. (2023). Diverse shear behaviors of clayey materials: Implications for differing landsliding behaviors within the same area in Niigata, Japan. *Engineering Geology*, *312*, 106932. https://doi.org/10.1016/J.ENGGEO.2022.106932

Yavari, N., Tang, A. M., Pereira, J. M. & Hassen, G. (2016). Effect of temperature on the shear strength of soils and the soil–structure interface. *Canadian Geotechnical Journal*, *53*(7), 1186–1194. https://doi.org/10.1139/CGJ-2015-0355

Yin, Y., Xing, A., Wang, G., Feng, Z., Li, B. & Jiang, Y. (2017). Experimental and numerical investigations of a catastrophic long-runout landslide in Zhenxiong, Yunnan, southwestern China. *Landslides*, *14*(2), 649–659. https://doi.org/10.1007/S10346-016-0729-Z

6   Case study of an active landslide at the flank of a water reservoir and its response during earthquakes

Abstract

Slow-moving active landslides are a widespread phenomenon and often cause major damage to infrastructure. Normally, such slow slides do not cause fatalities, but this can change during extreme events such as a heavy rain or a strong earthquake. In particular their response to earthquakes is only partially understood, while documented field observation of such cases are rare. Considering their mobile pre-seismic state, one would expect active slides to be highly susceptible to an acceleration during earthquakes. When such a landslide affects a flank of a water reservoir, the consequences of its collapse can be devastating due to subsequent tsunami waves overtopping the dam. In this article, a case study of a deep-seated slow-moving landslide with a volume of about 5 million m^3 at the flank of a water reservoir in the Swiss Alps is presented. Extensive field investigations and monitoring allow a profound understanding of the kinematics of the landslides and its dependency on the hydrological conditions. Together with laboratory ring shear tests, this forms the basis for quantifying rate effects in the shear zone over a very wide velocity range and allows formulating and calibrating an accurate mechanical landslide model. The material point method is used to investigate potential landslide scenarios during different earthquakes. The simulations show rather small co-seismic displacements and even for pessimistic scenarios, a threat from tsunami waves seems unlikely. This implies that slow-moving active landslides can be less susceptible to co-seismic acceleration than stable slopes due to their ductile behaviour.

6.1. Introduction

Landslides are a widespread natural hazard in mountainous regions and pose a threat to people and infrastructure. Of particular concern are landslides along lakes and reservoirs, where a collapse of the slide can cause a tsunami leading to catastrophic consequences. The Vajont landslide of 1963, remains one of the most devastating examples of the impact such events can have. As a result of this disaster, around 2000 people lost their lives and tremendous damage was caused (Hendron & Patton, 1987). In recent years, similar events of tsunamis generated by landslides (Gylfadóttir et al., 2017; Harbitz et al., 2014; Roberts et al., 2013) highlight the importance of understanding the behaviour of landslides and their consequences.

In this work, we follow the terminology of Lacroix et al. (2020) and define a slow-moving landslide as coherent mass that moves primarily by frictional sliding along a discrete shear zone that tends to be deep-seated (deeper than 3m). In contrast to other works (Cruden & Varnes, 1996; Hungr et al., 2014), this definition includes displacement rates ranging from a few millimetres to several meters per year. Slow-moving landslides are usually not directly associated with catastrophic events and are more likely to be the cause of slow-onset damage to infrastructures (Cevasco et al., 2018; Mansour et al., 2011; Puzrin et al., 2012). However, slow-moving landslides being in a state of dynamic equilibrium are often highly susceptible to changes in the environmental conditions such as precipitation and earthquakes and can pose a dormant hazard (Alvarado et al., 2019; Bontemps et al., 2020; Lacroix et al., 2020). In fact, the Vajont landslide experienced three years of slow motion at around 1m per year before the catastrophic acceleration in 1963 (Hendron & Patton, 1987). A similar transition from slow-moving to a fast acceleration has been observed for other landslides (Carlà et al., 2019; Handwerger et al., 2019; Intrieri et al., 2018). While it is well known that landslides can be influenced and triggered by earthquakes (Jibson et al., 1994; Keefer, 2002; Rodríguez et al., 1999), the response of slow-moving landslides to seismic shaking is sparsely reported and only a handful of cases can be found in literature. Most of these landslides show only small co-seismic displacements, ranging from less than a millimetre for La Sorbella landslide in Italy (Ruggeri et al., 2020) and a few centimetres for the Maca landslide in Peru (Bontemps et al., 2020; Lacroix et al., 2014) to a meter for several landslides in Nepal (Lacroix et al., 2022). It seems that slow-moving landslides are less susceptible to co-seismic acceleration as one would expect based on their pre-seismic active state.

The Newmark's sliding block analysis (Newmark, 1965) is usually applied to estimate the co-seismic displacements of slopes. It simulates a rigid block on an inclined plane that is subjected to an earthquake input motion. The real geometry and the geotechnical properties are simplified and reduced to two parameters, the inclination of the plane and the static safety factor of the block. The latter leads to problems in the analysis of active landslides, as these are in a quasi-static equilibrium. It has been shown that this type of analysis does not provide a reliable tool for assessing the behaviour of active landslides during earthquakes (Kohler & Puzrin, 2022). In recent years, rigorous stress-deformation analysis has

become the state of the art (Hashash & Groholski, 2010), often using the finite element method (FEM). When dealing with landslides, however, special techniques need to be applied, which include a proper large deformation formulation and do not suffer from mesh distortion. A comprehensive review of different numerical approaches was provided by Soga et al. (2016). Amongst them, the material point method (MPM) (Sulsky et al., 1994) has become popular for landslide simulations (Andersen & Andersen, 2010; Bandara et al., 2016) and has been extended by the implementation of seismic boundary conditions (Kohler et al., 2021).

In their recent study, Kohler & Puzrin (2022) show that MPM can accurately model the co-seismic response of La Sorbella landslide in Italy to moderate recorded ground motions. By subjecting the same model to stronger ground motions, they demonstrated the potential of this methodology to gain a better understanding of the landslide seismic behaviour and to serve as a tool for risk assessment. However, it is also emphasised that for a well-founded assessment, the in-depth knowledge of geotechnical and geophysical properties of an active landslide is required, based on extensive field measurements and appropriate experimental testing. Pinyol et al. (2022) present in a case study of the Marmayor landslide in Spain how the static and seismic action can be investigated using detailed geotechnical and hydrological models.

In this article, we present a case study of an active, slow-moving Marsc landslide located at the flank of the Luzzone water reservoir in the Swiss Alps. Extensive field measurements and monitoring form the basis for the in-depth investigation of the seasonal landslide behaviour, which will be presented in the first part of this paper. Combining these observations with the results of a lab program using the latest developments in ring shear testing, allows formulating well-founded geotechnical and hydrological models. This will be followed by the introduction of the MPM model and the corresponding constitutive models. Recorded earthquake signals underneath and at the surface of the landslide provide validation for the seismic response of the MPM model and the material parameters. Finally, we investigate the behaviour of the landslide during stronger earthquakes by subjecting the model to an array of input signals. The main goal of this article is to demonstrate how a comprehensive seismic analysis of an active landslide, including all steps from field measurements and laboratory testing to the subsequent numerical modelling, can be carried out and used to gain insights into the seismic landslide behaviour and the corresponding risks.

6.2. Case description

6.2.1. Location and history
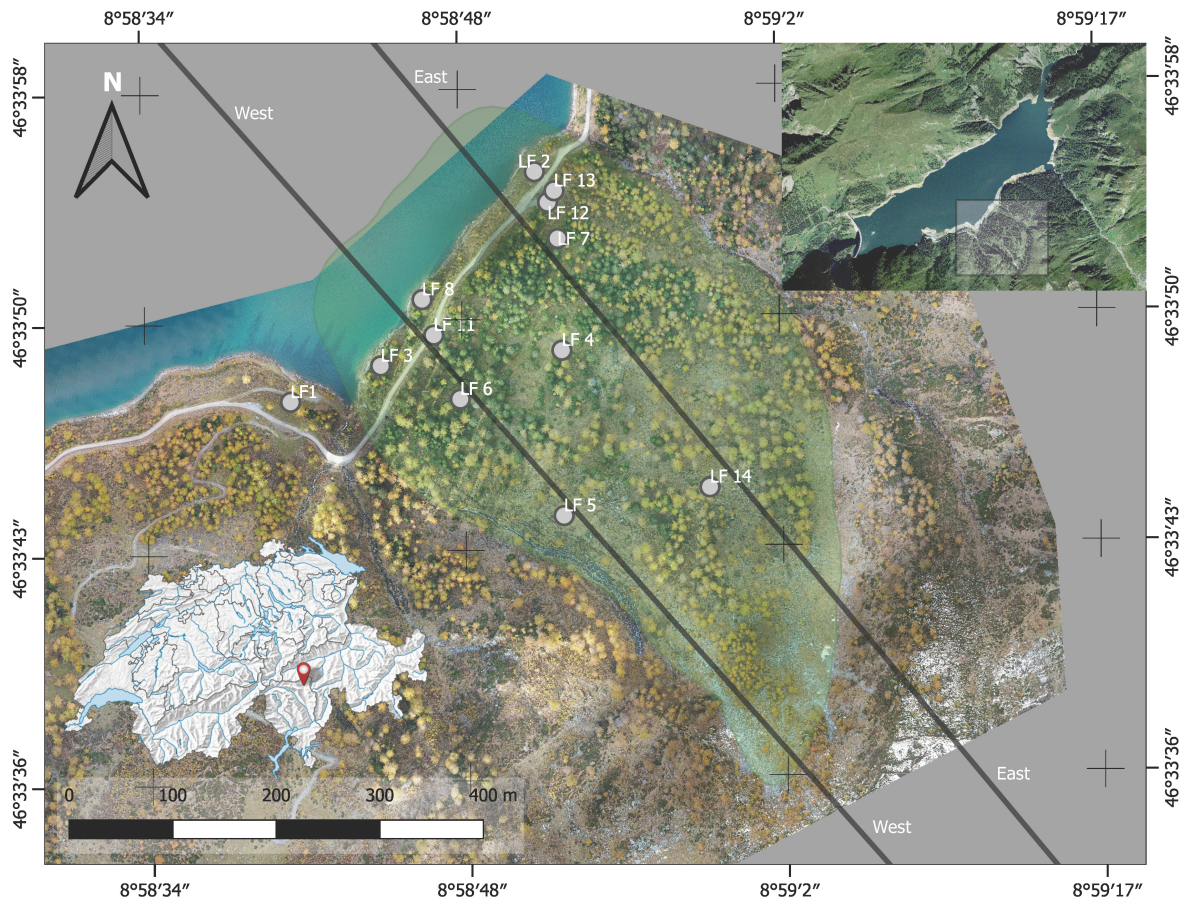
Figure 6.1: Map of the Marsc landslide. Location of the Luzzone water reservoir in southern Switzerland (bottom left) and location of the Marsc landslide at the flank of the reservoir (top right). Drone orthophoto showing the extent of the landslide (centre), location of the boreholes (LF1-8 and LF11-14) and cross sections East and West (middle). (source: Swiss Federal Office of Topography, swisstopo).

The Marsc landslide is located at the flank of the Luzzone water reservoir in the Canton Ticino, in the southern Swiss Alps (Figure 6.1). The Luzzone arch dam was constructed in the early 1960s and raised in the 1990s to the current height of 225 m. The storage capacity of the reservoir is at 108 million m³. Already during the first geological exploration for the construction of the dam, it was recognised that the area on the southern flank of the valley was that of an old landslide (Leupold, 1954). No evidence of movement could be detected during the construction and the filling of the reservoir. Later, however, sign of movements started to appear, necessitating intensive monitoring of the landslide since the 1990s. In the course of the latest field campaign in 2020, new core drillings were carried out and state of the art measuring instruments were installed.

6.2.2. Geology and geomorphology of the landslide

The Luzzone basin lies in a complex zone of sedimentary rocks, partly metamorphic and tectonically emplaced between the front of the Penninic nappes in the south and the Gotthard nappe in the north (Pfiffner, 2009; Pfiffner et al., 1990). It is characterized by a heterogeneous sequence of Jurassic phyllites and Triassic interbeds (e.g. dolomite, quartzite and phyllites), which were deformed and metamorphosed together with Permian gneiss conglomerate ("Verrucano") and Cretaceous schists ("Sosto-schist") during alpine folding (Figure 6.2) (Baumer et al., 2013; Vögeli et al., 2013). The rock sequence presents a dominant schistosity, parallel to the intensely folded rock stratigraphy. The folding axes lies parallel to the valley in SW-NE direction. The geomorphological development of the valley is largely dominated by fluvioglacial erosion, which is particularly evident on the southern shore of the lake in the form of morainic deposits (Baumer, 1964).
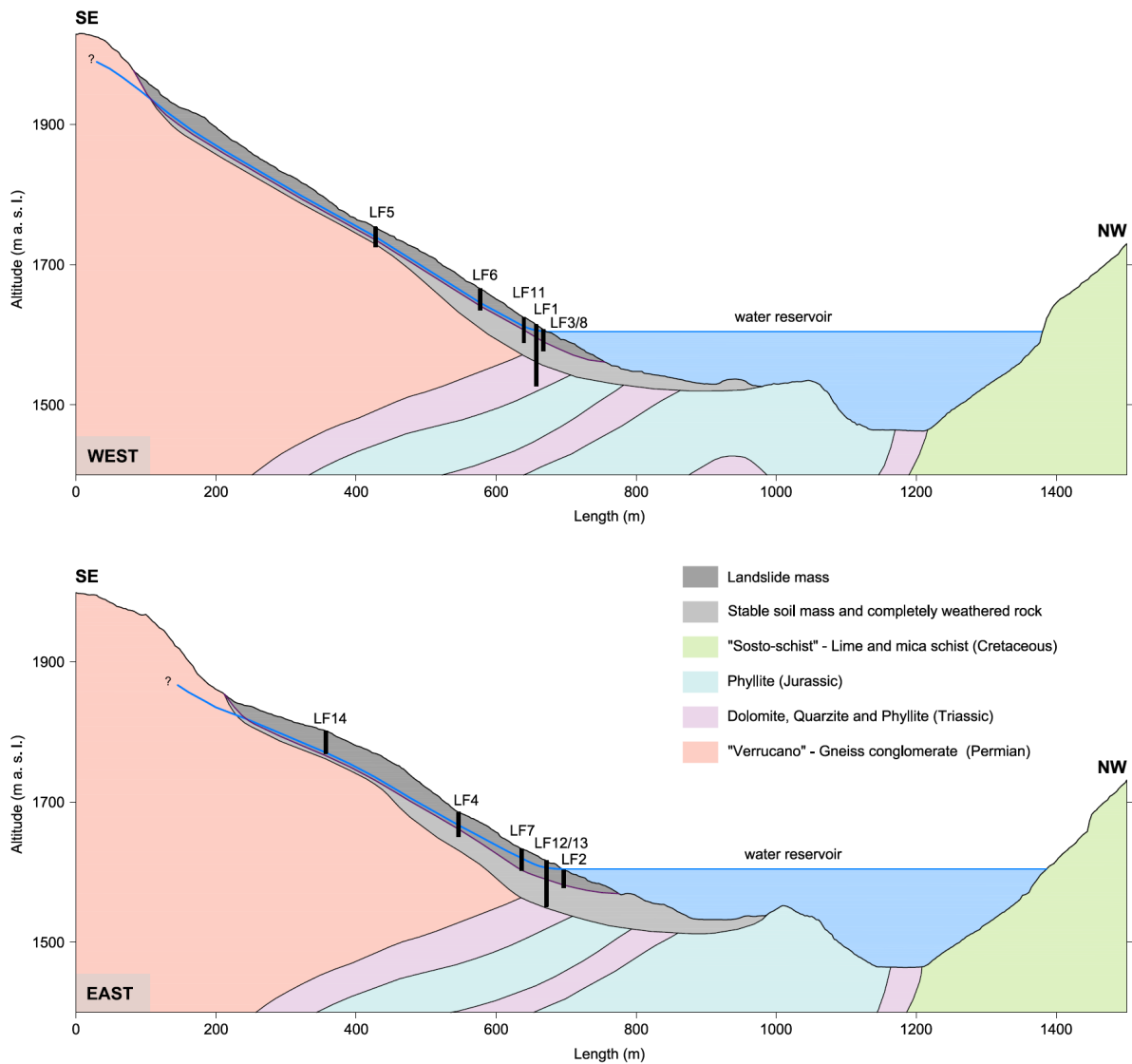
Figure 6.2: Geological cross sections of the landslide. Cross section West (top) and East (bottom) of the landslide including the water reservoir at maximal fill level (Baumer, 1993). The complex soil structure (including blocks and large boulders) is simplified as landslide mass and stable soil mass.

The Marsc landslide covers an area of almost 0.2 km² at the south-eastern flank of the reservoir and reaches from an elevation of 1560 m a.s.l. at the foot up to 1960 m a.s.l. at the top (Figure 6.3). The upper boundary runs along a steep scarp of highly fractured gneiss conglomerate. This regularly feeds the landslide with material by rockfall, which can be observed by numerous cobbles and boulders in this area. The width of the head scarp is only a few tens of metres, whereas the landslide widens towards the bottom to 400 m. Especially in the upper part, hardly any tree cover is present in the zone between the slide and the adjacent stable ground. This and the typically curved trunks of isolated trees highlight the moving area. At the maximal water level in the reservoir, the foot of the landslide is submerged by 40 m. However, when the reservoir level is low, the entire slide is exposed. It should also be mentioned that there is a second landslide, called Brunzano (Baumer, 1993), to the west of the one under consideration. This landslide is beyond the scope of this work as it is less active and there has been a strong decrease in the displacement rates over the last decade.
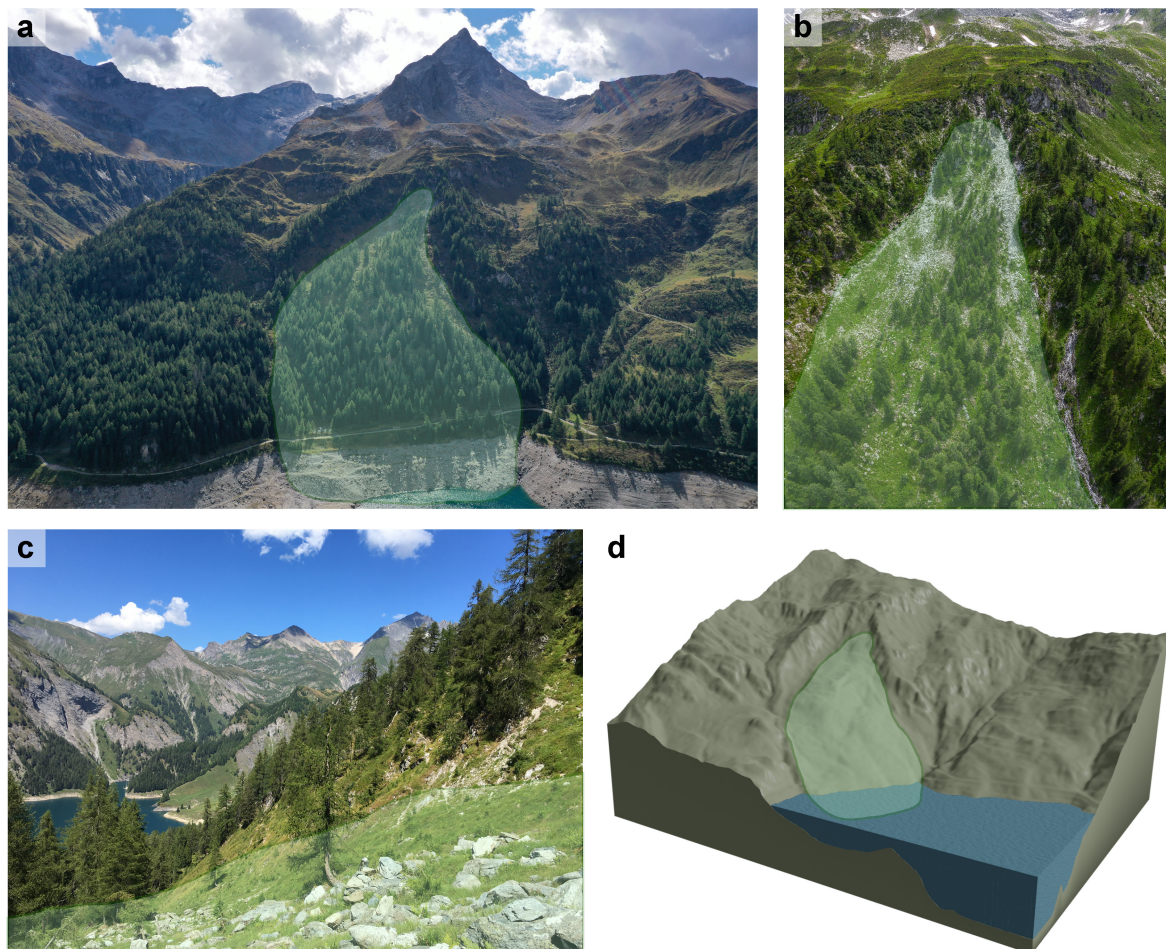
Figure 6.3: Images and 3D model of the landslide. Drone image showing the full extent of the landslide (a) and the upper part of the landslide including a headscarp (b). Image of the lateral boundary of the landslide (c). 3D terrain model of the landslide and the surroundings (d) (source DTM: Swiss Federal Office of Topography, swisstopo).

The cause of initiation and the age of the landslide are not known. However, the carbon dating of wooden relics found in a borehole at 20 m depth at the food of the slide indicate a large event around 320 BP. According to borings conducted at various locations (Figure 6.1), the slide consists of alternating layers of silty sand, gravel and embedded cobbles and boulders (Figure 6.4). The latter can be observed all over the surface of the slide. Inclinometer measurements have shown that it is a deep-seated landslide (Cruden & Varnes, 1996) with a distinct shear zone at a depth of 15 to 30 meters, which results in a total volume of the sliding mass of about 5 million m³. Below the shear zone, the borings reveal a similar highly disturbed engineering soil mass of variable thickness followed by several meters of a completely weathered Triassic rock. In fact, the layer starting at a depth of 55 m is a very dense silty sand, where the phyllitic texture with fine quartzite and dolomite bands is still clearly visible. This layer then shows a slow transition into fractured rock, followed by the intact bedrock in a depth of 60-70 m at the landslide's foot and at 20-30 m in the middle of the landslide. The soil material underneath the foot but above the completely weathered rock is presumably deposited by ancient landslides. The boreholes, which reach into this depth, show that since the beginning of the slide monitoring, all movement has been concentrated in the shear zone above this material. Furthermore, geodetic measurement points at the base of the slide show that the lower part of soil mass is not moving. The shear zone is located in a slightly finer graded layer of silt and silty sand with a thickness of 0.5-1 m. The average inclination of the shear zone is 30°, whereas the foot and the part in the southeast of the slide are milder.
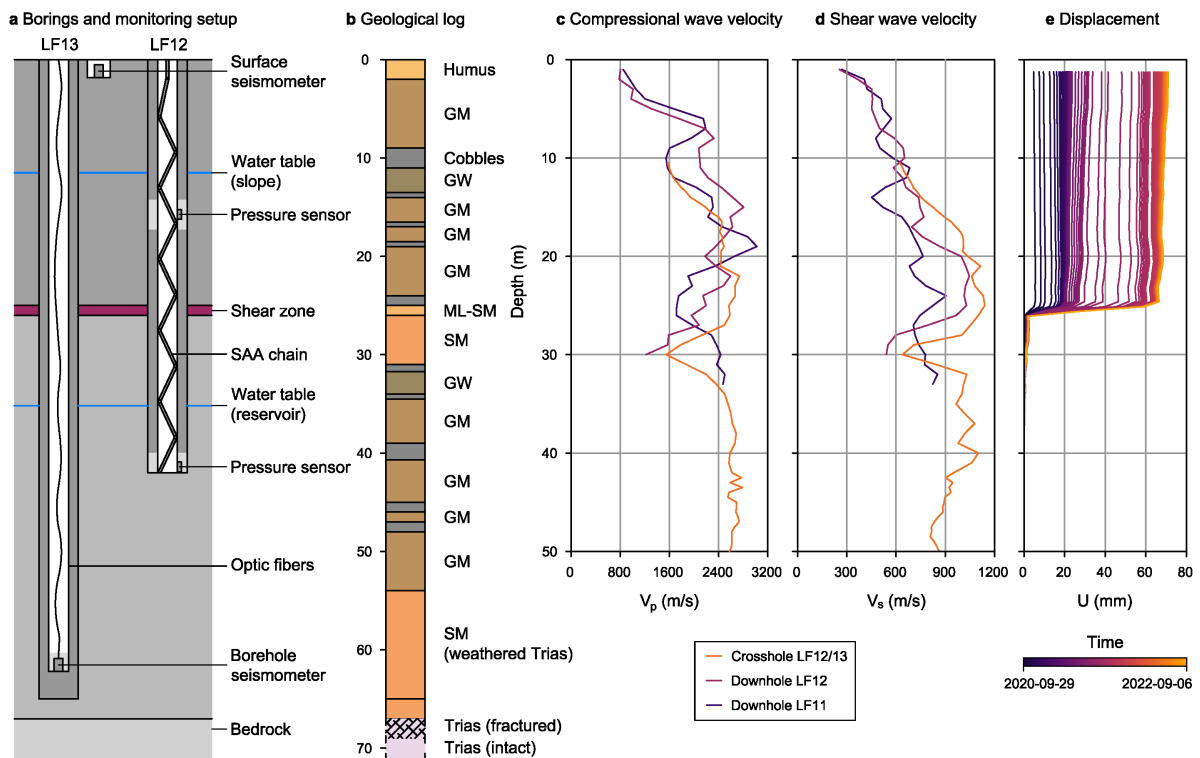
Figure 6.4: Monitoring setup, geological log and field measurements. Schematic drawing of the borings LF12/LF13 and the installed monitoring setup (a), geological log of boring LF13 (GM: silty gravel; GW: well-graded gravel; ML: silt; SM: silty sand) (b). Compressional (c) and shear (d) wave velocities from cross- and downhole testing between boreholes LF12/LF13. Landslide displacements from the SAA chain installed in borehole LF12 (e).

6.2.3. Landslide kinematics and hydrology

Due to the signs of landslide movements after the construction, a more detailed investigation of the area started in 1991. This included core drillings instrumented with inclinometers and a network of geodetic points to measure the surface displacements. The inclinometer measurements of the following years show that the landslide deforms mainly as a coherent mass with a distinct shear zone and little internal deformation. The highest annual displacement rates can be observed in the central and upper parts of the landslide (Figure 6.5). Furthermore, the western part (along profile "West") moves faster than the eastern part. The temporal evolution of the velocities, however, shows a variable behaviour during this time. After two year of slow movements at maximal values of 10 cm/year, the highest velocity of 1.2 m/year was measured in the upper part in 1993. This is mainly attributed to an exceptionally rainy period in October 1993. Such high velocities have not been measured since. After the dam was raised in 1998, the landslide showed an increase in movement over the next 4 years with a maximal measured velocity of 0.6 m/year in 2001. It is not clear how much of this was due to reservoir level rise and how much due to intense rainfall during this period. The phase of acceleration then ended and the slide has since shown a steadier behaviour with velocities of around 0.3 m/year at the top, 0.2 m/year in the western and less than 0.1 m/year at the eastern part (Figure 6.5). The accumulated displacements since the beginning of the measurements range from 2 m in the slower areas to almost 9 m in the fastest areas.

Based on observations during drilling and monitoring of standpipe piezometers, the presence of a single phreatic level in the landslide can be suggested. No signs of multiple or pressurised aquifers could be detected. It is assumed that the groundwater level runs approximately parallel to the shear zone, which can be explained by the presence of a fine, less permeable layer of several meters below the shear zone. Above the shear zone, the permeable gravelly layers lead to the observed fast reaction to rainfall events, confirmed by the strong correlation between displacements and precipitation. The piezometer measurements also show that the phreatic surface is influenced by the level of the reservoir. Above the landslide, neither the depth nor the behaviour of the groundwater table is known.

In order to gain a better understanding of the landslide and its dependence on hydrological conditions, new boreholes were drilled in 2020 and equipped with modern measuring systems with a high temporal resolution (Figure 6.4), including water pressure sensors attached to the outside of inclinometer tubes at various depths. To guarantee the water flow, the grouting was discontinued at the corresponding depth and replaced with a filter layer of silica sand. Shape Array sensors (SAA) were installed in the inclinometer tubes (Abdoun et al., 2009), built of linear sequences of instrumented rigid steel tube segments connected by flexible joints. In each of these segments three accelerometers are integrated to measure the tilt of each segment based on the acceleration relative to gravity in the x, y and z directions. The distribution of displacement along the SAA can be calculated from these tilts with respect to a fixed reference point.
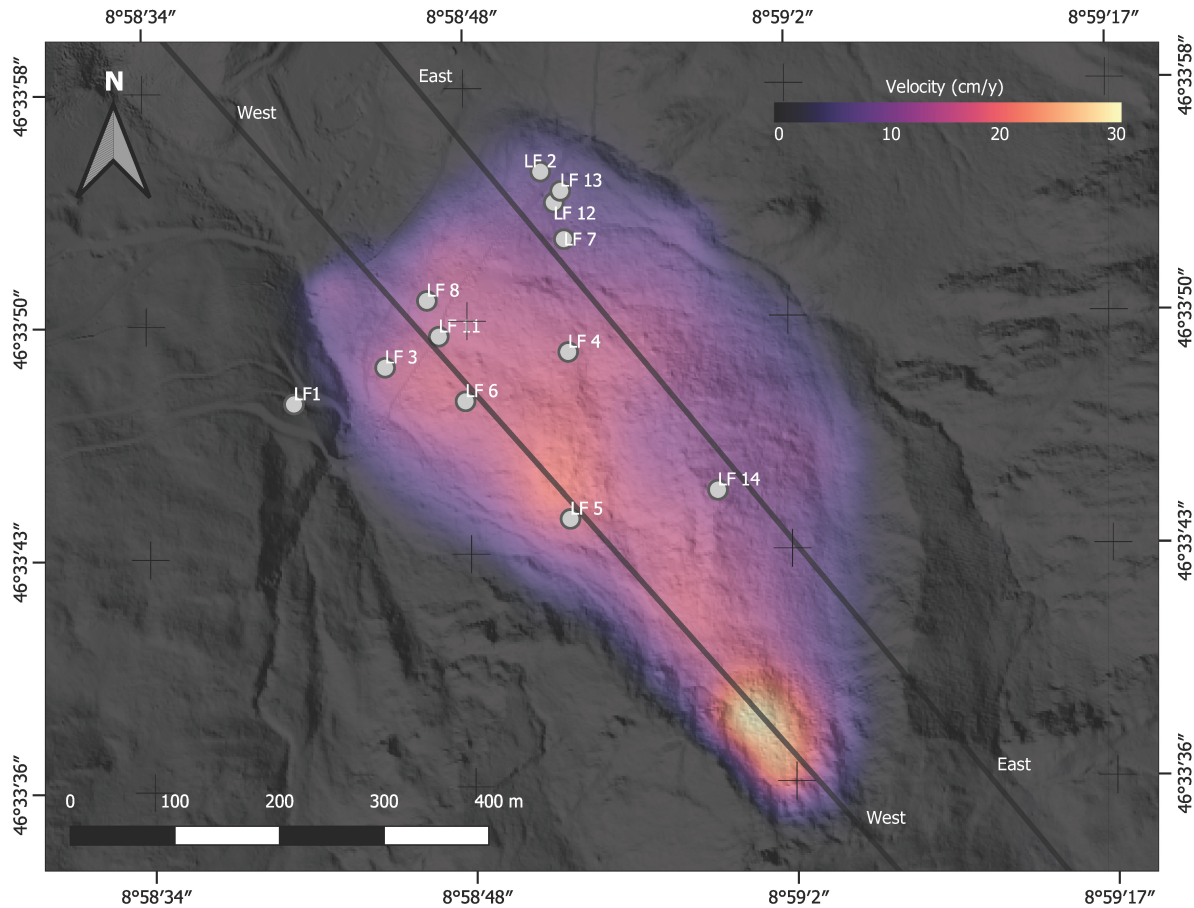
Figure 6.5: Spatial distribution of annual landslide velocities. The velocities are based on geodetic surface measurements from a fixed point on the opposite side of the lake and are taken in 2020 and 2021 (Grünefelder e Partner SA, 2022). (source DTM: Swiss Federal Office of Topography, swisstopo).

The setup for borehole LF12, located in the northeast, consists of a SAA and two water pressure sensors, one at the bottom of the borehole and one above the shear zone (Figure 6.4). The distribution of displacements along the SAA is shown in Figure 6.4 for different points in time and confirm the localised deformation pattern. The evolution of the landslide velocity and the water levels, derived from the water pressures, are presented in Figure 6.6 together with the level of the reservoir and the precipitation, measured 2 km from the landslide. The piezometric height obtained from the upper pressure sensor shows the groundwater level and illustrates the direct dependency and fast reaction time with precipitation. In general, a delay of 2-3 days in the peak of the groundwater level can be observed after heavy rainfall events. The pressure sensor at the bottom of the borehole behaves very differently. The comparison with the reservoir level shows that these are to a large extent identical with only small deviations during heavy rainfall events. At low reservoir level, the sensor remains dry. This suggests that the water level in the reservoir extends horizontally into the slope, but how far is not known. This also supports the assumption that the water in the landslide is flowing along the boundary of the less permeable layer below the shear zone.

The motion of the landslide is highly fluctuating and shows a strong seasonal pattern. The velocities range from 0.01 mm/d to peak values of 1 mm/d. Furthermore, there is a strong correlation between the logarithm of the velocity and the water table height, measured at the upper pressure sensor. However, the behaviour is not that straightforward, as can be clearly seen between May and July 2022. Despite high precipitation and a correspondingly high groundwater level, there is hardly any increase in landslide velocity. The cause is the interaction with the reservoir. At a low reservoir level, the foot of the landslide is not submerged providing a significantly more stable state. If the reservoir level is above 1600 m a.s.l., the landslide shows almost an immediate reaction to a rise in the groundwater level. However, it accelerates slightly slower than the rising water level resulting in a peak, which is delayed by about a day. This adds up to a delay between heavy rainfall and the peak in landslide velocity of about 3-4 days.
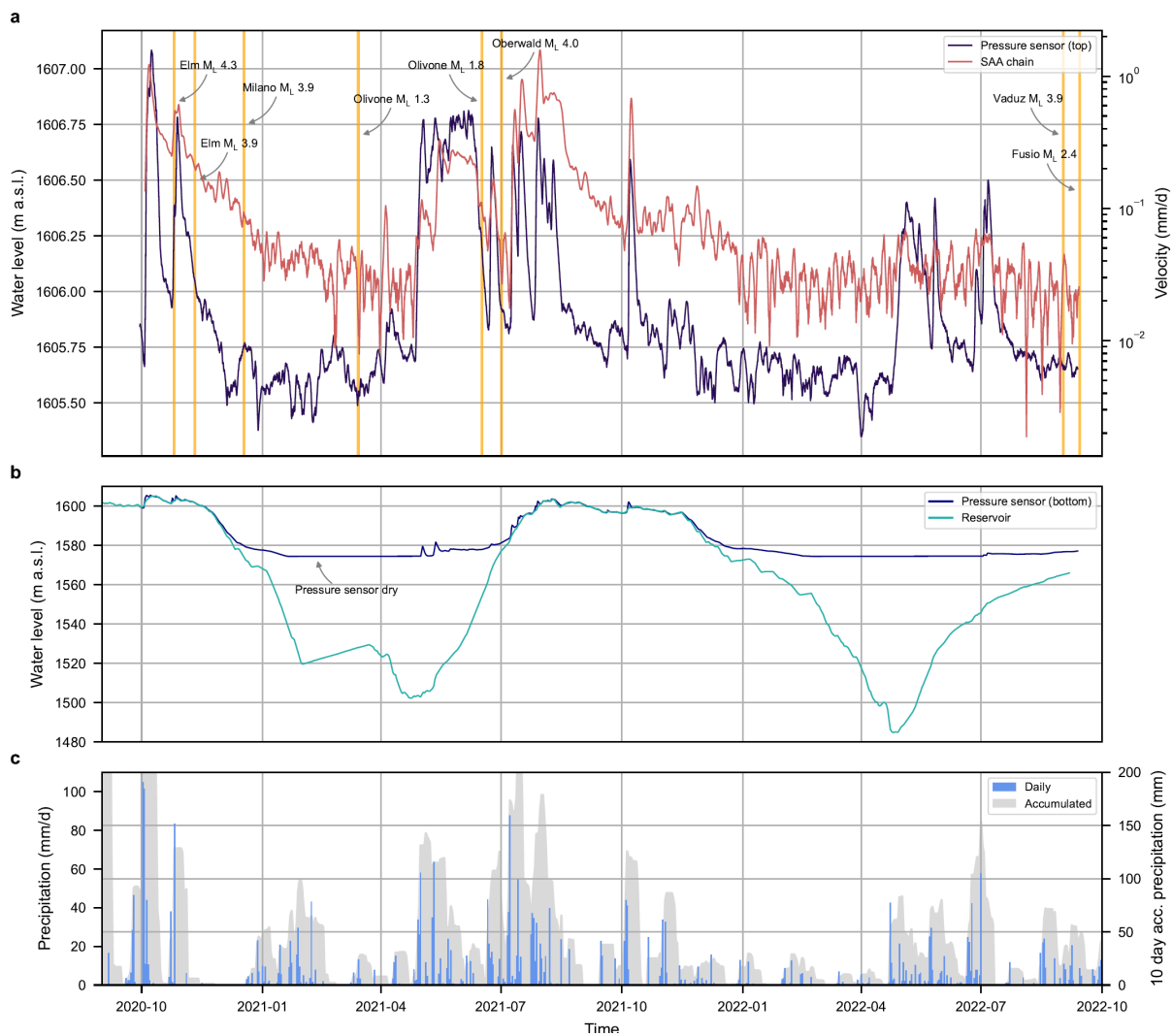
Figure 6.6: Landslide measurement. Landslide velocities from SAA chain, water level from upper pressure sensor in borehole LF12 and recorded earthquake events (a). (source earthquake characteristics: Swiss Seismological Service SED). Water level based on lower pressure sensor in borehole LF12 and reservoir level (b). Daily and 10 day accumulated precipitation measured at the dam 2 km from the landslide (c).

6.2.4. Geophysical characterization and earthquake monitoring

An extensive geophysical survey was carried out as part of the 2020 field campaign. This included downhole tests in various boreholes along the alpine road at the foot of the landslide. The boreholes LF12 and LF13 were drilled with a spacing of 13m, which allowed crosshole tests to be carried out. The results of the borehole measurements are shown in Figure 6.4. The P-wave and S-wave velocities show an increase down to about 20m depth. In the area of the shear zone and the fine layer below, a clear inversion of the velocity can be seen. Active and passive surface wave measurements were also carried out along longitudinal and transverse profiles (Figure 6.7). In addition to determining the S-wave velocity profile on a large part of the landslide, the aim of the surface measurements was primarily to explore the rock surface in the upper part. In combination with the geological log of the core drillings, the cross-sections in Figure 6.2 were made. Furthermore, the P-wave and S-wave velocity of the rock mass were measured at an outcrop of the Verrucano north of the landslide. This will serve as an approximation for the wave velocities of the underlying bedrock for the subsequent seismic analysis.
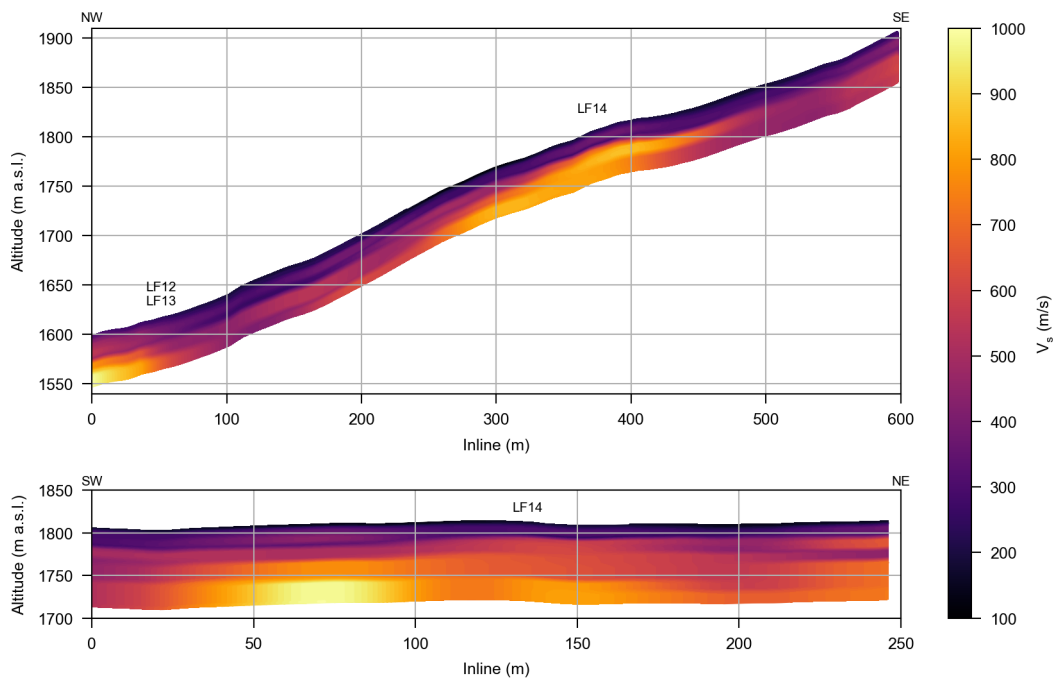
Figure 6.7: Shear wave velocity profiles. Longitudinal (a) and transversal (b) shear wave velocity profile based on active and passive surface wave analyses.

Since the main interest is the behaviour of the landslide during earthquakes, two seismometers were installed. The original intention was to drive the borehole LF13 into the bedrock in order to place a seismometer there. It turned out that the rock at this point is much deeper than originally assumed and could therefore not be reached. However, the surface wave measurements indicate that the underlying seismic bedrock is likely to be only couple of meters deeper. This is further confirmed by the comparison with the geological log of borehole LF1, which is located west of the landslide and was drilled deep into

the rock. Therefore, it was decided to place the seismometer at the base of the borehole. A second seismograph is placed in a manhole on the surface directly next to the borehole LF13. This arrangement of sensors allows for determining the amplification within the soil mass during recorded earthquakes. The transfer function $F_\theta(\omega)$ in the direction with azimuth θ between the two signals is given by (Kramer, 1996)

$$F_\theta(\omega) = \frac{\left|a_\theta^{top}(\omega)\right|}{\left|a_\theta^{bot}(\omega)\right|} = \frac{\left|a_N^{top}(\omega)\cos\theta - a_E^{top}(\omega)\sin\theta\right|}{\left|a_N^{bot}(\omega)\cos\theta - a_E^{bot}(\omega)\sin\theta\right|} \tag{6.1}$$

where ω represents the angular frequency. The Fourier transforms of the acceleration signals in θ-direction at the top and the bottom are denoted as $a_\theta^{top}(\omega)$ and $a_\theta^{bot}(\omega)$. The noisy Fourier amplitudes are smooth using the filter proposed by Konno & Ohmachi (1998). The transfer functions are shown in Figure 6.8 as polar plots for four recorded earthquake motions. The amplification shows a strong dependency on the direction, which is expected due to the complex topography. Clearly different amplification patterns can be observed depending on the location of the epicentre, which can also be attributed to the mountainous topography. A fairly uniform distribution can be seen for the deep Milano earthquake, whereas for the shallow earthquakes a pronounced directional dependence can be observed. However, for all the earthquakes, a first natural frequency of about 5 Hz can be detected in the landslide direction. The higher natural frequencies cannot be clearly distinguished and are in the range of 10-15 Hz. Continuous monitoring has the purpose to detect reaction of the landslide to earthquakes. Since all events recorded so far have been either very weak or farther away from the landslide, it is not surprising that no influence on the landslide has been observed (Figure 6.6).
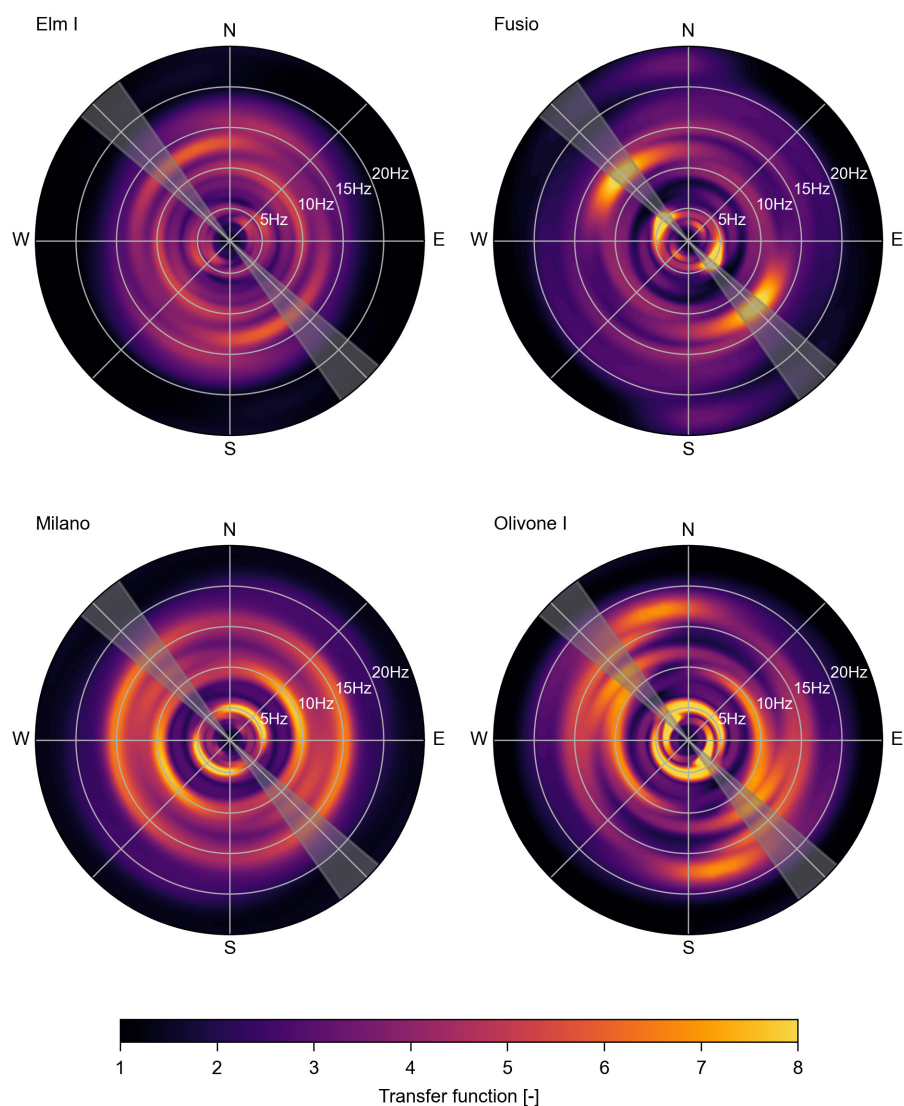
Figure 6.8: Transfer functions of recorded earthquakes. Polar plots of the transfer functions obtained from the earthquake signal at the bottom of the borehole and the surface. The direction of the landslide is shown by the shaded area in grey. Earthquake characteristics (local magnitude M_L, depth D, epicentral distance R (direction to epicentre)): Fusio $M_L = 2.4$, $D = 7.7$ km, $R = 28$ km (*West*). Elm I $M_L = 4.3$, $D = 1.4$ km, $R = 40$ km (*North*). Milano $M_L = 3.9$, $D = 56$ km, $R = 120$ km (*South*). Olivone I $M_L = 1.8$, $D = 7.8$ km, $R = 10$ km (*South*).

6.3.   Landslide model

6.3.1. Material Point Method (MPM)

The MPM is a numerical technique used in computational mechanics to simulate material behaviour under a very wide range of deformations. The material is represented as Lagrangian particles, while the equations of motion are solved on an Eulerian grid (Sulsky et al., 1994). The Eulerian solution procedure allows for the material to undergo large deformations, whereas the Lagrangian material representation provides a convenient way of tracking material properties and constitutive state variables (e.g. stresses and strains). In this work the seismic MPM framework proposed by Kohler et al. (2021) is applied. The

basic MPM code closely follows the concepts proposed by Stomakhin et al. (2013) and Jiang et al. (2015).

The MPM model of the Marsc landslide based on cross-section "West" is shown in Figure 6.9. The rock is simplified as homogenous elastic base, whereas the soil is separated into the strata of stable soil mass, shear zone and landslide. The reservoir is also included in the model by discretizing the water with material points. The groundwater table is introduced at its highest measured level, and the corresponding water pressure distribution is pre-calculated by solving numerically the problem of saturated flow through porous media using the software Optum G2 (Optum, 2021). Therefore, a seepage face boundary condition was used based on the groundwater table shown in Figure 6.9. It is neglected that the groundwater flow along the less permeable layer in the slope. As a result, the water pressure increases further below this layer. This simplification is justified because it is the water pressure in and above the shear zone that is decisive for the landslide behaviour. The results are transferred to the MPM model by assigning the static water pressure field to the corresponding material points.

The seismic MPM procedure consists of two main steps (Kohler et al., 2021). First, the static stress field within the slope is computed using kinematic boundary conditions and ramping up gravity as a body force using a smooth step. In a second step, the actual earthquake simulation is performed making use of the concept of a compliant base (Lysmer & Kuhlemeyer, 1969) and the lateral boundaries simulated as free-field columns (Wolf, 1989; Zienkiewicz et al., 1989).
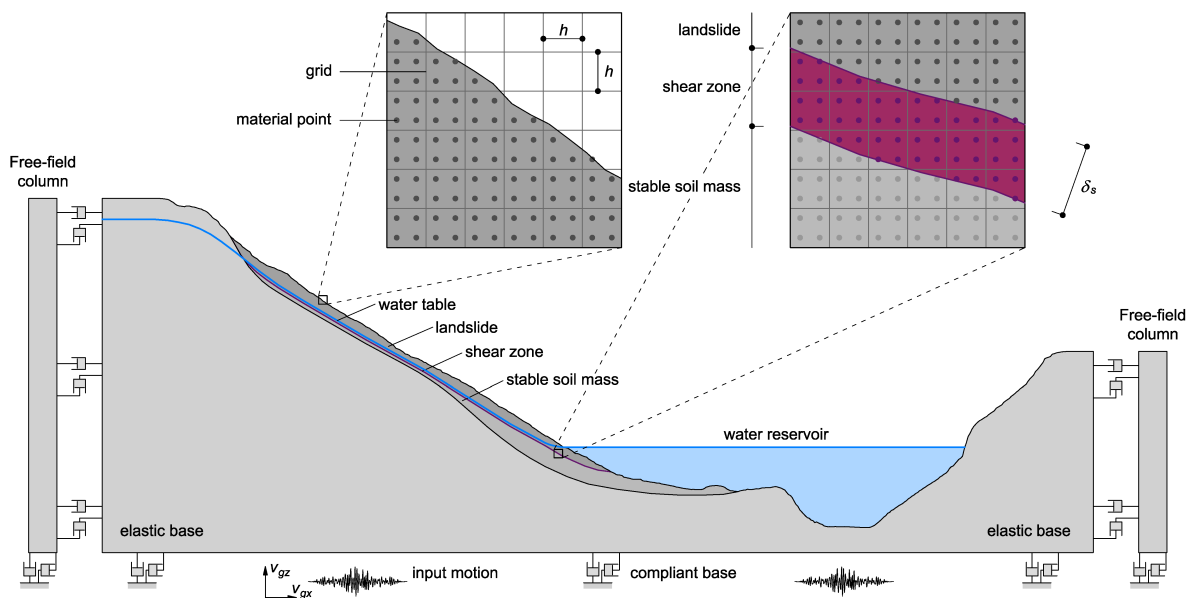
Figure 6.9: MPM landslide model. Schematic view of the MPM model of the landslide based on cross-section west, including the free-field columns at the lateral boundaries. The grid size is denoted with h and the thickness of the shear zone with δ_s. The earthquake motion is applied by a vertical and horizontal component denoted with ground velocities v_{gz} and v_{gx}.

6.3.2. General constitutive models

The simulation of complex phenomena like landslides involves multiple materials and therefore requires an appropriate selection of constitutive models. For a consistent application of finite strain elastoplasticity, it is common to use the multiplicative decomposition of the deformation gradient $F = F^e F^p$ into an elastic F^e and plastic contribution F^p (Lee, 1969). It is convenient to introduce the Henky strain $\boldsymbol{\varepsilon}$ (Hencky, 1928) as a measure to describe the elastic deformation as

$$\boldsymbol{\varepsilon} = \frac{1}{2}\ln\boldsymbol{B}^e = \frac{1}{2}\ln\left(F^e(F^e)^T\right) \tag{6.2}$$

where $\boldsymbol{B}^e$ denotes the elastic left Cauchy–Green strain tensor. This provides both a description of a purely elastic material (e.g., elastic base) and the elastic part of an elastoplastic material. The Kirchhoff stress $\boldsymbol{\tau}$ can be defined analogously to the commonly applied small-strain approach as

$$\boldsymbol{\tau} = 2\mu\boldsymbol{\varepsilon} + \lambda\mathrm{tr}(\boldsymbol{\varepsilon})\boldsymbol{I} \tag{6.3}$$

with the Lamé constants μ and λ, and the identity tensor $\boldsymbol{I}$. The soil (e.g., stable soil mass and landslide) is modelled with a Mohr-Coulomb yield criterion defined by

$$f(\boldsymbol{\tau}, \alpha) = (\tau_{max} - \tau_{min}) + (\tau_{max} + \tau_{min})\sin\varphi(\alpha) - 2c(\alpha)\cos\varphi \tag{6.4}$$

where τ_{max} and τ_{min} are the maximum and minimum principal stresses of the Kirchhoff stress tensor. The friction angle φ and the cohesion c of the material are both a function of the accumulated deviatoric plastic strain α in order to include isotropic strain hardening or softening. The plastic potential to define plastic flow is introduced as

$$g(\boldsymbol{\tau}, \alpha) = (\tau_{max} - \tau_{min}) + (\tau_{max} + \tau_{min})\sin\psi(\alpha) \tag{6.5}$$

where the dilatation angle ψ is a function of the accumulated deviatoric plastic strain as well. The implemented material model would allow to consider any piecewise linear function for the friction angle, dilation angle and cohesion. For the sake of simplicity, only a linear softening from the peak values φ, c and $\psi = \varphi$ to the residual values φ_r, c_r and $\psi_r = 0$ at the corresponding accumulated deviatoric plastic strain at the residual state α_r is considered. Applying the simplified regularization technique of a smeared crack approach (Rots et al., 1985) to avoid any dependency on the grid size, the plastic strain at residual state can be linked to the displacement δ_r (Kohler et al., 2021; Soga et al., 2016).

Different approaches exist to include damping in the simulation, from simplified approaches to complex nonlinear constitutive models (Kramer, 1996). Energy dissipation in materials is often represented by the introduction of viscous damping, which is mathematically convenient and computationally very efficient. In this case, the total stress $\boldsymbol{\tau}$ can be split into elastic and viscous contributions as

$$\boldsymbol{\tau} = \boldsymbol{\tau}^e + \boldsymbol{\tau}^v \tag{6.6}$$

where the elastic stress $\boldsymbol{\tau}^e$ is given by equation (6.3). The viscous stress $\boldsymbol{\tau}^v$ is introduced proportional to the deviatoric elastic strain rate as

$$\boldsymbol{\tau}^v = 2\eta \left(\dot{\boldsymbol{\varepsilon}} - \frac{1}{3}\mathrm{tr}(\dot{\boldsymbol{\varepsilon}})\boldsymbol{I} \right) \tag{6.7}$$

where the viscosity η can be chosen to match the damping ratio ξ at frequency f as (Kramer, 1996)

$$\eta = \frac{\mu\xi}{\pi f} \tag{6.8}$$

This can be interpreted as the stiffness proportional part of the classical Rayleigh damping, where damping increases linearly with frequency. The difference is that here only the deviatoric contribution is taken into account.

Water is simulated as weakly compressible using the Cole equation of state (Batchelor, 1967; Cole, 1948), which is usually applied in smooth particle hydro dynamics (SPH). The hydrostatic Cauchy stress tensor is given as

$$\boldsymbol{\sigma} = -p\boldsymbol{I} \tag{6.9}$$

The pressure p follows from the equation of state as a function of density ρ

$$p = \frac{\rho_0 c_s^2}{\gamma} \left(\left(\frac{\rho}{\rho_0} \right)^{\gamma} - 1 \right) \tag{6.10}$$

where $\rho_0 = 1000$ kg/m^3 is the reference density, $\gamma = 7$ and the speed of sound $c_s = 1500$ m/s, assuming only small changes in water density. In SPH a smaller speed of sound is usually chosen to avoid small explicit time steps (Monaghan, 1994). Since, the time increment is limited by the high stiffness of rock, the correct speed of sound is used here. This limits the density variations in the presented model to a maximum of 1‰.

6.3.3. Shear zone model

The shear zone is modelled by a viscoplastic material model based on the consistency model (W. M. Wang et al., 1997; Wedage et al., 1998). This model has been adopted for shear zones using an appropriate large strain formulation (Kohler & Puzrin, 2022). A Drucker-Prager yield surface matched to a Mohr-Coulomb surface in plane strain for flow at constant volume is assumed

$$f(\boldsymbol{\tau}, \dot{\alpha}) = \sqrt{J_2(\boldsymbol{s})} + \frac{J_1(\boldsymbol{\tau})}{3}\sin(\varphi_r^{NA}(\dot{\alpha})) \tag{6.11}$$

where $J_2(s)$ denotes the second invariant of the deviatoric stress tensor $s = \tau - 1/3 \, \mathrm{tr}(\tau)I$ and $J_1(\tau) = \mathrm{tr}(\tau)$ the first invariant of the stress tensor. The parameter defining the residual strength in the shear zone is the friction angle φ_r^{NA}, where the subscript emphasizes the difference to the residual angle φ_r that relates normal σ_n and shear stress τ_{nt} in the shear zone in the usual form $\tau_{nt} = \sigma_n \tan \varphi_r$. This difference is a consequence of the non-associated flow rule and the special kinematics of a shear zone. A detailed explanation is provided by Krabbenhoft et al. (2012), where the following relation between these angles is derived

$$\varphi_r^{NA} = \arcsin(\tan \varphi_r) \tag{6.12}$$

This relation is only valid for flow at constant volume and in the fully associated case they are identical ($\varphi_r^{NA} = \varphi_r$). Combining equations (6.11) and (6.12) leads to a description of the yield surface in terms of the angle φ_r

$$f(\tau, \dot{\alpha}) = \sqrt{J_2(s)} + \frac{J_1(\tau)}{3} \tan(\varphi_r(\dot{\alpha})) = \sqrt{J_2(s)} + \frac{J_1(\tau)}{3} \mu(\dot{\alpha}) \tag{6.13}$$

For the sake of convenience, the angle φ_r will be called residual friction angle in the following. This is consistent with Coulomb friction and the definition of the friction coefficient $\mu = \tan \varphi_r$. The frictional behaviour of the shear zone is introduced as a logarithmic function of the rate of the deviatoric plastic strain $\dot{\alpha}$ as

$$\mu(\dot{\alpha}) = \tan \varphi_r(\dot{\alpha}) = \tan \varphi_0 \left(1 + A \bullet \ln \left(\frac{\dot{\alpha} + \dot{\alpha}_0}{\dot{\alpha}_0} \right) \right) \tag{6.14}$$

where φ_0, A and $\dot{\alpha}_0$ are material parameters (Alonso et al., 2016; Handwerger et al., 2016; Wedage et al., 1998). The landslide velocity v can be linked to the rate of the equivalent plastic strain $\dot{\alpha}$ for a given shear zone thickness δ_s, assuming simple shear conditions, as

$$\dot{\alpha} = \frac{v}{\sqrt{3}\delta_s} \tag{6.15}$$

This link between velocity and strain rate is again based on the smeared crack approach proposed by Rots et al. (1985) and ensures that the results do not depend on the shear zone thickness. It is important to note that this also means that thickness of the numerical shear zone does not have to match the real conditions. More details on the rate dependent shear zone model and implementation details can be found in Kohler & Puzrin (2022).

6.3.4. Material parameters

The homogeneous elastic base is modelled using the wave velocities measured at the rock outcrop close to the landslide (Table 6.1). The great variability in the stratigraphy makes it difficult to assess the soil parameters based on lab testing, since the larger grain fractions cannot be taken into account. Various triaxial shear tests have been conducted on the finer layers from various depths (Halter, 1994). In addition, several large scale triaxial test were carried out on samples from different depths within the landslide mass, in which the gravel content could also be included. The comparison of these tests confirms a large scatter of soil strength, although the influence of the cobbles and boulders has not yet been account for. Nonetheless, this complex layered structure (except the shear zone) is modelled as homogenised material with parameters listed in Table 6.1, and the compressional and shear wave velocity linearly increasing from $v_{p,soil}^0$ and $v_{s,soil}^0$ to maximal values of $v_{p,soil}^{max}$ and $v_{s,soil}^{max}$ at a depth d_{max}. Based on the seismic tests (Figure 6.4), it is assumed that the drop in wave velocities in the depth at around 25-30 m can be attributed to the fine layer of the shear zone. Therefore, the shear zone is modelled with the corresponding lower seismic velocities $v_{p,shear}$ and $v_{s,shear}$ (Table 6.1).

For an accurate simulation of the landslide during earthquake shaking, the behaviour of the shear zone is crucial (Kohler & Puzrin, 2022). The mechanical properties of the shear zone can back-calculated from the field displacement and pore water pressure measurements or determined directly by laboratory tests; ideally both methods should lead to the same result. The high temporal resolution of the available landslide measurements and the observed strong correlation between landslide velocity and groundwater level allow for accurate back-calculation of the shear zone parameters. Therefore, scenarios of the observed different levels of groundwater and reservoir (Figure 6.6) are analysed using the strength-reduction method. On the one hand, this was done using MPM, whereby the friction angle of the shear zone was reduced incrementally until an unstable state was reached. For control purposes, the analogous procedure was also carried out with the software Optum G2 (Optum, 2021) based on finite element limit analysis using both lower and upper bound elements. For both methods, the groundwater level was introduced as previously described, but with the corresponding depth according to the scenarios. The obtained friction angle and the corresponding landslide velocity are presented in Figure 6.10a. Due to a rather different geometry and a strong simplification of the actual stratigraphy, it is not surprising that the results from different cross section do not match. However, for both cross-sections a strong linear correlation and similar inclinations of the regression lines can be observed, which in the semi-logarithmic plot of Figure 6.10 a correspond to the rate dependency parameter A (equation 6.14). The earthquake simulation can therefore be performed using this parameter in connection with the reference friction angle φ_0 corresponding to the cross section that is analysed (Table 6.1).

Care must be taken when back-calculating parameters using field displacement and pore water pressure measurements, as strictly speaking the calibration only covers the observed range of landslide velocities. While this procedure allows for reliable simulation of the landslide at velocities in the annually observed range, during an earthquake significantly higher velocities can be expected. To investigate the behaviour at these higher velocities, ring shear test have been conducted on samples retrieved from the landslide shear zone. The resulting slow residual friction angle at a velocity of 0.01 mm/min from different samples lies in the range of $\varphi_r = 24° \pm 1$ (Figure 6.10b), which is well below the minimum required value based on the strength-reduction analysis of the most stable scenario. Such a discrepancy between field and laboratory is a common problem and can have various causes (Corominas et al., 2005; van Asch et al., 2007). In this case, one of the main reasons is that only the fraction smaller than 2 mm could be tested in the ring shear apparatus, leaving gravel size particles constituting approximately 20% of material by weight excluded. In addition, the shear surface is modelled as smooth, but in reality it is rather an irregular surface, deviating around cobbles and blocks. Given the inhomogeneous structure of the landslide, it must also be questioned how representative local conditions are for the entire landslide. For this reason, the results of the ring shear tests cannot be directly transferred to the landslide model. Nevertheless, the ring shear tests are very important because they allow the behaviour of the shear zone to be studied at much higher speeds, which are not observed during the annual movements. Different test protocols covering a wide range of velocities have thus been conducted on the shear zone samples. The results show a strong rate hardening behaviour (Figure 6.10b). By normalising the friction with the corresponding slow residual friction coefficient μ_0 (the value defined using regression at the lowest measured velocity in each case), the rate dependency obtained from laboratory tests can be compared to the one back-calculated from the field measurements (Figure 6.10c). Despite the clear difference in shearing velocity, a similar trend of the rate hardening can be observed. In fact, the rate dependency parameter of $A = 0.03$ obtained by a regression of the ring shear results is only slightly higher than the value $A = 0.02$ based on the field observations. In the landslide analysis it is not unusual to obtain an order of magnitude difference in these values (Z. Li et al., 2020; van Asch et al., 2007). The reason that in this study they appear to be so close can be attributed to exceptionally high quality of both the field and the lab data. The value of $A = 0.02$ has been adopted as a conservative estimate for the rate effects.
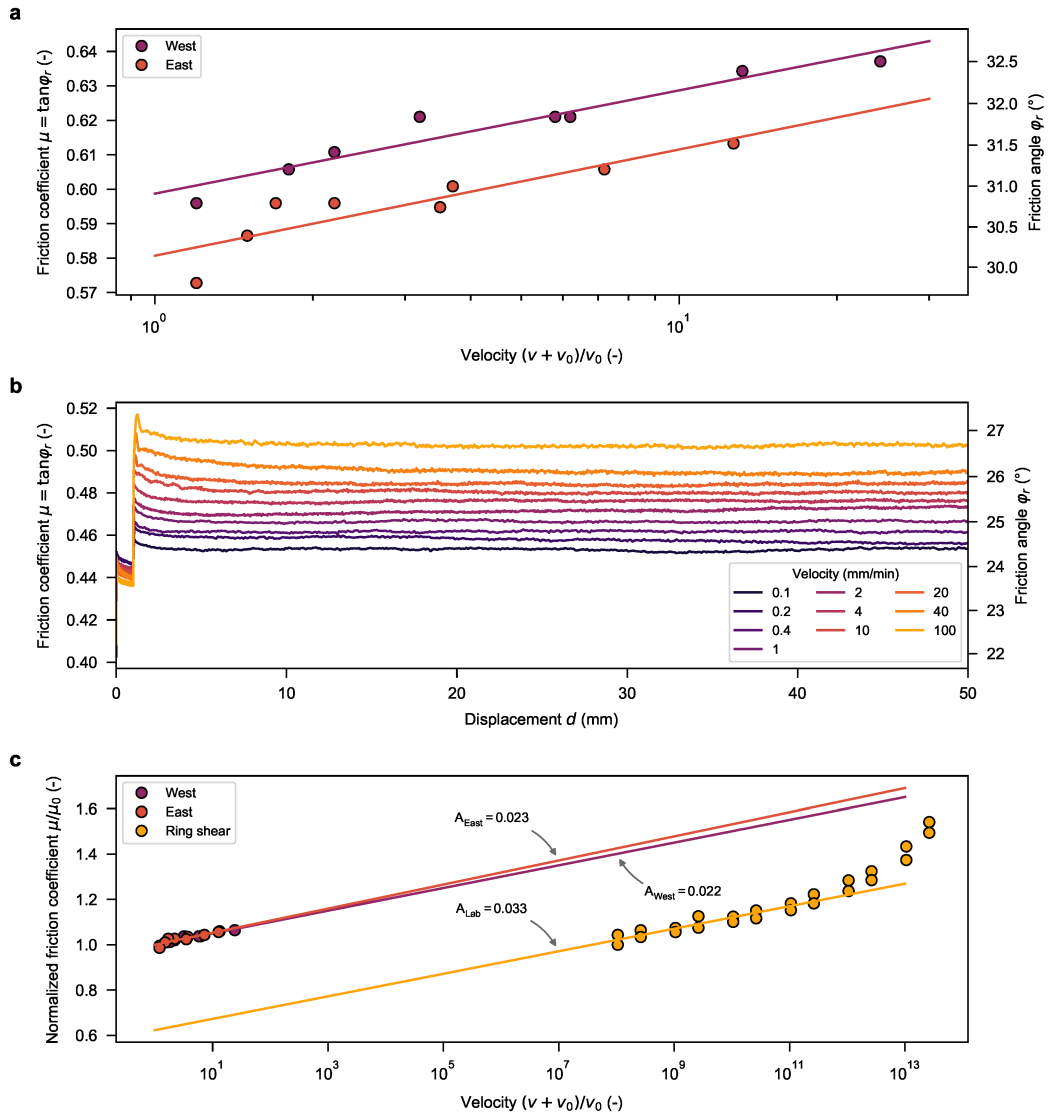
Figure 6.10: Rate dependency of the shear zone. Results of the strength reduction analysis for different groundwater and reservoir levels (a). Rings shear tests results on samples from the landslide shear zone at different shearing velocities (b). Comparison of the rate dependency derived from field observations and lab testing (c). The ring shear test results from the three highest velocities are not considered for the regression to not overestimate the rate dependency at lower velocities.

Table 6.1: Material parameters

Type	Parameter	Symbol	Value
Geometry	Grid size	h	0.5 m
	Number of MPs per grid cell	n_{MP}	2×2
Elastic base (rock)	Compressional wave velocity	$v_{p,base}$	3600 m/s
	Shear wave velocity	$v_{s,base}$	2200 m/s
	Density	ρ_{base}	2700 kg/m^3
Landslide and stable soil mass	Minimal compressional wave velocity	$v_{p,soil}^0$	700 m/s
	Maximal compressional wave velocity	$v_{p,soil}^{max}$	2500 m/s
	Minimal shear wave velocity	$v_{s,soil}^0$	200 m/s
	Maximal shear wave velocity	$v_{s,soil}^{max}$	900 m/s
	Depth of maximal wave velocity	d_{max}	18 m
	Density	ρ_{soil}	2100 kg/m^3
	Friction angle of slide	φ_{soil}	36°
	Cohesion of slide	c_{soil}	15 kPa
	Residual friction angle of slide (only Section 6.4.3)	$\varphi_{r,soil}$	31.0°
	Residual cohesion of slide (only Section 6.4.3)	$c_{r,soil}$	0 kPa
	Residual shear displacement of slide (only section 6.4.3)	$\delta_{r,soil}$	0.2 m
Shear zone	Compressional wave velocity	$v_{p,shear}$	1200 m/s
	Shear wave velocity	$v_{s,shear}$	600 m/s
	Shear zone thickness	δ_s	1.0 m
	Reference friction angle (west/east)	φ_0	31°/30°
	Reference velocity	v_0	0.1 mm/day
	Rate dependency parameter	A	0.02
Water	Reference density	ρ_0	1000 kg/m^3
	Density ratio exponent	γ	7
	Speed of sound	c_s	1500 m/s

6.4.   Seismic analysis

6.4.1.   Response to recorded earthquakes

In a first set of simulations, the model is validated against registered earthquakes. For this purpose, the MPM model for cross-section "East" is subjected to the signals, recorded by the seismometer inside borehole LF13. Due to the location of the sensor close to the intact rock surface within the stiff layer of completely weathered rock, the signal is treated as rock motion and directly applied to the MPM model. The results can be assessed using the transfer function (equation 6.1) between borehole and surface seismometer, which is calculated from the motion of two material points at the corresponding locations. The results are presented in Figure 6.11 for the recorded motions (in landslide direction) and the MPM simulations for different damping ratios. Since these earthquakes are very weak and therefore nonlinearity due to plasticity and large deformations is negligible, the amplification calculated in the MPM model is the same for all recorded earthquakes and thus, only the response to the Milano signal is shown. As has already been shown (Figure 6.8), the measured amplification is strongly directional and earthquake dependent. However, the recordings as well as the simulations show a clear fundamental frequency at around 4-5 Hz. The peak is less narrow in the measured signals, which is most likely due to the gradual transition from weathered to intact rock as well as 3D effects and is in agreement with the results from the geophysical survey. At higher frequency it becomes more diffuse and an increased amplification can be observed in the range of 10-20 Hz, which for the simulations including damping is already drastically decreased above 15 Hz. The influence of damping is even more evident above 20 Hz by a significant overestimation of amplification. However, these high modes are less of importance for slope stability analysis, since the corresponding modal masses are negligible compared to the lower modes (Kramer & Smith, 1997). In order not to underestimate the amplification between 10 and 15 Hz and to get a conservative analysis, viscous damping will not be considered in the following. For stronger earthquakes, viscous damping is anyway going to be small compared to the frictional one because of plasticity in the landslide body and friction in the shear zone.
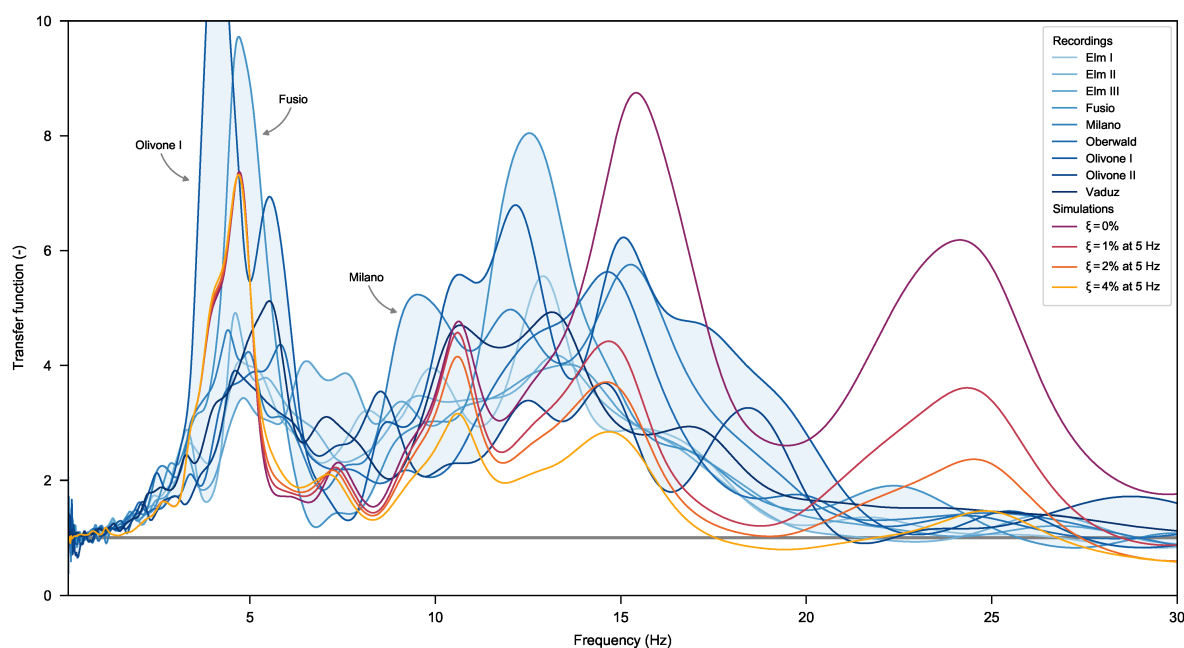
Figure 6.11: Comparison of the transfer function from recordings and simulations. The transfer function from the earthquake signal between the two seismometers is obtained for the direction of the landslide. The shaded area represents the envelope of the transfer functions from the recorded earthquakes. The simulated transfer functions are shown for different damping ratios.

6.4.2. Response to strong motion

In the above analysis of recorded earthquakes, MPM simulations produced negligible landslide displacements. This is consistent with the fact that no reaction of the landslide has been recorded in the field measurements (Figure 6.6). To assess the potential landslide response to stronger motions, the model is subjected to a set of available ground motion records presented in Table 6.2 ([dataset] Luzi et al., 2020). The seismic stations are classified as ground type A according to Eurocode 8 (Comité Européen de Normalisation, 2004) and are thus suitable as input on the elastic base. Following previous studies on co-seismic displacements (Jibson, 2007; Keefer, 2002), the Arias Intensity was chosen as the relevant intensity measure for the selection of signals. The goal is to get an idea about the order of magnitude for the corresponding landslide displacement. For a proper risk assessment, a representative set of input motions characteristic for the local seismic hazard during a defined return period should be selected instead.

The simulation for the Chichi earthquake is performed for both cross-sections to investigate the differences in their response and to determine which one is more relevant for further analysis. In order to separate the influence of geometry, this analysis is performed with a rate-independent shear zone ($A = 0$) and an assumption of a safety factor of $SF = 1.01$. The comparison of the evolution and the final displacements are presented in Figure 6.12. In the cross-section "West" the landslide moves nearly as a coherent body during the earthquake and shows almost identical behaviour at the top and bottom. The pattern of the "East" cross-section is clearly different, as the landslide behaves differently in the

upper and lower parts, with the upper, flatter part hardly undergoing any co-seismic deformation. It was already observed in the spatial distribution of the annual displacements (Figure 6.5) that this section exhibits considerably smaller yearly displacements than the rest of the landslide. While the lower part behaves similarly to the cross-section "West", it also shows a slightly lower final displacement. Therefore, in the following, to stay on the conservative side, all simulations will be carried out on the steeper cross-section "West".

Table 6.2: Earthquake data for strong motions

Earthquake	**Central Italy**	**Irpinia**	**Aegean Sea**	**Izmit**	**Chichi**
Date	30-10-2016	23-11-1980	30-10-2020	17-08-1999	20-09-1999
Magnitude M_W	6.6	6.9	7.0	7.6	7.7
Station	IT-MNF	IT-MNF	KO-GMLD	TK-4101	A-C074
Epicentral distance R_{epi} (km)	26.0	28.3	19.7	3.4	34.2
Considered direction	E	N	N	E	E
Arias intensity I_A (m/s)	0.16	0.27	0.67	0.98	1.09
Peak ground acceleration PGA_h [m/s^2]	1.31	0.94	2.12	2.29	2.29
Peak ground velocity PGA_v [m/s]	0.06	0.17	0.20	0.38	0.30
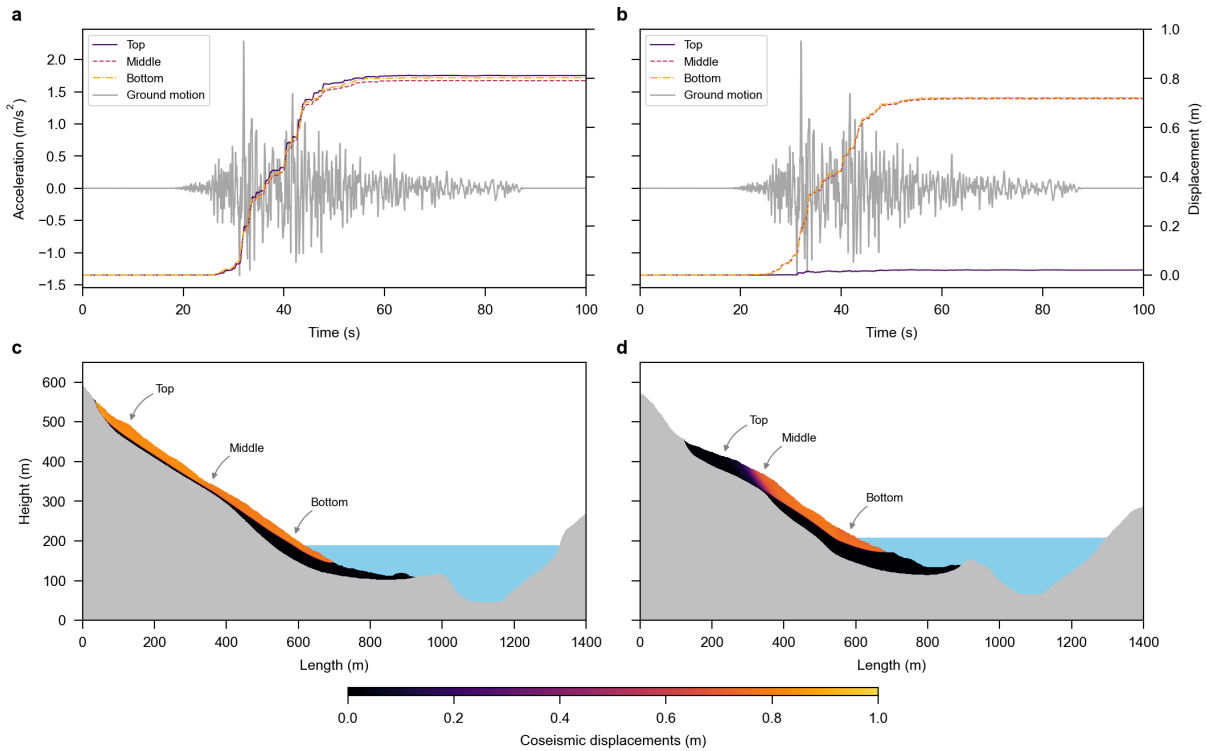
Figure 6.12: Comparison of the MPM simulation for cross section west and east. Earthquake acceleration and evolution of co-seismic displacements for cross sections west (a) and east (b). Distribution of the final displacements and location of the output points for the evolution for cross sections west (c) and east (d).

In order to achieve a better understanding of the landslide behaviour during different earthquakes (Table 6.2) and to investigate the influence of rate dependency in the shear zone, a parametric study has been performed. The shear zone is modelled by varying the rate dependency coefficient in the range of $A = 0.01 - 0.03$, around the values observed in field and lab measurements. The rate independent case ($SF = 1.01$) is also included in the simulations, in order to get a conservative estimate of the response. The resulting co-seismic displacements are presented in Figure 6.13. An identical pattern can be observed for all earthquakes, where the rate independent case leads to the largest displacements. As expected, an increase in rate dependency parameter A has the effect of reducing the co-seismic displacements. Considering the mobile quasi-static pre-seismic state of the landslide, the predicted motion of the landslide is surprisingly low, even without any rate dependency in the shear zone. As already suggested in other studies (Jibson, 2007; Keefer, 2002), the Arias intensity is the preferred seismic parameter to investigate effects of earthquakes on the landslide displacements. The summary of the results (Figure 6.13f) shows a direct correlation between the final displacements and the Arias intensity for a rate independent shear zone. For the other cases, however, the trend is not that conclusive. Comparing the Chichi earthquake (Figure 6.13d) with the Izmit event (Figure 6.13e), it can be observed that they both reach relatively high Arias intensities, but in a different manner. While in Chichi it is achieved via one large impulse, in Izmit it required several smaller ones. For low rate dependency, a higher Aries intensity in Chichi results in higher co-seismic displacements than in Izmit, which is consistent with the general trend (Figure 6.13f). In contrast, for high rate dependency, Chichi produces lower displacements, despite a higher Arias intensity. The reason for this could be that a higher rate dependent resistance will be mobilized during one large impulse in Chichi than in several small ones in Izmit, due to the higher velocity. However, for weaker earthquakes this does not seem to hold (e.g. Figure 6.13a, b).
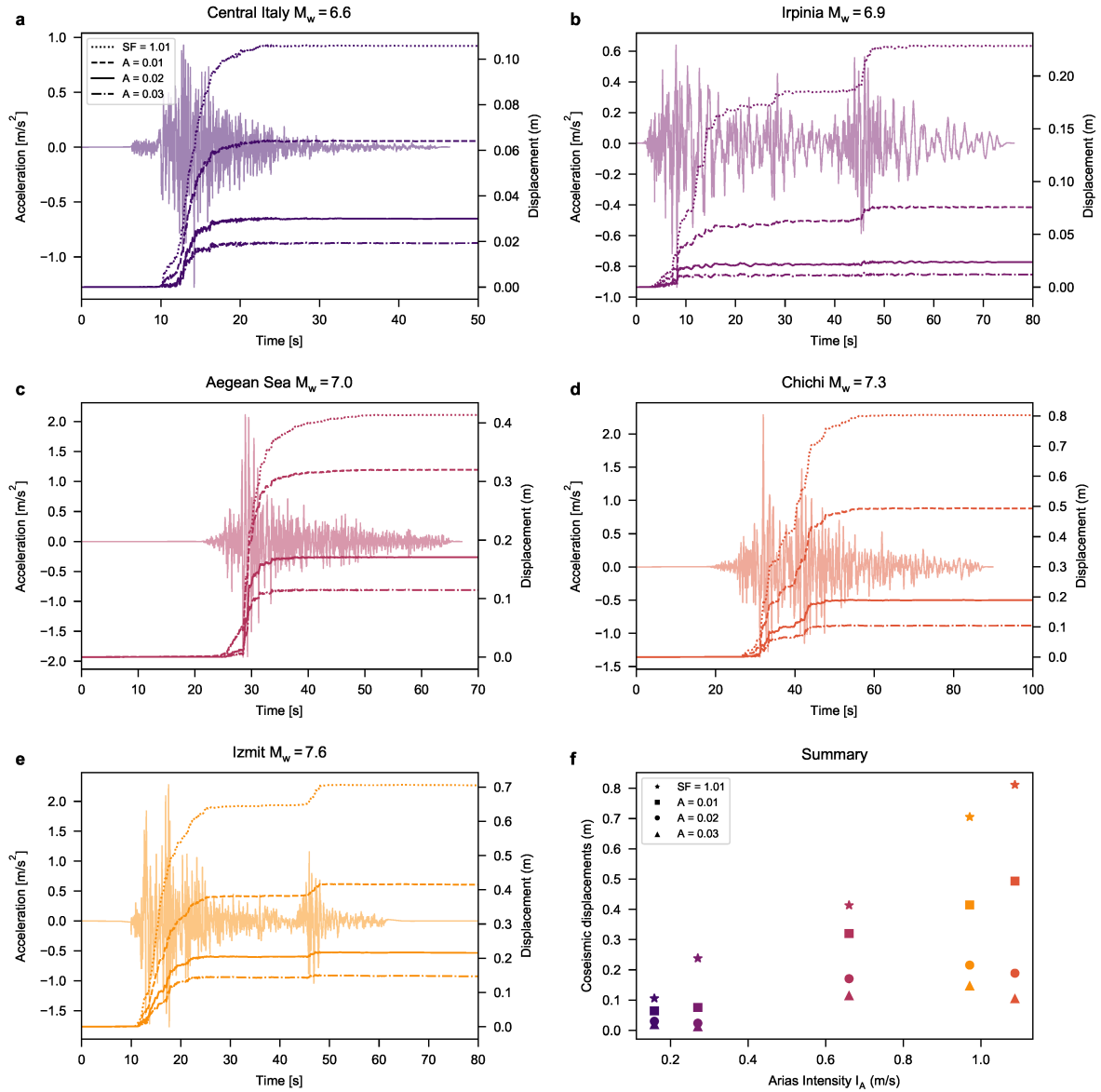
**Figure 6.13:** Results from parametric study. Ground acceleration and evolution of co-seismic displacements calculated at the bottom of the landslide (see Figure 6.12) for different earthquake events (a-e). The simulations are performed each for a rate independent shear zone and for three different rate dependency parameter A. Summary plot showing the final co-seismic displacements against the corresponding Arias intensity (f).

6.4.3. Simulation of pessimistic scenarios

The preceding simulations have shown that even when rate dependency is neglected, only moderate co-seismic displacements are to be expected. For this reason, the corresponding wave heights in the reservoir were not evaluated, as they are negligibly small. Based on the field and laboratory measurements, it can be assumed that these are realistic scenarios for the actual behaviour during a potential earthquake. However, there might be other effects which have not been considered so far and could cause a catastrophic response. These are, on the one hand, a potential softening in the landslide body (Kohler & Puzrin, 2022) due to the formation of new shear zones in other fine graded layers or the generation of excess pore water pressures due to cycling loading (e.g. in the sandy layers). On the other hand, a strength reduction in the shear zone also due to excess pore pressures as a consequence of cycling loading (Kohler & Puzrin, 2023), frictional heating (Alonso et al., 2016; Vardoulakis, 2002) or other reasons for negative rate effects (Tika et al., 1996). In order to assess these scenarios, additional simulations are performed where a softening of the landslides mass from the peak values φ, c to the residual values φ_r, c_r (Table 6.1) and a rate softening in the shear zone ($A < 0$) are included. Due to the introduction of negative rate dependency, the initial safety factor $SF = 1.1$ is assumed, which does not represent an active state of the landslide, but is necessary to keep it in an equilibrium state before the earthquake.

The results of the simulations are presented in Figure 6.14. The evolution of displacements (Figure 6.14a) shows that a small negative rate effect, even when combined with a softening in the landslide mass, does only slightly increase the landslide displacements compared to the rate independent case. Assuming a strong negative rate effect ($A = -0.01$), the landslide starts accelerating even before the earthquake and thus is in an initially unstable state. When this is combined with the softening of the landslide mass, a considerably larger acceleration occurs. This is illustrated by the corresponding landslide velocity and mobilized friction coefficient in the shear zone (Figure 6.14b). The earthquake in this case has only a marginal influence on the landslide. It should be emphasized that the landslide does not reach a stable state at the end, but exhibits an unstable stick-slip behaviour and continues to move at a velocity of about 1 m per day. The spatial distribution of displacements (Figure 6.14c, d) and velocities (Figure 6.14e, f) shows that the landslide initially moves as a coherent body. However, the final displacements reveal that two new shear surfaces were formed due to the softening in the landslide mass. While the upper part experienced larger displacements, the submerged foot of the landslide moved less, due to resistance of the reservoir. The evolution of the vertical displacement of different points on the water surface allows an estimation of the wave height in the reservoir (Figure 6.14g). The highest wave of about half a meter occurs on by breaking on the steep opposite rock flank. The freeboard of the reservoir exceeds this wave height by far and thus an overtopping seems unlikely based on this simulation.
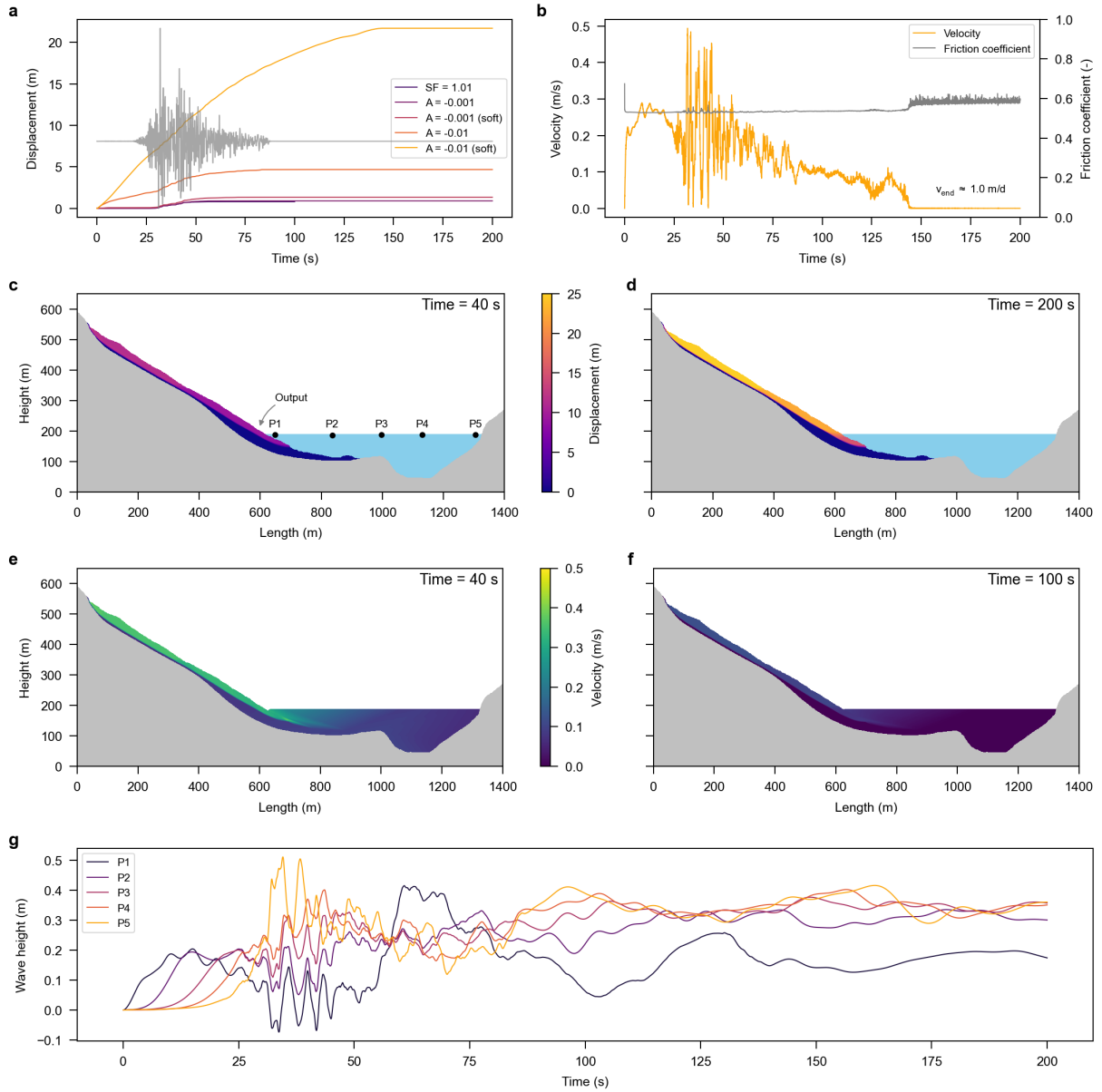
Figure 6.14: Results from the pessimistic simulation. Earthquake acceleration and evolution of landslide displacements at the bottom (marked in c) for different scenarios, where "soft" referrers to the softening in the landslide mass (a). Landslide velocity and mobilized friction coefficient in the shear zone for the worst scenario (b). Spatial distribution of displacements (c and d) and velocities (e and f). Wave height for the worst scenario at different locations (marked in c) along the water surface (g). The applied ground motion is from the Chichi earthquake.

6.5. Discussion

6.5.1. Field and lab measurements

High quality field measurements and lab experiments are critical for achieving a better understanding of the mechanical behaviour of a landslide. Although, they are equally important and complementary to each other, they can provide inconsistent results (Z. Li et al., 2020; van Asch et al., 2007). This has also been encountered in this study when determining the properties of the shear zone. All samples retrieved from the shear zone have a significant gravel content, which has a great influence on the shear resistance (Chang & Phantachang, 2016). Furthermore, the inhomogeneous structure of the landslide with cobbles and boulders can also have a strong influence (C. Wang et al., 2021). This highlights the importance of field measurements and back calculations. However, care should be taken when extrapolating rate effects from slow annual movements to the high velocities that may occur during an earthquake. For the presented landslide, the comparison with ring shear tests performed on shear zone samples shows a good agreement over a wide range of velocities. This is assumed to be due to the fact that the fine matrix controls rate effects in the shear zone (Y. R. Li et al., 2013; Wen & Jiang, 2017).

The seismometers were installed primarily to record moderate to strong earthquakes and a potential response of the landslide by the SAA chain. While no such earthquakes occurred during the 2.5 years of monitoring, valuable information could be also gained from several recorded weak motions. They provided important geophysical information and helped to assess amplification inside the landslide. The relevance of site amplification in seismic slope stability assessment is widely acknowledged (e.g. Bourdeau & Havenith, 2008; Del Gaudio & Wasowski, 2011) and should not be neglected, even though a direct relation between the observed amplification and potential co-seismic displacement cannot be established (e.g., Gischig et al. (2015)).

6.5.2. Co-seismic displacements

Considering the mobile quasi-static state of an active landslide, large co-seismic displacements can be expected and would also be predicted by a classical Newmark type analysis. Nevertheless, the simulations presented here show rather small displacements, even for a strong earthquake and even after neglecting the rate hardening effect. Similar results have been found in other studies (Kohler & Puzrin, 2022; Pinyol et al., 2022), which highlights the importance of the model representing the actual kinematics of a landslide. Observations of real landslides confirm these numerical results. For example, La Sorbella landslide shows co-seismic displacements of less than 1 mm during three earthquakes of the central Italy sequence (Ruggeri et al., 2020). The Maca landslide in Peru also moved only a few centimetres during two earthquakes (Bontemps et al., 2020; Lacroix et al., 2014). Similar observations were made for numerous landslides during the strong Sarpol-e-Zahab (Iran) and Gorkha (Nepal) earthquakes using remote sensing techniques (e.g. InSAR), with only one showing a displacement

greater than one meter (Cheaib et al., 2022; Lacroix et al., 2022). Furthermore, Keefer (1984) concluded from the study of 40 earthquakes that pre-existing deep-seated landslides generally do not get reactivated during earthquakes with moderate to large magnitudes.

The observations and simulations suggest that active landslides are significantly less susceptible to earthquakes than previously thought and a rather moderate response can be expected. This finding is supported by the fact that most of these landslides are rather old and thus likely to have withstood various extreme events such as strong earthquakes or heavy rainfalls. In addition, these often are the remains of historical catastrophic landslide events and processes involving large strength losses have already been completed. This is especially true for the Marsc landslide and the presented scenario with significant softening of landslide mass can be considered very unlikely. Based on the ring shear tests, negative rate effects in the shear zone can also be excluded. On the contrary, the experimental results indicate a larger increase in shear resistance at very high velocities, which was neglected in the presented simulations. It should also be pointed out that the introduction of a negative rate dependency over the entire velocity range requires a pre-seismic state with a safety factors higher than one. The usually observed slow movements controlled by hydrology (e.g. Carlà et al., 2021; Pinyol et al., 2022) would not be possible under such conditions.

6.5.3. Catastrophic collapse

Despite the expected small co-seismic displacements and the rather unlikely scenario of a catastrophic collapse, it is important to also include pessimistic scenarios given the potential consequences for a water reservoir and the valley below. This is emphasized by the event of Vajont (Hendron & Patton, 1987) and other landslides showing a transition from slow-moving to a fast acceleration (Carlà et al., 2019; Handwerger et al., 2019; Intrieri et al., 2018). However, the scenarios simulated here show that, even under these pessimistic assumptions, no severe consequences are expected for the Marsc landslide. Although negative rate effects have been observed in laboratory tests on different soils (Tika et al., 1996), they have not been confirmed in the ring shear tests on the Marsc landslide material. The residual strength of the landslide mass was assumed to be equal to the value, which was back-calculated for the shear zone. This is a rather conservative assumption for the gravelly stratigraphy.

A major difference of the catastrophic events is that these are often characterized by rather brittle material behaviour due to the presence of rock. A similarly brittle behaviour is found in soil slopes primarily during first-time failure, where mechanisms such as strain softening (Skempton, 1985) or cyclic excess pressures (Kramer, 1996) are dominant. These effects are one of the main reasons for the seismic triggering of debris flows and are often observed during strong earthquakes (Rodríguez et al., 1999; Yang et al., 2014). An old slow-moving landslide that has probably experienced several extreme events during its life, behaves much more ductile and is less likely to fail suddenly. As the case of Vajont shows, caution is required when the hydro-mechanical condition of a landslide is significantly disturbed

(e.g., by filling of the reservoir). Although, the Marsc landslide is strongly influenced by the reservoir, the history and the continuous monitoring has shown that this lies well within an acceptable range. This is confirmed by the Three Gorges Project in China, where it was found that the risk of catastrophic landslide events was mainly concentrated to the period of filling the reservoir (Yin et al., 2016). Furthermore, the Vajont landslide is characterized by rather different geological conditions of a rockslide and a thin, clayey basal sliding surface (Paronuzzi et al., 2021), which is believed to have caused the collapse due to frictional heating (Alonso et al., 2016; Vardoulakis, 2002).

6.5.4. Limitations

In this study, only co-seismic displacements of the landslide are modelled and the post-seismic motion observed for several active landslides (Lacroix et al., 2022, 2014) is not considered. Following the results of a recent study by Kohler & Puzrin (2023), excess pore pressure generated during the earthquake could propagate into the shear zone leading to a period of increased landslide velocity for several days to weeks. For the generation of tsunami waves, however, this effect is less relevant. When considering structures in contact with a landslide, this can be important and should be investigated in the future using suitable constitutive models. This requires the application of a hydro-mechanically coupled approach, which would also allow to further investigate the interplay between the landslides and the hydrological conditions. In fact, the examination of slope failures in the epicentral area of the 1980 Irpinia earthquake has revealed that the hydrological conditions greatly affect the seismic susceptibility of pre-existing landslides (Wasowski et al., 2002). Furthermore, the nonlinear stress-strain behaviour of soil during cycling loading (Kramer, 1996) and potential liquefaction of the landslide mass could strongly influence the landslide acceleration and the simulated co-seismic displacements. However, this does not only apply to active landslides but also to initially stable slopes. Based on the findings from this study, it can be assumed that first time failures are more susceptible to a catastrophic collapse than slow-moving landslides, as they have a greater potential for softening mechanisms and a more brittle behaviour.

It should be pointed out that a two-dimensional hydrodynamic model does not provide an accurate representation of the reservoir. In order to properly assess the generation and propagation of tsunami waves a three-dimensional model covering the entire basin is necessary (Cicoira et al., 2022; Rauter et al., 2022). For the Marsc landslide this is of particular importance, because, unlike Vajont, the landslide is small compared to the reservoir (Crosta et al., 2016). For this very reason, the predicted wave heights can be considered conservative. Another shortcoming of the presented approach is the strict separation of the water and soil material. The entrainment of water at the landslide toe and the transformation into turbidity currents can influence the results and should be investigated further by coupled techniques (Bandara & Soga, 2015; Yamaguchi et al., 2019).

6.6. Conclusions

We present a case study of an active slow-moving landslide at the flank of a water reservoir in the Swiss Alps. Extensive field investigations and measurements allow a profound understanding of the kinematics of the landslides and its dependency on the hydrological conditions. This reveals the interaction between groundwater table in the landslide, reservoir level and observed velocities, and forms the basis for geotechnical landslide model. We show how the rate dependency parameters of the shear zone can be back-calculated from these field measurements and extrapolated to high velocities using ring shear tests. Two installed seismometers, in a borehole and at the surface, allow quantifying the amplification within the soil mass based on recorded earthquake signals.

We show that MPM provides a suitable numerical approach to model the response to earthquakes. The recorded earthquake signals are used to validate the MPM model for low magnitude events. For a landslide at the flank of a water reservoir, the main interest lies in a potential risk of tsunami waves caused by a catastrophic collapse of the landslide. Therefore, the model is subjected to different strong motions from past events. These simulations confirm previous findings of co-seismic displacements in the range of a few centimetres to about one metre, even when rate hardening effects in the shear zone are neglected. Although, this can cause major damage to structures on or in contact with the landslide, regarding the generation of waves such displacements are insignificant. Despite being rather unlikely, more pessimistic scenarios are investigated where negative rate effects in the shear zone and a softening in the landslide mass is considered. We show that this can indeed cause a collapse of the slope and generate waves in the reservoir. However, the corresponding wave heights from the two-dimensional analysis would not even overtop the dam. The wide range of co-seismic displacement for different modelled scenarios, emphasizes the importance of properly assessing rate effects in the shear zone. In case of sensitive structures or housing built on the landslide it is essential to rule out any negative rate effects.

In general, with this case study, we illustrate the entire process of formulating and calibrating an accurate mechanical model to investigate landslide response to earthquakes, which will result in a more reliable risk assessment for slow-moving landslides. Based on our simulations in this and other studies it can be concluded that active landslides, despite their mobile state, can be less susceptible to co-seismic acceleration than it has been previously intuitively implied and even supported by the conventional Newmark's analysis.

Acknowledgments

Notations

Small Latin letters

a_θ^{top}	acceleration time history of top seismometer in θ-direction	n_{MP}	number of MPs per grid cell
a_θ^{bot}	acceleration time history of bottom seismometer in θ-direction	p	pressure
base	elastic base	s	deviatoric stress tensor
c	cohesion	shear	shear zone
c_s	speed of sound	soil	soil mass
d_{max}	depth of maximal wave velocity	tr($\bullet$)	trace of tensor
f	frequency	v_0	reference velocity
$f(\boldsymbol{\tau})$	failure surface	v_p	pressure wave velocity
$g(\boldsymbol{\tau})$	plastic potential	v_s	shear wave velocity
h	grid size (MPM)		

Capital Latin letters

A	viscosity parameter	$J_1(\bullet)$	first invariant of tensor
$\boldsymbol{B}^e$	elastic left Cauchy-Green strain tensor	$J_2(\bullet)$	second invariant of tensor
$\boldsymbol{F}$	deformation gradient	M_W	earthquake magnitude
$\boldsymbol{F}^e$	elastic deformation gradient	PGA_h	horizontal peak ground acceleration
$\boldsymbol{F}^p$	plastic deformation gradient	PGA_v	vertical peak ground acceleration
$F_\theta(\omega)$	transfer function in θ-direction	R_{epi}	epicentral distance
$\boldsymbol{I}$	identity tensor	SF	safety factor
I_A	Arias intensity		

Small Greek letters

α	plastic strain	ρ	density
$\dot{\alpha}$	rate of plastic strain	ρ_0	reference density
$\dot{\alpha}_0$	reference strain rate	$\boldsymbol{\sigma}$	Cauchy stress tensor
β	slope inclination (benchmark)	$\boldsymbol{\tau}$	Kirchhoff stress tensor
γ	Cole exponent for water	$\boldsymbol{\tau}^e$	elastic Kirchhoff stress tensor
δ_r	residual shear displacement	τ_{max}	maximal principle stress
δ_s	shear zone thickness	τ_{min}	minimal principle stress
$\boldsymbol{\varepsilon}$	Hencky strain tensor	$\boldsymbol{\tau}^v$	viscous Kirchhoff stress tensor
η	viscosity	φ	friction angle
θ	direction	φ_r	residual friction angle
λ	first Lamé constant	φ_0	reference friction angle
μ	second Lamé constant / friction coefficient	φ_r^{NA}	non-associated residual friction angle
μ_0	slow residual friction coefficient	ψ	dilation angle
ξ	damping ratio	ω	angular frequency

References

Abdoun, T., Bennett, V., Thevanayagam, S., Dobry, R., Shantz, T. & Jang, D. (2009). Wireless MEMS-based System For Real-timeGeotechnical Instrumentation Of Active Slopes. *WIT Transactions on The Built Environment*, *108*, 617–624. https://doi.org/10.2495/SAFE090571

Alonso, E. E., Zervos, A. & Pinyol, N. M. (2016). Thermo-poro-mechanical analysis of landslides: from creeping behaviour to catastrophic failure. *Géotechnique*, *66*(3), 202–219. https://doi.org/10.1680/jgeot.15.LM.006

Alvarado, M., Pinyol, N. M. & Alonso, E. E. (2019). Landslide motion assessment including rate effects and thermal interactions: Revisiting the canelles landslide. *Canadian Geotechnical Journal*, *56*(9), 1338–1350. https://doi.org/10.1139/cgj-2018-0779

Andersen, S. & Andersen, L. (2010). Modelling of landslides with the material-point method. *Computational Geosciences*, *14*(1), 137–147. https://doi.org/10.1007/s10596-009-9137-y

Bandara, S., Ferrari, A. & Laloui, L. (2016). Modelling landslides in unsaturated slopes subjected to rainfall infiltration using material point method. *International Journal for Numerical and Analytical Methods in Geomechanics*, *40*(9), 1358–1380. https://doi.org/10.1002/nag.2499

Bandara, S. & Soga, K. (2015). Coupling of soil deformation and pore fluid flow using material point method. *Computers and Geotechnics*, *63*, 199–214. https://doi.org/10.1016/J.COMPGEO.2014.09.009

Batchelor, G. K. (1967). *An Introduction to Fluid Dynamics*. Cambridge University Press. https://doi.org/10.1063/1.3060769

Baumer, A. (1964). Geologie der gotthardmassivisch-penninischen Grenzregion im oberen Bleniotal. https://doi.org/10.3929/ETHZ-A-000089708

Baumer, A. (1993). Diga Luzzone - Rapporto Geologico. Internal report.

Baumer, A., Egli, W., Frey, J. D., Riemann, W., Uhr, A., Vögeli, S. & Wiederkehr, M. (2013). *Blatt 1233 Greina - Geologischer Atlas Schweiz 1:25 000*. Bundesamt für Landestopografie swisstopo.

Bontemps, N., Lacroix, P., Larose, E., Jara, J. & Taipe, E. (2020). Rain and small earthquakes maintain a slow-moving landslide in a persistent critical state. *Nature Communications*, *11*(1), 1–10. https://doi.org/10.1038/s41467-020-14445-3

Bourdeau, C. & Havenith, H. B. (2008). Site effects modelling applied to the slope affected by the Suusamyr earthquake (Kyrgyzstan, 1992). *Engineering Geology*, *97*(3–4), 126–145. https://doi.org/10.1016/J.ENGGEO.2007.12.009

Carlà, T., Gigli, G., Lombardi, L., Nocentini, M. & Casagli, N. (2021). Monitoring and analysis of the exceptional displacements affecting debris at the top of a highly disaggregated rockslide. *Engineering Geology*, *294*, 106345. https://doi.org/10.1016/J.ENGGEO.2021.106345

Carlà, T., Intrieri, E., Raspini, F., Bardi, F., Farina, P., Ferretti, A., … Casagli, N. (2019). Perspectives on the prediction of catastrophic slope failures from satellite InSAR. *Scientific Reports*, *9*(1), 1–9. https://doi.org/10.1038/s41598-019-50792-y

Cevasco, A., Termini, F., Valentino, R., Meisina, C., Bonì, R., Bordoni, M., … De Vita, P. (2018). Residual mechanisms and kinematics of the relict Lemeglio coastal landslide (Liguria, northwestern Italy). *Geomorphology*, *320*, 64–81. https://doi.org/10.1016/J.GEOMORPH.2018.08.010

Chang, W. J. & Phantachang, T. (2016). Effects of gravel content on shear resistance of gravelly soils. *Engineering Geology*, *207*, 78–90. https://doi.org/10.1016/J.ENGGEO.2016.04.015

Cheaib, A., Lacroix, P., Zerathe, S., Jongmans, D., Ajorlou, N., Doin, M. P., … Abdallah, C. (2022).

Landslides induced by the 2017 Mw7.3 Sarpol Zahab earthquake (Iran). *Landslides*, *19*(3), 603–619. https://doi.org/10.1007/S10346-021-01832-0

Cicoira, A., Blatny, L., Li, X., Trottet, B. & Gaume, J. (2022). Towards a predictive multi-phase model for alpine mass movements and process cascades. *Engineering Geology*, *310*, 106866. https://doi.org/10.1016/J.ENGGEO.2022.106866

Cole, R. H. (1948). *Underwater explosions*. Princton University Press.

Comité Européen de Normalisation. (2004). *EN 1998-1 Eurocode 8: design of structures for earthquake resistance, part 1: general rules, seismic actions and rules for buildings*. European Committee for Standardization.

Corominas, J., Moya, J., Ledesma, A., Lloret, A. & Gili, J. A. (2005). Prediction of ground displacements and velocities from groundwater level changes at the Vallcebre landslide (Eastern Pyrenees, Spain). *Landslides*, *2*(2), 83–96. https://doi.org/10.1007/S10346-005-0049-1

Crosta, G. B., Imposimato, S. & Roddeman, D. (2016). Landslide spreading, impulse water waves and modelling of the Vajont rockslide. *Rock Mechanics and Rock Engineering*, *49*(6), 2413–2436. https://doi.org/10.1007/S00603-015-0769-Z/TABLES/1

Cruden, D. M. & Varnes, D. J. (1996). Landslide types and processes. *Special Report - National Research Council, Transportation Research Board*, *247*.

Del Gaudio, V. & Wasowski, J. (2011). Advances and problems in understanding the seismic response of potentially unstable slopes. *Engineering Geology*, *122*(1–2), 73–83. https://doi.org/10.1016/J.ENGGEO.2010.09.007

Gischig, V. S., Eberhardt, E., Moore, J. R. & Hungr, O. (2015). On the seismic response of deep-seated rock slope instabilities — Insights from numerical modeling. *Engineering Geology*, *193*, 1–18. https://doi.org/10.1016/J.ENGGEO.2015.04.003

Grünefelder e Partner SA. (2022). Bacino Luzzone - Frana sponda sinistra, Misurazioni geodetiche di controllo. Internal report.

Gylfadóttir, S. S., Kim, J., Helgason, J. K., Brynjólfsson, S., Höskuldsson, Á., Jóhannesson, T., … Løvholt, F. (2017). The 2014 Lake Askja rockslide-induced tsunami: Optimization of numerical tsunami model using observed data. *Journal of Geophysical Research: Oceans*, *122*(5), 4110–4122. https://doi.org/10.1002/2016JC012496

Halter, H. (1994). Speicher Luzzone - Geotechnische Untersuchung zur Stabilität der linksufrigen Böschung. Internal report.

Handwerger, A. L., Huang, M. H., Fielding, E. J., Booth, A. M. & Bürgmann, R. (2019). A shift from drought to extreme rainfall drives a stable landslide to catastrophic failure. *Scientific Reports*, *9*(1), 1–12. https://doi.org/10.1038/s41598-018-38300-0

Handwerger, A. L., Rempel, A. W., Skarbek, R. M., Roering, J. J. & Hilley, G. E. (2016). Rate-weakening friction characterizes both slow sliding and catastrophic failure of landslides. *Proceedings of the National Academy of Sciences*, *113*(37), 10281–10286. https://doi.org/10.1073/pnas.1607009113

Harbitz, C. B., Glimsdal, S., Løvholt, F., Kveldsvik, V., Pedersen, G. K. & Jensen, A. (2014). Rockslide tsunamis in complex fjords: From an unstable rock slope at Åkerneset to tsunami risk in western Norway. *Coastal Engineering*, *88*, 101–122. https://doi.org/10.1016/J.COASTALENG.2014.02.003

Hashash, Y. M. & Groholski, D. R. (2010). Recent advances in non-linear site response analysis. *Fifth Interantional Conference on Recent Advances in Geotechnical Earthquake Engineering and Soil Dynamics and Symposium in Honor of Professor I.M. Idriss*, *29*(6), 1–22.

Hencky, H. (1928). Über die Form des Elastizitätsgesetzes bei ideal elastischen Stoffen. *Zeitschrift Für Technische Physik*, *6*.

Hendron, A. J. & Patton, F. D. (1987). The vaiont slide — A geotechnical analysis based on new geologic observations of the failure surface. *Engineering Geology*, *24*(1–4), 475–491. https://doi.org/10.1016/0013-7952(87)90080-9

Intrieri, E., Raspini, F., Fumagalli, A., Lu, P., Del Conte, S., Farina, P., … Casagli, N. (2018). The Maoxian landslide as seen from space: detecting precursors of failure with Sentinel-1 data. *Landslides*, *15*(1), 123–133. https://doi.org/10.1007/S10346-017-0915-7

Jiang, C., Selle, A., Teran, J. & Stomakhin, A. (2015). The Affine Particle-In-Cell Method. *ACM Transactions on Graphics*, *34*(4).

Jibson, R. W. (2007). Regression models for estimating coseismic landslide displacement. *Engineering Geology*, *91*(2–4), 209–218. https://doi.org/10.1016/J.ENGGEO.2007.01.013

Jibson, R. W., Prentice, C. S., Borissoff, B. A., Rogozhin, E. A. & Langer, C. J. (1994). Some observations of landslides triggered by the 29 April 1991 Racha earthquake, Republic of Georgia. *Bulletin Seismological Society of America*, *84*(4), 963–973.

Keefer, D. K. (1984). Landslides caused by earthquakes. *GSA Bulletin*, *95*(4), 406–421.

Keefer, D. K. (2002). Investigating landslides caused by earthquakes - A historical review. *Surveys in Geophysics*, *23*(6), 473–510. https://doi.org/10.1023/A:1021274710840

Kohler, M. & Puzrin, A. M. (2022). Mechanism of Co-Seismic Deformation of the Slow-Moving La Sorbella Landslide in Italy Revealed by MPM Analysis. *Journal of Geophysical Research: Earth Surface*, *127*(7), e2022JF006618. https://doi.org/10.1029/2022JF006618

Kohler, M. & Puzrin, A. M. (2023). Mechanics of coseismic and postseismic acceleration of active landslides. *Communications Earth & Environment*. https://doi.org/10.1038/s43247-023-00797-3

Kohler, M., Stoecklin, A. & Puzrin, A. M. (2021). A MPM framework for large deformation seismic response analysis. *Canadian Geotechnical Journal*. https://doi.org/10.1139/cgj-2021-0252

Konno, K. & Ohmachi, T. (1998). Ground-motion characteristics estimated from spectral ratio between horizontal and vertical components of microtremor. *Bulletin of the Seismological Society of America*, *88*(1), 228–241. https://doi.org/10.1785/BSSA0880010228

Krabbenhoft, K., Karim, M. R., Lyamin, A. V. & Sloan, S. W. (2012). Associated computational plasticity schemes for nonassociated frictional materials. *International Journal for Numerical Methods in Engineering*, *90*(9), 1089–1117. https://doi.org/10.1002/NME.3358

Kramer, S. L. (1996). *Geotechnical Earthquake Engineering*. *Engineering* (Vol. 6). https://doi.org/10.1007/978-3-540-35783-4

Kramer, S. L. & Smith, M. W. (1997). Modified Newmark Model for Seismic Displacements of Compliant Slopes. *Journal of Geotechnical & Geoenvironmental Engineering*, *123*(July), 635–644. https://doi.org/10.1061/(ASCE)1090-0241(1997)123:7(635)

Lacroix, P., Gavillon, T., Bouchant, C., Lavé, J., Mugnier, J. L., Dhungel, S. & Vernier, F. (2022). SAR and optical images correlation illuminates post-seismic landslide motion after the Mw 7.8 Gorkha earthquake (Nepal). *Scientific Reports*, *12*(1), 1–13. https://doi.org/10.1038/s41598-022-10016-2

Lacroix, P., Handwerger, A. L. & Bièvre, G. (2020). Life and death of slow-moving landslides. *Nature Reviews Earth and Environment*, *1*(8), 404–419. https://doi.org/10.1038/S43017-020-0072-8

Lacroix, P., Perfettini, H., Taipe, E. & Guillier, B. (2014). Coseismic and postseismic motion of a landslide: observations, modelling, and analogy with tectonic faults. *Geophysical Research Letters*, *41*, 6676–6680. https://doi.org/10.1002/2014GL061170

Lee, E. H. (1969). Elastic-Plastic Deformation at Finite Strains. *Journal of Applied Mechanics*, *36*(1), 1–6. https://doi.org/10.1115/1.3564580

Leupold, W. (1954). Geologisches Gutachten zur Akkumulieranlage im Luzzonetal. Internal report.

Li, Y. R., Wen, B. P., Aydin, A. & Ju, N. P. (2013). Ring shear tests on slip zone soils of three giant landslides in the Three Gorges Project area. *Engineering Geology*, *154*, 106–115. https://doi.org/10.1016/J.ENGGEO.2012.12.015

Li, Z., Hu, F., Qi, S., Hu, R., Zhou, Y. & Bai, Y. (2020). Deformation characteristics of the shear zone and movement of block stones in soil-rock mixtures based on large-sized shear test. *Applied Sciences (Switzerland)*, *10*(18), 6475. https://doi.org/10.3390/APP10186475

Luzi, L., Lanzano, G., Felicetta, C., D'Amico, C. M., Russo, E., Sgobba, S., … Group, O. W. (2020). Engineering Strong Motion database (ESM) (Version 2.0). https://doi.org/10.13127/ESM.2

Lysmer, J. & Kuhlemeyer, R. L. (1969). Finite Difference Model for Infinite Media. *Journal of Engineering Mechanics*, *95*, 859–877.

Mansour, M. F., Morgenstern, N. R. & Martin, C. D. (2011). Expected damage from displacement of slow-moving slides. *Landslides*, *8*(1), 117–131. https://doi.org/10.1007/S10346-010-0227-7

Monaghan, J. J. (1994). Simulating Free Surface Flows with SPH. *Journal of Computational Physics*, *110*(2), 399–406. https://doi.org/10.1006/JCPH.1994.1034

Newmark, N. M. (1965). Effects of Earthquakes on Dams and Embankments. *Géotechnique*, *15*(2), 139–160. https://doi.org/10.1680/geot.1965.15.2.139

Optum, C. E. (2021). Optum G2. Retrieved from www.optumce.com

Paronuzzi, P., Bolla, A., Pinto, D., Lenaz, D. & Soccal, M. (2021). The clays involved in the 1963 Vajont landslide: Genesis and geomechanical implications. *Engineering Geology*, *294*, 106376. https://doi.org/10.1016/J.ENGGEO.2021.106376

Pfiffner, O. A. (2009). *Geologie der Alpen. Geologie der Alpen*. Bern: Haupt. https://doi.org/10.36198/9783838586106

Pfiffner, O. A., Frei, W., Valasek, P., Stäuble, M., Levato, L., DuBois, L., … Smithson, S. B. (1990). Grustal shortening in the Alpine Orogen: Results from deep seismic reflection profiling in the eastern Swiss Alps, Line NFP 20-east. *Tectonics*, *9*(6), 1327–1355. https://doi.org/10.1029/TC009I006P01327

Pinyol, N. M., Di Carluccio, G. & Alonso, E. E. (2022). A slow and complex landslide under static and seismic action. *Engineering Geology*, *297*, 106478. https://doi.org/10.1016/j.enggeo.2021.106478

Puzrin, A. M., Schmit, A. & Schwager, M. V. (2012). Case studies of constrained creeping landslides in Switzerland. *Proceedings of 11th International Symposium on Landslides and Engineered Slopes ISL*, *2*, 1795–1800.

Rauter, M., Viroulet, S., Gylfadóttir, S. S., Fellin, W. & Løvholt, F. (2022). Granular porous landslide tsunami modelling – the 2014 Lake Askja flank collapse. *Nature Communications*, *13*(1), 1–13. https://doi.org/10.1038/s41467-022-28296-7

Roberts, N. J., McKillop, R. J., Lawrence, M. S., Psutka, J. F., Clague, J. J., Brideau, M. A. & Ward, B. C. (2013). Impacts of the 2007 landslide-generated Tsunami in Chehalis Lake, Canada. *Landslide Science and Practice: Risk Assessment, Management and Mitigation*, *6*, 133–140. https://doi.org/10.1007/978-3-642-31319-6_19

Rodríguez, C. E., Bommer, J. J. & Chandler, R. J. (1999). Earthquake-induced landslides: 1980-1997. *Soil Dynamics and Earthquake Engineering*, *18*(5), 325–346. https://doi.org/10.1016/S0267-7261(99)00012-3

Rots, J. G., Nauta, P., Kusters, G. M. A. & Blaauwendraad, J. (1985). Smeared Crack Approach and Fracture Localization in Concrete. *Heron*, *30*(1).

Ruggeri, P., Fruzzetti, V. M. E., Ferretti, A. & Scarpelli, G. (2020). Seismic and Rainfall Induced Displacements of an Existing Landslide: Findings from the Continuous Monitoring. *Geosciences 2020, Vol. 10, Page 90*, *10*(3), 90. https://doi.org/10.3390/GEOSCIENCES10030090

Skempton, A. W. (1985). Residual strength of clays in landslides, folded strata and the laboratory. *Géotechnique*, *35*(1), 3–18. https://doi.org/10.1680/geot.1985.35.1.3

Soga, K., Alonso, E., Yerro, A., Kumar, K. & Bandara, S. (2016). Trends in large-deformation analysis of landslide mass movements with particular emphasis on the material point method. *Géotechnique*, *66*(3), 248–273. https://doi.org/10.1680/jgeot.15.LM.005

Stomakhin, A., Schroeder, C., Chai, L., Teran, J. & Selle, A. (2013). A material point method for snow simulation. *ACM Transactions on Graphics*, *32*(4), 1. https://doi.org/10.1145/2461912.2461948

Sulsky, D., Chen, Z. & Schreyer, H. L. (1994). A particle method for history-dependent materials. *Computer Methods in Applied Mechanics and Engineering*, *118*(1–2), 179–196. https://doi.org/10.1016/0045-7825(94)90112-0

Tika, T. E., Vaughan, P. R. & Lemos, L. J. (1996). Fast shearing of pre-existing shear zones in soil. *Géotechnique*, *46*(2), 197–233. https://doi.org/10.1680/geot.1996.46.2.197

van Asch, T. W. J., Van Beek, L. P. H. & Bogaard, T. A. (2007). Problems in predicting the mobility of slow-moving landslides. *Engineering Geology*, *91*(1), 46–55. https://doi.org/10.1016/J.ENGGEO.2006.12.012

Vardoulakis, I. (2002). Dynamic thermo-poro-mechanical analysis of catastrophic landslides. *Geotechnique*, *52*(3), 157–171. https://doi.org/10.1680/GEOT.2002.52.3.157

Vögeli, S., Galster, F. & Wiederkehr, M. (2013). *Greina (LK 1233) - Erläuterungen*. Bundesamt für Landestopografie swisstopo.

Wang, C., Dong, J., Huang, Z., Zhou, J. & Yang, J. (2021). Effect of Cobble Content on the Shear Behaviour of Sand-Cobble Mixtures. *Advances in Civil Engineering*, *2021*, 1–9. https://doi.org/10.1155/2021/5554617

Wang, W. M., Sluys, L. J. & De Borst, R. (1997). Viscoplasticity for instabilities due to strain softening and strain-rate softening. *International Journal for Numerical Methods in Engineering*, *40*(20), 3839–3864. https://doi.org/10.1002/(SICI)1097-0207(19971030)40:20<3839::AID-NME245>3.0.CO;2-6

Wasowski, J., Del Gaudio, V., Pierri, P. & Capolongo, D. (2002). Factors controlling seismic susceptibility of the Sele valley slopes: The case of the 1980 Irpinia earthquake re-examined. *Surveys in Geophysics*, *23*(6), 563–593. https://doi.org/10.1023/A:1021230928587

Wedage, A. M. P., Morgenstern, N. R. & Chan, D. H. (1998). A strain rate dependent constitutive model for clays at residual strength. *Canadian Geotechnical Journal*, *35*(2), 364–373. https://doi.org/10.1139/t97-085

Wen, B. P. & Jiang, X. Z. (2017). Effect of gravel content on creep behavior of clayey soil at residual state: implication for its role in slow-moving landslides. *Landslides*, *14*(2), 559–576. https://doi.org/10.1007/S10346-016-0709-3

Wolf, J. P. (1989). Soil-structure-interaction analysis in time domain. *Nuclear Engineering and Design*, *111*(3), 381–393. https://doi.org/10.1016/0029-5493(89)90249-5

Yamaguchi, Y., Takase, S., Moriguchi, S. & Terada, K. (2019). Solid–liquid coupled material point method for simulation of ground collapse with fluidization. *Computational Particle Mechanics*. https://doi.org/10.1007/s40571-019-00249-w

Yang, C. M., Yu, W. L., Dong, J. J., Kuo, C. Y., Shimamoto, T., Lee, C. T., … Miyamoto, Y. (2014). Initiation, movement, and run-out of the giant Tsaoling landslide — What can we learn from a simple rigid block model and a velocity–displacement dependent friction law? *Engineering Geology*, *182*(PB), 158–181. https://doi.org/10.1016/J.ENGGEO.2014.08.008

Yin, Y., Huang, B., Wang, W., Wei, Y., Ma, X., Ma, F. & Zhao, C. (2016). Reservoir-induced landslides and risk control in Three Gorges Project on Yangtze River, China. *Journal of Rock Mechanics and Geotechnical Engineering*, *8*(5), 577–595. https://doi.org/10.1016/J.JRMGE.2016.08.001

Zienkiewicz, O. C., Bicanic, N. & Shen, F. Q. (1989). Earthquake Input Definition and the Trasmitting Boundary Conditions. In *Advances in Computational Nonlinear Mechanics* (pp. 109–138). Vienna: Springer Vienna. https://doi.org/10.1007/978-3-7091-2828-2_3

7   Conclusions and Outlook

7.1.   Conclusions and main results

Active landslides pose a particular challenge in geotechnical engineering because standard safety assessment approaches are often not applicable, they are strongly influenced by environmental factors, and their size and heterogeneity make reliable modelling extremely difficult. In recent years, great efforts have been made to study and understand their behaviour under changing seasonal conditions. Their response to earthquakes, however, has been considerably less studied and appropriate models have been lacking. It was recognised that for a fundamental research on this topic all three components, namely *mechanical modelling*, *experimental testing* and *field investigation*, have to be addressed. Due to the lack of appropriate modelling techniques and laboratory test devices, new methods and technologies were developed for both aspects. Combined with an extensive field investigation campaign, a complete risk assessment of an active landslide has been demonstrated. These and the main findings are subsequently summarized.

7.1.1.   Mechanical modelling

The seismic behaviour of landslides was split into a co-seismic and post-seismic response. Each was addressed with a different modelling technique:
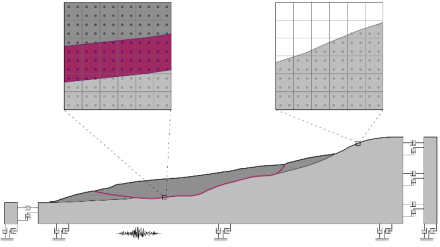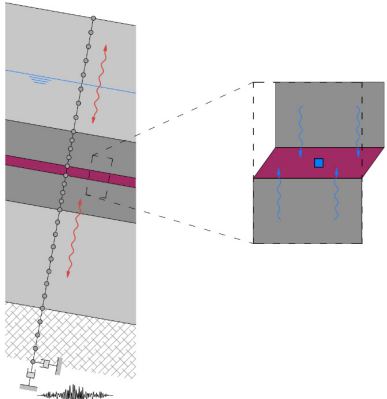
(i)   *Co-seismic*: The co-seismic response of active landslides or slopes in general is simulated by explicit, dynamic MPM. Therefore, a high performance MPM framework including rigorous large strain constitutive models and seismic boundary conditions was implemented in C++. The comparison to an independent FE simulation benchmarks the modelling technique and highlights the advantage for long duration strong motions. This approach was successfully applied to the slow-moving La Sorbella landslide in Italy, where co-seismic displacements were recorded during three moderate earthquakes. The 2D landslide geometry is represented in the model by an elastic base, an elastoplastic soil mass and a rate-dependent shear zone of finite thickness. The simulation of the recorded earthquakes allowed the landslide model to be validated. Furthermore, the unexpectedly small co-seismic displacements of the landslide can be explained by geometric effects, since the different parts of the landslide are accelerated to different degrees by the earthquake. The motion of the unstable upper part is restrained by the less mobilized lower part. The simulation for strong motions provides further insight into the mechanics of the landslide during seismic shaking and highlights the importance of geometry and rate effects. It was shown, that although the predicted displacement can cause severe damage to infrastructure, a catastrophic collapse can only be provoked by rate-softening behaviour in the shear zone in combination with a strain-softening landslide mass.

(ii)   *Post-seismic*: Based on the observed post-seismic landslide activity and its presumed origin in excess pore water pressures, a hydro-mechanically coupled FE model for infinite landslide conditions has been proposed. The landslide is represented by slope-parallel layers of base, stable soil, shear zone and landslide mass. The shear zone is modelled by a rate-hardening friction law and is assumed to have reached its critical state, thus no excess pore water pressure develops. As part of the stable soil and landslide mass, the so-called adjacent soil layers are introduced above and underneath the shear zone. These layers have not yet reached a critical state and are therefore susceptible to excess pore water pressure generation during cyclic loading. This pore pressure can later propagate into the shear zone leading to an acceleration of the landslide due to the reduction of the effective stress. This behaviour is considered using a multi-surface plasticity model. The comparison with field observations shows that this model can explain the post-seismic acceleration of active landslides over several days to months. A detailed parametric study reveals the underlying mechanisms and identifies the governing factors: (*i*) ground motion intensity; (*ii*) rate-dependency; (*iii*) pre-seismic velocity and (*iv*) consolidation time. The latter emphasises the analogy with one-dimensional consolidation theory, where the time for dissipation of the excess pore water pressure in the adjacent layers is controlled by their permeability and thickness.

An overview and comparison of the two models and the required inputs is provided in Table 7.1. Although the coupled FE model also includes the co-seismic response, a proper 2D MPM simulation is clearly preferable due to the strong influence of the geometry. Although the simulations for infinite landslide conditions cover the wide scatter of field observations and allow a general understanding of the mechanism, it is only of limited suitability for a single case study of co-seismic displacements. The post-seismic response, on the other hand, is more difficult to captures accurately, since the required constitutive parameters are usually not available. Even when cyclic tests are carried out on extracted soil samples, it is hardly possible to determine the exact in-situ conditions. Ultimately, such an exact simulation seems unreasonable, since two earthquakes of similar intensity (i.e. PGA, PGV and Arias intensity) can produce a response that is several orders of magnitude different. This method is therefore intended to provide a general understanding of the underlying mechanisms and to assess whether this phenomenon can occur in individual cases.

While the MPM model presented has only been applied in this thesis to slow-moving soil slides, it is readily applicable to the other types of active landslides. The framework allows great flexibility in representing different geometries and materials. In particular, active rockslides can be simulated using appropriate constitutive models and parameters. As the code developed is a full 3D implementation, simulations are not restricted to 2D geometries. However, the computational cost for most landslides are still extremely high and would require a coarse representation of the geometry for current high performance hardware.

Table 7.1: Overview and comparison of numerical models

	Co-seismic	Post-seismic
Particularities	2D geometry - large deformations 2D propagation of seismic waves - seismic boundary conditions	- infinite slope condition - hydro-mechanically coupled 1D propagation of seismic waves - seismic boundary conditions
Numerical approach	explicit, dynamic MPM	implicit, dynamic hydro-mechanically coupled FEM
Constitutive models	- base: elastic - soil mass: Mohr-Coulomb with isotropic softening - shear zone: rate-dependent, finite strain Drucker-Prager - water: Cole equation of state	- base: elastic - soil mass: multi-surface kinematic hardening model - shear zone: rate-dependent frictional
Required properties	- compressional and shear wave velocity - friction angle and cohesion - rate dependent strength of shear zone - density	- compressional and shear wave velocity - monotonic stress-strain curve or modulus reduction curve - shear strength and volumetric coupling parameters - rate dependent strength of shear zone - pre-seismic velocity - permeability - density
Further input	input ground motion	input ground motion

7.1.2. Experimental testing

To investigate the shearing behaviour of shear zones, an improved ring shear apparatus has been developed at ETH Zurich. This apparatus incorporates the latest developments of ring shear devices combined with an improved shear box, which allows reducing friction, and simultaneously preventing leakage of water and soil into the gap between the confinement rings. This allows reliable assessment of rate effects over a very wide range of shearing rates and, at the same time, provides insight into the thermo-hydro-mechanical processes through local pore water pressure and temperature sensors.

In contrast to the clay-dominated landslides materials, less is known about rate effects in materials characterized by a high content of granular fractions as they are often found in steep active landslides. Therefore, an extensive experimental program was conducted on shear zone samples from two alpine landslides in Switzerland. The results provide insight into the transient behaviour during slow to fast shearing and reveal a moderately positive rate effect. This is consistent with the observed behaviour of these landslides, which is controlled by the rate-dependency of the shear zone and pore water pressure changes due to precipitation.

It is shown that during rapid shear, either zero or negative pore water pressure is generated in these soils. While there was a temperature increase in the sample at high velocities, the associated water expansion was insufficient to compensate for the negative pressures. Only very rapid and extensive shearing resulted in considerable temperature and pore water pressure increases, confirming that frictional heating can indeed lead to excess pressures. However, the tested material only experiences this effect after prolonged shearing and does not result in a complete loss of shear strength. On the contrary, the reduction in shear strength causes a reduction in heat generation, allowing a new steady state to be reached. Based on these observations, catastrophic failure seems unlikely for these landslides. Nonetheless, the results suggest that less permeable soils may experience negative rate effects due to frictional heating during very rapid shearing.

7.1.3. Field investigation

The numerical and experimental investigations have shown that an active landslide is a complex system with various interactions. In order to understand the behaviour of such a landslide, extensive investigations and measurements are usually required. A case study was therefore carried out on the Marsc landslide at the Luzzone water reservoir in Switzerland. This provides an in-depth understanding of the kinematics of the landslide and reveals the interaction between the groundwater level in the landslide, the reservoir level and the observed velocities. This has been the basis for the formulation and calibration of the geotechnical landslide model. The main controlling factor, the rate-dependency in the shear zone, can be back-calculated from the field measurement. However, as this only covers the seasonal range of velocities, extrapolation to high velocities during seismic shaking needs to be critically assessed. This is where ring shear tests come in. These have shown that the shear zone material exhibits

a positive rate effect even during fast shearing. The subsequent simulations for different strong motions confirm previous findings of only small to moderate co-seismic displacements, even when the rate-hardening effect is neglected. In order to assess the potential risk of tsunami waves from a catastrophic collapse of the landslide, more pessimistic scenarios are investigated, taking into account negative rate effects in the shear zone and softening in the landslide mass. The simulations show that this could indeed cause waves in the reservoir, but these would not overtop the dam. Although negative rate effects due to frictional heating have been observed during very rapid shearing, such high velocity is only achieved in the simulation when negative rate effects are already present at low shear rates. Otherwise, even in the presence of an earthquake, the landslide would not accelerate to this extent and over such a long distance to generate this frictional heat. A catastrophic collapse due to frictional heating therefore seems unlikely.

7.1.4. Implications

All the results of this thesis indicate that active landslides can be less susceptible to co-seismic acceleration than previously thought. There are two main reasons for this - the rate dependency of the shear strength and the geometry of the landslide. Both are neglected by the conventional Newmark's sliding block analysis, making it unsuitable for active landslides. However, the MPM technique presented is a powerful tool that incorporates these and other factors that may be required for the analysis of other types of active landslides.

Seasonally varying velocity of an active landslide controlled by precipitation is usually assumed to be possible only for a rate-hardening shear strength. Small co-seismic displacements can be expected for such landslides if the shear zone also exhibits a positive or at least no negative rate effect at higher shear rates. This hypothesis is supported by the fact that these are often the remains of slope failures or old landslides that have already withstood such extreme events and show a rather ductile behaviour. A major difference of catastrophic events is that these are often characterized by rather brittle material behaviour due to the presence of rock or unsheared soil. This suggests that stable slopes may be more susceptible to catastrophic failure during strong earthquakes.

These findings does not imply that the seismic behaviour of active landslides is irrelevant. On the one hand, potential scenarios need to be carefully assessed if major consequences are to be expected, e.g. in the case of water reservoirs. On the other hand, if infrastructure and buildings are built on or in contact with the landslide, estimation of co- and post-seismic displacements can be critical. This leads to the proposed approach for a single case analysis shown in Table 7.2. The basis is provided by numerical modelling, with the complexity and accuracy of the model depending on the potential consequences and the reliability required. For a preliminary estimate of displacements or to simulate different scenarios, a parametric study based on literature values and a rough geometry may be sufficient. The model can be refined by field investigation if a more detailed study is necessary, or if the previous analysis has

identified potential problems. Again, the extent and thus the cost of these investigation depend on the required accuracy and reliability. Based on the above findings, a field campaign should have as its main objective the geotechnical characterisation in order to identify brittle material behaviour or softening mechanisms. If further refinement is needed, field monitoring can provide insight into the landslide behaviour and calibration of the numerical model. Finally, if samples are available, laboratory tests can be carried out. Once more, the focus should be on identifying softening mechanisms. A simple classification and consultation of literature values may be sufficient to carry out a parametric study for a remote landslide, whereas for houses and infrastructure a detailed characterisation of rate effects using ring shear testing may be required. In case post-seismic acceleration can be decisive, oedometer and cyclic tests (i.e. triax, simple shear or hollow cylinder) are recommended to investigate the cyclic generation of excess pore water pressure.

Table 7.2: Approach for single case analysis

	Mechanical modelling	Field investigation	Experimental testing
Goals / Topics	• co- and post-seismic simulations • modelling displacements & velocities • simulation of potential scenarios • hazard & risk assessment	• geotechnical characterization • geometry • kinematics • hydrology • seismic monitoring	• general material behaviour • material strength • rate effects • cyclic behaviour
Possible techniques and tools	• MPM • FEM	• geological exploration • inclinometer, pore water pressure sensors • remote sensing, GNSS, tachymetry • surface wave analysis, borehole testing, seismometer	• classification • ring shear • oedometer • triax • simple shear • hollow cylinder

7.2.   Outlook and future research

Unfortunately, there are only a few documented cases of active landslides where co-seismic displacements have been measured. This may indeed indicate that active landslides are less susceptible to a seismic acceleration than previously assumed. Nevertheless, it is important to apply the presented approach to further case studies. In particular, validation for moderate co-seismic displacements in the range of a few metres is still pending. Many of the active landslides are rather remote and therefore not of direct interest, but thanks to the increasing number of studies using remote sensing technologies, it is expected that they will contribute to further research.

The presented model for the co-seismic analysis can be used to simulate different types of active landslides due to the flexibility of MPM. In this work, however, this has only been done for slow-moving soil slides, making the application to rockslides an important next step. Due to the more brittle behaviour of rock, it is to be expected that these can be more susceptible for a co-seismic acceleration. This needs to be investigated using appropriate constitutive models and parametric/case studies.

For the generation of tsunami waves, post-seismic acceleration is usually not of interest, as this is still a slow process of days to months. For infrastructures in contact with an active landslides, however, the situation is different. For such an analysis, it can be of interest to include the correct geometry in the simulation. The recently developed coupled MPM represents a suitable extension of the presented landslide model and would allow to study this topic and assess such cases. This would also enable the effect of liquefaction of the landslide mass by cyclic shearing to be investigated. While this seems unlikely for the permeable gravel-dominated Marsc landslide, it may be a critical mechanism for fine-grained landslides.

For future landslide assessment, it is important to refine the knowledge of rate effects in landslide shear zones and create a large dataset for the typical soils. The aim for a widespread engineering application is to avoid the need for extensive and complex ring shear tests, which are usually not available. The preliminary results on very rapid shearing have confirmed that the phenomenon of frictional heating can indeed lead to an increase in pore water pressure. Whilst this is not very pronounced in the materials tested, the results suggest that in less permeable soils frictional heating may be a source of negative rate effects. Experimental investigation of other soils is therefore essential.